Structural Evolution and Mechanisms of Fatigue in Polycrystalline Brass

Carstensen, Jesper Vejlø

Publication date:
1998

Document Version
Publisher's PDF, also known as Version of record

Citation (APA):
Carstensen, J. V. (1998). Structural Evolution and Mechanisms of Fatigue in Polycrystalline Brass. Technical University of Denmark, Danish Center for Applied Mathematics and Mechanics. (DCAMM report; No. S79). (Denmark. Forskningscenter Risoe. Risoe-R; No. 1005(EN)).

Risø-R-1005(EN)

Structural Evolution and Mechanisms of Fatigue in Polycrystalline Brass

Jesper Vejlø Carstensen

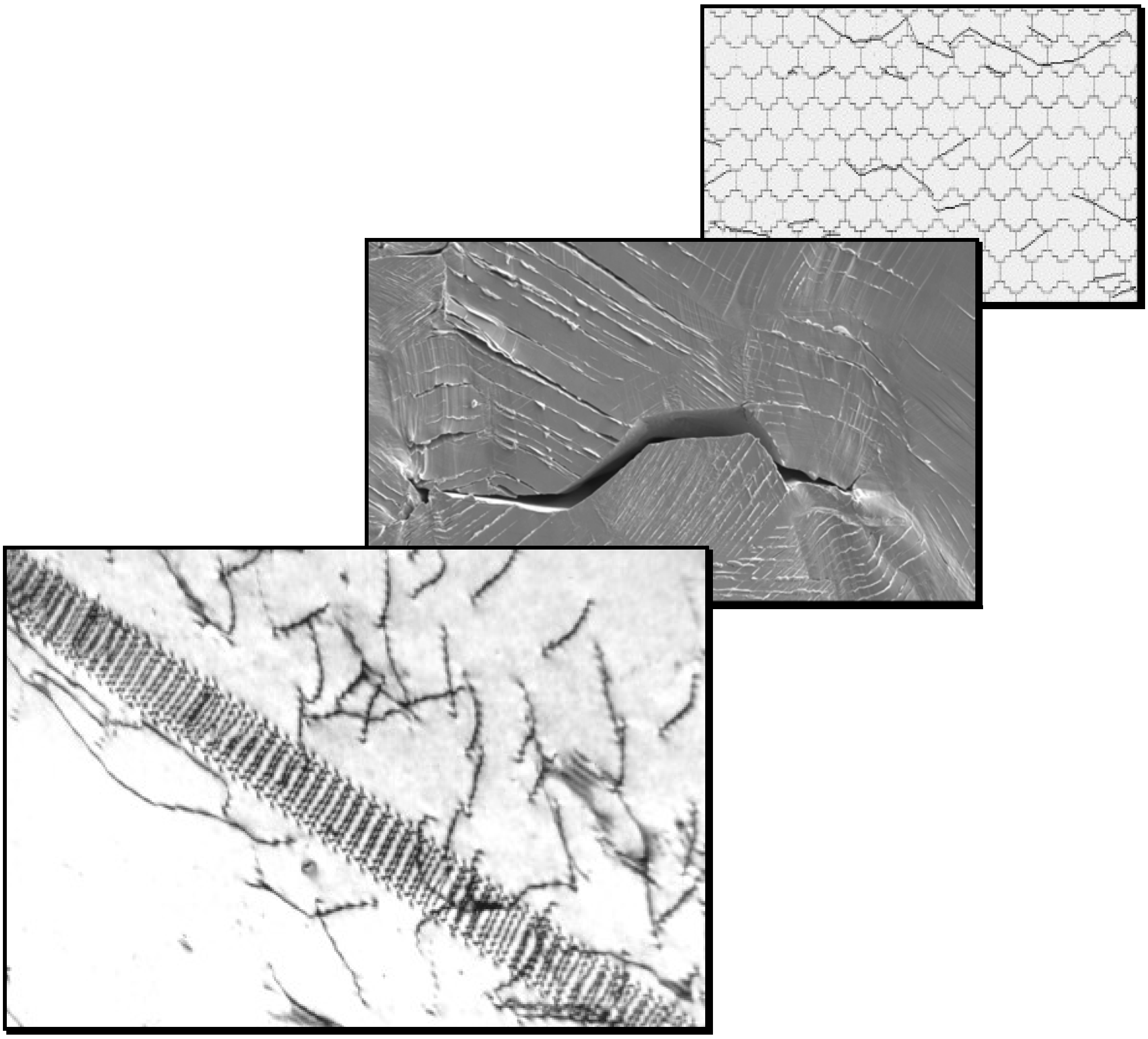

Risø National Laboratory, Roskilde
March 1998

Abstract The plastic strain controlled fatigue behaviour of polycrystalline Cu-15%Zn and Cu-30%Zn has been investigated with the aim of studying the effect of slip mode modification by the addition of zinc to copper. It has been clearly demonstrated, that true cyclic saturation does not occur in the plastic strain controlled fatigue of brass. This complicates the construction of a cyclic stress-strain (CSS) curve and thus the comparison with copper. A method to overcome this complication has been suggested. Surface observations on fatigued brass specimens show that individual grains tend to deform by Sachs type single slip. This behaviour has been described by the self-consistent Sachs-Eshelby model, which provides estimates of the CSS curve for brass polycrystals. Successive stages of primary hardening, softening and secondary hardening has been observed in the plastic strain controlled fatigue of brass. It has been found that the primary hardening is attributed to an increase of intergranular stresses whereas the secondary hardening apparently is attributed to an increase of friction stresses. Investigations of the structural evolution show that the softening behaviour can be explained by the presence of short-range order (SRO). SRO promote the formation of extended dipole arrays which hardens the material. The formation of intense shear bands destroy the dipole arrays, which explains the cyclic softening. The present results reveal that Cu-30%Zn is a pure planar slip alloy, while Cu-15%Zn displays both planar and wavy slip. The mechanical and structural behaviour observed in brass resembles recent observations in 316L austenitic stainless steels, and the present results reveal that Cu-30%Zn and 316L have approximately the same fatigue life curve. This emphasizes brass as being a convenient model system for the industrially important austenitic steels. A quantitative fatigue damage characterization has been carried out using a classification of surface cracks based on their length and growth behaviour. This has provided the basis for using a numerical Monte Carlo type model, which has been further developed to account for the observed intergranular damage evolution on Cu-30%Zn. With these modifications the model predicts the fatigue life curve of Cu-30%Zn and 316L.

Frontpage: the three pictures illustrate the different scales involved in the present fatigue research. In the foreground a TEM micrograph shows a regular array of dislocation dipoles embedded in comparatively undislocated crystal. Underneath a SEM micrograph shows a surface microcrack formed in the boundaries between different crystal grains. In the background a numerical simulation of fatigue surface crack evolution is illustrated.

(This thesis is part of the requirements to obtain the Ph.D. degree from the Technical University of Denmark. The thesis is also available as DCAMM report no. S79 and as an electronic document on *http://www.risoe.dk/rispubl*)

ISBN 87-550-2347-9

ISSN 0106-2840

Afdelingen for Informationsservice, Risø, 1998

Resumé Den plastisk-tøjnings-kontrollerede udmattelsesopførsel af polykrystallinsk Cu-15%Zn og Cu-30%Zn er blevet undersøgt med henblik på at studere, hvorledes deformationsmønstret ændres ved tilsætning af zink til kobber. Det er klart blevet demonstreret, at sand cyklisk mætning ikke sker i plastisk-tøjnings-kontrolleret udmattelse af messing. Dette komplicerer konstruktionen af en cyklisk spændings-tøjnings (CSS) kurve, og dermed også en sammenligning med kobber. En metode til at overvinde denne komplikation er blevet foreslået. Overfladestudier på udmattede messing-emner viser, at individuelle korn har tendens til at deformere v.h.a. Sachs-type enkelt-slip. Denne opførsel er blevet beskrevet v.h.a. den selvkonsistente Sachs-Eshelby model, som giver et skøn for CSS kurven for messing polykrystaller. Succesive stadier af primær hærdning, blødgøring og sekundær hærdning er observeret i plastik-tøjnings-kontrolleret udmattelse af messing. Det er blevet vist, at den primære hærdning er forårsaget af en stigning i intergranulære spændinger, mens den sekundære hærdning synes at være en effekt af stigende friktionsspændinger. Undersøgelser af strukturudviklingen viser, at den cykliske blødgøring kan forklares med tilstedeværelsen af nærorden (SRO). SRO forårsager dannelsen af udstrakte dipol arrangementer, som hærder materialet. Dannelsen af intense forskydningsbånd nedbryder dipole arrangementerne, hvilket forklarer blødgøringen. De nærværende resultater viser, at Cu-30%Zn er et rent planslip materiale, mens Cu-15%Zn udviser både planslip og bølgeslip. Den mekaniske og strukturelle obførsel observeret i messing er meget lig nylige observationer i 316L austenitisk rustfrit stål, og de nærværende resultater viser, at Cu-30%Zn og 316L har omtrent den samme udmattelseslevetids-kurve. Dette fremhæver messing som værende et bekvemt modelsystem for de industrielt vigtige austenitiske stål. En kvantitativ udmattelsesskade-karakterisering er blevet foretaget baseret på en klassificering af overfladerevner i forhold til deres længde og vækstopførsel. Dette danner basis for anvendelsen af en numerisk Monte Carlo type model, som er blevet videreudviklet for at tage hensyn til den observerede intergranulære skadesudvikling på Cu-30%Zn. Med disse modifikationer er modellen i stand til at forudsige udmattelseslevetiden for Cu-30%Zn og 316L.

Contents

Preface

This thesis is submitted in partial fulfillment of the requirements for obtaining the Ph.D. degree at the Technical University of Denmark. The research described was carried out under the supervision of Professor Viggo Tvergaard, Department of Solid Mechanics at the Technical University of Denmark, and Dr.Techn. Ole Bøcker Pedersen, Materials Research Department at Risø National Laboratory.

The project was carried out within the Engineering Science Centre for Structural Characterization and Modelling at the Materials Research Department at Risø, but I would like to thank both my supervisors for pleasant collaboration and support; Viggo for introducing me to the field of solid mechanics and for always taking the time to discuss theoretical and practical problems; Ole for his stimulating and inspiring supervision and invaluable guidance throughout my work.

During the summer 1996 I spent 3 months as a visiting Ph.D. student at Ecole Nationale Superieure des Mines de St. Etienne, France, under the supervision of Professeur Thierry Magnin. I gratefully thank Thierry for introducing me to the field of fatigue damage and for sharing his computer code with me. I would also like to thank him for ensuring a pleasant visit for my family and me. The people at Centre Science des Matériaux et des Structures are appreciated for their tolerance regarding my deficiency in French, and I would particularly like to thank Olivier Madelaine-Dupuich for a fruitful collaboration.

I would like to express my thanks to the staff members at Materials Research Department at Risø. Especially, I would like to thank Dr. Jørgen Bilde-Sørensen for his electron microscope supervision and for introducing me to the world of dislocation theory, Dr. Techn. Dorte Juul Jensen and Preben Olesen for their help with the texture measurements, Frank Adrian for his assistance with the mechanical testing, Bjørn S. Johansen for helping out with the plastic strain control software, Helmer Nilsson for his metallurgical guidance, and Dr. Henrik Christoffersen and Jørgen Lindbo for introducing me to 'the art of thin foil preparation.'

Finally, my loving thanks to my wife Gritt and my children Julie and Malthe for their love and support throughout these years, and for their patience and tolerance during the writing of this thesis.

1 Introduction

When metallic materials are subject to cyclic plastic strains of sufficient magnitude they eventually suffer fatigue failure under mechanical loads, which may lie far below the tensile strength. Fatigue is a widespread problem in safe and economic utilization of industrial materials. It limits the useful life of structural components and often the catastrophic break-down of an airplane or other engineering construction can be traced to an unexpected fatigue failure. However, fatigue failure is the outcome of a gradual weakening of the material and microscopical observation of metallic materials, prior to fatigue failure, reveals a process of formation of microcracks, which accumulate into the fatal macroscopical crack responsible for fatigue failure. This fatigue process determines the fatigue life of the material, i.e. the number of strain cycles endured before fatigue failure. It is obviously of considerable scientific and industrial interest to understand and model the fatigue process in terms of the underlying mechanisms of crack initiation and accummulation.

Fatigue involves a hierarchy of mechanisms and structures, ranging from individual dislocations to macroscopic cracks, and it depends upon the microstructure and the chemical composition of the material. Specific industrial materials display specific fatigue processes, which cannot always be meaningfully compared. Therefore, basic studies of fatigue are increasingly made using well-characterized and relatively simple *model systems*, like single crystals of pure FCC metals. Such studies lead to comparable experimental observations, which may be assembled into coherent maps of the fatigue process to provide a physical basis for realistic fatigue modelling.

Copper has been a popular model system, and years of fundamental research on this system have resulted in a wealth of information on basic mechanisms of fatigue. An important result of these studies is the identification of cross-slip as being a key process in the fatigue of metals. Cross-slip is the mechanism by which a screw dislocation changes its slip plane and the deformation of copper is characterized by frequent cross-slip events. This deformation mode is called *wavy slip* in contrast to the *planar slip* mode with a low cross-slip frequency. The understanding of fatigue mechanisms is much less advanced for planar slip materials than for wavy slip materials, although industrially important materials like the austenitic steels deform by planar slip. Thus there is a need for fatigue studies of well-characterized planar slip materials.

The present thesis describes an experimental and theoretical investigation of fatigue in the model system of polycrystalline brass, in which the addition of zinc to copper changes the slip mode from wavy to planar slip. The background for the investigation is the existing knowledge about mechanisms of fatigue in copper single crystals and polycrystals. In copper the localization of plastic deformation in slip bands or the accommodation problems at grain boundaries lead to formation of trans- and intergranular cracks, respectively. Moreover, the fatigue life of polycrystalline copper depends strongly on grain size, while the cyclic stress-strain behaviour is strongly influenced by texture.

Two polycrystalline brass alloys, Cu-15%Zn and Cu-30%Zn, were included in the investigation and the alloys were produced and characterized with respect to grain size distribution and texture. Mechanical fatigue tests were supplemented with characterization of dislocation microstructures in the material and sliplines and crack formation on its surface. The aim was to identify dislocation mechanisms of crack initiation and to characterize how the damage state evolves through accumulation of cracks in planar slip materials. The experimental observations were analyzed in terms of an existing deformation model for polycrystals and a modified version of an existing model describing the damage evolution.

Chapter 2 surveys the existing information on mechanisms of fatigue in copper and brass. The purpose is to outline the background for the present study. As a supplement, Appendix A provides some relevant information about brass including a basic description of dislocation cross-slip in fatigue. To further facilitate the reading, Appendix C contains a list of the symbols and abbreviations used throughout the thesis. **Chapter 3** describes the detailed characterization of the materials used in the present work as well as the conditions under which they were mechanically tested. The chapter also includes a description of the microscopical techniques used to characterize the evolution of dislocation microstructures and damage states during fatigue.

The results are presented in the form of micrographs, figures and tables, and they have been grouped in three different chapters (chapter 4-6). Each chapter is closed with a separate discussion. **Chapter 4** summarizes the mechanical behaviour, including cyclic hardening/ softening curves, cyclic stress-strain curves and fatigue life curves. **Chapter 5** presents a microscopical investigation of the observed cyclic hardening/softening behaviour together with a characterization of the fatigue damage evolution. Also, the basic mechanisms involved in the hardening/softening and damage behaviour are discussed. These mechanisms form the basis for applying the two models presented in **chapter 6**. The cyclic stress-strain curve is analyzed using the self-consistent Sachs-Eshelby model (PEDERSEN *ET AL.*, 1982) and a Monte Carlo type damage model (BATAILLE & MAGNIN, 1994) is further developed and used to simulate the damage evolution. **Chapter 7** outlines the conclusions.

2 Background

Basic mechanisms of fatigue have been investigated for decades and most attention has been offered to wavy slip materials since the discovery of persistent slip bands (THOMPSON *ET AL.*, 1956). In wavy slip materials the dislocations can easily change their slip plane by cross slip, which is essential for formation of 3D composite (wavy) structures. The role of cross slip in fatigue has been recognized since early studies and MCGRATH & THURSTON (1963) suggested that the fatigue behaviour is controlled by cross slip. This now seems to be a well established fact due to intense research, and the progress in understanding basic mechanisms of fatigue can, to a great extent, be attributed to studies of experimental model systems. The favoured model system has been copper for which it has recently been possible to establish so-called fatigue mechanism maps (PEDERSEN, 1990). These maps are shown in Figure 2.1.

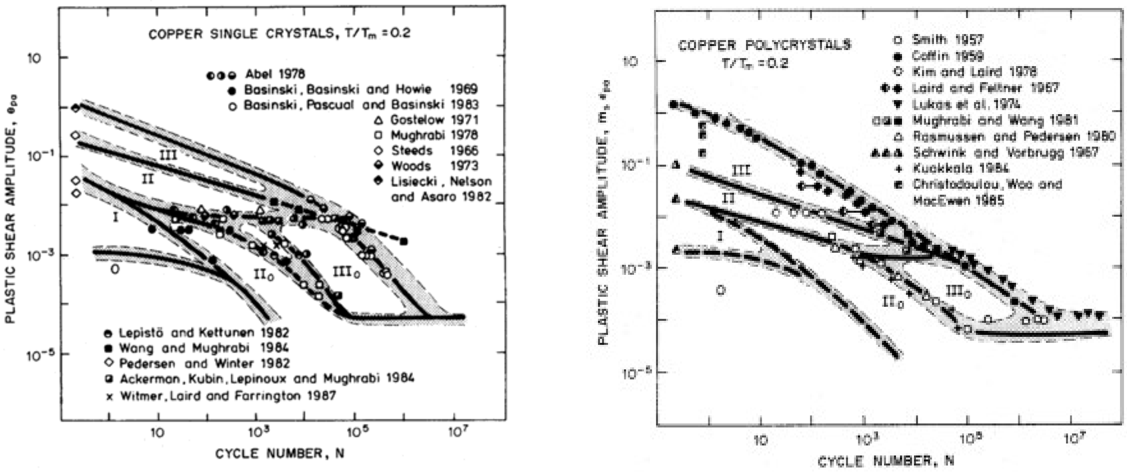

(a)

(b)

Figure 2.1 Fatigue mechanism maps for (a) single slip oriented copper single crystals, and (b) texture-free copper polycrystals, cyclically strained at room temperature (PEDERSEN, 1990). The different fields O, I, II, II_0, III and III_o are correlated with different stages in the fatigue process.

When alloying elements, such as zinc or aluminium, are added to copper the cross slip frequency is reduced and the tendency to form 2D (planar) structures increases. This planar slip behaviour is commonly correlated with a reduced stacking fault energy (SFE) and the range 20-30 mJ/m^2 is suggested as the transition range below which no PSBs are formed (MAGNIN *ET AL.*, 1989). However, NEUHÄUSER *ET AL.* (1986) argued that high friction, rather than a decrease in stacking fault energy, is the main reason for the transition from homogeneous to heterogeneous glide. The high friction would be due to the presence of short-range ordering (SRO) or short-range clustering. GEROLD AND KARNTHALER (1989) compared a wide range of metals and alloys and found a correlation between planar slip and the presence of short range order or clustering. This has recently been supported by other authors (HONG & LAIRD, 1990A; VOGT *ET AL.*, 1993; WOLF *ET AL.*, 1994; PLESSING *ET AL.*, 1997). Whatever the explanation, various copper based alloys have been studied as model systems for planar slip materials in order to compare with the extensive experimental information on copper, but still the information on fatigue mechanisms in planar slip materials, which include the industrially important austenitic steels, is scarce.

As mentioned in chapter 1, the model system chosen for this study is brass in which increasing addition of zinc to copper changes the deformation mode from pure wavy to pure planar slip. In the following a survey of the available observations on cyclic deformation of copper and brass will be given. The comparison of observations made by different investigators are often complicated due to differences in test conditions. Fatigue tests are sometimes conducted at constant stress amplitudes and sometimes at constant (total) strain amplitudes, but, as it is the plastic strain that produces the fatigue damage, it is convenient to conduct the fatigue tests at constant plastic strain amplitudes. Therefore, the emphasis in the following survey will be on experimental observations from uniaxial fatigue tests at constant plastic strain amplitudes.

The survey will point out the lack of information on basic mechanisms of fatigue in planar slip materials, and in particular brass. Furthermore, it will be emphasized that the effect of polycrystallinity seems to have been ignored. These facts are incentive for the present study of fatigue of polycrystalline brass.

2.1 Cyclic plasticity

The study of cyclic plasticity includes investigations of dislocation microstructures and of the cyclic stress and strain response. One important observation in plastic strain controlled fatigue of copper is the presence of cyclic saturation, i.e. the stress amplitudes remain constant for a large number of cycles. This constant stress amplitude is called the saturation stress, σ_{sat}, and it is common to compare saturated crystals by plotting the saturation stresses at different plastic strain amplitudes in a so-called cyclic stress-strain curve (HANCOCK & GROSSCREUTZ, 1969). In the following this curve will be referred to as the CSS curve.

2.1.1 Copper

Cyclic deformation of copper is dominated by the presence of persistent slip bands. The basic mechanisms of these slip bands are most conveniently studied in single crystals and therefore emphasis will be on the description of the PSB behaviour in copper single crystals. However, the main effects of polycrystallinity will be briefly considered.

Single crystals

During cyclic deformation slip bands, or striations as they were formerly called, appear on the surface of initially electropolished specimens. In early studies of fatigue THOMPSON *ET AL.* (1956) found that when a fatigued copper polycrystal is lightly electropolished (2 µm), although many of the striations disappeared, some remained, which they therefore called persistent slip bands (PSBs). This name has passed into general use and the investigation of PSBs and their influence on the fatigue behaviour has been subject for intense studies ever since. The main reason for this attention is, that PSBs have been found to act as preferential sites for the nucleation of fatigue cracks (see e.g. PLUMBRIDGE & RYDER, 1969; KATAGIRI *ET AL.*, 1977; MUGHRABI *ET AL.*, 1979; BASINSKI *ET AL.*, 1983; BASINSKI & BASINSKI, 1984; MUGHRABI *ET AL.*, 1983). The earliest studies of fatigue focused on crack initiation processes but with the development of transmission electron microscopes a shift of emphasis towards dislocation studies occurred. In the 60s vast studies of dislocation structures in fatigued copper were performed. BASINSKI ET AL (1969) investigated the development of dislocation arrangements during the early stages of cyclic hardening of copper single crystals. They revealed the formation of a 3D network of interconnected veins packed tightly with mainly primary edge dislocations in dense multipole configurations, separated by dislocation-poor regions. This structure, called the matrix structure, is a metastable structure and a local breakdown occurs after the veins have hardened to a critical extent at which they can no longer accommodate the imposed plastic strain amplitude (see e.g. MUGHRABI *ET AL*. 1979). The veins condense into a so-called wall structure, which appears as a characteristic ladder-like structure when viewed in a (121)-section. This is illustrated in Figure 2.2.

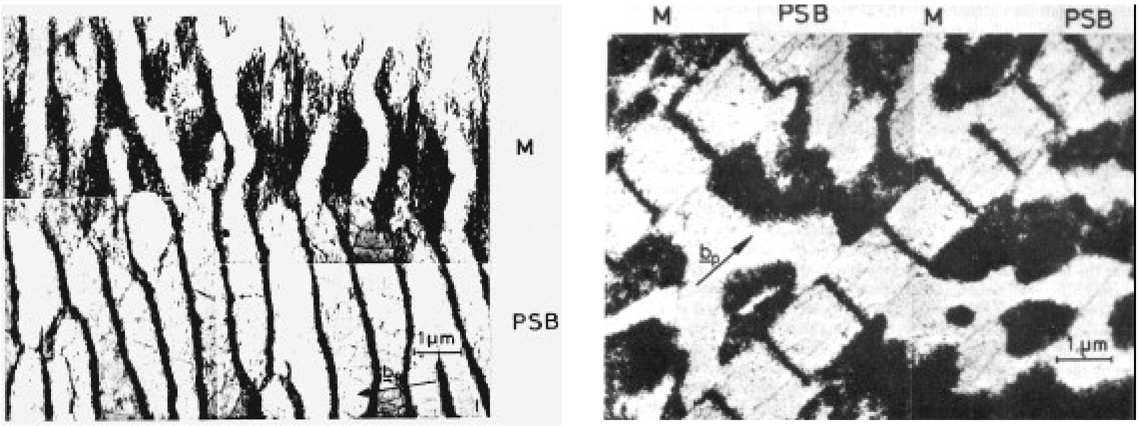
(a) (b)

Figure 2.2 (a) TEM-micrograph of a section that is very slightly inclined to the primary glide plane (111) of a copper single crystal. The vein structure has condensed into a wall structure. (b) When viewed in a (121)-section the wall structure appears as the characteristic ladder-like structure (the micrographs are taken from MUGHRABI ET AL.*, 1979).*

A correlation between this particular microstructure and PSB surface reliefs was first reported by LAUFER & ROBERTS (1964), and this establishes the ladder-like structure as being characteristic of PSBs. Since then intense studies of the dislocation structures in copper single crystals lead to the proposal of a simple model of the behaviour of the PBSs in single crystals as a bulk feature (WINTER, 1974). The model considers the fatigue properties of copper as being correlated with a two-phase system, the two phases being the inactive matrix structure and the active PSB structure. Therefore the model is called the two-phase model, and it originates from the observation that the relative amount of PSBs increases with increasing plastic strain amplitude. The fatigued crystal seems to adjust the relative amounts of the active and inactive phases to accommodate the applied strain amplitude, γ_{pa}, resembling the liquid-vapour system where the relative amounts of the two phases are adjusted to fill the container. In the equilibrium state this can be expressed by the rule of mixtures:

$$\gamma_{pa} = f_{PSB} \cdot \quad _{PSB} + (\quad - \quad _{PSB}) \cdot \gamma_{matrix} \qquad (2\ 1)$$

$_{PSB}$ is the volume fraction of PSBs, $_{PSB}$ is the plastic strain amplitude in the PSBs and $_{matrix}$ is the plastic strain amplitude in the matrix. The analogy has one serious limitation: the

this limitation the two-phase model gives a correct description of the behaviour of copper single crystals in fatigue tests at constant strain as well as stress amplitudes (INTER, 1974 Figure 2.3

the experimentally observed CSS curve for copper single crystals.

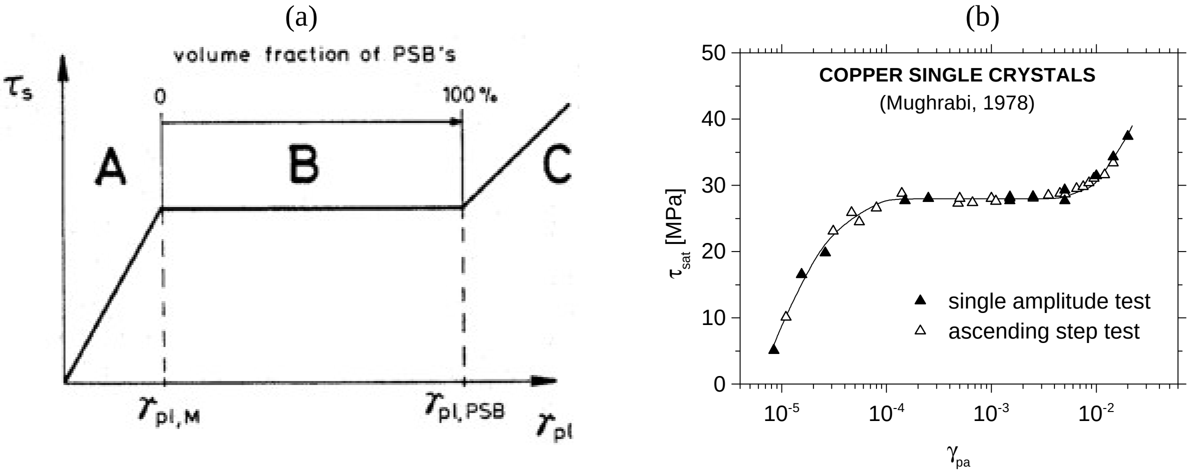

Figure 2.3 (a) The idealized CSS curve for single crystals, based on the two-phase model (MUGHRABI ET AL., 1979). In range B the volume fraction of PSBs increases to accommodate the increasing plastic strain amplitude, and as a result the saturation stress remains unchanged. (b) The experimentally observed CSS curve for single slip oriented copper single crystals supports the predictions of the two-phase model (MUGHRABI, 1978).

According to this, the CSS curve falls into three regimes. In range A, cyclic strain hardening occurs more or less homogeneously and τ_{sat} increases with increasing γ_{pa}. The transition to range B is marked by the first development of PSBs and the deformation now becomes inhomogeneous and strongly localized in the PSBs. As γ_{pa} is increased in range B, the volume fraction of the PSBs increases according to the rule of mixtures (Equation 4.1). The saturation stress, representing essentially the stress required for the localized deformation of the soft PSBs, remains virtually unchanged until the end of the 'plateau' range B, when the entire crystal is filled with PSBs. This stress is called the plateau stress, τ_{plat}. Deformation at higher γ_{pa} in range C leads once again to a new structure and an increase of τ_{sat}. In the two-phase model the values $\gamma_{matrix}{\approx}10^{-4}$ and $\gamma_{PSB}{\approx}10^{-2}$ at the extremes of range B (see Figure 2.3b) are identified with the plastic strain amplitudes that can be accommodated by the matrix and the PSBs, respectively. Thus the average localization factor, i.e. $\gamma_{PSB}/\gamma_{matrix}$, is approximately 10^2.

Studies of fatigue hardening, preceding cyclic softening and/or saturation, show that work-hardening rates of about a third of the elastic shear modulus can be observed in single crystals of copper (PEDERSEN & WINTER, 1982). This suggests that there is a large volume fraction of obstacles to plastic flow, which are essentially non-deformable and give rise to inclusion stresses of considerable magnitude. The much lower hardening rates in cycles after saturation, when PSBs have formed, suggest a lower volume fraction of obstacles. This is supported by TEM observations, and the obstacles are observed to be clumps of tightly packed edge dislocations embedded in almost perfect crystal. In the terminology of the two-phase model the characteristic wall structure of PSBs can be referred to as a 'condensed' structure in comparison with the 'uncondensed' matrix structure. The condensation of the obstacles corresponds to a decrease in volume fraction, which explains the observed decrease in hardening rates, when PSBs are formed.

However, recent work on the effect of temperature (LISIECKI & PEDERSEN, 1991; HOLZWARTH & ESSMANN, 1994) shows that in copper f_{PSB} is reduced, rather than increased, by a reduction in temperature, which is the exact opposite of expectations on the basis of the two-phase analogy. Furthermore it has been shown (PEDERSEN & WINTER, 1995) that cyclic saturation is not a steady state and that cyclic straining after saturation of the stress amplitude is associated with continued evolution of the dislocation structure of the matrix. These observations demonstrate the insufficiency of the two-phase model and has lead to the development of a more satisfactory model for the process of cyclic saturation in fatigue of metals (PEDERSEN, 1996). The model, which is referred to as the static-dynamic (SD) model, distinguish between two structure components: A *dynamic* structure of mobile screw dislocations causes plastic deformation and builds up a heterogeneous *static* structure of edge multipoles, which deformation hardens the material. The static structure is unstable and eventually it transforms, or condenses, into the softer PSBs in which the deformation is concentrated. The static structure can be thought of as being a very hard but unstable 3D network in which fluxes of screw dislocations are moving back and forth. In Figure 2.4 a schematic representation of a PSB is shown.

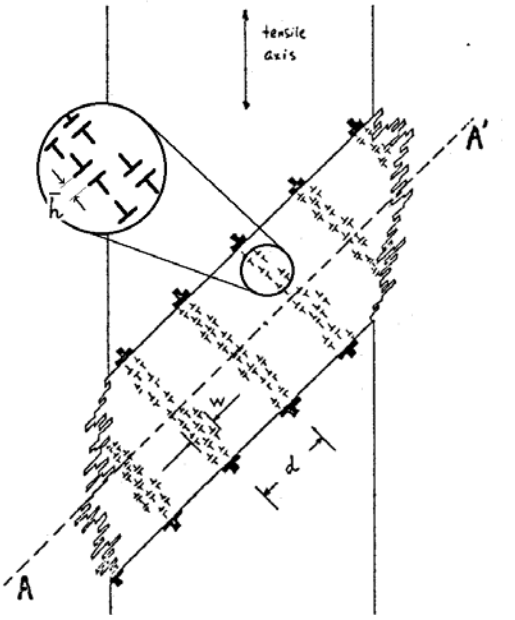

Figure 2.4 A schematic representation of a PSB. The mobile screw dislocations are moving in and out of the plane of the paper between the edge multipole walls. This causes shear in the A-A' direction. Intrusions and extrusions are formed where the PSB breaks through the surface (BROWN, 1981).

The SD model shows, that the density of the dynamic structure dictates the scale of the static structure. There is no limit to the production of mobile screw dislocations by the static structure, so the density is therefore limited by the screw annihilation distance, y_s. This means, that the scale of the static structure is dictated by y_s. The model predicts, that the wall spacing, d, of the PSBs depends on y_s through the following relation:

$$d = 4 \cdot \pi \cdot y_s \tag{2.2}$$

This comes from considering the Orowan stress and the passing stress for the mobile screw dislocations. The average spacing, $\bar{h}$, of the edge dipoles in the PSB walls is proportional to the wall spacing:

$$\bar{h} = A \cdot d \tag{2.3}$$

which is supported by experimental observations (PEDERSEN, 1996). The proportionality factor, A, predicted by the SD model, depends on the width, w, of the PSB walls and the Burgers vector:

$$A = \frac{10^{-3}}{\pi} \cdot \sqrt{\frac{w}{b}} \qquad (2.4)$$

Based on these equations the model predicts, that the screw annihilation distance, y_s, dictates both the microscale (i.e. the wall spacing, d) and the nanoscale (i.e. the dislocation spacing, $\bar{h}$). A change of y_s would therefore be expected to result in a *quantitative* scale change of the static structure, but not a *qualitative* change. When the temperature is reduced, the cross-slip frequency is reduced, as cross-slip is a thermally activated process (see Appendix A). The screw dislocations are enabled to come closer to each other before they annihilate, i.e. the annihilation distance is reduced. The model thus predicts, that the scale of the static structure should be refined when reducing the temperature, and this prediction is supported by observations of copper fatigued at different temperatures (BASINSKI *ET AL.*, 1980; LISIECKI & PEDERSEN, 1991; HOLZWARTH & ESSMANN, 1994). Apart from providing quantitative accounts of the available observations of the effects of temperature and cumulative strain on the dislocation structure and CSS behaviour, the model allows the observed fragmentation of primary matrix walls to be understood in terms of a line tension model (PEDERSEN & WINTER, 1995). This model also shows that irreversible matrix hardening drives the continued condensation, whereby matrix walls reduce their volume and cause localization of cyclic strain with slip instabilities and hence fatigue damage. Compared to the idealized two-phase model the SD model therefore provides a more comprehensive description of the fatigue mechanisms associated with the PSB formation.

In single slip oriented copper crystals the formation of PSBs is commonly accompanied by cyclic softening. Stress peaks (hardening followed by softening) have been reported at low plastic strain amplitudes by several authors (KETTUNEN & KOCKS, 1972; WOODS, 1973; WINTER, 1974; JIN, 1989) and at high amplitudes by others (MUGHRABI, 1978; GONG *ET AL.*, 1996), and recently GONG *ET AL.* (1997) suggested, that this behaviour is related to the operation of secondary slip. This is supported by observations of cyclic softening in copper crystals oriented for double slip (JIN & WINTER, 1984; GONG *ET AL.*, 1996; 1997), and multiple slip (LEPISTÖ & KETTUNEN, 1986), which also show that crystals of orientation [001] and [111] harden much more rapidly than single glide crystals. In [001] copper crystals the pronounced secondary slip leads to the formation of the characteristic labyrinth structure, a two-dimensional wall structure, which was first reported by RASMUSSEN & PEDERSEN (1980). The saturation stresses of such crystals are remarkably higher than those found in single glide crystals and the corresponding CSS curve does not display a plateau (GONG *ET AL.*, 1997). These results emphasize the importance of the crystallographic orientation on the cyclic behaviour of single crystals, which are expected to reflect on the behaviour of polycrystalline materials if crystallographic texture is present.

Polycrystals

In single crystals PSBs are a bulk phenomena, but in polycrystals it was considered a surface phenomena since early studies (e.g. THOMPSON *ET AL.*, 1956; LUKAS *ET AL.* 1968). With the development of the two-phase model (WINTER, 1974) this issue, however, became controversial. Some persisted in the opinion that PSBs were a surface phenomena (see e.g. MUGHRABI, 1979), while others were convinced that persistent slip was not confined to the surface (see e.g. Rasmussen & Pedersen, 1979). The controversy came to an end when independent observations in polycrystals of ferritic steel (Pohl *et al.*, 1980) and copper (Winter *et al.*, 1981) proved the existence of bulk PSBs. The behaviour of copper polycrystals would therefore, to a certain extent, be expected to behave like single crystals. Investigations of cyclic stress and strain behaviour of copper polycrystals show, that cyclic saturation is indeed not a single crystal phenomena (see e.g. Mughrabi & Wang, 1981). However, the existence of a plateau on the polycrystal CSS curve has been a subject of controversy. Numerous investigations seem to indicate that an increase of the grain size increases the tendency to form a plateau or quasi-plateau (Mughrabi, 1979; Rasmussen & Pedersen, 1980; Figueroa *et al.* 1981; Lukás & Kunz, 1985; Llanes *et al.* 1993; Liu *et al.*, 1994). This can be understood as a change from polycrystal to multi-crystal behaviour, eventually approaching the single crystal behaviour when extremely coarse grained material is considered (Kettunen & Tiainen, 1981; Kuokkala *et al.*, 1982). In a wide range of grain sizes the polycrystal CSS curve, however, shows an upward slope with saturation stress amplitudes which are higher than those found for single crystals. This can be explained in terms of internal stresses adding to the saturation stress, as predicted by the self-consistent Sachs-Eshelby (SCSE) model (Pedersen *et al.*, 1982). This model will be explained in more detail in chapter 6.1.1, but it predicts a grain size independent CSS curve with an upward slope. In Figure 2.5 the model predictions are compared with CSS curves for polycrystalline copper with different grain sizes and texture.

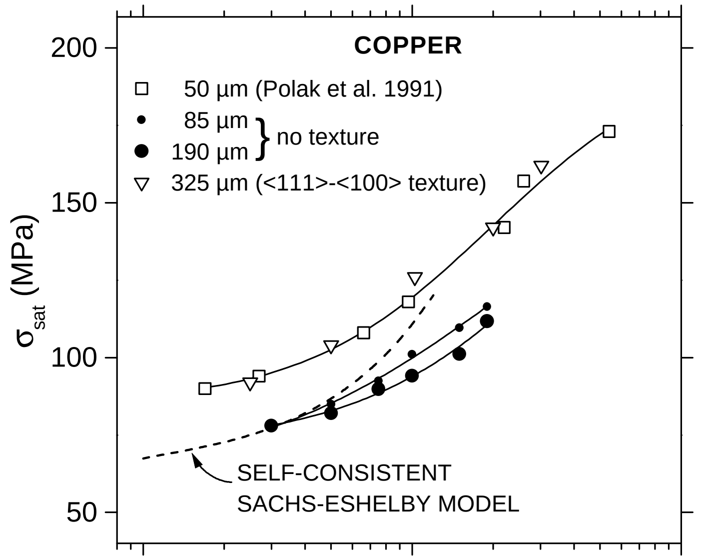

Figure 2.5 Effects of texture and grain size on the CSS curves for polycrystalline copper (Carstensen & Pedersen, 1997b). The grain size has only minor effects on the saturation stresses, while the presence of a [111]á100ñ texture has major effects. Recent texture measurements carried out on the small grained copper (50µm) revealed the presence of a [111]á100ñ texture (Pedersen et al., 1997).

The figure shows, that the SCSE model accounts for the CSS curve for texture-free Cu in the limit of small plastic strain amplitudes ($\varepsilon_{pa} \leq 10^{-3}$). The small grain size effects observed for $\varepsilon_{pa} > 10^{-3}$ are suggested to be due to grain boundary modifications of the dislocation microstructures (BRØNDSTED *ET AL.*, 1983) resembling the grain size effect observed in monotone deformation (HANSEN & RALPH, 1982). The negligible effect of grain size on the saturation stresses is a generally accepted fact and it has been demonstrated by several investigations of copper polycrystals (see e.g. LUKÁS & KUNZ, 1987; PERALTA *ET AL.*, 1995). The effect of texture is, however, often neglected. In a recent paper LUKAS & KUNZ (1996) divided different material parameters into those that have a major effect on the fatigue characteristics (the CSS curve and fatigue life curve) and those that have a minor effect on these characteristics. The term ‘minor effect’ was defined as “a change of stress amplitude (for constant plastic strain amplitude) not exceeding a few tens of per cent or a change of fatigue life (for constant stress or strain amplitude) not exceeding a factor of about 5”. Using this definition CARSTENSEN & PEDERSEN (1997B) demonstrated by comparison of experimental data (Figure 2.5), that texture and chemical composition both have major effects on the CSS behaviour.

2.1.2 Brass

The transition from wavy to planar slip is correlated with a reduction of the cross slip frequency and thereby a reduction of the screw annihilation distance, y_s. According to the SD model this will lead to a refinement of the dislocation microstructure, resembling a reduction of temperature. However, the SD model is based on a 3D dislocation structure (the vein structure) from which PSBs develop. In planar slip materials the microstructure is two-dimensional and thus the fatigue mechanisms are different from those of wavy slip metals. This disables (or reduces the validity of) the SD model and it raises a number of outstanding questions, as will be demonstrated in the following.

Single crystals

Fatigue mechanism maps, like those shown in Figure 2.1, characterize the different stages in the fatigue process of copper. These maps are based on a vast amount of experimental observations and in comparison only little information exist on the fatigue process in brass. Early studies of dislocation microstructures in fatigued Cu-30%Zn (SEGALL & FINNEY, 1963; STRUTT, 1963; YOUSSEF, 1970) showed microstructures very different from those observed in fatigued copper. The dislocations were found to be arranged in groups similar to the early stage of monotonic deformation. LUKAS & KLESNIL (1970; 1971) investigated the dislocation structures in single crystals of Cu-15%Zn and Cu-31%Zn, and in Figure 2.6. the structures viewed in the cross slip plane are compared with the characteristic PSB structure found in copper.

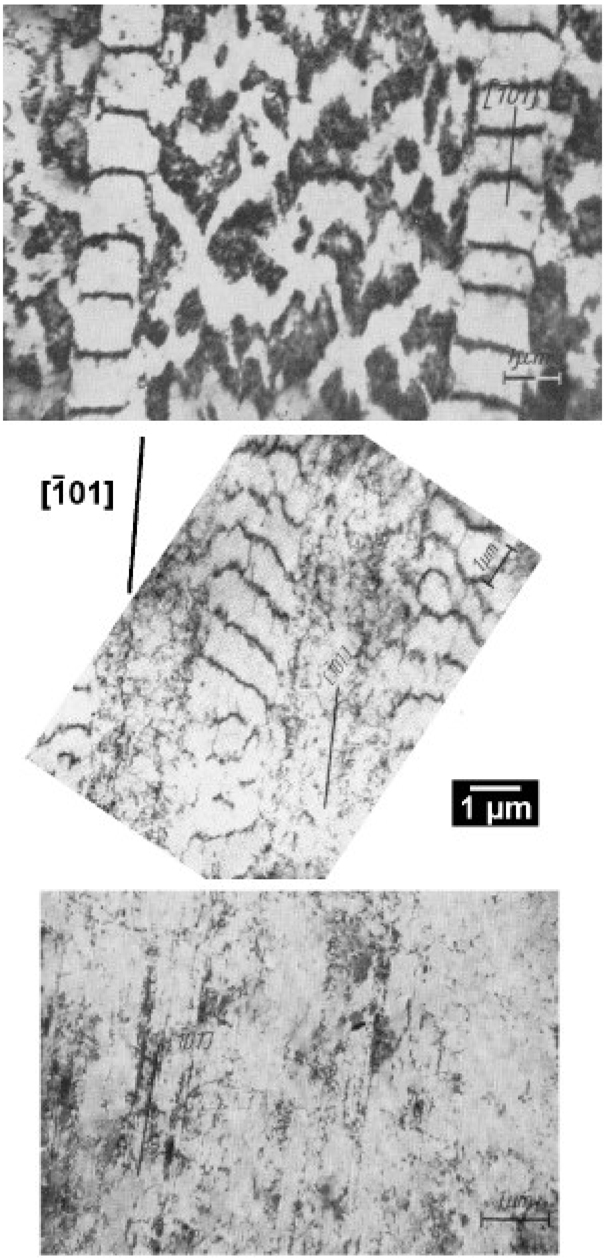

Figure 2.6 Typical dislocation structures found in the cross slip plane of single slip oriented crystals of copper(top), Cu-15%Zn(middle), and Cu-31%Zn(bottom). (LUKAS & KLESNIL, 1970; 1971).

As seen on Figure 2.6b PSB-like structures were found in Cu-15%Zn, and compared to the PSBs in copper (Figure 2.6a) the wall spacing, d, is reduced. This is in agreement with the predictions of the SD model. However, the matrix structure is not as heterogeneous as in copper and it is difficult to distinguish between condensed and uncondensed phase. This demonstrates the change of fatigue mechanisms, which is even more evident in Cu-30%Zn (Figure 2.6c). LUKAS & KLESNIL (1973) suggested a simple connection between the stacking fault energy, the applied plastic strain amplitude and the observed dislocation microstructure. This is illustrated in Figure 2.7.

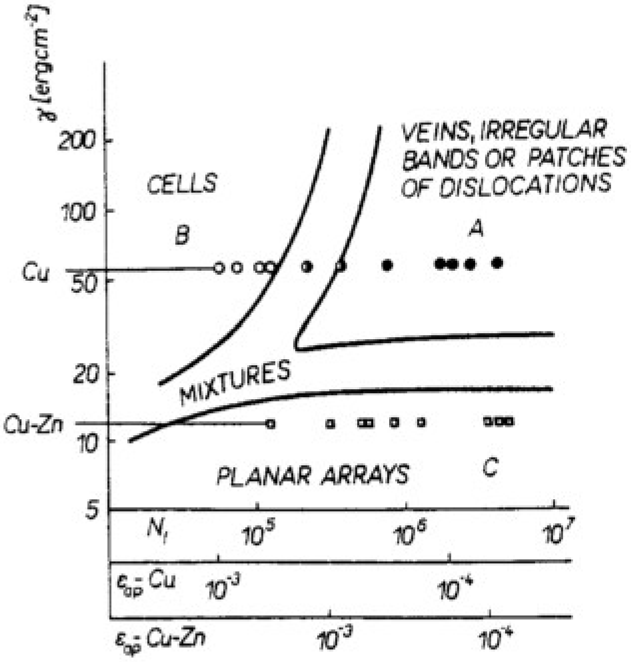

Figure 2.7 Dislocation microstructures in dependence on the stacking fault energy and on the plastic strain amplitude. (Lukas & Klesnil, 1973). The indications for Cu-Zn refer to Cu-31%Zn.

The stacking fault energies are 27 and 15 mJ/m^2 for Cu-15%Zn and Cu-30%Zn, respectively (see Appendix A). Figure 2.7 therefore suggests that the dislocation structure in Cu-15%Zn consists of mixtures of wavy and planar slip structures. This is in agreement with more recent studies (Kaneshiro *et al.*, 1988; Hong & Laird, 1990a), which indicate that Cu-15%Zn marks the transition from wavy slip to planar slip in brass. The planar arrays found in Cu-31%Zn indicate rather different fatigue mechanisms, but only few mechanical data were supplied with the early studies of brass, which prevented investigations of such mechanisms. Recent studies of Cu-22%Zn single crystals (Lukas *et al.*, 1991; 1992) revealed cyclic softening when cycling at high plastic strain amplitudes. This resembles observations made in copper (Mughrabi, 1978), but it has also been observed in austenitic steels (Li & Laird, 1994) and Cu-Al (Woods, 1973). In copper, as mentioned above, the softening is assumed to be attributed to the presence of secondary slip. In Cu-Al the softening were suggested to be a result of short-range order (SRO), which were broken down by the fatigue process. Woods (1973) conducted an experiment to support this theory, as illustrated in Figure 2.8. A specimen was cycled into the softening stage. It was then annealed for 10 hours at 240°C to restore the SRO, which assumably had been broken down by the cyclic deformation. Subsequent cyclic deformation revealed a new stage of hardening followed by softening, which was interpreted as evidence for the theory. The mechanisms controlling the process were, however, not investigated.

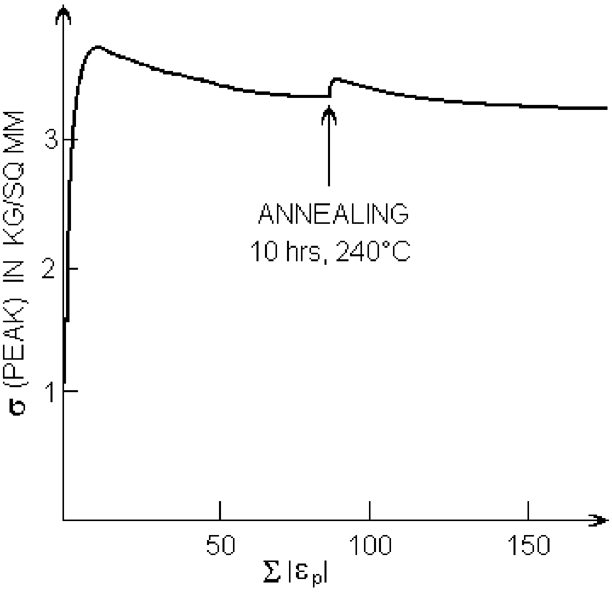

Figure 2.8 The cyclic softening observed in Cu-5at.%Al was suggested to be attributed to short-range order, which assumably was broken down by the cyclic deformation. An annealing test was made to support this theory (WOODS, 1973).

One of the interesting characteristics in the cyclic deformation of planar slip alloys is strain bursts, which have frequently been observed in single crystals of Cu-Al (e.g. ABEL *ET AL.*, 1979; HONG & LAIRD, 1990B; INUI *ET AL.*, 1990). Each strain burst is found to be accompanied by the sudden appearance of a slip band, suggesting it to be caused by a sudden activation of dislocation sources. The surface is observed to become completely filled with slip bands by the repetition of strain bursts irrespective of strain amplitude. Slip in the bands, which carry the whole strain just before a strain burst, is believed to become inactive after a few successive strain bursts, because the newly-formed bands take up the strain. Since the localized slip shifts around the gauge length, because of the short active life of slip bands, the overall deformation becomes rather homogeneous (LAIRD & BUCHINGER, 1985; YAN *ET AL.*, 1986). For this reason, the regions of localized strain are not called persistent slip bands (PSBs), but rather Persistent Lüders Bands (PLBs). The PLBs are found to be associated with a characteristic microstructure, which consists of densely dislocated arrays on closely parallel primary glide planes. Primary dislocations are dominant, but strong secondary activity appears on the critical and conjugate planes. These observations were made on cyclically deformed Cu-16at.%Al, which have an extremely low stacking fault energy (~6 mJ/m^2, GALLAGHER, 1970). However, BUCHINGER *ET AL.* (1986) argued that similar structures would be expected to be found in Cu-30%Zn.

Another characteristic of Cu-16at.%Al single crystals is the absence of cyclic saturation (ABEL *ET AL.*, 1979; HONG & LAIRD, 1990B), which obviously complicates the construction of a CSS curve. The observations made on single crystals of Cu-22%Zn show that a pronounced stage of cyclic saturation is not evident as it is in copper. Nevertheless, LUKAS *ET AL.* (1991; 1992) claimed that it is “easy to choose the ‘saturated’ value of the shear stress amplitude for the construction of the CSSC”. They chose the value corresponding to 50% of fatigue life, and revealed two plateaus on the CSS curve. One at intermediate plastic strain amplitudes and one at very low plastic strain amplitudes. A similar observation was recently made by WANG (1994) in Cu-30%Zn single crystals oriented for single slip, but his saturation stresses were read at 4000 cycles. The obtained CSS curves are shown on Figure 2.9 and compared to the CSS curve for copper single crystals.

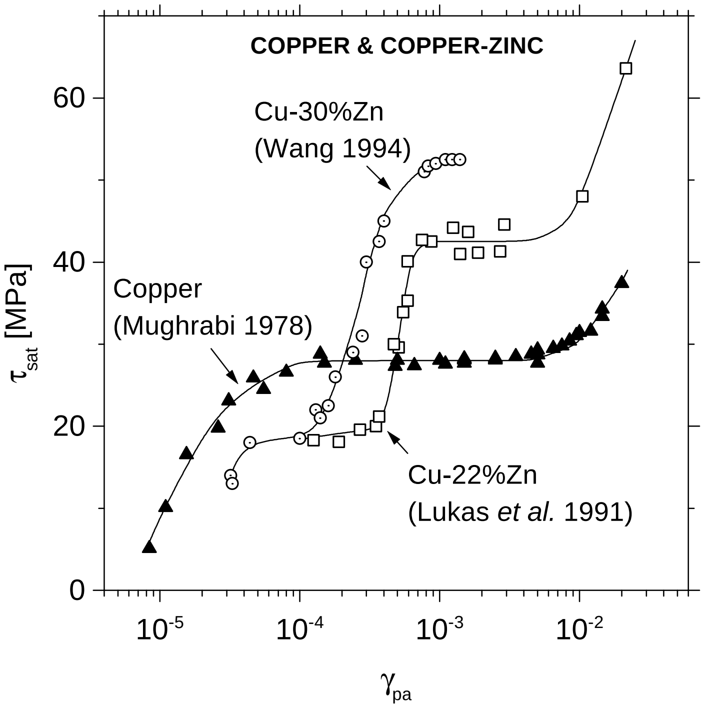

Figure 2.9 CSS curves for single glide crystals of copper (MUGHRABI, 1978), Cu-22%Zn (LUKÁS ET AL., 1991) and Cu-30%Zn (WANG, 1994).

The shape of the CSS curves found for Cu-22%Zn and Cu-30%Zn resembles the shape of the CSS curve for copper. However, the curves are based on different definitions of saturation stresses, which raises the question of how to determine the saturation stresses in these alloys?

Polycrystals

The problem with definition of saturation stresses in brass was first discovered in studies of polycrystals. POLÁK *ET AL.* (1974) investigated polycrystalline Cu-31%Zn cycled at low plastic strain amplitudes and they revealed “an exceptionally long primary stage” of cyclic hardening. Nevertheless, they concluded that saturation still exists. Other investigations of polycrystalline Cu-30%Zn fatigued at constant total strain amplitudes (MARCHAND *ET AL.*, 1983; BOUTIN *ET AL.*, 1984A) show little tendency to saturation - especially at the lower amplitudes. BOUTIN *ET AL.* (1984B) stressed “that it is doubtful whether true stress saturation occurs prior to fatigue failure for tests on 70-30 α brass carried out in air”. This emphasizes the need for a proper definition of the saturation stresses. The investigations by MARCHAND *ET AL.* (1983) and BOUTIN *ET AL.* (1984A) reveal cyclic softening at the high amplitudes similar to the observations made in Cu-22%Zn single crystals. This phenomena is therefore not an effect of polycrystallinity.

Only little information exists on strain controlled cyclic plasticity in polycrystalline planar slip materials. Cu-Al seems to have been the favoured planar slip model system, and the single crystal behaviour has been thoroughly investigated by LAIRD and co-workers. However, only little attention has been offered to the effect of polycrystallinity and the work by LAIRD *ET AL.* (1986) seems to be the only detailed study of Cu-Al polycrystals. The information on polycrystalline brass is equally insufficient and the four references mentioned above are the only available investigations providing detailed information about strain controlled cyclic plasticity of polycrystalline brass. The present investigations therefore seem to add to a relatively unexplored field.

2.2 Fatigue

The purpose of studying basic fatigue mechanisms is to understand the process leading to fatigue failure. Without information about these mechanisms it is difficult to design materials with improved fatigue resistance. The fatigue resistance is measured by the number of cycles, N_f, a material can resist an imposed load before it fails. It is common to distinguish between low cycle fatigue (LCF) and high cycle fatigue (HCF), however the distinction is controversial. Some define LCF as cyclic deformation leading to failure within a certain number of cycles, e.g. 10.000 cycles (see e.g. LEMAITRE, 1992). Others define LCF according to the density of surface cracks. The density is one or two orders of magnitude larger in LCF than in HCF (BRECHET *ET AL.*, 1992).

Empirical laws have been suggested for LCF and HCF. In the LCF domain the Coffin-Manson law can be used to describe the fatigue behaviour (COFFIN, 1971):

$$N_F \cdot \varepsilon_{pa}^{\beta} = \text{const.} \tag{2.5}$$

where ε_{pa} is the applied plastic strain amplitude. In the HCF domain the Basquin law can be used (BASQUIN, 1910):

$$N_F \cdot \sigma_{a}^{\alpha} = \text{const.} \tag{2.6}$$

where σ_a is the applied stress amplitude. These two empirical laws suggest LCF to be the term for (plastic) strain controlled fatigue, and HCF to be the term for stress controlled fatigue. This distinction will be used in this thesis and emphasis will be on LCF.

In LCF of wavy slip materials, such as copper, fatigue damage results mainly from cyclic strain localization in PSBs leading to transgranular cracking (MUGHRABI *ET AL.*, 1983; HUNSCHE & NEUMANN, 1988; MA & LAIRD, 1989). Transgranular damage is best studied in single crystals, and a special method, the sharp-corner technique, has been developed to study the process of crack initiation in PSBs (BASINSKI & BASINSKI, 1984). In Figure 2.10 micrographs are shown of the same area on a copper single crystal at different numbers of deformation cycles. From these pictures it is seen, how the crack initiates and grows into the bulk along the PSB. However, the mechanism explaining how a PSB can develop into a crack is still controversial. A simple model was proposed by MOTT (1958), in which it is suggested that cracks are formed as cavities underneath extrusions in the PSBs through a cross slip mechanism. The material above these cavities will eventually be extruded to form cracks. This process is shown in Figure 2.11.

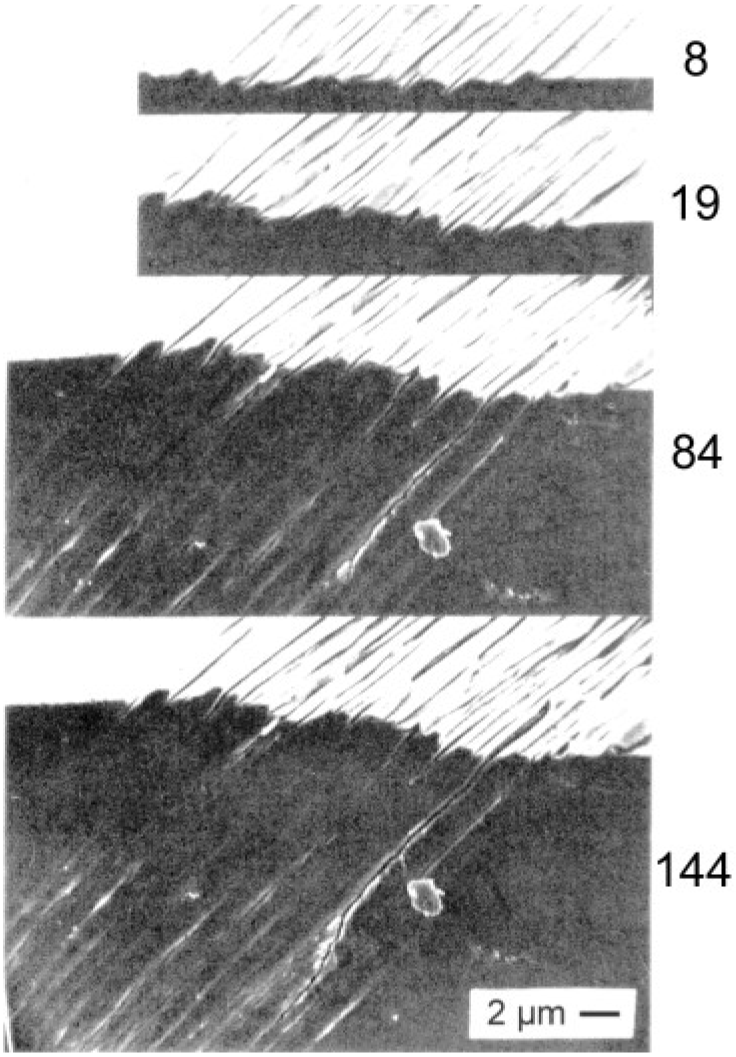

Figure 2 10 The same area of a copper single crystal at 8, 19, 84 and 144 wing the origin and growth of cracks. The special sharp-

face, respectively (B & BASINSKI .

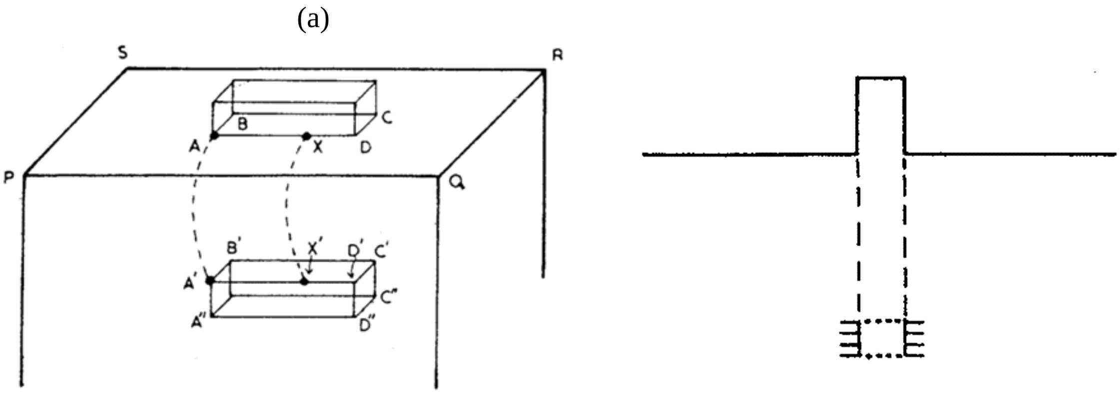

Figure 2.11 Mechanism of fatigue crack formation. (a) Dislocation movement in a crystal during crack formation in fatigue. (b) Crack at the base of an extrusion (MOTT, 1958).

From studies of PSBs in AgCl ROWN & O (1985) demonstrated that PSBs are associated

with glide bands formed in unidirectional deformation. They developed a composite model which showed that near the free surface, a PSB produces stress singularities which promote

o-

n-

n-

d-

BASINSKI

BASINSKI which show that the slip activity in a PSB is concentrated into sharp ‘persistent slip lines’, or PSLs. The PSL consist of small groups of extrusions and intrusions. The extr-sions grow to a length of about 4 µm, while some of the intrusions grow beyond this length.

such surface cracks, ranging in length between about 4 µm and 100 µm. The length of the *dee-est* y-

about 100 µm depth begins to accelerate under the stress intensity amplitude at its tip.

The studies of single crystals provide important information about the fatigue mechanisms r-sponsible for transgranular cracking. However, industrial materials are polycrystalline and the

polycrystalline copper show, that the interaction between PSBs and grain boundaries promote the initiation of intergranular cracks. A pile-up mechanism has been suggested to explain the ESSMANN ., 1981) Figure 2.12.

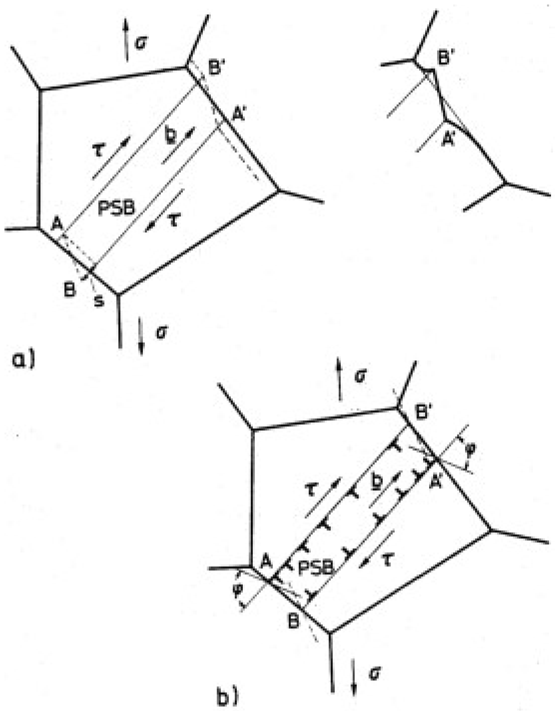

2. Interaction between PSBs and grain boundaries in polycrystals (schematically for tensile phase). is shear stress. (a) Effect due to homoge-neous shear localized in a PSB bounded by grain boundaries. Distortion at grain boundary is indicated on the right. (b) Counteracting effect due to pi-ing-up of PSB-matrix interface dislocations against grain boundaries. MUGHRABI ET AL).

Since early studies (McGrath & Thurston, 1963) intergranular cracking has been correlated with wavy slip materials while planar slip materials are considered to be dominated by transgranular cracking. Different explanations have been offered to account for these observations. Laird & Feltner (1967) argued that the planar slip mode of deformation prevents grain boundary folding and therefore crack nucleation is mainly transgranular. Mughrabi *et al.* (1983) claimed that in planar slip materials, random irreversible slip of large dislocation groups gives rise to a pronounced surface roughness and thereby leads to slip band cracking. Recently Rolim Lopes & Charlier (1993) considered the importance of intergranular stresses on the cyclic behaviour and found that with increasing grain size the tendency to form intergranular cracks increases. This behaviour was explained in terms of the geometrically necessary dislocations theory (Ashby, 1970), which considers the necessity to fulfill compatibility requirements among the grains in a polycrystal. It is suggested that this process induces accumulation of geometrically necessary dislocations, the density, ρ_G, of which scales with the grain diameter as $\overline{D}^{-1}$. This means that a fine grain size leads to a high value of ρ_G, which can accommodate intergranular stresses by redistributing stresses within the grains. For the coarse grained material the intergranular stresses can be accommodated by inducing secondary slip at the grain boundaries. As a result, the fine grained material is dominated by transgranular cracking which is believed to be a slower damage process, resulting in an improvement of the fatigue life. This effect of grain size on fatigue life is supported by other experimental observations in copper and brass (see e.g. Forrest & Tate, 1965; Lukás & Kunz, 1987).

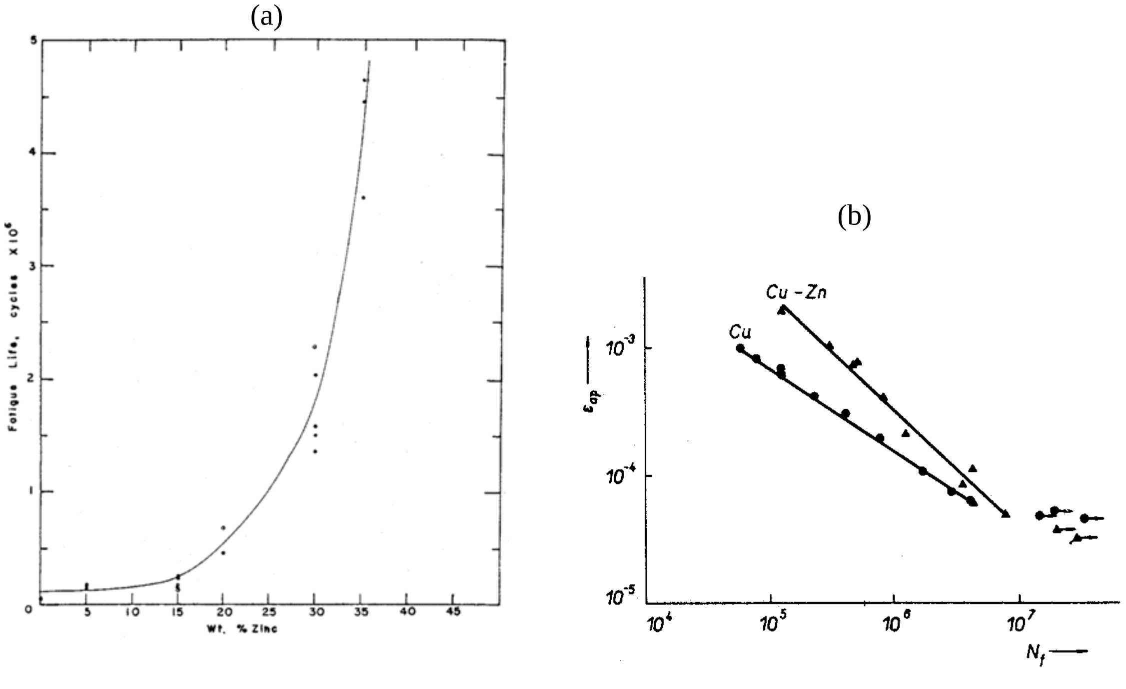

Figure 2.13 (a) Fatigue life against per cent zinc for copper and Cu-Zn alloys cycled at a stress amplitude of ~125 MPa (McGrath & Thurston, 1963). (b) Fatigue life curves for copper and Cu-31%Zn cycled at constant plastic strain amplitudes (Lukas et al., 1974).

Other parameters are known to have an important effect on fatigue life. A reduction of temperature increases fatigue life due to the refinement of the scale of the dislocation structures (as mentioned above). The environment has effect on fatigue life, and cycling in vacuum is known to prolong fatigue life considerably (see e.g. Wang *et al.*, 1984; Gerland *et al.*, 1989). This

thesis focuses on the effect of chemical composition which also has an effect on fatigue life. M GRATH HURSTON (1963) n stress controlled fatigue of brass the addition of up to 15% zinc to copper had no significant influence on fatigue life. As further additions of LUKAS .) showed that the increase in fatigue life seems to depend on the plastic strain amplitude. At high plastic strain r-
Figure 2.13.

life. The present investigations will contribute to the understanding of the mechanisms responsible for this effect.

3 Characterization Methods

As stated in chapter 1 and 2 it is essential to have well-characterized materials as well as well-specified test conditions when investigating basic mechanisms of fatigue. Features like grain size, texture and chemical composition play important roles on the fatigue properties. So do deformation-mode, -rate and -temperature. In this chapter the investigated materials will be characterized and the test conditions will be described. The microscopical techniques used, to study the structural evolution, will also be characterized.

3.1 Materials characterization

The materials investigated in this thesis are two brass alloys with different zinc contents. One alloy is a copper-15%zinc and the other a copper-30%zinc. These were initially examined by Energy Dispersive X-ray analysis (EDX) revealing less than 0.1wt% impurities in both alloys. The alloys will be referred to as Cu-15%Zn and Cu-30%Zn respectively.

3.1.1 Processing

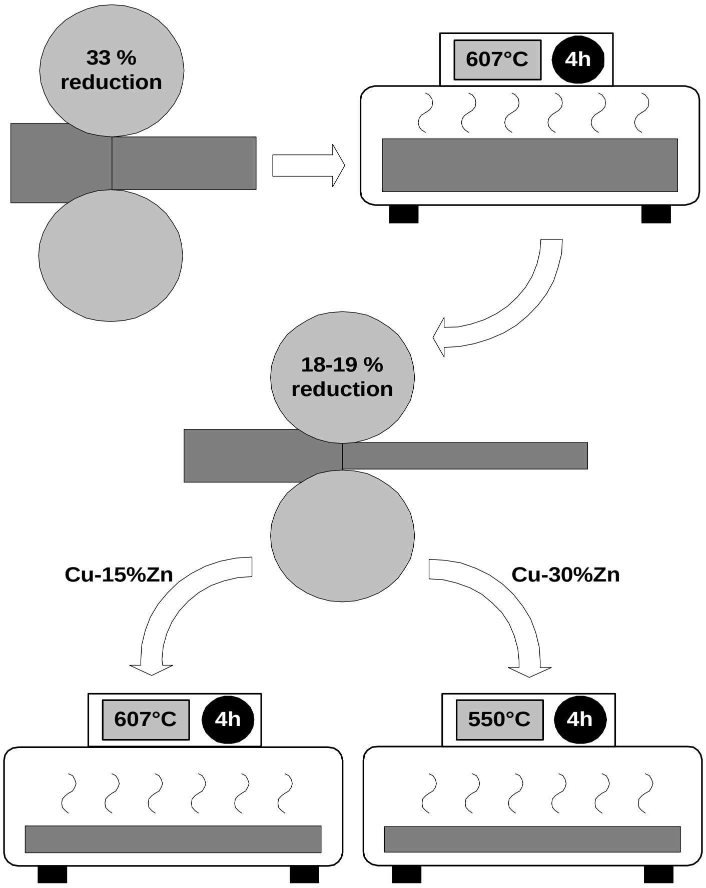

Figure 3.1 Schematic of the processing of the two alloys Cu-15%Zn and Cu-30%Zn.

Successive rolling and heat treatments were designed to obtain two texture-free brasses with identical average grain sizes. From an initial thickness of 29 mm plates of Cu-15%Zn and Cu-30%Zn were rolled to a thickness of 19.5 mm. This corresponded to a 33 % reduction, which was followed by annealing in vacuum for 4 hours at 607°C. The plate thicknesses were then reduced a further 18-19 % by rolling. Cu-15%Zn and Cu-30%Zn were finally annealed in vacuum for 4 hours at 607°C and 550°C respectively. In Figure 3.1 these procedures are illustrated schematically. To obtain the same grain sizes it was necessary the chose equal homologous temperatures for the heat treatments. The melting point, T_m, for Cu-15%Zn is ~1283K (see Appendix A) and thus the annealing temperature 607°C=880K corresponds to the homologous temperature $0.685 \cdot T_m$. Cu-30%Zn has a lower melting point $T_m \approx 1200K$, which explains the lower annealing temperature ($0.685 \cdot 1200K = 823K = 550°C$).

3.1.2 Grain size distribution

In Figure 3.2 examples of the grain structure are shown for both alloys.

(a)

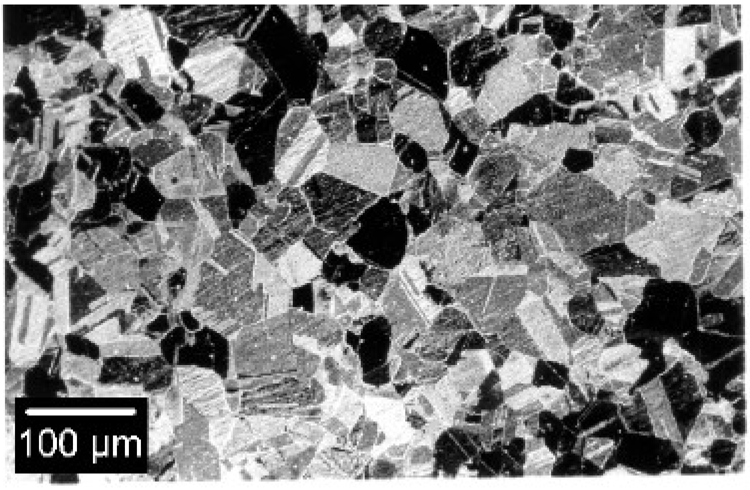

(b)

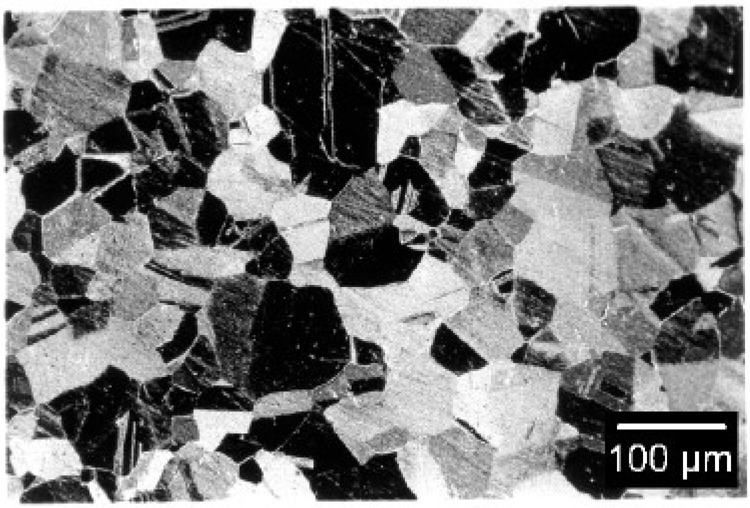

Figure 3.2 Optical micrographs showing the initial grain structure of (a) Cu-15%Zn, and (b) Cu-30%Zn. Annealing twins traverse a lot of the grains.

To enhance the grain structure pieces of the two alloys were first grinded and polished down to 3 µm diamonds and subsequently chemically polished using an OP-S solution (see Appendix B). The smooth cross-sections were then etched using a potassium-dichromate solution (see Appendix B). The grain size distribution was determined by the linear intercept method using an optical microscope, a LCD camera and the AXIODOC® software from Zeiss (AXIODOC® is an interactive system for microscopic image acquisition, measuring and archiving). Lines were made forming a grid on characteristic areas of the cross-sections and for each gridline α the length of the gridline, L_α, the number of boundaries intersected by the gridline, n_α, and the length of the individual gridline intercepts, l_β, were made. The average grain size, $\overline{D}$, was then approximated by (EXNER, 1972):

$$\overline{D} = \frac{3}{2} \cdot \frac{\sum\limits_{\text{all gridlines}} L_\alpha}{\sum\limits_{\text{all gridlines}} n_\alpha} \tag{3.1}$$

In Table 3.1 the obtained average grain sizes are shown. As seen on Figure 3.2 a lot of the grains contain annealing twins resulting from the heat treatments described in chapter 3.1.1 . When measuring the intercepts a distinction was therefore made between grain boundary intercepts and twin boundary intercepts and the average grain sizes were calculated both with and without counting the twin boundary intercepts.

Table 3.1 Average grain sizes measured using the linear intercept method. Two different grain sizes are obtained according to whether or not twin boundaries are included

Alloy	Grain size [µm]	
	counting twins	ignoring twins
Cu-15%Zn	40	45
Cu-30%Zn	60	65

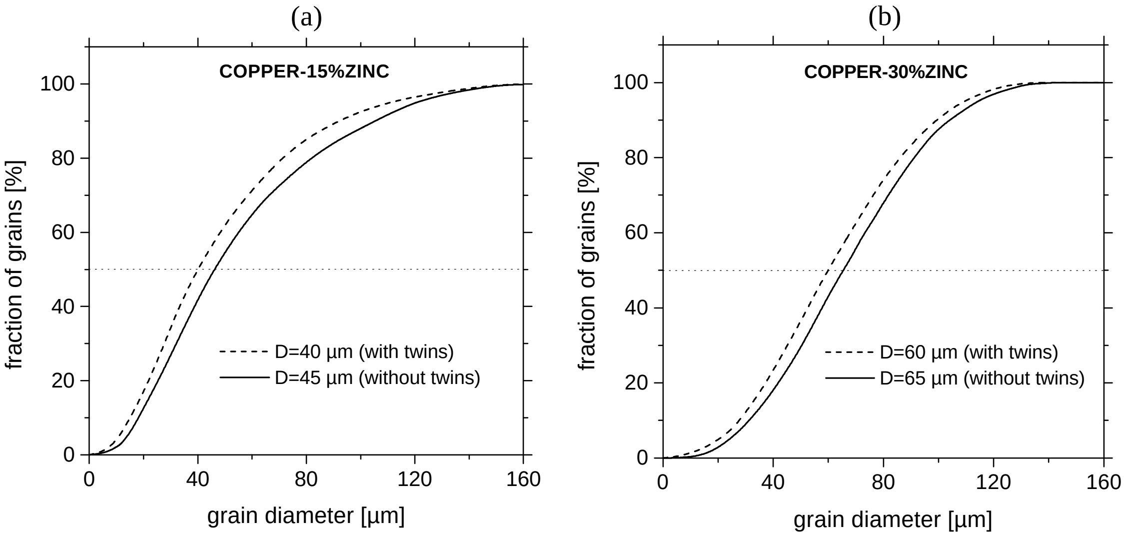

Figure 3.3 Cumulative grain size distribution based on the measured linear intercepts, (a) Cu-15%Zn, and (b) Cu-30%Zn.

The small differences in grain sizes may very well be due to the fact that Cu-30%Zn was annealed at a too high homologous temperature after the first rolling (see chapter 3.1.1). The differences are though so small that they can be neglected in comparison of the results for the two brasses.

Approximately 1000 intercept lengths were measured on the two alloys corresponding to 31.6mm of total gridline length (ΣL_{α}). From the distribution of intercepts, l_{β}, the spatial grain size distribution was calculated using principles described by Exner (1966; 1972). The curves on Figure 3.3 are the results of these calculations.

3.1.3 Texture

The textures were carefully measured using neutron diffraction. Cylindrical stubs of Cu-15%Zn and Cu-30%Zn with a length of 10.0 mm and a diameter of 6.0 mm were cut and polished on the ends using 1000 × grid SiC paper. The stubs were then chemically etched using a nickel chloride solution (see Appendix B). The textures were measured on these stubs using the TAS-7 spectrometer at Risø's reactor DR3. A position sensitive detector was used so as to reduce the measuring time and the Orientation Distribution Functions (ODFs) were determined by the series expansion method (For more details see Juul Jensen *et al.*, 1984). In Figure 3.4 the obtained ODFs are shown.

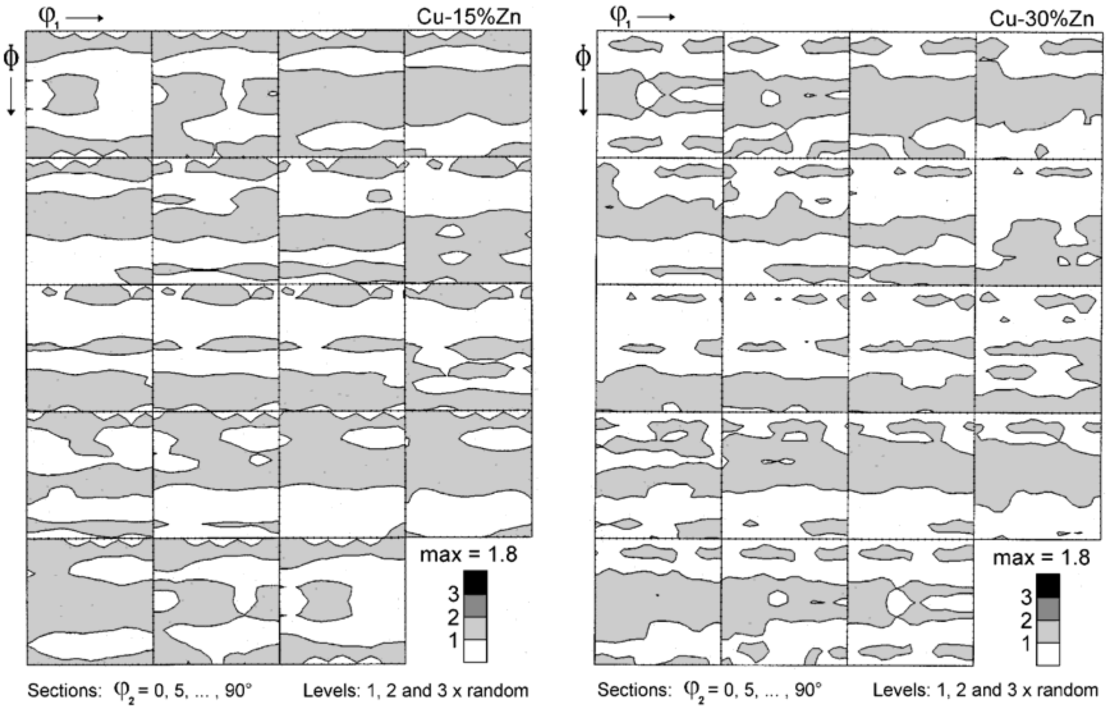

(a) (b)

Figure 3.4 Orientation Distribution Functions for (a) Cu-15%Zn, and (b) Cu-30%Zn, measured by neutron diffraction. Both materials are practically texture free.

The maximum intensity is 1.8 times random for both Cu-15%Zn and Cu-30%Zn which indicates that the alloys are virtually texture free (perfect randomness corresponds to an intensity of 1, which is not achievable in practice).

3.1.4 Mechanical properties

The present study focuses on plastic strain controlled fatigue. To enable control of the plastic strain, it is necessary to have information about the modulus of elasticity, E. Uniaxial tension tests were performed using an Instron 8501 servohydraulic testing machine (this machine was also used for the fatigue tests). The tests were run up to a total strain of 4.0% on rectangular specimens (see chapter 3.2). In Figure 3.5 the obtained stress-strain curves are shown.

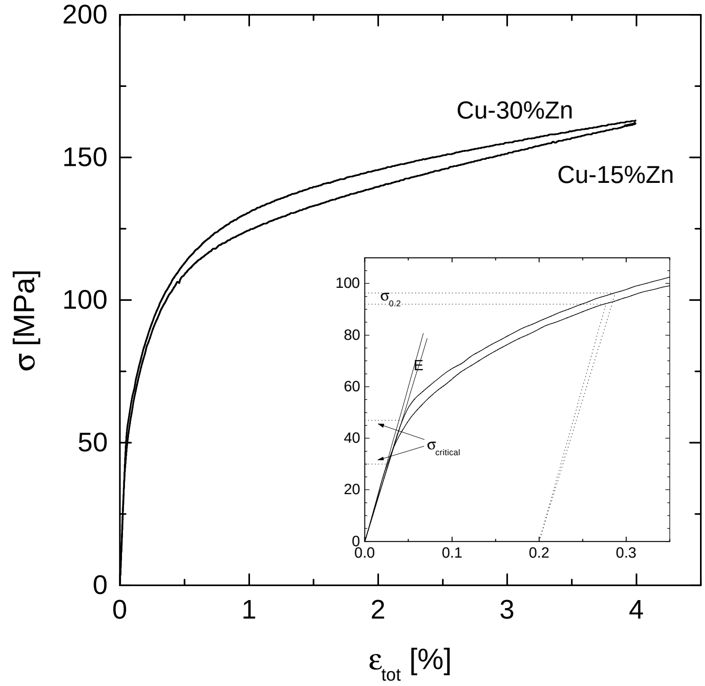

Figure 3.5 Stress-strain response for uniaxial tension test performed on both Cu-15%Zn and Cu-30%Zn.

The inserted curves show an enlargement of the yield region indicating the reading of elastic properties. These properties are listed in Table 3.2.

Table 3.2 Mechanical properties for Cu-15%Zn and Cu-30%Zn measured in a simple tensile test.

Alloy	Modulus of Elasticity, E [GPa]	Onset of 1st yield, $\sigma_{critical}$ [MPa]	Yield stress, $\sigma_{0.2}$ [MPa]
Cu-15%Zn	120	30	92.0
Cu-30%Zn	110	47	96.3

3.2 Specimen preparation

Specimens of both alloys with total length 10.0 cm and 4.0 x 6.0 mm² cross sections were cut in the rolling direction for use in cyclic plasticity experiments. Prior to testing each specimen was first grinded with 1000 × grid SiC paper and then mechanically polished with 3 µm diamonds on all four sides to ensure a smooth surface. Specimens to be used for surface studies were furthermore electropolished on one side in the gauge area using a D2-electrolyte. The resulting cross sections were approximately 3.8 x 5.8 mm².

For fatigue life experiments shouldered specimens of Cu-30%Zn were lathe turned to a total length of 8.0 cm and 5.0 mm in diameter in the gauge area. While still in the lathe the specimens were grinded with 4000 × grid SiC paper followed by a final mechanical polishing with 0.1 μm Al_2O_3. This resulted in a smooth and reproducible surface on the entire gauge area. The resulting diameter was approximately 4.9 mm. In Figure 3.6 the two types of specimens are shown schematically.

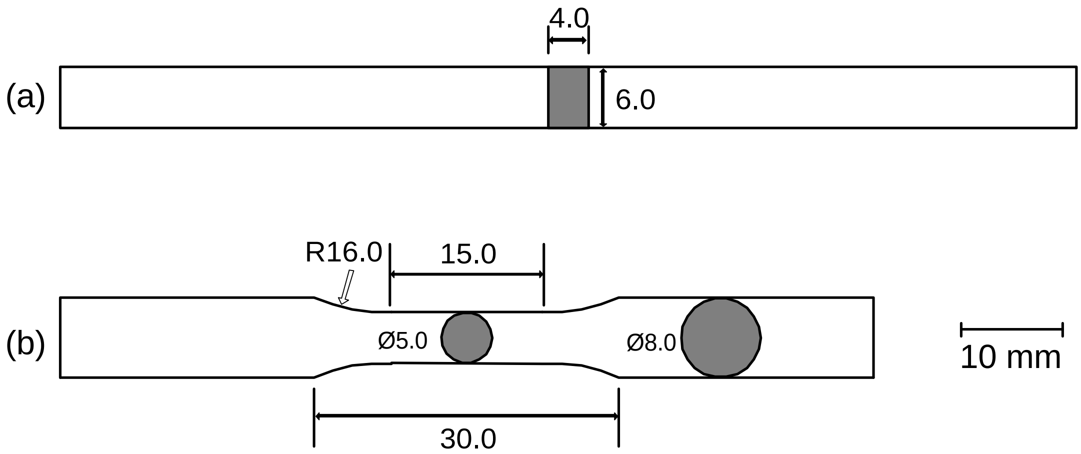

Figure 3.6 Specimens used for (a) cyclic plasticity and surface study experiments, and (b) fatigue life experiments.

3.3 Mechanical Testing

The fatigue tests were all carried out at room temperature in air, and thus the effects of temperature and environment were not investigated. The prepared specimens were cyclically deformed at constant plastic strain amplitudes and zero mean strain in tension-compression using a computer controlled servohydraulic testing machine (Instron 8501). The deformation was carried out at constant strain rate, which was chosen so that the average cycling frequency was approximately 1 Hz for the cyclic plasticity experiments and approximately 2 Hz for the fatigue life experiments. Stress readings were obtained from a ±20 kN strain gauge load cell, and the strain was measured by a clip-on extensometer attached directly on the specimen surface. For the fatigue life experiments cellulose glue was applied at both edges of the extensometer to prevent crack initiation at artificial notches. Load/extension data were recorded by the computer with a frequency of 200 Hz.

To prevent buckling of the rectangular specimens at the high plastic strain amplitudes, it was necessary to keep the jaws of the testing machine close. Thus the gauge length (=distance between the shoulders of the extensometer) was only 5 mm at the highest amplitudes. At the low plastic strain amplitudes buckling was not a problem so the distance between the jaws could be increased. This enabled a larger gauge length which improved the accuracy of strain measurements and control of the plastic strain amplitude. At the lowest amplitudes the gauge length was 35 mm.

The described variation of the gauge length enabled plastic strain controlled deformation in a wide range of plastic strain amplitudes. The plastic strain amplitude, ε_{pa}, was determined by averaging $\Delta\varepsilon_p/2$ of all recorded stress-strain loops in the actual experiment. The anelastic strain was taken into account to avoid underestimation of ε_{pa} (see chapter 4.2). The accuracy of the amplitude control is illustrated in Figure 3.7. Except for two cases, all tests were cycled with a plastic strain amplitude deviation of less than 10%.

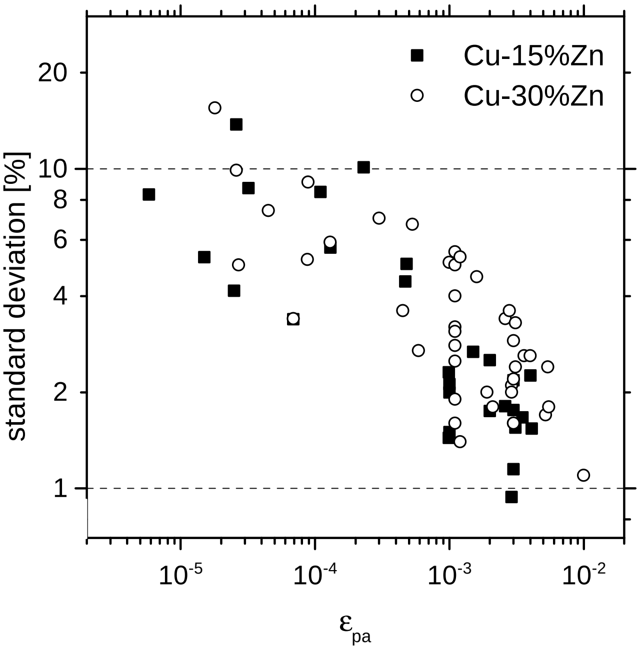

Figure 3.7 Standard deviation vs. plastic strain amplitude for fatigue experiments carried out on Cu-15%Zn and Cu-30%Zn.

3.4 Microscopy

After cyclic deformation the specimens were investigated using different microscopical techniques. Transmission electron microscopy (TEM) was used to study the dislocation microstructures. The surface damage, i.e. slip bands and microcracks, was studied on a large scale using optical microscopy (OM) and on a finer scale using scanning electron microscopy (SEM).

3.4.1 Transmission electron microscopy (TEM)

The investigations of dislocation microstructures were carried out on a JEOL 2000FX operating at 200 kV using a LaB_6 filament. The thin foils were prepared and mounted in a double tilt holder with the edge markings on the foils (see Figure 3.8-5) aligned along the x-direction of the tilt holder.

Thin foil preparation

An automatic precision cutter (Struers Accutom-5) was used to cut slices parallel to the loading direction from the gauge area of the cyclically deformed specimens (see Figure 3.8-1). These slices, with an initial thickness of approximately 300 µm, were thinned down to 150 µm (2) using still finer SiC-paper. On each sample the loading direction was marked by a straight line using a regular pencil (3) and a 3 mm disc was punched out (4) using a specially designed punching tool. The loading direction was permanently marked (5) by fine cuts at the edge of the disc (where the straight line intersects the edge) and the disc was thinned down further to a final thickness of 100-120 µm using 4000 × grid SiC-paper.

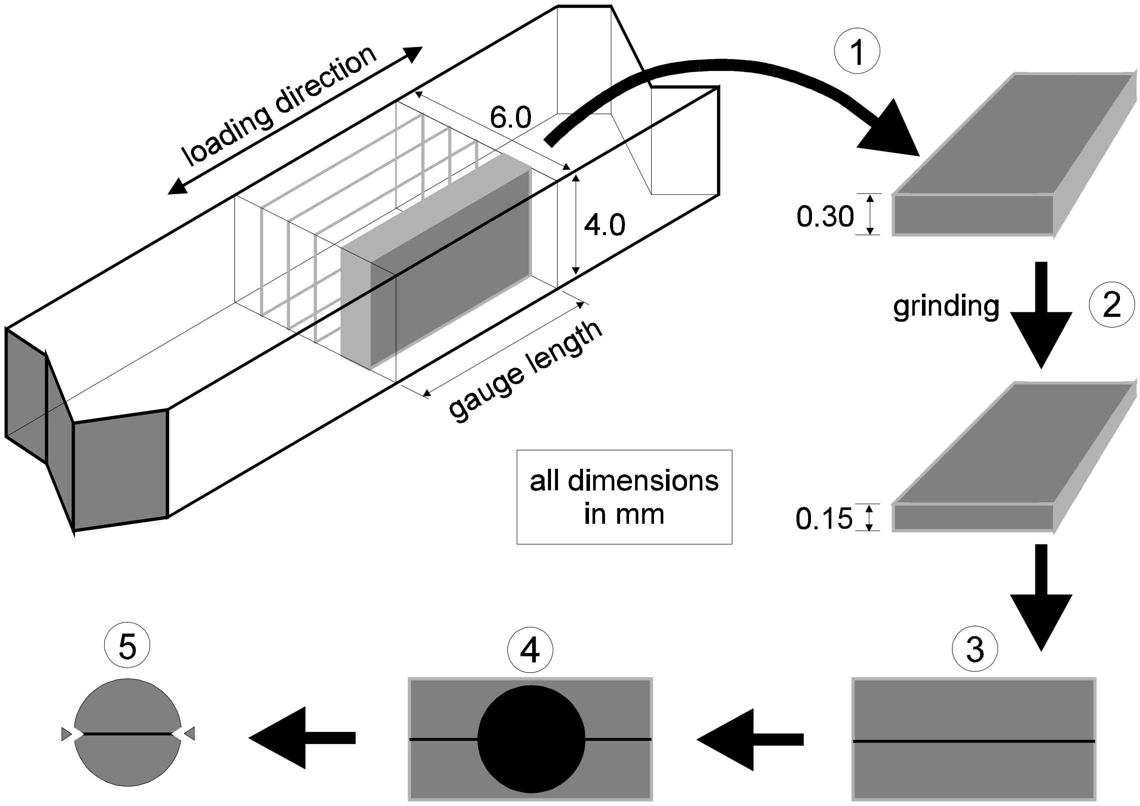

Figure 3.8 Preparation of thin foils for TEM. (1) Cutting of slices parallel to the loading direction, (2) thinning of samples from 300 µm to 150 µm, (3) marking of the loading direction, (4) punching out discs for jetpolishing, and (5) permanent marking of loading direction (edge cuts).

Prior to use in the TEM the discs were jet polished in a semi-automatic jet polisher (Struers Tenupol-3) using a D2 electrolyte (see Appendix B). The optimum results were achieved using a constant current of 80 mA, a constant flow rate of 5.5 (arbitrary unit), a photosensitivity of 10 (arbitrary unit) and a temperature of 7-8 °C. The electrolyte was cooled by liquid nitrogen. The discs were polished until a hole in the middle appeared (detected by a photosensitive detector). Near the edges of such a hole the discs are very thin, typically 100 nm, which enable penetration of electrons. Holed discs of this kind are called thin foils.

Imaging

According to quantum mechanics electrons can act as waves and thus we can get diffraction from the atomic planes in a crystalline sample. The diffracted beams satisfy the geometrical requirements of Bragg’s law, in that each set of parallel crystal planes diffract electrons in a specific direction. In the TEM an aperture is placed in the objective back focal plane to permit only one beam to form the image. When the beam transmitted directly through the specimen is selected, a bright-field image is displayed, whereas when one of the diffracted beams is chosen, a dark-field image is observed. This is illustrated in Figure 3.9.

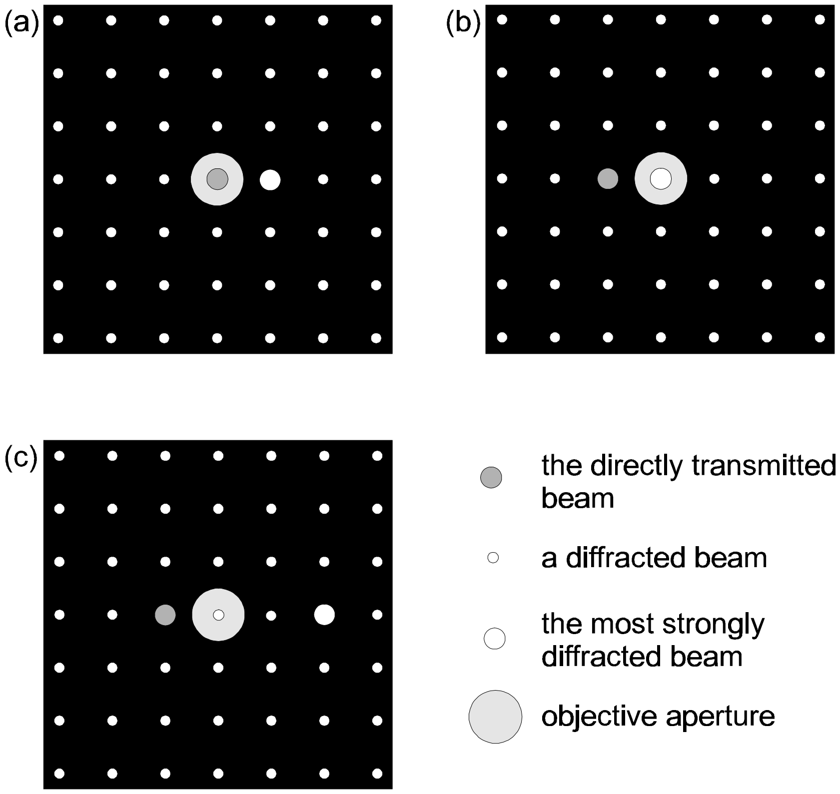

Figure 3.9 The beam selection for the different types of TEM-images viewed in diffraction mode. (a) Bright field image, (b) dark field image, and (c) $\mathbf{g}(3\mathbf{g})$ *weak-beam technique (used in a few cases in this study). The optical axis is in the centre of the objective aperture.*

The image simply reveals the variation in intensity of the selected electron beam as it leaves the specimen. Image contrast arises if variations in beam intensity occur from one part of the specimen to another. Dislocations (and many other crystal defects) bend crystal planes and thus strong intensity variations can result. The dislocations appear as dark lines in a bright-field image and as bright lines in a dark-field image. In the present study mainly bright-field images were chosen. The images were recorded using a Polaroid camera with 6x9 negatives.

Shadowing effects, due to variation of the crystal orientation, is often a problem in bright-field images at the lower magnifications. The JEOL 2000FX has a Hollow Cone device attached to the microscope which is able to eliminate or reduce the shadowing effects (for more details about the Hollow Cone technique see CHRISTOFFERSEN, 1996). A disadvantage of using the Hollow Cone technique is a reduced sharpness of the images. At lower magnifications this is often not so crucial considering the benefits of the reduced shadowing effects. In the present study the Hollow Cone technique was used whenever the resulting image was considered to be improved.

The width, w, of a dislocation image depends on the effective extinction distance, ξ_g^{eff}, which is the periodicity by which the beam intensity oscillates (COCKAYNE, 1973). Assuming a two-beam condition (i.e. only one set of crystal planes is at, or close to, the Bragg angle), the following apply (LORETTO & SMALLMAN, 1975):

$$w \approx \frac{\xi_g^{eff}}{3} \tag{3.2}$$

$$\xi_g^{\text{eff}} = \frac{1}{\sqrt{s^2 + 1/\xi_g^2}} \tag{3.3}$$

where ξ_g is the extinction distance at the Bragg angle and s the deviation from the Bragg angle. ξ_g depends on the material investigated and on the given reflection so it follows that w can be decreased only by increasing s. In a bright-field image s≈0 and w is typically 10-50 nm. Thus closely spaced dislocations may not be resolved. To overcome this disadvantage the so-called weak-beam technique can be used. By tilting the specimen away from the Bragg orientation, ξ_g^{eff} is reduced and so is the dislocation width. In other words, strong diffraction from a dislocation occurs only where the bending of the planes is strong; that is near the centre of the dislocation. Thus the weak-beam images of dislocations are much narrower, typically 1-2 nm (COCKAYNE, 1973; LORETTO & SMALLMANN, 1975).

In order to obtain information from dense agglomerates of dislocations (see chapter 5.1.2) the weak-beam technique was used in a few cases. The beam selection used is simplified in Figure 3.9c (for more details see LORETTO & SMALLMAN, 1975). It is a so-called **g**(3**g**) weak-beam technique and it is one of the possible techniques to reveal the fine structures of dislocations (another frequently used weak-beam technique is the **g**(-**g**) technique).

Diffraction patterns and trace analysis

By combining the crystallographic and orientation information provided by the selected area diffraction pattern with the geometry of the corresponding electron micrograph, comprehensive crystallographic details can be deduced about features such as stacking faults, dislocation lines etc. This means that the habit planes or crystallographic directions of these features can be determined. This type of analysis is known generally as trace analysis (HIRSCH *ET AL.*, 1965). The selected area diffraction pattern is a spot pattern which depends on the crystal structure (FCC, BCC etc.) and on the orientation of the specimen (grain) with respect to the incident electron beam.

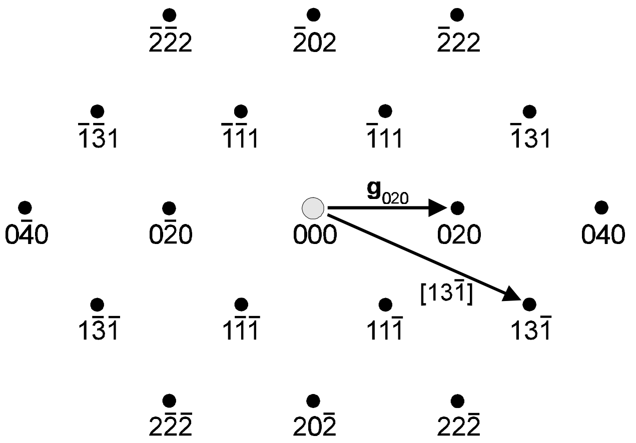

Figure 3.10 Diffraction (spot)pattern from a FCC crystal with the electron beam in the [101] direction. The [$13\bar{1}$] direction and the diffraction vector $\boldsymbol{g}_{020}$ *are indicated by an arrow.*

When the specific diffraction pattern is recognized it is possible to index the different spots in the diffraction pattern. The recognition is based on a model of the reciprocal lattice for the given crystal structure. In the present study a computer program (Electron Diffraction 4.2) was used to simulate different diffraction patterns, which were then compared to diffraction patterns obtained in TEM. This enabled a recognition and subsequent indexing of the diffraction patterns. The diffraction pattern shown on Figure 3.10 is the pattern obtained for a FCC crystal with the beam in the [101] direction.

It is important to realize that a TEM diffraction pattern determines the crystallographic orientation of the specimen relative to the electron beam, and that it gives no indication of the tilt of the plane of the specimen. As stated by HIRSCH *ET AL.* (1965) the most serious source of error and uncertainty in trace analysis arises from tilt of the specimen, so that it is no longer perpendicular to the electron beam. If the specimen is tilted an angle ϕ from the perpendicular position the image of a planar feature is rotated from its direction calculated for the case of no tilt. The magnitude, ε, of this rotation is given by:

$$\cot\varepsilon = \cot\beta + \tan\theta\cdot\csc\beta\cdot\cot\phi \tag{3.4}$$

where β is the angle between the tilt axis and the direction of the planar trace, and θ is the angle between the plane of the planar feature and the original foil plane. As the diffraction pattern is unaffected by the tilt a direct correlation between the indexed diffraction pattern and the image is not possible unless the tilt angle is known. However, a planar feature is often best viewed when cut close to its normal direction, that is with the angle θ being close to 90°. In this case ε is only slightly affected by the tilt. When these effects are taken into account it is possible to compare the indexed diffraction pattern with the corresponding image and thereby give the crystallographic direction of different features in the image. Besides this, the specific reflection is customarily specified by the diffraction vector, $\mathbf{g}$. In Figure 3.10 the diffraction vector $\mathbf{g}_{020}$ is shown as an example.

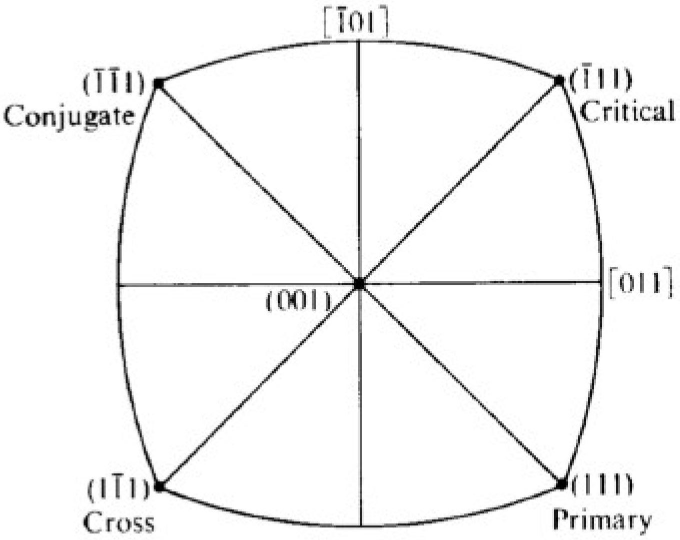

Figure 3.11 The destinction between different slip systems in FCC metals usually refers to the glide planes only. These are named the primary, critical, conjugate and cross glide plane, respectively (KELLY & GROVES, 1970).

Even though FCC metals tend to deform on their most highly stressed slip system, certain amounts of glide on other systems are usually observed. Since the slip plane of a glide system is easily observed the slip systems are usually identified by reference to the glide plane only. The slip plane of the most highly stressed system is called the primary glide plane and the names given to the others are shown in Figure 3.11. These names can be used to index different planar features in TEM micrographs.

Kikuchi patterns and crystallographic orientations

Most diffraction patterns have a complicated network of lines superimposed on them. These lines can be grouped into pairs, the two members of each pair being parallel and having a separation equal to the distance from the central spot to some diffracted spot on the pattern. Each spot hkl on the diffraction pattern is in fact associated with such a pair of lines, which are called the (hkl) Kikuchi lines. These lines are formed by inelastically scattered electrons which spread out in solid cones from every scattering centre and are not generally Bragg reflected. Together the Kikuchi lines form a Kikuchi pattern and, unlike the diffraction pattern, this pattern moves rigidly with the crystal. This make Kikuchi patterns ideal for determining the crystallographic orientation of the crystal. The intensities of the Kikuchi lines decrease with decreasing foil thickness but by using microdiffraction, where the electrons are condensed into a narrow beam, it is possible to observe Kikuchi lines even from very thin areas. In Figure 3.12 a Kikuchi pattern, obtained from one of the Cu-30%Zn specimens in the present study, is shown.

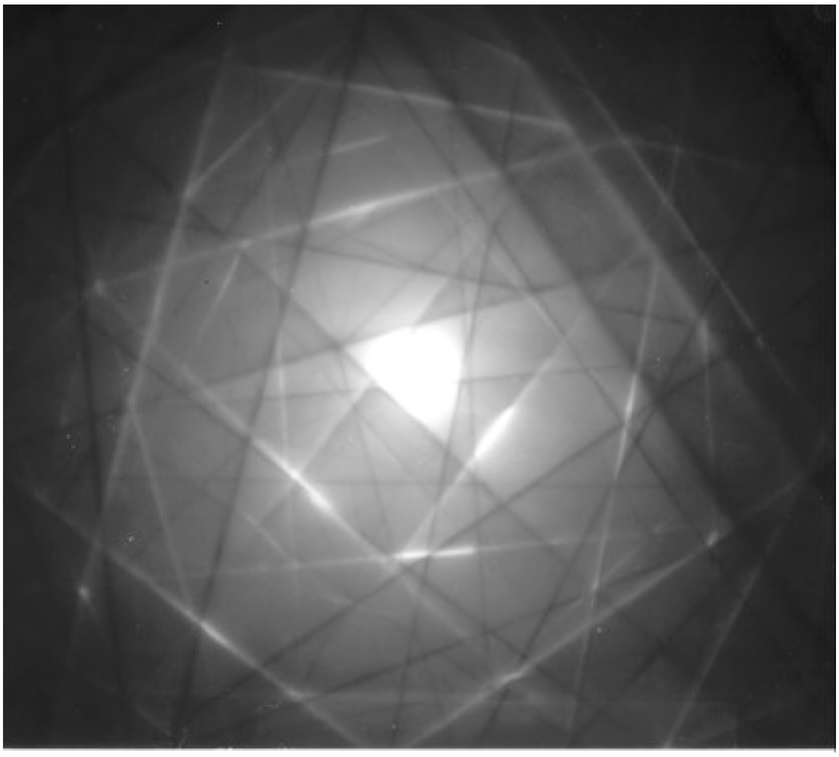

Figure 3.12 Kikuchi pattern from a Cu-30%Zn specimen. One Kikuchi band pair consists of two parallel lines, one white and one black.

The traditional manual analysis of Kikuchi patterns is time consuming and inconvenient, and thus a semi-automatic method has been developed (see KRIEGER LASSEN, 1995 for details) for determining the crystallographic orientation based on a Kikuchi pattern. The procedure is as follows: a Kikuchi pattern is obtained in diffraction mode without the selected area aperture using a small spot size. The pattern is recorded using a CCD camera and is then transferred to a computer. Using image processing procedures the positions of up to 11 Kikuchi band pairs can be extracted from the digitized pattern and a reliable and robust indexing of the localized bands is obtained. When the indexing is completed the crystallographic orientation is supplied in terms of Euler angles. This procedure was used to determine the orientation of crystal grains (see chapter 5.1.2).

3.4.2 Scanning electron microscopy (SEM)

In SEM an electron beam is scanned across the specimen surface and scattered electrons are detected to form an image of the surface. The so-called secondary electrons give information of the topography and are used to generate a 3D surface image. The backscattered electrons give information about atomic number, topography and (indirect) crystallographic orientation.

In the present project the SEM investigations were carried out on a JEOL 840 SEM but in a few cases a JEOL 5310 low vacuum SEM was used. The microscopes were operated at different acceleration voltages in the range between 7 and 15 kV and the obtained images were recorded using a CCD camera and transferred to a computer.

Table 3.3 Series of SEM observations were made for studies of microcrack evolution. At each plastic strain amplitude a specimen was cycled for N_{inc} cycles and selected surface areas were imaged in SEM. Subsequently the specimen was cycled further N_{inc} cycles and the same surface areas were imaged in SEM. This procedure was repeated.

plastic strain amplitude	N_{inc}	ΣN	ε_{cum}
$1.1x10^{-3}$	1000	1000	4,4
	2000	3000	13
	3000	6000	26
	4000	10000	44
	5000	15000	66
	5000	20000	88
	5000	25000	110
	5000	30000	132
	5000	35000	154
$2.2x10^{-3}$	1200	1200	9,6
	2800	4000	32
	4000	8000	64
	4000	12000	96
	4000	16000	128
$3.4x10^{-3}$	600	600	7,9
	1400	2000	26
	2000	4000	53
	2000	6000	79
	2000	8000	106

To observe the microcrack evolution rectangular specimens fatigued at different plastic strain amplitudes were studied in SEM at different number of cycles. The specimens were mounted directly in the SEM without any further preparation (for initial preparation see chapter 3.2 on page 33). Images were generated using secondary electrons. At each plastic strain amplitude a specimen was initially cycled for N_{inc} cycles and selected surface areas were imaged in SEM. Subsequently the specimen was cycled further N_{inc} cycles and the same surface areas were imaged in SEM. A special specimen holder ensured a reproducible mounting of the specimens so that the same areas could be located. The procedure was repeated beyond ε_{cum}=100. In Table 3.3

the series of observations are listed. From the series of SEM images it is possible to study the initiation and propagation of single microcracks and average crack growth rates can be estimated. This is done in chapter 5.2.3 .

3.4.3 Optical microscopy (OM)

When studying the surface damage on a large scale it is often more convenient to use an OM instead of a SEM. In the present project a Leitz OM was used to study the slip bands and surface cracks on fatigued specimens and images were recorded using an ordinary camera. From the obtained optical micrographs it is possible to reveal the nature of fatigue micro- and macrocracks and the slip bands can be evaluated to determine the slip mode (see chapter 5.2.1). Optical micrographs from surfaces of specimens cycled at different plastic strain amplitudes are used to estimate the fraction of plastically deformed grains (e.g. grains with slip bands) as function of the plastic strain amplitude (see chapter 5.2.1).

4 Mechanical Behaviour

In this chapter the characterization of the mechanical behaviour of cyclically deformed brass will be given. Cyclic hardening/softening curves are presented in chapter 4.2 and characteristic features are extracted and presented as cyclic stress-strain (CSS) curves in chapter 4.3. Fatigue life curves are presented in chapter 4.4 and compared to fatigue life curves of other relevant materials. The obtained results are discussed in chapter 4.5 and in particular the construction of CSS curves will be questioned.

4.1 Mechanical test results

In Table 4.1 and Table 4.2 the obtained test results are listed. The quantities σ_y, σ_{max}, σ_{min}, δ, N^{min}, σ_a^{min}, N^{100} and σ_a^{100} are determined from the cyclic hardening curves and will be explained in more detail in chapter 4.3. The specimens denoted with four digit numbers (e.g. 1526) are rectangular specimens (cf. Figure 3.6 on page 34), while other designations (e.g. 30_a) are used for shouldered specimens.

Table 4.1 Mechanical test results for Cu-15%Zn.

ε_{pa} [x10^{-4}]	N	ε_{cum}	$\dot{\varepsilon}$ [x10^{-2} s^{-1}]	σ_y [MPa]	σ_{max} [MPa]	σ_{min} [MPa]	δ [%]	N^{min}	σ_a^{min} [MPa]	N^{100}	σ_a^{100} [MPa]	specimen [no.]
0,058	10000	0,2	0,36	-15,0	-	-	-	140	42,2	-	-	1526
0,15	10000	0,6	0,24	-5,0	-	-	-	140	57,7	-	-	1524
0,25	60000	6	0,36	-2,5	-	-	-	150	64,1	-	-	1527
0,26	10000	1	0,83	-2,5	-	-	-	140	62,4	-	-	1521
0,32	10000	1	0,40	0,0	-	-	-	150	65	-	-	1523
0,69	10000	3	0,43	5,0	-	-	-	160	76,5	-	-	1528
1,1	415924	176	1,5	12,5	-	-	-	175	82,5	235849	96,0	1522
1,3	220800	111	0,71	12,5	-	-	-	170	81,5	198413	98,0	1525
2,5	100000	101	1,2	22,5	-	-	-	180	97,5	100000	112,0	1503
5,4	50000	108	1,4	35,0	-	-	-	350	108,9	46296	116,6	1514
5,5	50000	110	1,4	37,5	-	-	-	250	110,0	45455	116,8	1508
11	25000	110	2,0	45,0	120,8	116,3	3,7	2000	116,4	22727	117,8	1504
11	25	0,1	2,0	-	-	-	-	-	-	-	-	1512
12	250	1	2,0	-	-	-	-	-	-	-	-	1511
12	12500	58	2,0	47,5	127,4	120,3	5,6	2500	120,4	-	-	1509
12	2500	12	2,0	47,5	-	-	-	2500	116,3	-	-	1510
16	16666	107	2,4	50,0	131,3	122,2	6,9	6000	122,7	15625	123,0	1502
21	9600	82	2,8	50,0	139,3	124,7	10,5	6500	124,8	-	-	1519
23	12500	115	3,2	50,0	148,0	127,7	13,7	8800	128,1	10870	128,3	1501
28	10000	112	3,2	52,5	152,0	131,0	13,8	8500	131,9	8929	131,9	1505
32	83	1	3,6	-	-	-	-	-	-	-	-	1517
32	833	11	3,6	-	-	-	-	-	-	-	-	1513
32	9	0,1	3,6	-	-	-	-	-	-	-	-	1518
32	4167	54	3,6	50,0	157,3	137,2	12,8	3700	137,2	-	-	1516
33	8333	110	3,6	50,0	157,3	137,1	12,8	4000	139,0	7576	137,0	1506
38	5700	87	4,4	52,5	163,7	137,2	16,2	4000	139,5	-	-	1507
42	2600	44	4,8	50,0	169,1	145,0	14,3	4000	147,0	-	-	1520
43	2500	43	4,8	50,0	164,2	142,0	13,5	4000	144,0	-	-	1515

Table 4.2 Mechanical test results for Cu-30%Zn.

ε_{pa} [x10^{-4}]	N	ε_{cum}	$\dot{\varepsilon}$ [x10^{-2} s^{-1}]	σ_y [MPa]	σ_{max} [MPa]	σ_{min} [MPa]	δ [%]	N^{min}	σ_a^{min} [MPa]	N^{100}	σ_a^{100} [MPa]	specimen [no.]
0,18	25300	2	0,19	-15,0	-	-	-	100	58	-	-	3030
0,25	10000	1	0,24	-12,5	-	-	-	100	62	-	-	3031
0,27	10000	1	0,36	-10,0	-	-	-	100	59	-	-	3029
0,45	200000	36	0,48	-2,5	-	-	-	110	75	-	-	3032
0,69	10000	3	0,60	0,0	-	-	-	120	76,1	-	-	3028
0,88	45000	16	0,36	5,0	-	-	-	125	78,4	-	-	3027
0,89	215500	76	1,2	5,0	-	-	-	130	80,0	281849	108,0	3014
1,4	1000000	560	1,2	15,0	-	-	-	130	84,5	178571	112,6	30_a
3,2	100000	128	1,6	22,5	-	-	-	135	100,5	78125	133,4	3018
5,2	75000	156	1,6	25,0	-	-	-	135	106,5	48077	132,0	3006
6,2	50000	124	1,6	35,0	-	-	-	130	113,2	40323	139,2	3026
6,5	136000	354	1,7	35,0	-	-	-	140	107,6	38462	134,1	30_g
12	2500	12	2,4	50,0	-	-	-	270	140,0	-	-	3017
12	250	1	2,4	50,0	-	-	-	-	-	-	-	3016
13	25000	125	3,3	55,0	-	-	-	280	130,0	20000	144,4	3002
13	5000	26	2,3	55,0	-	-	-	250	128,4	-	-	30_f
13	25000	128	2,3	55,0	-	-	-	250	126,3	19531	144,1	30_j
13	37500	192	2,3	55,0	-	-	-	280	129,1	19531	146,7	30_i
13	54000	276	2,7	55,0	-	-	-	300	129,0	19531	149,2	30_e
13	15000	77	2,3	55,0	-	-	-	250	127,5	-	-	30_k
13	63600	326	2,7	55,0	-	-	-	260	128,6	19531	147,1	30_b
13	12500	65	3,3	55,0	-	-	-	350	135,4	-	-	3001
13	37500	195	3,3	52,5	132,1	131,7	0,3	280	132,0	19231	145,4	3003
14	25	0,1	3,2	55,0	-	-	-	-	-	-	-	3015
18	16667	123	3,2	57,5	151,2	149,1	1,4	480	149,4	13587	159,9	3011
22	12500	109	3,2	60,0	171,2	168,0	1,9	850	168,0	11521	174,4	3024
24	17500	170	4,0	57,5	172,4	165,6	3,9	1000	165,6	10288	172,0	3007
31	10000	122	4,0	60,0	174,7	167,2	4,3	850	167,3	8197	174,0	3010
32	7420	93	4,0	60,0	178,2	170,5	4,3	850	170,6	7937	177,0	3013
32	7920	103	4,4	60,0	183,6	175,0	4,7	900	175,0	7716	180,0	3019
33	83	1	4,0	62,5	-	-	-	-	-	-	-	3022
33	833	11	4,0	65,0	-	-	-	-	-	-	-	3021
33	8	0,1	4,0	60,0	-	-	-	-	-	-	-	3023
33	4167	55	4,0	60,0	184,4	174,9	5,2	860	175,4	-	-	3020
33	8800	117	4,0	62,5	185,4	175,1	5,6	900	175,4	7508	179,3	3008
34	7500	101	4,0	62,5	177,9	168,5	5,3	900	178,9	-	-	3025
34	17600	239	3,3	62,5	172,6	163,2	5,4	1000	164,1	7353	169,7	30_h
40	6600	106	4,8	60,0	192,9	180,4	6,5	900	180,5	6250	185,0	3009
45	4910	88	5,2	65,0	197,0	182,4	7,4	850	185,1	-	-	3012
54	4420	95	4,3	60,0	200,8	184,0	8,4	1400	185,4	4630	188,7	30_d
57	1550	35	15,2	60,0	218,9	198,2	9,5	800	195,0	-	-	3005
58	2000	46	14,4	60,0	215,2	197,0	8,5	1000	196,9	-	-	3004
110	2450	108	6,7	62,5	221,1	197,0	10,9	1610	197,3	2273	197,5	30_c

where ε_{pa} = the constant plastic strain amplitude
N = the number of cycles at which the specimen has been deformed
ε_{cum} = the cumulative plastic strain = $4 \cdot N \varepsilon_{pa}$
$\dot{\varepsilon}$ = the constant plastic strain rate
σ_y = the hysteresis yield stress
σ_{max} = the stress at maximum hardening before (/if) softening occurs
σ_{min} = the stress after softening before (/if) secondary hardening occurs
δ = the softening parameter defined as $(\sigma_{max}-\sigma_{min})/\sigma_{max}$
N^{min} = the number of cycles at the minimum locus $(d\sigma_a/dN)_{min}$
σ_a^{min} = the stress amplitude at the minimum locus $(d\sigma_a/dN)_{min}$
N^{100} = the number of cycles at $\varepsilon_{cum} = 100$
σ_a^{100} = the stress amplitude at $\varepsilon_{cum} = 100$

4.2 Cyclic hardening/softening

All specimens were cyclically deformed at constant plastic strain amplitudes and typical hysteresis loops are shown in Figure 4.1.

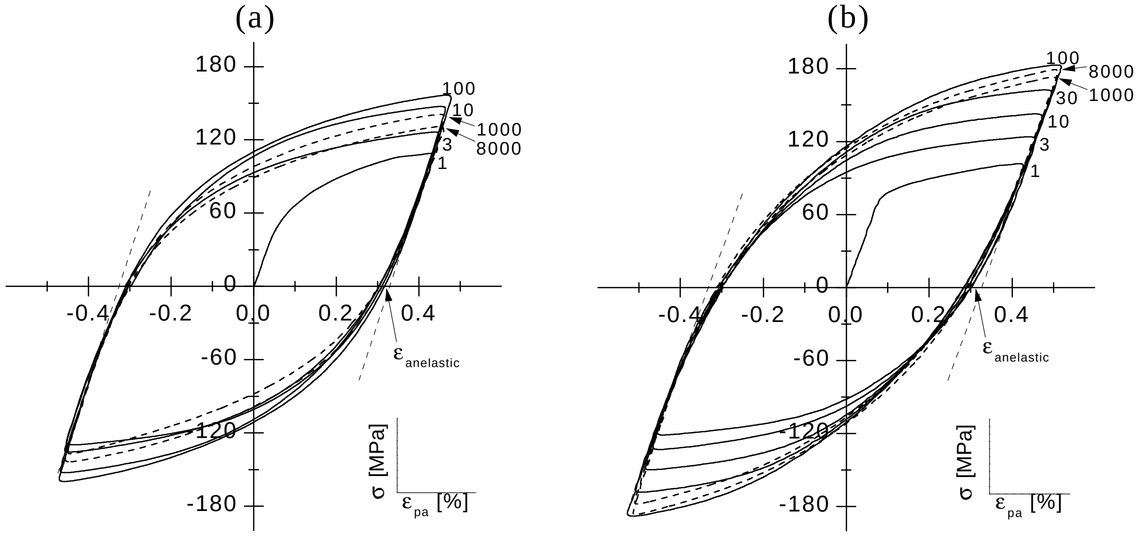

Figure 4.1 Hysteresis loops at different numbers of cycles illustrating the cyclic hardening/softening for (a) Cu-15%Zn, and (b) Cu-30%Zn, cycled at $e_{pa}=3.3x10^{-3}$*. The maximum stress is reached after approximately 100 cycles in both alloys and the subsequent cyclic softening is followed by secondary hardening in Cu-30%Zn.*

The hysteresis loops reveal primary cyclic hardening in both Cu-15%Zn and Cu-30%Zn. The loop shape changes towards a more pointed shape with increasing number of cycles, the pointedness being more pronounced in Cu-30%Zn than in Cu-15%Zn. Both alloys exhibit anelastic strain at stress relief as indicated on Figure 4.1. This is taken into account when determining the plastic strain amplitude (cf. chapter 3.3). Another interesting observation is that the compressive stress amplitudes are a few percent larger than the tensile stress amplitudes. This is illustrated in Figure 4.2 where the tensile and compressive stress amplitudes are plotted vs. the number of cycles for selected plastic strain amplitudes.

Because of these differences in stress amplitudes, it is convenient to use the average stress amplitude, $\sigma_a=(\sigma_{tens}-\sigma_{comp})/2$ when comparing the hardening/softening curves for different plastic strain amplitudes. This is done in all subsequent hardening/softening curves throughout this thesis. The curves in Figure 4.3 demonstrate clearly that true cyclic saturation does not occur in the plastic strain controlled fatigue of Cu-30%Zn. At the high plastic strain amplitudes, i.e. higher than $\sim10^{-3}$, primary cyclic hardening is followed by softening and subsequent secondary hardening. This transforms gradually into one continued hardening stage at the low amplitudes. Cu-15%Zn displays a similar hardening/softening behaviour but the primary and secondary hardening are less pronounced. So is the absence of cyclic saturation, i.e. at intermediate amplitudes ($10^{-3} < \varepsilon_{pa} < 3x10^{-3}$) the stresses tend to saturate after a stage of cyclic softening.

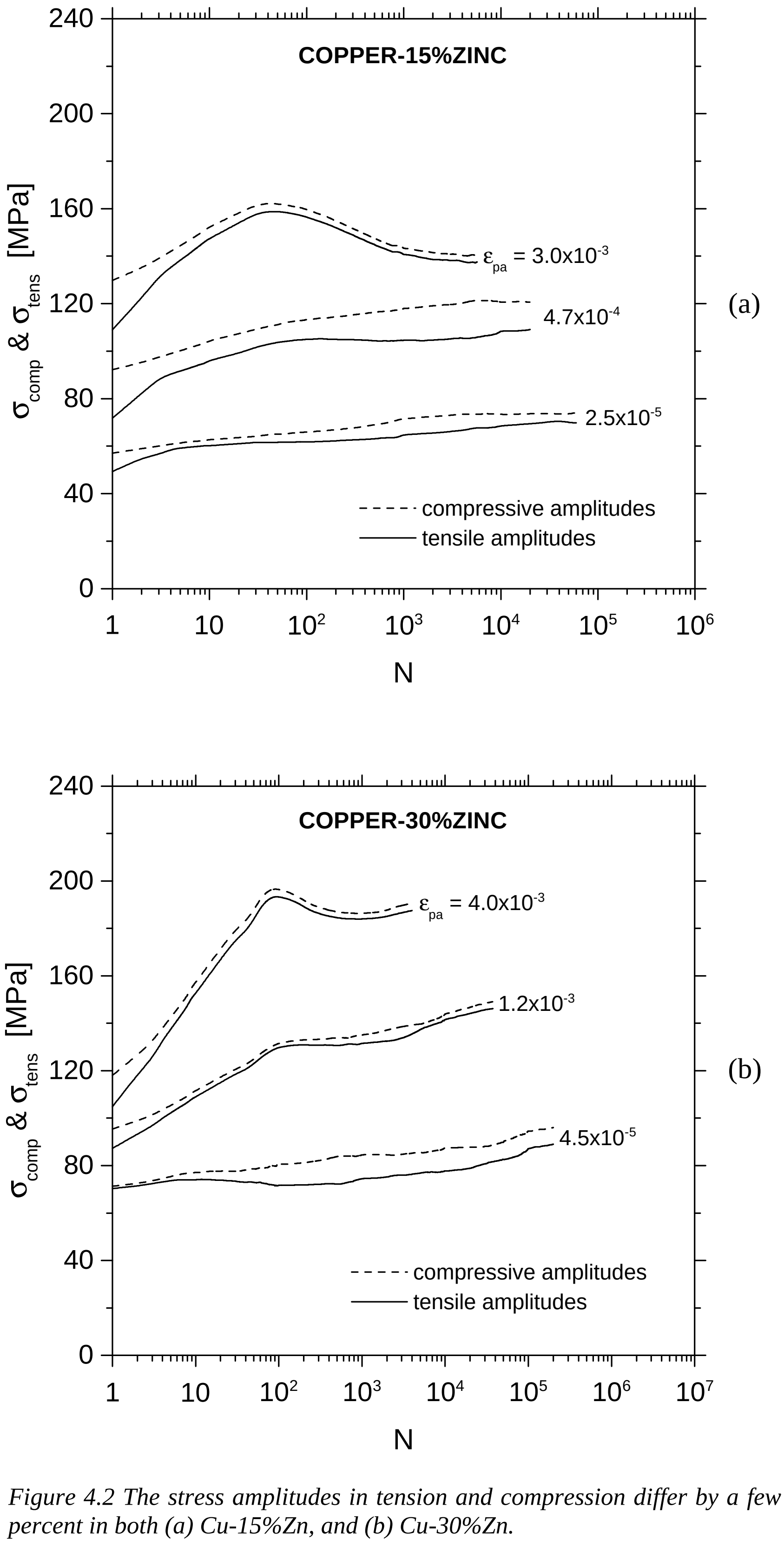

Figure 4.2 The stress amplitudes in tension and compression differ by a few percent in both (a) Cu-15%Zn, and (b) Cu-30%Zn.

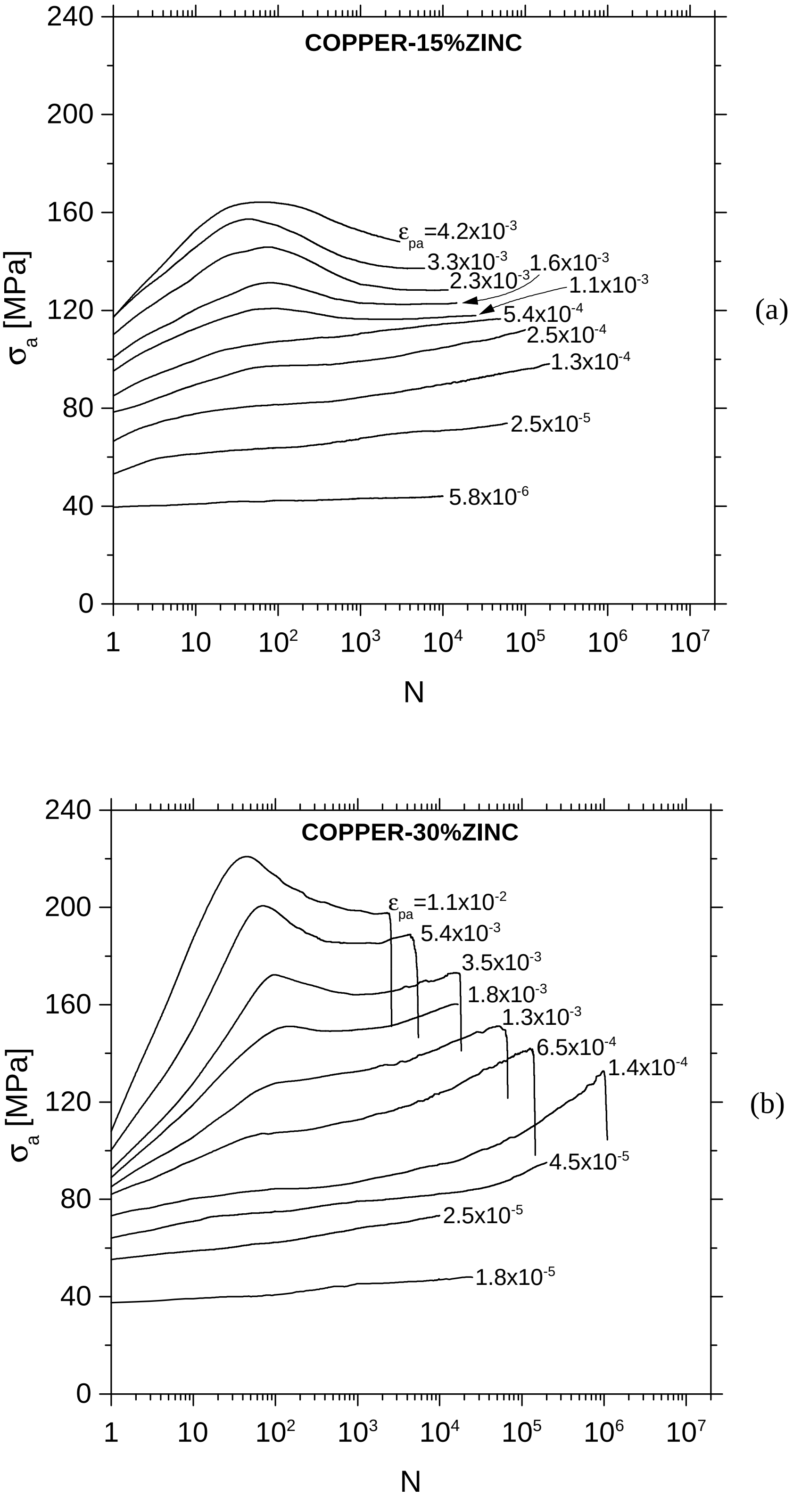

Figure 4.3 Cyclic hardening/softening curves (stress amplitude vs. number of cycles) for specimens cycled at different plastic strain amplitudes. (a) Cu-15%Zn, and (b) Cu-30%Zn. The absence of cyclic saturation is clearly demonstrated for Cu-30%Zn. For Cu-15%Zn it is most evident at the low amplitudes.

A more quantitative analysis of the cyclic hardening/softening behaviour can be obtained by using the scheme suggested by COTTRELL (1953). This scheme provides estimates of the friction stress, σ_f, and the effective back stress, σ_b^{eff}, as illustrated in Figure 4.4, and it is frequently used to analyze plastic strain controlled fatigue data (see e.g. KUHLMANN-WILSDORF & LAIRD, 1979; YAN *ET AL.*, 1986; CARSTENSEN & PEDERSEN, 1998).

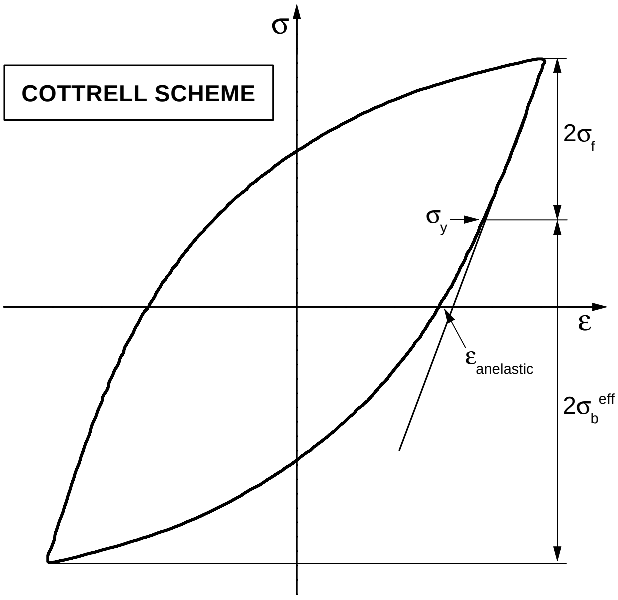

Figure 4.4 The Cottrell scheme (COTTRELL, 1953) can be used to determine the friction stress, s_f, and the effective back stress, s_b^{eff} based on the shape on the hysteresis loop.

In this definition the hysteresis loop is considered symmetrical, i.e. the small differences in stress levels between tension and compression half cycles (cf. Figure 4.2) are neglected. A slightly different scheme, the Handfield-Dickson scheme, is often used to analyse total strain controlled fatigue data (DICKSON *ET AL.*, 1984). However, in the following analysis the Cottrell scheme will be used, and therefore σ_f and σ_b^{eff} can be expressed as (cf. Figure 4.4):

$$\sigma_f = \frac{\sigma_a - \sigma_y}{2} \tag{4.1}$$

$$\sigma_b^{eff} = \frac{\sigma_a + \sigma_y}{2} \tag{4.2}$$

where σ_a is the peak stress amplitude and σ_y is the hysteresis yield stress. In polycrystals the effective back stress, σ_b^{eff}, often referred to as the internal stress, can be divided into an *intragranular* stress contribution associated with non-homogeneous microstructures, and an *intergranular* stress contribution associated with the oscillating mismatch of plastic strain between the cyclically deforming grains. The former (equal to the back stress for single crystals) is known to oppose the imposed strain resulting in the well-known Bauschinger effect. The latter can be described by a self-consistent Sachs-Eshelby model (see chapter 6.1.1). In Figure 4.5 the evolution of σ_a, σ_b^{eff} and σ_f is shown for Cu-15%Zn and Cu-30%Zn cycled at ε_{pa}=3.3x10^{-3}, corresponding to the hysteresis loops depicted in Figure 4.1.

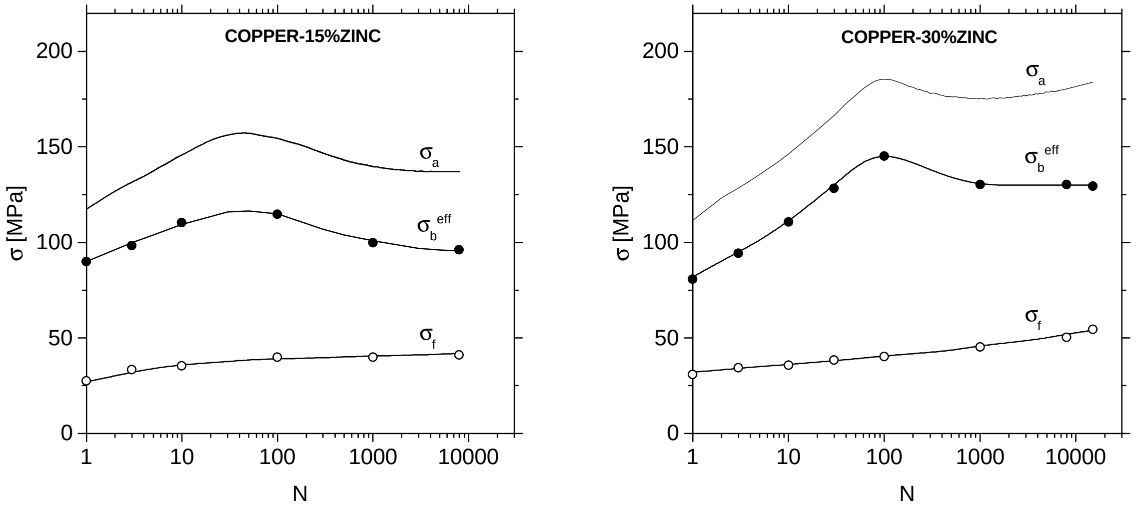

Figure 4.5 The evolution the friction stress, s_f*, and the effective back stress,* s_b^{eff}*, at* $e_{pa}=3.3x10^{-3}$*. The stresses are calculated using the Cottrell scheme on the hysteresis loops shown in Figure 4.1.*

Figure 4.5 reveals that the observed primary hardening and subsequent softening is correlated with changes of the effective back stress while the variation of friction stress seems to promote the secondary hardening. The slow continuous increase of σ_f is observed at amplitudes beyond ~10^{-3}, and it is most pronounced in Cu-30%Zn. At lower amplitudes σ_f tends to be more or less constant. A continuous increase of σ_b^{eff} is observed in both alloys at amplitudes below ~10^{-3} but at higher amplitudes the characteristic stress peaks are observed. The maximum stress amplitude, σ_{max}, appears after $\varepsilon_{cum}\approx 1$ independently of the plastic strain amplitude.

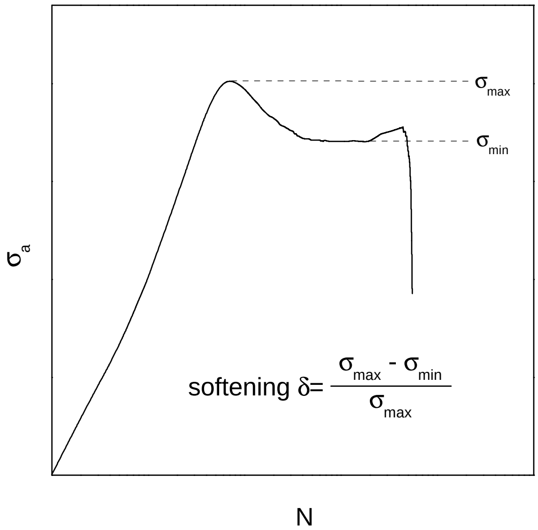

Figure 4.6 The cyclic softening parameter is defined as function of the maximum stress amplitude reached after primary cyclic hardening, and the minimum stress amplitude after cyclic softening.

To quantify the subsequent cyclic softening a so-called cyclic softening parameter, δ, is defined:

$$\delta = \frac{\sigma_{max} - \sigma_{min}}{\sigma_{max}} \tag{4.3}$$

where σ_{min} is the stress amplitude after softening and before secondary cyclic hardening (see Figure 4.6). The relation between δ and ε_{pa} is shown in Figure 4.7.

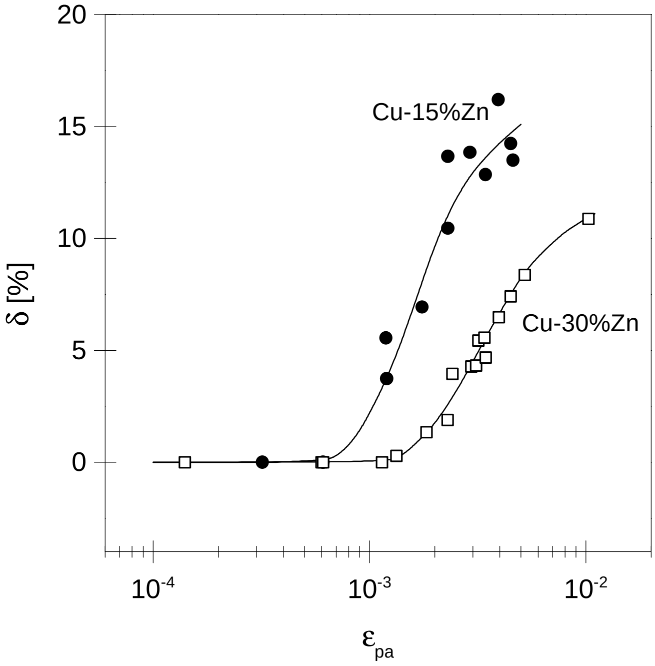

Figure 4.7 The cyclic softening parameter vs. the plastic strain amplitude for Cu-15%Zn and Cu-30%Zn showing that softening is more pronounced in Cu-15%Zn.

From Figure 4.7 it is seen, that cyclic softening increases with the plastic strain amplitude and that it is more pronounced in Cu-15%Zn than in Cu-30%Zn.

4.3 Cyclic stress-strain curves

The cyclic stress-strain (CSS) curve is the saturation stresses plotted vs. the plastic strain amplitudes. For pure copper detailed CSS curves are available from the literature and to compare with copper we want to construct the CSS curves for Cu-15%Zn and Cu-30%Zn. The non-existence of true cyclic saturation in brass evidently complicates the comparison of different measurements of ‘saturation stress’. In an initial construction of CSS curves the ‘saturation stress’ was tentatively defined as the stress amplitude σ_a at $\varepsilon_{cum}=4\cdot N\cdot\varepsilon_{pa}=100$. In Figure 4.8 the resulting CSS curve for texture-free Cu-30%Zn is compared with curves reported for Cu-30%Zn with unspecified texture (BOUTIN *ET AL.*, 1984; LUKÁS & KLESNIL, 1973). The relatively small differences between the polycrystal curves can be interpreted as mainly texture effects (CARSTENSEN & PEDERSEN, 1997B) but by comparing these curves with the CSS curve reported for single slip oriented single crystals (WANG, 1994) large differences are seen. The polycrystal curves exceeds the single crystal curve by up to 200% at the low amplitudes whether the polycrystal data are converted by the Sachs factor or the Taylor factor. It is suggested that this mainly reflects different definitions of the ‘saturation stress’. WANG (1994) assumed that an approximate cyclic saturation was reached after 4000 cycles. Comparing with the $(d\sigma_a/dN)_{min}$ locus (i.e. the stress σ_a^{min} after N^{min} cycles, where the slope $d\sigma_a/dN$ reaches a minimum) in Figure 4.9, it is suggested that WANG’s value of 52 MPa for the plateau stress includes some secondary cyclic hardening.

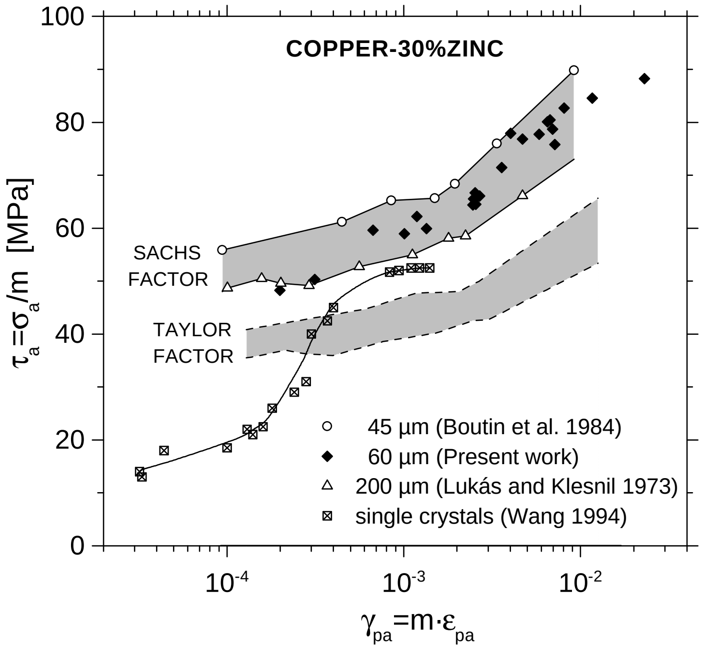

Figure 4.8 Large differences between CSS curves for single crystals and polycrystals are seen, especially at the lowest amplitudes, whether multiple slip (Taylor factor) or single slip (Sachs factor) is assumed for the polycrystals.

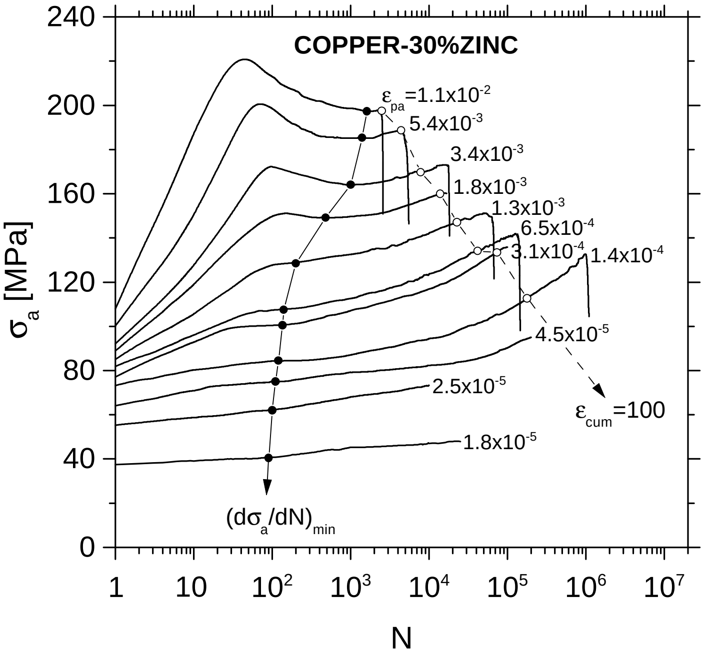

Figure 4.9 Strong secondary cyclic hardening is observed for Cu-30%Zn even at the lowest amplitudes. It is important to define the 'saturation' stress. Using e_{cum}=100 as the definition will include secondary cyclic hardening, so instead it is suggested to use the (d s$_a$/dN)$_{min}$ locus.

However even more secondary cyclic hardening is included in 'saturation stresses' measured at the ε_{cum}=100 locus (i.e. the stress σ_a^{100} after $N^{100}=25/\varepsilon_{pa}$ cycles). By using the $(d\sigma_a/dN)_{min}$ locus the single crystal/polycrystal discrepancy is avoided and a good agreement is found, especially if the single crystal plateau stress is somewhat overestimated (see Figure 4.10).

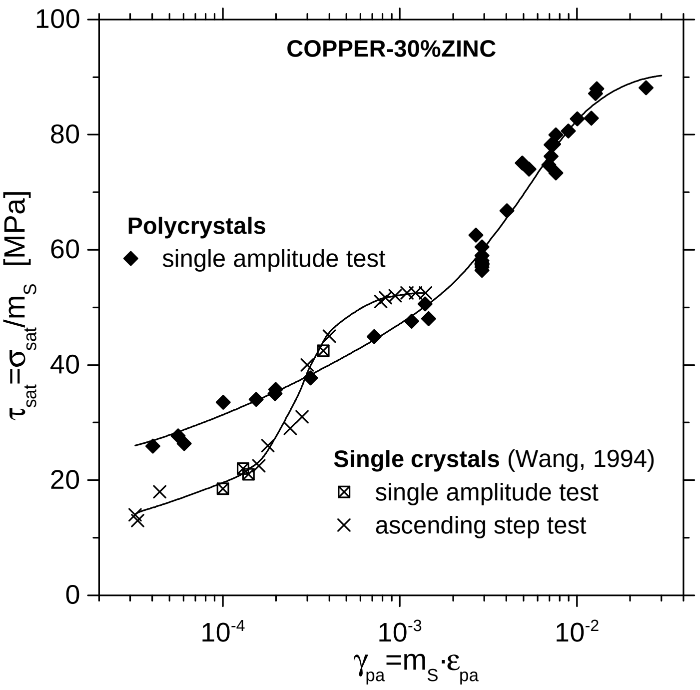

Figure 4.10 The differences at the lowest amplitudes between the present polycrystal CSS curves and those measured for single crystals disappear with the use of comparable definitions of 'saturation stress'. The ($ds_a/dN)_{min}$ definition is used for the polycrystals.

The ($d\sigma_a/dN)_{min}$ locus is therefore used to determine the CSS curve for the Cu-15%Zn polycrystals and in Figure 4.11 it is compared to the CSS curves for Cu-30%Zn and copper polycrystals.

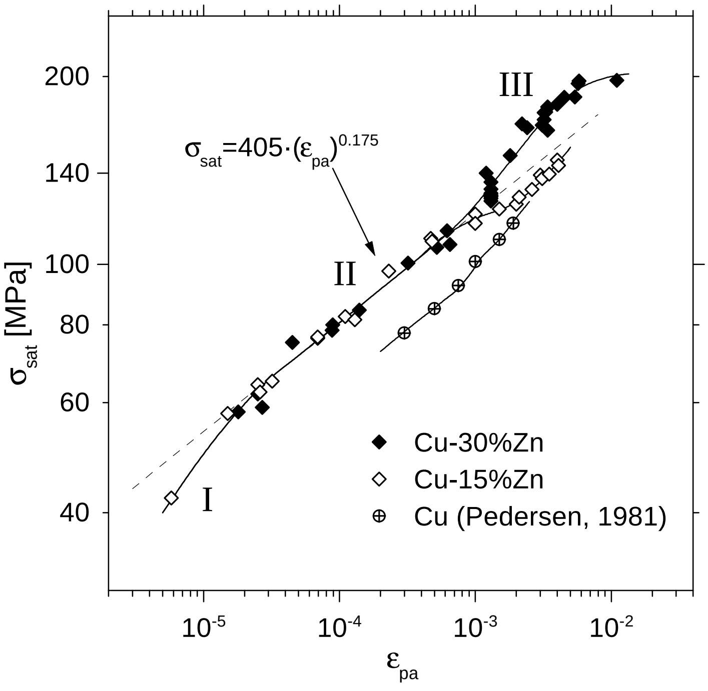

Figure 4.11 The CSS curves for Cu-15%Zn and Cu-30%Zn polycrystals determined at the ($ds_a/dN)_{min}$ locus (note: double-logarithmic plot). For comparison the CSS curve for copper polycrystals is shown (PEDERSEN, 1981). The three materials are all texture-free with comparable grain sizes.

Using the $(d\sigma_a/dN)_{min}$ construction it appears that the CSS curve for Cu-15%Zn and Cu-30%Zn can be divided into three regimes. This is most obvious when the CSS data are presented in a double logarithmic plot, as in Figure 4.11, because it stresses the power law relation in regime II:

$$\sigma_{sat} = \sigma_0 \cdot \left(\varepsilon_{pa}\right)^n \tag{4.4}$$

where σ_0 and n are constants. A description by such a law applies to the limited range $3x10^{-5} < \varepsilon_{pa} < 10^{-3}$ with $\sigma_0 = 405$ MPa and n = 0.175. This also seems to be the case for the texture-free polycrystals presented in Figure 4.11 (PEDERSEN, 1981), though with a different σ_0. The CSS curves for Cu-15%Zn and Cu-30%Zn overlap in regime II (and regime I?) when the $(d\sigma_a/dN)_{min}$ construction is used. In regime III the CSS curve for Cu-15%Zn shifts towards the CSS curve for copper.

To further analyse the observed CSS behaviour the Cottrell scheme (see Figure 4.4 on page 48) can be used to provide estimates of the friction stress, σ_f, and the effective back stress, σ_b^{eff}. In Figure 4.12 the ‘saturated’ values of σ_f and σ_b^{eff} are plotted vs. the plastic strain amplitude for Cu-15%Zn and Cu-30%Zn. The term ‘saturated’ refers to the values at $(d\sigma_a/dN)_{min}$.

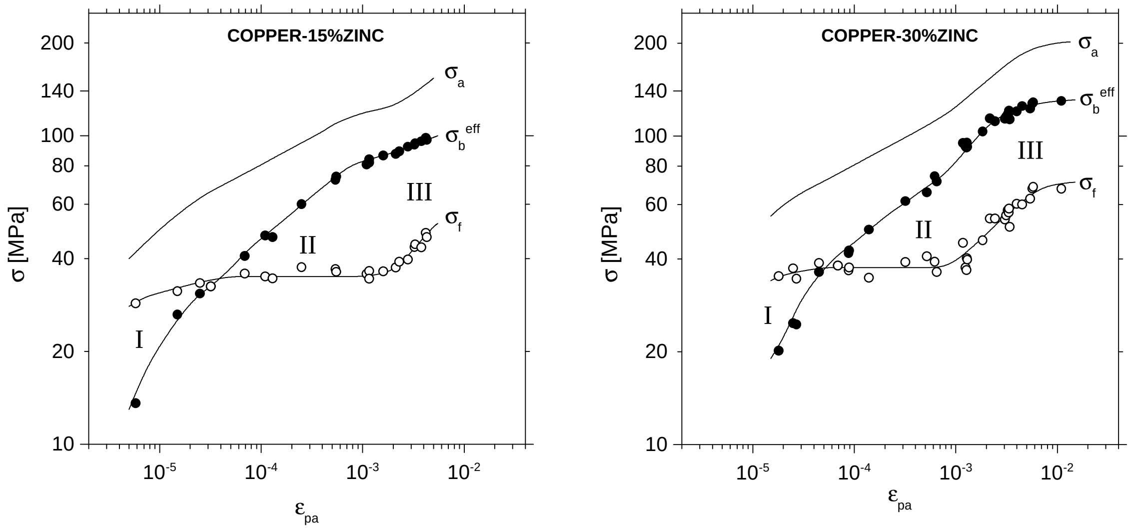
(a) (b)

Figure 4.12 The Cottrell scheme can be used to resolve the CSS curves for brass polycrystals into contributions from friction stress and effective back stress. (a) Cu-15%Zn, and (b) Cu-30%Zn. (note: double-logarithmic plot).

These figures show, that the friction stress increases slowly with ε_{pa} in regime I and remains constant throughout regime II. In regime III a more pronounced increase of the friction stress is observed. The friction stress exceeds the effective back stress in regime I, but this changes at the transition to regime II. In regime II the effective back stress follows a power law relation similar to Equation 4.4. After the transition to regime III the effective back stress deviates from the power law relation, for Cu-15%Zn towards lower values and for Cu-30%Zn towards higher values.

4.4 Fatigue life

The fatigue life of a given material is often referred to as the number of cycles, N_F, leading to fracture. This, however, is in some sense a misleading definition because the final rupture may involve 5-10% of N_F (Bataille & Magnin, 1994). On the cyclic hardening curve the final rupture is seen as a rapid decrease in stress amplitude and it can be correlated with the formation of a few type IV cracks which propagate through the specimen leading to failure (Magnin *et al.*, 1985). It thus seems more appropriate to define fatigue life as the number of cycles, N_i, to form the fatal crack, a type IV crack (the crack type definition will be described in chapter 5.2.3). This definition is used in the present study and N_i is determined from the cyclic hardening curves as shown on Figure 4.13.

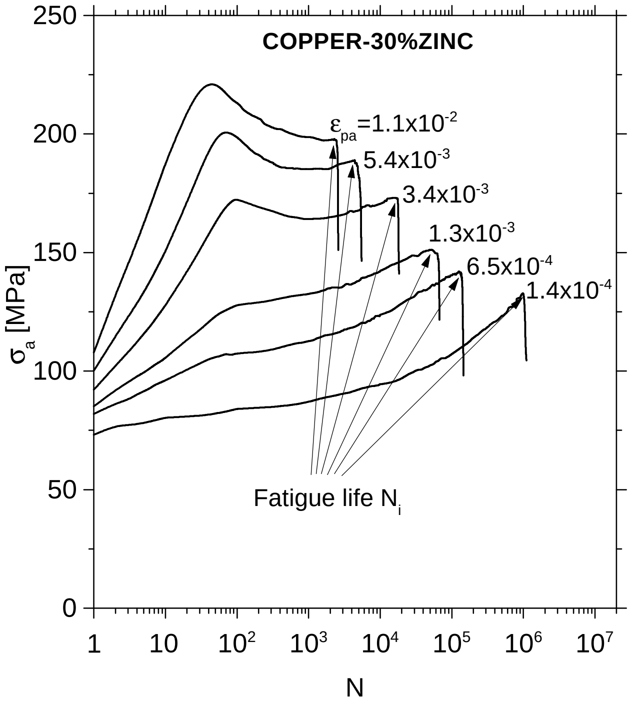

Figure 4.13 Fatigue life is defined as the number of cycles, N_i, to form a type IV crack which also corresponds to the number of cycles for which a rapid decrease in stress amplitude is observed.

The following fatigue lives were recorded for Cu-30%Zn:

Table 4.3 Fatigue life recorded for Cu-30%Zn cycled at different plastic strain amplitudes.

plastic strain amplitude, ε_{pa}	fatigue life, N_i
1.4×10^{-4}	1000000
6.5×10^{-4}	133000
1.3×10^{-3}	63600
3.4×10^{-3}	17600
5.4×10^{-3}	4420
1.1×10^{-2}	2450

The data in Table 4.3 are presented in Figure 4.14 and compared with fatigue life data for 316L steel (BATAILLE & MAGNIN, 1994).

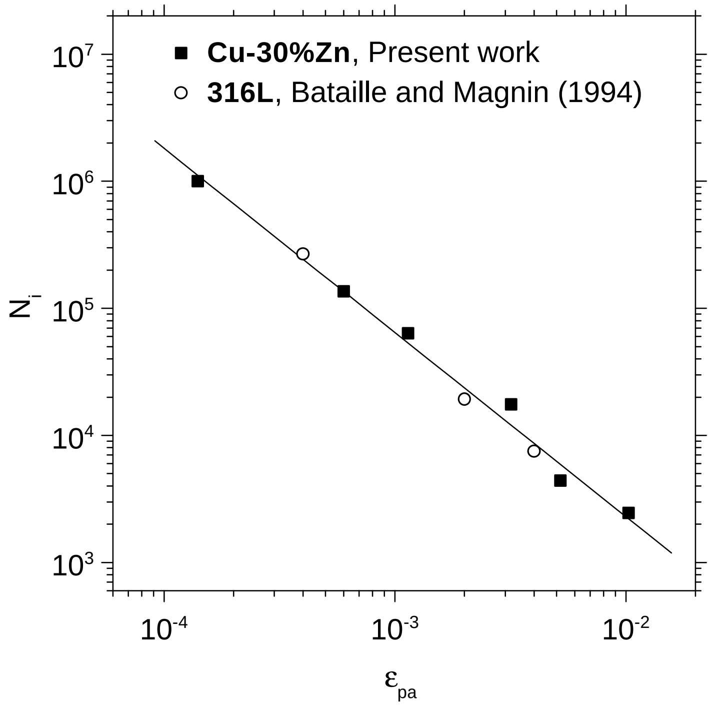

Figure 4.14 Fatigue life curves for Cu-30%Zn and 316L with comparable grain sizes (65µm and 50µm respectively). The two materials have approximately the same fatigue life curve.

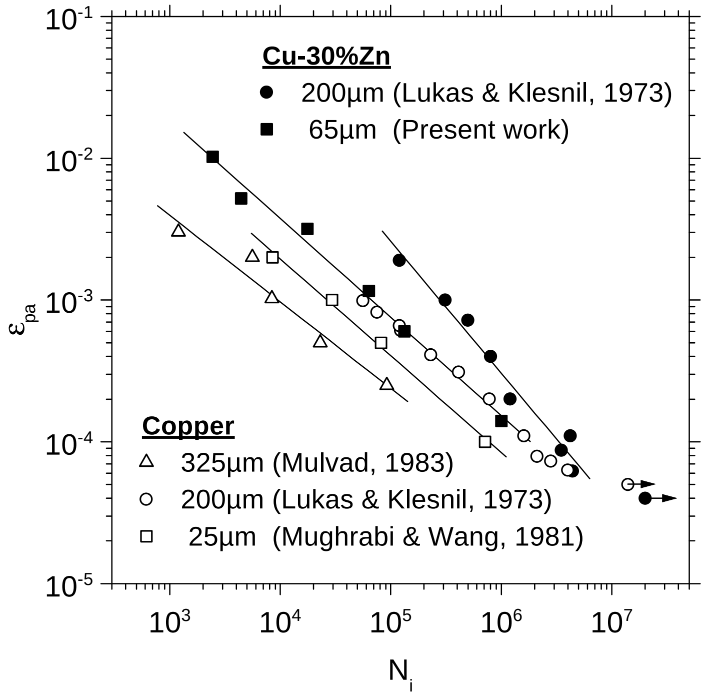

Figure 4.15 Fatigue life curves for polycrystalline copper and Cu-30%Zn with different grain sizes and textures (✪/✶=texture free; Δ=fiber texture; ✧/O=unspecified texture).

This comparison shows that Cu-30%Zn and 316L have approximately the same fatigue life curve. The grain size of the two materials presented in Figure 4.14 are comparable, and thus it can be excluded from the evaluation of the life curves. The grain size is known to have a major effect on fatigue life (cf. chapter 2), but in the present study Cu-30%Zn with only one grain size (65µm) have been investigated. In Figure 4.15 comparison is made with available fatigue life data for coarse grained Cu-30%Zn (200µm) and, in addition, fatigue life curves is shown for copper with different grain sizes. When comparing the fatigue life curve for texture-free fine grained copper (✶) with our fatigue life curve for texture-free Cu-30%Zn (✪) it is seen that the addition of zinc to copper increases fatigue life by a factor of 2-3. This increase would be expected to be even larger if the grain size of the two materials were more comparable.Figure 4.15 shows that in copper fatigue life decreases by a factor of 2-3 when the grain size is increased from 25µm (✶) to 325µm. The data for 200 µm copper (O) and Cu-30%Zn (✧) taken from LUKÁS & KLESNIL (1973) display unexpected increases of fatigue life compared to the 25µm copper (✶) and the present 65µm Cu-30%Zn (✪), respectively. These data are from fatigue tests carried out on a high frequency (~80Hz!) resonant type push-pull machine and provided no information about the texture of their specimens.

4.5 Discussion

One of the main observations presented in this chapter is the apparent absence of cyclic saturation in plastic strain controlled fatigue of brass. This is in contrast to previous investigations by POLAK *ET AL.* (1974). They investigated plastic strain controlled fatigue of Cu-31%Zn and presented cyclic hardening curves for $\varepsilon_{pa}<10^{-3}$ with “an exceptionally long initial stage”. However, they claimed that “saturation still exists”. In Figure 4.16 their hardening curves are compared to curves obtained in the present study.

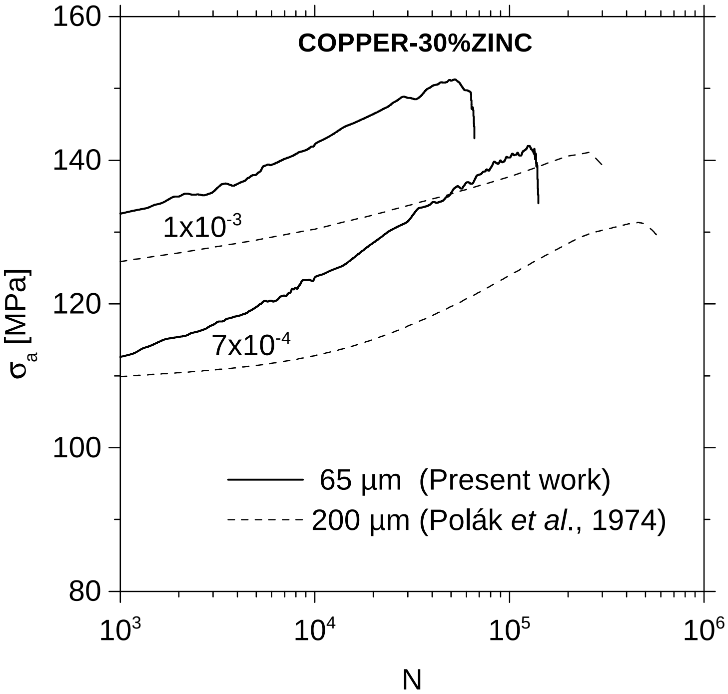

Figure 4.16 Cyclic hardening curves from the present study are compared with hardening curves presented by POLAK ET AL. (1974). The differences (5-15%) in stress amplitudes are accompanied by marked differences in fatigue life.

It seems clear, that none of these curves display a pronounced stage of saturation. It is noted, that the stress amplitudes are 5-15% lower in the coarse grained material and that fatigue life is remarkably increased. The complete set of fatigue life data were reported by LUKÁS & KLESNIL (1973) and LUKÁS *ET AL.* (1974), and it is compared with the present results in Figure 4.15. From this comparison it seems that fatigue life increases with increasing grain size. This is an interesting observation, which is diametrical opposed to the observations made on copper (see also chapter 2). An explanation for this behaviour is not obvious. The investigations by LUKÁS & KLESNIL (1973), POLÁK *ET AL.* (1974) and LUKÁS *ET AL.* (1974) were conducted on a high frequency (~80Hz) resonant type push-pull machine which differ from the servohydraulic testing at 1-2 Hz used in the present study. This may explain the unexpected increase of fatigue life, which is also seen in high frequency cycling of copper (cf. Figure 4.15). However, more recent studies of total strain controlled fatigue of Cu-30%Zn (MARCHAND *ET AL.*, 1983) show a similar 'inverse' grain size effect, though with a less marked increase of fatigue life. Thus the high frequency does not seem to solely explain the observations. The cyclic hardening observed in Cu-30%Zn is associated with an increase of the effective back stresses, as analyzed by using the Cottrell scheme (see Figure 4.5 on page 49). The effective back stresses comprise the intergranular stresses, which are assumed to be independent of grain size (cf. chapter 2 and 6.1.1), and the intragranular stresses, which are associated with the dislocation microstructures. The differences in stress amplitudes depicted in Figure 4.16 therefore have to reflect microstructural differences, which could be the result of differences in texture. The material investigated in the present study was texture-free, so the decreased stress amplitudes observed for the coarse grained material could be due to the presence of a soft texture. This is not unlikely, as this material was annealed for only 1 hour at 600°C (POLÁK *ET AL.*, 1974). It is therefore suggested, that the unexpected increase of fatigue life is a texture effect, which is probably enhanced by the high frequency cycling. However, more investigations at identical test conditions are needed to confirm this suggestion.

In Cu-30%Zn the absence of cyclic saturation is evident at all amplitudes, whereas Cu-15%Zn tends to saturate when cycled at $\varepsilon_{pa}>10^{-3}$ (see Figure 4.3 on page 47). This could be due to a change in dislocation behaviour, which also seems to be reflected by the CSS behaviour shown in Figure 4.11 on page 52. In regime I and II the CSS curve for Cu-15%Zn coincide with the one for Cu-30%Zn, but at the transition to regime III (at $\varepsilon_{pa}\approx10^{-3}$) the CSS curve for Cu-15%Zn shifts towards the curve for copper. A tentative explanation for this could be, that Cu-15%Zn at low amplitudes displayed mainly planar slip and at high amplitudes mainly wavy slip. The dislocation structures in Cu-15%Zn is known to consist of copper-type (wavy) structures and Cu-30%Zn type (planar) structures (LUKÁS & KLESNIL, 1970; KANESHIRO *ET AL.*, 1988) and based on a model of cross-slip inhibition HONG & LAIRD (1990A) suggested that a transition from wavy to planar slip occurs at 13at.%Zn for Cu-Zn alloys. Thus Cu-15%Zn can be considered to be in the transition range. A similar transition alloy is the industrially important 316L austenitic steel, which have approximately the same stacking fault energy as Cu-15%Zn (see Appendix A). In this alloy KRUML *ET AL.* (1997) reported a change in deformation mode from mainly planar slip a low plastic strain amplitudes ($<10^{-4}$) to mainly wavy slip at high amplitudes ($>10^{-3}$). It is suggested, that a similar transition exists for Cu-15%Zn and that the transition occurs at $\varepsilon_{pa}\approx10^{-3}$, i.e. at the transition from regime II to III. The analysis of friction and effective back stress based on the Cottrell scheme (Figure 4.12 on page 53) show that the transition is accompanied by an increase of the friction stress. This can be explained by the enforcement of secondary slip, which is likely to be provoked by the increasing internal stresses. This is in agreement with KRÖNER (1961), who concluded from continuum mechanics considerations, that small plastic strains up to ~10^{-3} can be accomplished compatibly by single slip with some elastic accommodation. The transition from planar to wavy slip in Cu-15%Zn is therefore suggested to be induced by secondary slip.

Cyclic softening is observed in both Cu-15%Zn and Cu-30%Zn in regime III, i.e. at $\varepsilon_{pa}>10^{-3}$. From the analysis of friction and effective back stresses (Figure 4.5 on page 49) the softening is found to be associated with changes in effective back stresses. This could be due to microstructural changes, i.e. decomposition of a characteristic microstructure established during the primary hardening stage, or due to relaxation of intergranular stresses caused by secondary slip. It is interesting to note, that the cyclic softening increases with the plastic strain amplitude and that it is more pronounced in Cu-15%Zn than in Cu-30%Zn. The former is related to the increased primary hardening with the plastic strain amplitude, but the latter is, at first, an unexpected result. However, the analysis based on the Cottrell scheme shows, that the friction stresses continue to increase during cycling and thus impede the softening. The increase in friction stresses is more pronounced in Cu-30%Zn, due to the higher solute content, which explains the effect on the softening. The cyclic hardening/softening behaviour observed for brass in the present study is similar to previous observations made on Cu-30%Zn (MARCHAND *ET AL.*, 1983; BOUTIN *ET AL.*, 1984), Cu-Al (ABEL *ET AL.*, 1979; YAN *ET AL.*, 1986) and on 316L (e.g. GERLAND *ET AL.*, 1987; 1989).

The asymmetry behaviour between tension and compression is observed in both Cu-15%Zn and Cu-30%Zn. This observation has been reported frequently in cyclic deformation of copper and copper alloys (e.g. KEMSLEY & PATERSON, 1960; WADSWORTH, 1963; ABEL, 1978; MUGHRABI, 1978; ABEL *ET AL.*, 1979; ECKERT *ET AL.*, 1987) but no convincing explanations have been offered. MA *ET AL.* (1990) investigated the phenomena in copper single crystals and suggested that in saturation the dominant factor controlling the asymmetry appears to be deformation constraint associated with strain localization. More generally they suggested that in ductile materials the asymmetry is explained by “inhomogeneous deformation and associated differential constraints during tension and compression”. This is not a very satisfactory explanation, but no attempts shall be made to further investigate the phenomena in the present study.

The construction of a CSS curve for polycrystalline brass is complicated by the apparent absence of cyclic saturation. In pure copper cyclic saturation corresponds to a static structure of edge dislocation multipoles, which remains virtually unchanged during continued cycling (this is not completely true as argued by PEDERSEN & WINTER, 1995 and PEDERSEN, 1996). The absence of cyclic saturation in brass is consequently suggested to reflect that no static dislocation structure is generated during cyclic deformation. The CSS curve for copper compares the stress amplitude needed to generate a static dislocation structure when cycling at different plastic strain amplitudes and as this is not possible in brass it seems questionable whether it makes sense to construct a CSS curve for this alloy. Nevertheless, it is convenient to construct a CSS curve for brass in order to compare with the curve for copper, and to do this in a logical way it is of great importance to define the ‘saturation stress’ so that it resembles the saturation stress in copper as much as possible. In the literature the mid-life stress amplitudes are often used to construct the CSS curve (see e.g. POLÁK *ET AL., 1974;* MARCHAND *ET AL.*, 1983). It is obvious, when looking at Figure 4.9 on page 51, that this definition will include different contributions from secondary hardening dependent on the imposed plastic strain amplitude. This is also the case when using a fixed cumulative strain (e.g. ε_{cum}=100) as the definition, and the resulting CSS curve correlates poorly with the single crystal CSS curve, especially at the low plastic strain amplitudes. Instead CARSTENSEN & PEDERSEN (1997B) suggests to use the $(d\sigma_a/dN)_{min}$ locus, and by doing that the low amplitude discrepancies are reduced (cf. Figure 4.10). The $(d\sigma_a/dN)_{min}$ locus can be thought of as the centre of a narrow stage of cyclic saturation and it thus resembles the saturation stage observed in copper. At this point it should be noted, that copper polycrystals not always display a pronounced stage of saturation. Outside and near the limits of the single crystal plateau cyclic softening and secondary hardening are frequently observed. At the highest amplitudes ($\varepsilon_{pa} > 3x10^{-3}$) one continued hardening stage has been observed whereas at the lowest amplitudes ($\varepsilon_{pa} < 3x10^{-4}$) primary cyclic hardening is seen followed by continued softening (see e.g. MUGHRABI & WANG, 1981; POLÁK *ET AL.*, 1991).

When comparing data for polycrystals with data for single crystals it is necessary to convert the stresses and strains (see also chapter 6.1). For conversion of the brass polycrystal data it seems obvious to use the Sachs factor instead of the Taylor factor (see Figure 4.8 on page 51). At high ε_{pa} the multiple slip Taylor conversion underestimates the single crystal curve, which cannot be explained in terms of intergranular stresses. The Sachs conversion, however, provides a logical estimate of the CSS curve. Looking at the CSS curve constructed using the $(d\sigma_a/dN)_{min}$ locus (Figure 4.10 on page 52) we note that the two apparent plateaus on the single crystal Cu-30%Zn CSS curve are not observed on the polycrystal Cu-30%Zn CSS curve. The absence of the plateau at intermediate amplitudes can be explained in terms of high intergranular stress contributions (see chapter 2 and 6.1.1). The low amplitude plateau observed for Cu-30%Zn single crystals is suggested to be an orientation effect similar to that observed in copper single crystals. GONG *ET AL.* (1996; 1997) showed that the width of the CSS plateau in copper single crystals depend on the crystal orientation and that e.g. [001] copper single crystals does not show any plateau behaviour. Absence of a plateau has also been observed for $[\bar{1}11]$ copper single crystals by LEPISTÖ & KETTUNEN (1986). For the texture-free Cu-30%Zn polycrystals investigated in the present study no low amplitude CSS plateau is observed because of the random orientation distribution.

As mentioned above, the CSS curves for Cu-15%Zn and Cu-30%Zn can be divided into three regimes (Figure 4.11 on page 52). In regime II the CSS curve can be described by a power law relation (Equation 4.4). Similar observations was made for copper polycrystals (MUGHRABI & WANG, 1981) and the exponent, n, found for the power law relation in regime II was exactly the same (n = 0.175) as found for brass in the present study. These similarities of the CSS curves support the suggestion that the $(d\sigma_a/dN)_{min}$ locus is the correct choice when constructing the CSS curve.

The addition of zinc to copper increases the fatigue resistance. In Figure 4.15 on page 55 the obtained fatigue life curve for texture-free Cu-30%Zn is compared with the curve for texture-free copper (MUGHRABI & WANG, 1981). This comparison reveals that fatigue life is increased 2-3 times when 30% zinc is added to copper, which can be explained by the decreased slip irreversibility and the more homogeneous deformation in Cu-30%Zn. It is interesting to note that brass and 316L steel, which display rather similar mechanical behaviour, also seem to have approximately the same fatigue life curve (Figure 4.14). This emphasizes Cu-30%Zn as an excellent choice of model system for austenitic steels.

5 Evolution of Structure and Damage

Investigations of the dislocation microstructures in planar slip materials are, as previously mentioned, more scarce than in wavy slip materials. Thus, the dislocation studies in the present project has been focused mainly on Cu-30%Zn, and mechanisms responsible for the cyclic hardening/softening behaviour in this alloy are investigated.

The formation of surface slip bands can be thought of as the first step of damage evolution. Slip bands are the result of the dislocation microstructures generated by the plastic deformation and they play an important role in the formation of microcracks. The microcracks evolve and coalesce to form macrocracks which eventually lead to final failure. In chapter 5.2 the damage process will be illustrated for Cu-30%Zn. Comparison will be made with a 316L austenitic stainless steel, which is an example of an industrial material with low stacking fault energy. This steel is of particular interest because it has approximately the same fatigue life curve as Cu-30%Zn (see chapter 4.4).

5.1 Dislocation microstructures

In chapter 5.1.1 the hardening/softening behaviour observed in Cu-30%Zn is characterized by series of TEM micrographs. Micrographs from Cu-15%Zn are presented in chapter 5.1.2 to reveal the mixed nature of the deformation mode in this alloy.

5.1.1 Copper-30%Zinc

Specimens were strained into the stages of primary hardening, softening and secondary hardening at a fixed plastic strain amplitude, as shown on Figure 5.1. The specimens were investigated by TEM to reveal the microstructural evolution associated with these stages.

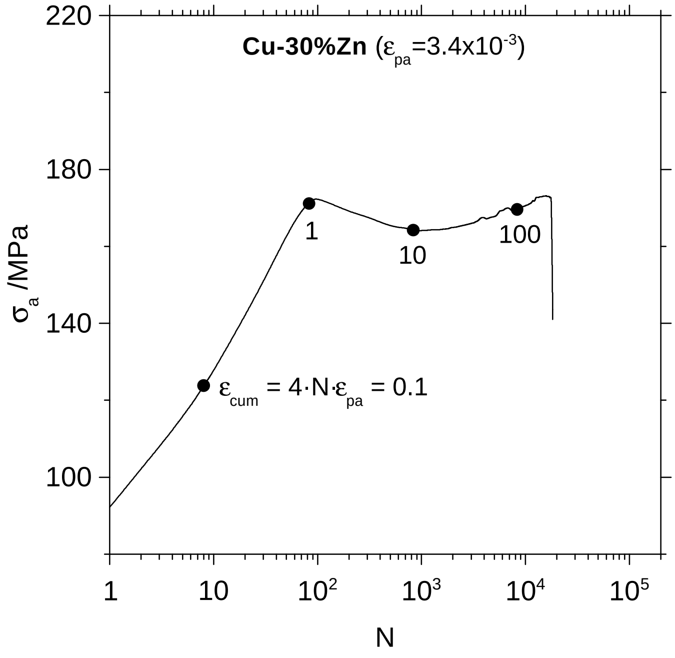

Figure 5.1 The observed hardening/softening behaviour was investigated using TEM on specimens cycled to different cumulative plastic strains at $e_{pa}=3.4x10^{-3}$.

Primary hardening

The primary hardening stage extends to $\varepsilon_{cum}\approx 1$ independent of the plastic strain amplitude. It was found that specimens strained into the primary hardening stage contained arrays of edge dislocation dipoles. The formation of these dipole arrays is evident already at $\varepsilon_{cum}=0.1$, as shown in Figure 5.2.

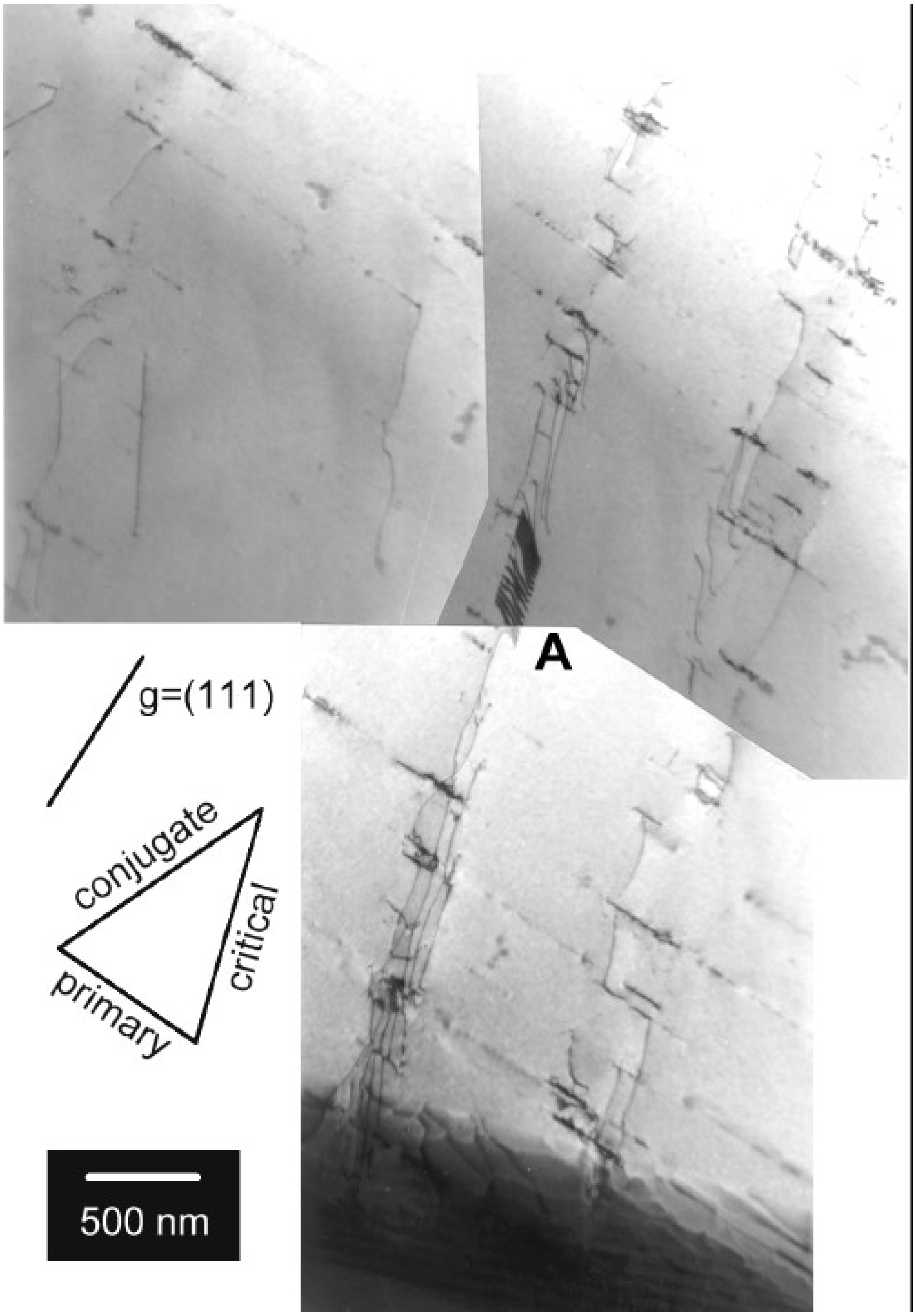

Figure 5.2 Dislocation microstructure in the primary hardening stage ($e_{cum}=0.1$) of Cu-30%Zn cycled at $e_{pa}=3.4x10^{-3}$. Formation of a dipole array is evident at A and it seems to be formed by cross-slip of dislocations moving on the primary glide plane.

Dislocations moving on the primary slip plane seem to form a dipole array (marked with A) apparently by a cross-slip mechanism. They continue to form and grow and at the end of the primary hardening stage extended arrays of dipoles are seen in comparatively undislocated crystal. This is illustrated in Figure 5.3.

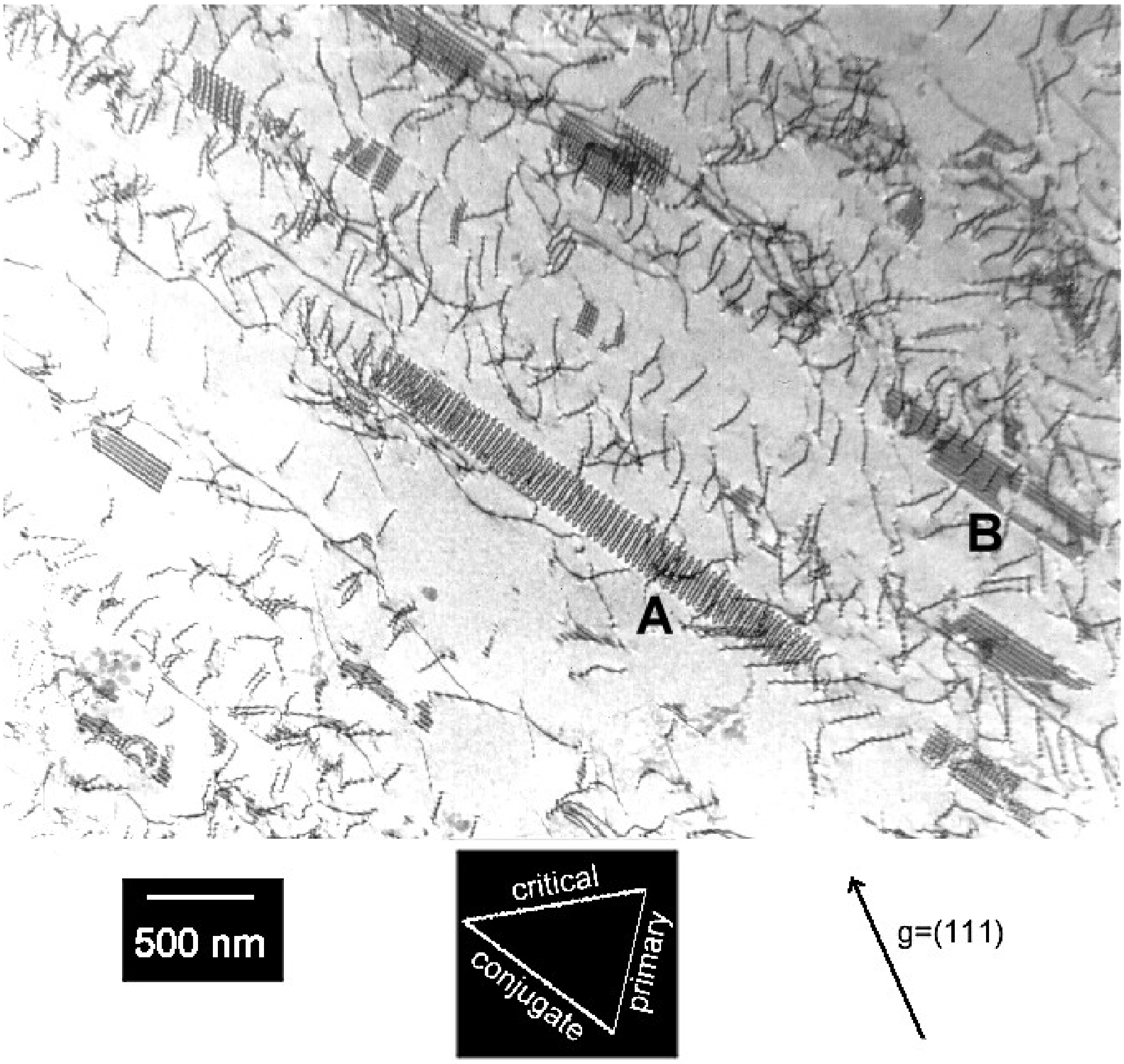

Figure 5.3 Dislocation microstructure at the end of the primary hardening stage ($e_{cum}=1$) of Cu-30%Zn cycled at $e_{pa}=3.4x10^{-3}$.

It is clear that the dislocations move in groups and by cross-slip the characteristic dipole arrays are formed (the dipole arrays are sometimes referred to as multipoles, but to avoid any misunderstanding the term dipole array will be used here). From the appearance of the dipole arrays a tentative distinction can be made between two different types of arrays. These are marked with A and B respectively in Figure 5.3 and examples are shown in Figure 5.4 at a higher magnification.

(a)

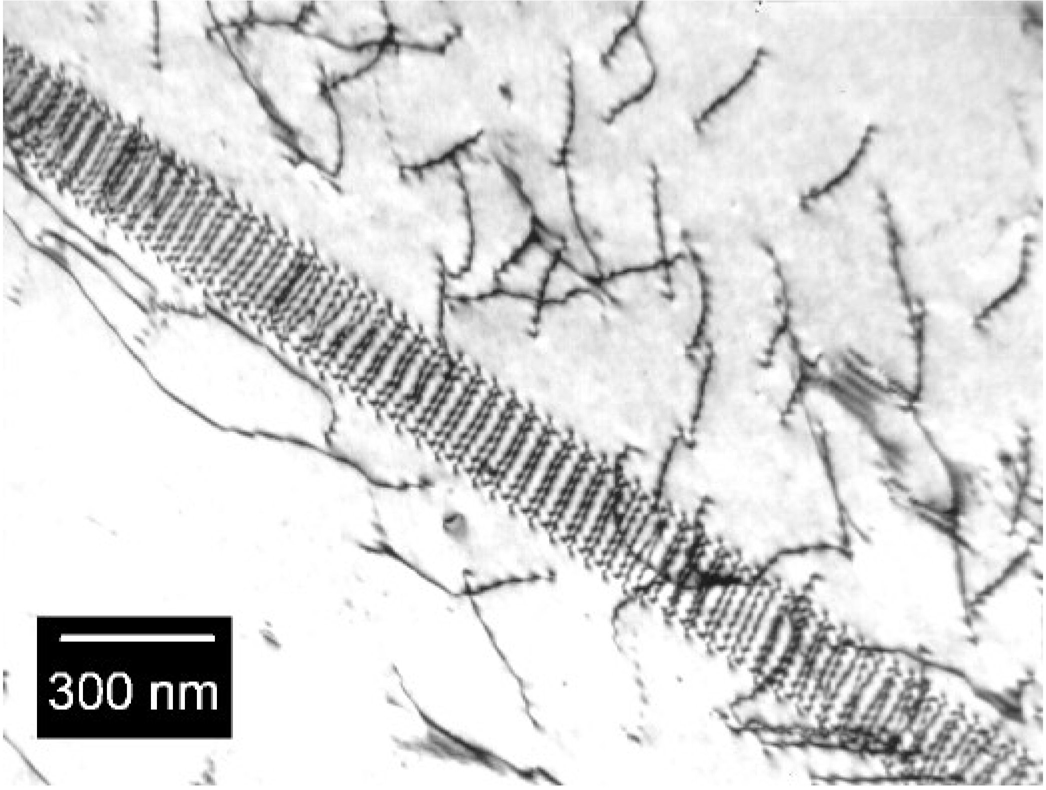

(b)

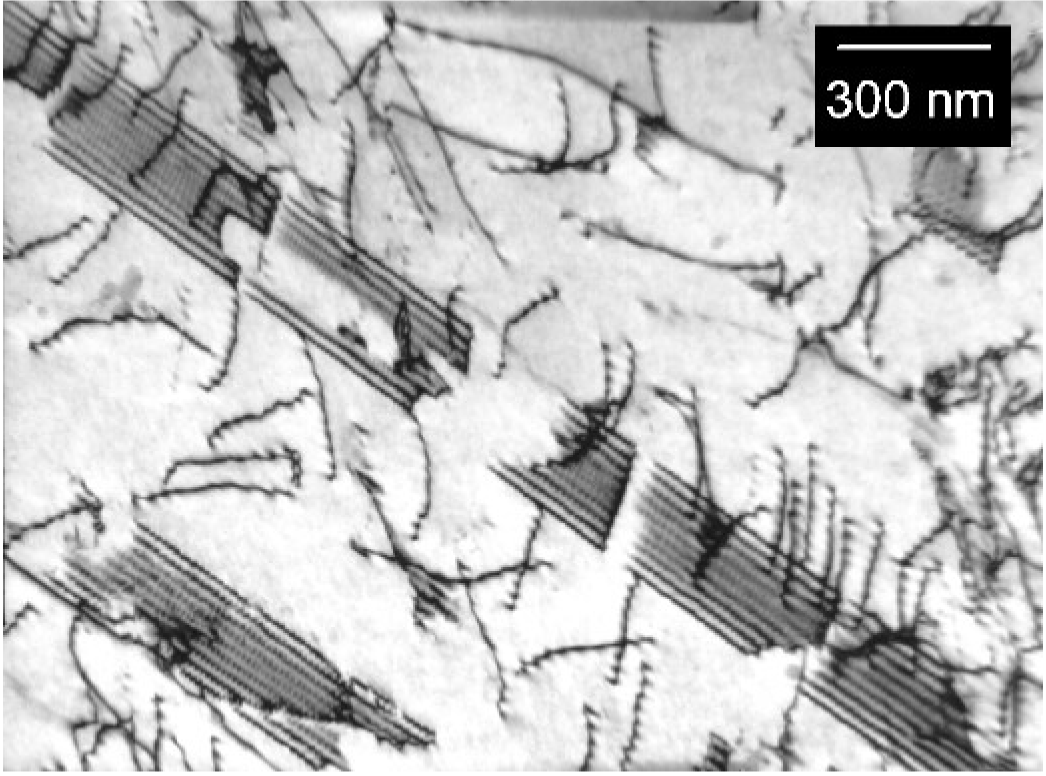

Figure 5.4 Two apparently different types of dipole arrays are observed in Cu-30%Zn. (a) The array marked with A in Figure 5.3 is a regularly spaced array of dipoles. (b) The array marked with B in Figure 5.3 appears to be a stacking fault band. Diffraction conditions are the same as in Figure 5.3.

The dislocation array shown in Figure 5.4a is a regularly spaced array of paired dislocations. Each pair is a dipole which can be established by looking at the fringes on the side of the individual dislocations. These fringes appear on one side of each dislocation due to the dissociation of the partials (only one of the partials are visible). The fringes are on opposite sides on the two dislocations constituting a pair, which means that the dislocations are of opposite sign. Hence it appears that the paired dislocations are dipoles.

The array shown in Figure 5.4b displays a characteristic fringe pattern and thus it appears to be a stacking fault band. However, a closer look on the structure leads to a different conclusion. In Figure 5.5 the same array is viewed at a slightly different tilt angle (and a higher magnification) revealing an interesting structure perpendicular to the fringe pattern.

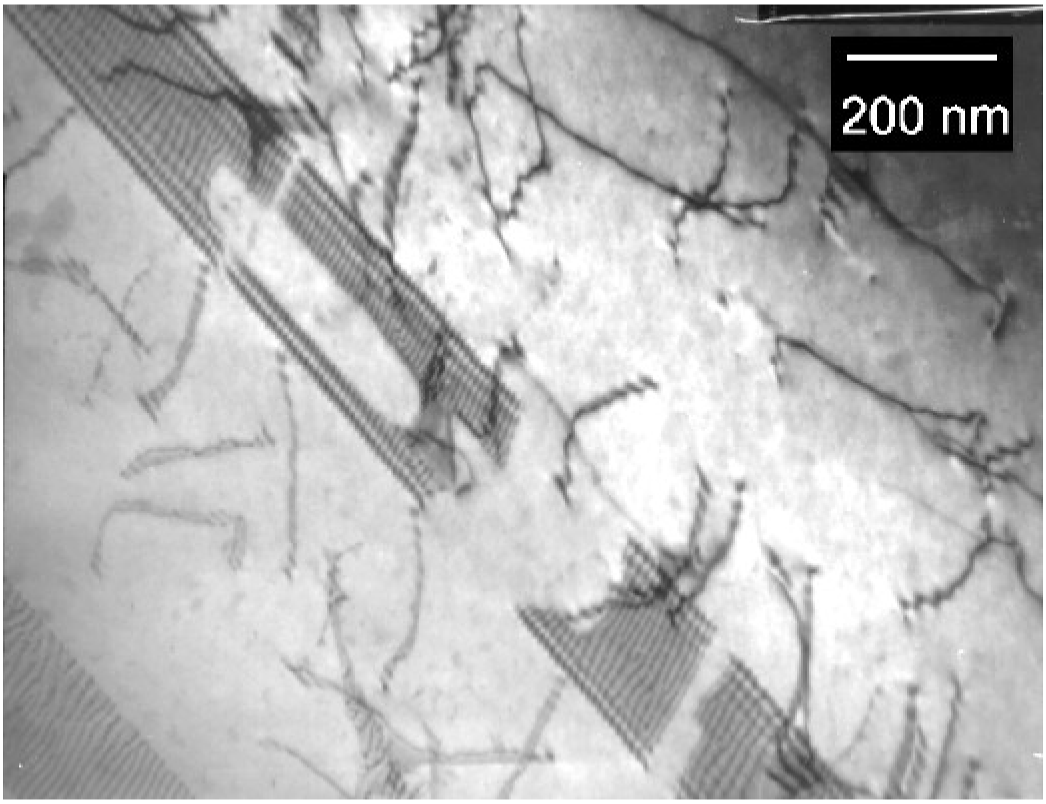

Figure 5.5 When the array shown in Figure 5.4b is viewed at a different tilt angle, an interesting structure becomes visible perpendicular to the fringe pattern. The fringe pattern is now less pronounced.

This “finger print”-structure is also an array of dipoles, but the dipoles are very closely spaced. This explains the fringe pattern which is simply a Moiré effect. In Figure 5.6 another example of a closely spaced dipole array is shown.

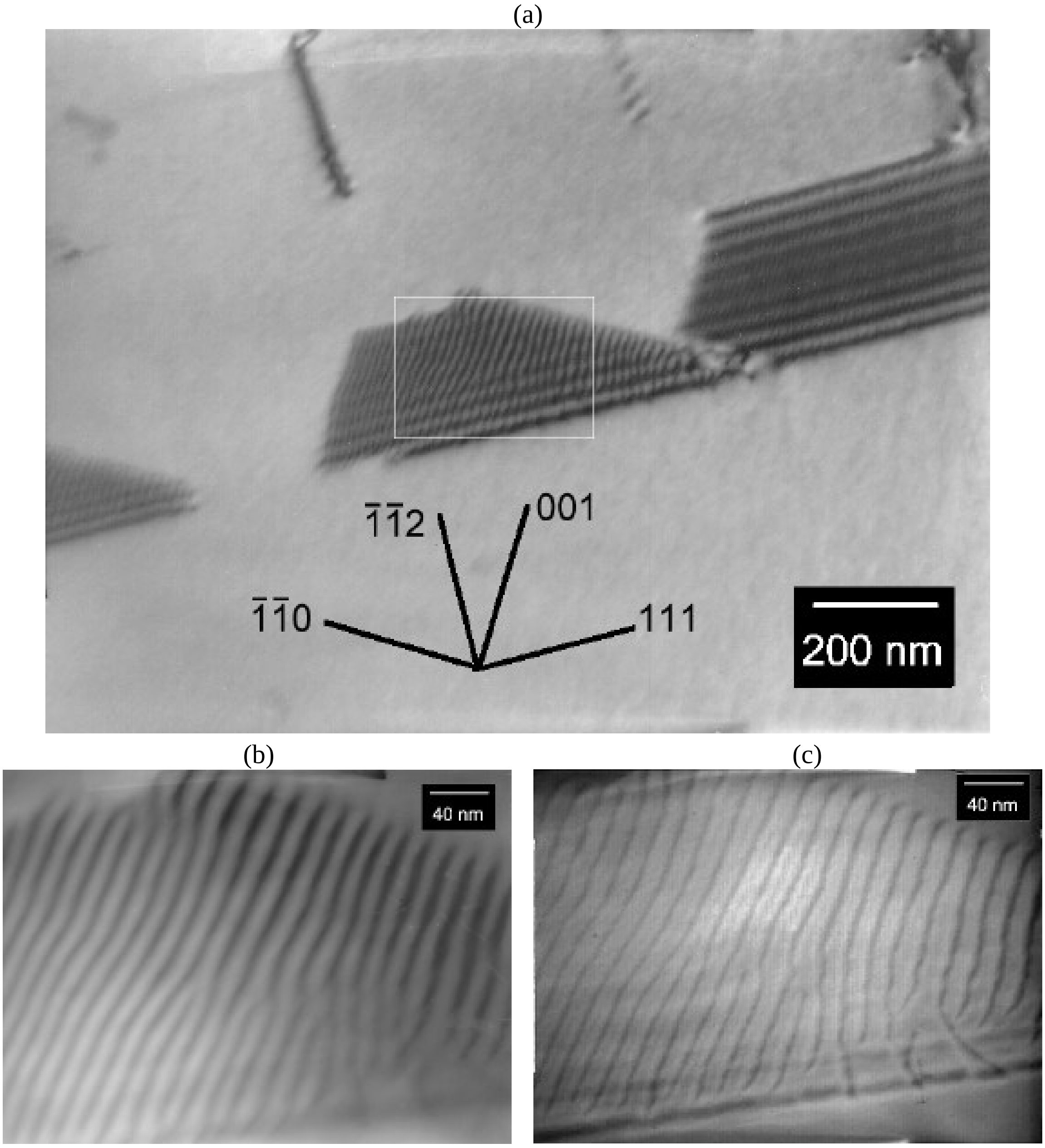

Figure 5.6 A closely spaced dipole array (a) with Moiré fringes. At higher magnification (b) the dipole structure perpendicular to the Moiré fringes can be seen revealing the characteristic "finger print"-structure. In (c) the structure is viewed at a weak beam condition to narrow the width of the dislocation images (the contrast has been inverted to compare directly with the bright field contrast in (b)). Faint traces of the dislocations in the lower slip plane appear halfway between the dislocations in the upper slip plane.

Figure 5.6b shows a bright field image of the "finger print" structure. The resolution is not sufficient to enable a distinction between the individual dislocations in the dipoles, i.e. each dipole appears as if it was a single dislocation. By using a weak beam technique (see chapter 0 on page 36) the width of the dislocation images is reduced and the individual dislocations may be resolved as seen in the micrograph on Figure 5.6c. The dislocations in the lower slip plane appear as faint lines halfway between the dislocations in the upper slip plane. The average dipole spacing, measured directly on the micrograph, is approximately 150 Å and thus the dipole height is assumed to be 75 Å. This assumption is based on a 45° dipole configuration, which corresponds to the position of minimum interaction energy of the dipole dislocations.

When comparing the dipole arrays of Figure 5.4, Figure 5.5, Figure 5.6 and Figure 5.7 differences in the dipole spacing are evident. The smaller the spacing between the slip planes (i.e. the dipole height) the closer the dislocations pack together. Two dipole arrays are sometimes seen to interact with each other as shown in Figure 5.7.

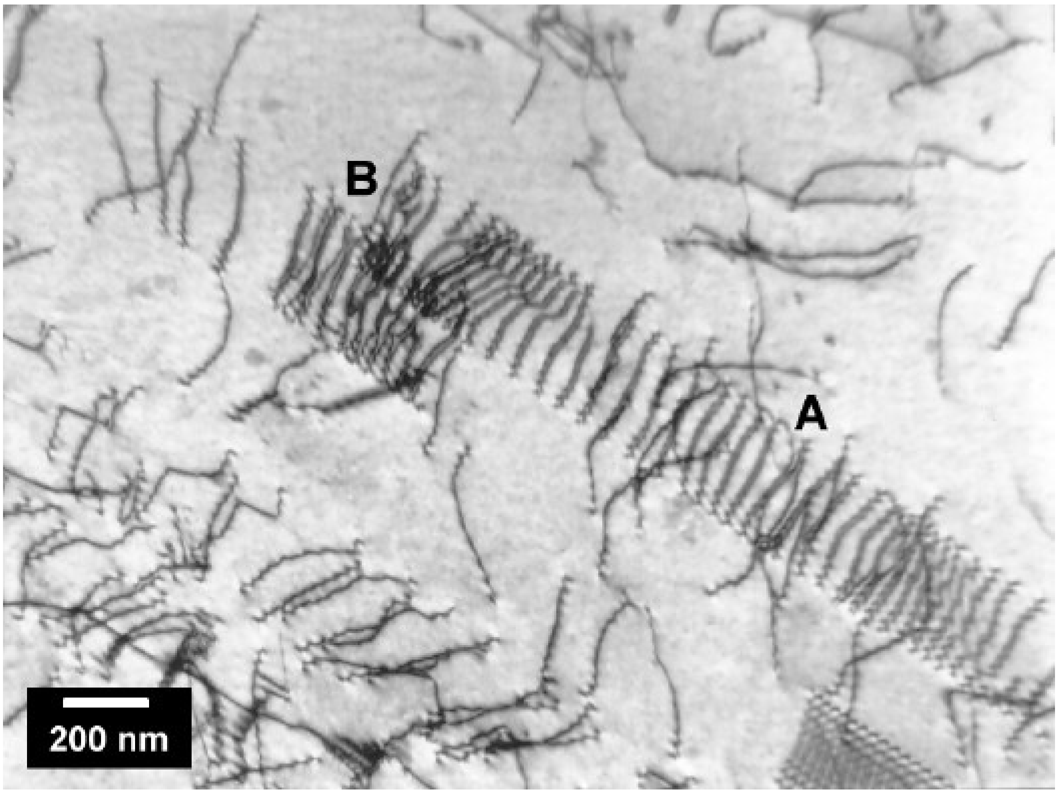

Figure 5.7 Considerable variations of the dipole spacing is found even within the same crystal grain. The figure shows a dipole array, marked with an A, taken from the same grain as the arrays shown in Figure 5.4. The measured dipole spacing is approximately 650 Å. An interaction between two arrays is seen at B. Diffraction conditions are the same as in Figure 5.3.

Softening

At plastic strain amplitudes $\varepsilon_{pa}>1.5x10^{-3}$ Cu-30%Zn display softening when cycled beyond $\varepsilon_{cum}\approx 1$. The softening becomes more pronounced with increasing ε_{pa} (cf. Figure 4.7 on page 50). The onset of softening is accompanied by formation of intense shear bands (ISBs) forming preferentially at grain boundaries. The shear bands consist of densely dislocated arrays with high slip activity on both the primary, critical and conjugate plane. An example is shown in Figure 5.8.

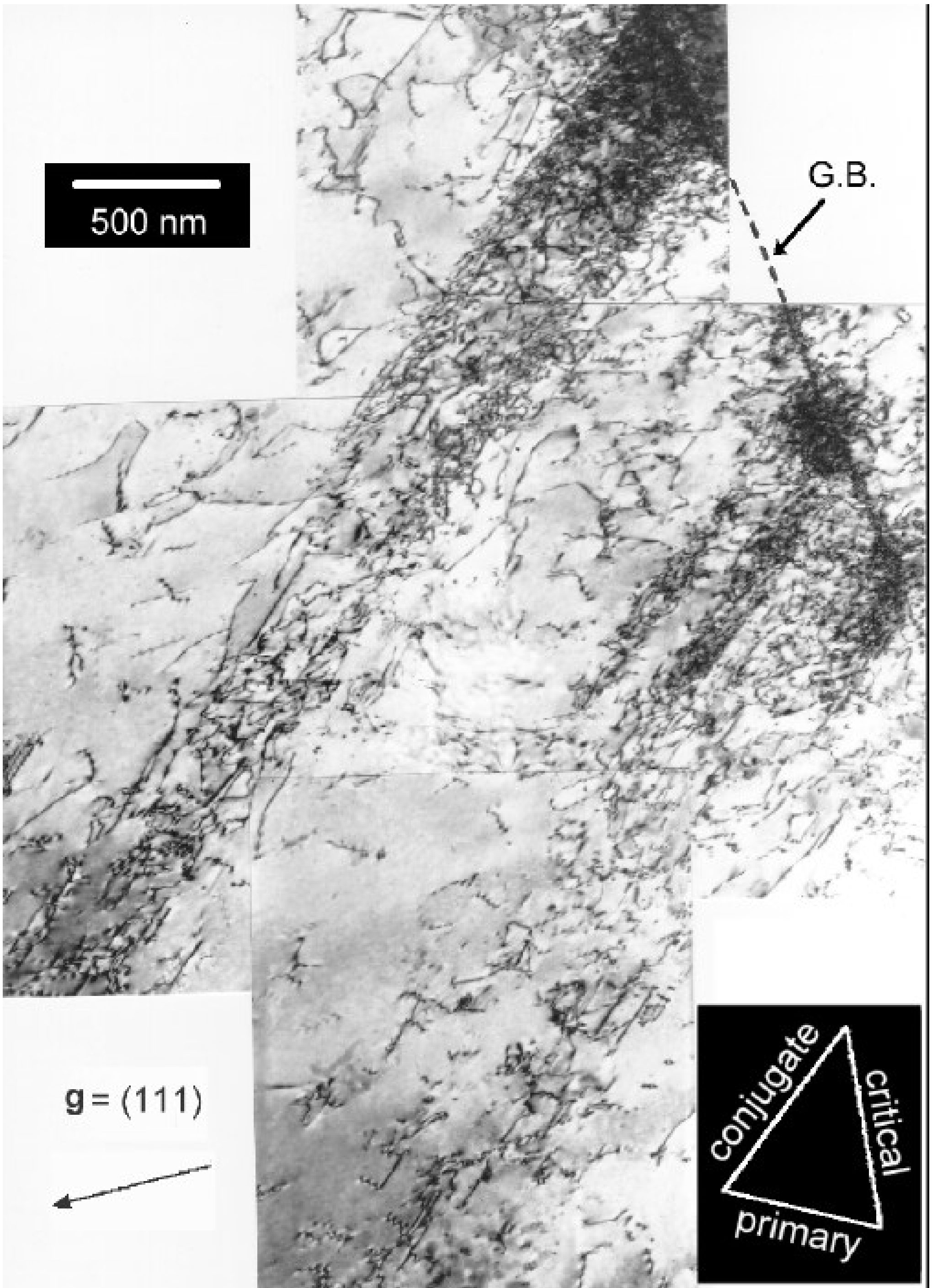

Figure 5.8 Intense shear bands (ISBs) form preferentially at grain boundaries (G.B) and grow into the crystal. The ISBs are first observed at the onset of cyclic softening. The picture show Cu-30%Zn cycled to $e_{cum}=1$ *at* $e_{pa}=3.4x10^{-3}$.

After completion of cyclic softening a fairly uniform structure of planar dislocation arrays are seen (see Figure 5.9). The initially formed dipole arrays are not observed in specimens cycled to $\varepsilon_{cum}=10$.

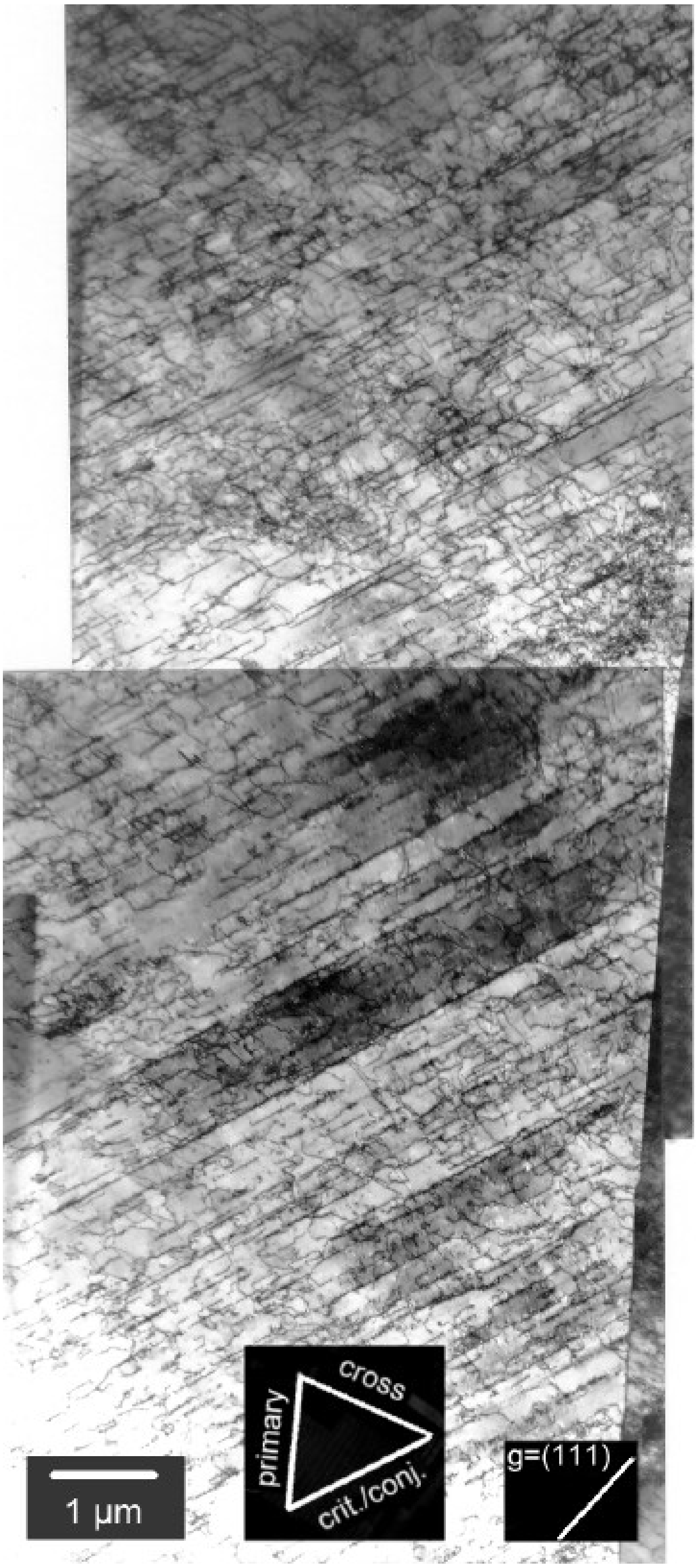

Figure 5.9 A fairly uniform structure of planar dislocation arrays are seen after completion of cyclic softening. No dipole arrays was found at this stage. The picture shows Cu-30%Zn cycled to $e_{cum}=10$ *at* $e_{pa}=3.4x10^{-3}$*. The polycrystal is found to contain a fairly uniform structure of planar dislocation arrays not qualitatively different from that observed after* $e_{cum}=10$*.*

Secondary hardening

Continued cycling into the stage of secondary cyclic hardening doesn’t lead to any qualitative changes in the dislocation microstructure. The structure is still a fairly uniform distribution of planar dislocation arrays as shown in Figure 5.10. When comparing the dislocation structures after ε_{cum}=10 (Figure 5.9) with those after ε_{cum}=100 (Figure 5.10) the only observable difference is a quantitative change in dislocation density.

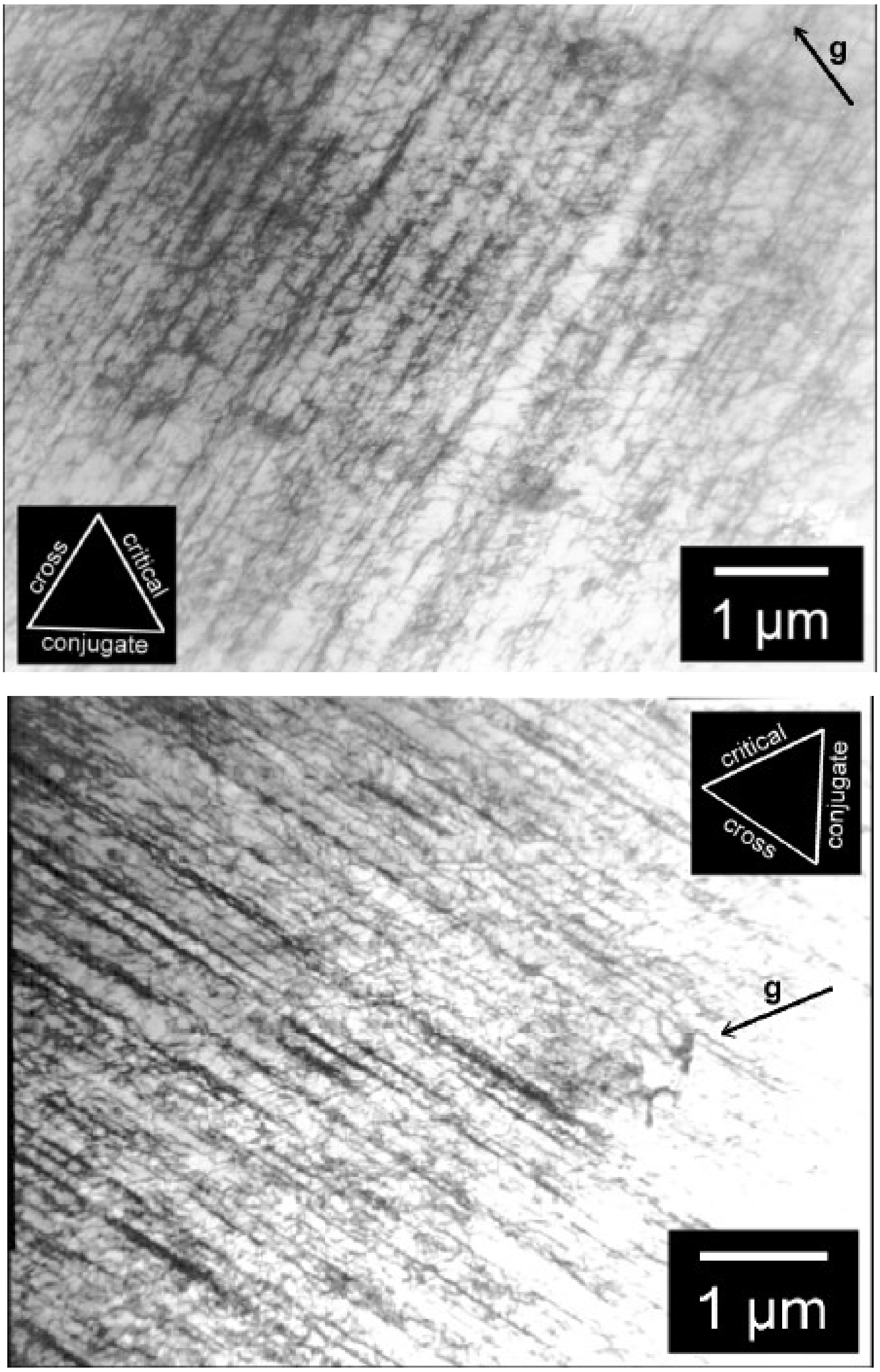

Figure 5.10 In the stage of secondary cyclic hardening (e_{cum}=100) the polycrystal is found to contain a fairly uniform structure of planar dislocation arrays not qualitatively different from that observed after e_{cum}=10. The Hollow Cone technique was used when recording these micrographs.

5.1.2 Copper-15%Zinc

The dislocation microstructures in Cu-15%Zn are mixtures of copper-like structures (wavy) and Cu-30%Zn-like structures (wavy). At low amplitudes the planar structures clearly dominate but at high amplitudes the wavy slip structures become more well-developed and dislocation cells are frequently observed. In Figure 5.11 and Figure 5.12 examples are shown of the different types of structures observed in Cu-15%Zn.

(a)

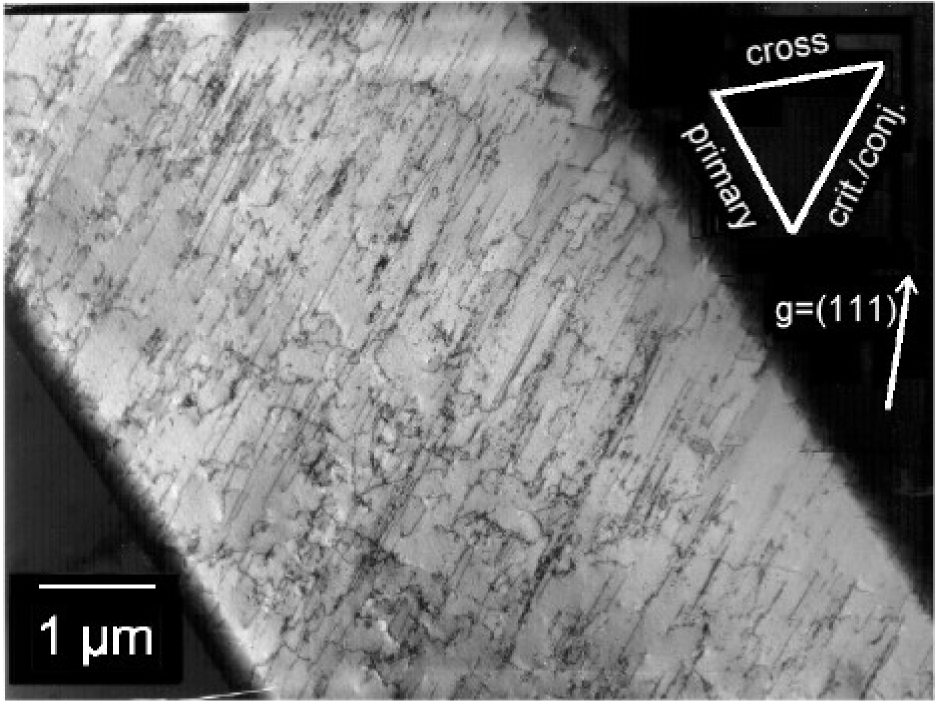

(b)

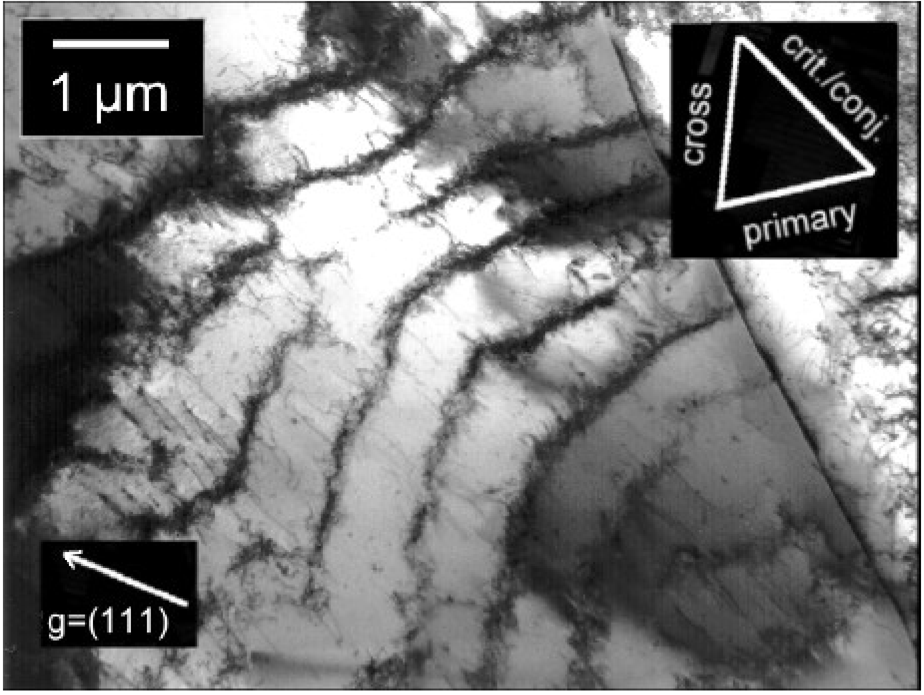

Figure 5.11 Typical dislocation structures in Cu-15%Zn (a) Planar slip structure, $e_{pa}=5.5x10^{-4}$, N=50000 cycles, and (b) wavy slip structure, $e_{pa}=3.3x10^{-3}$, N=8333. The Hollow Cone technique was used when recording this micrograph.

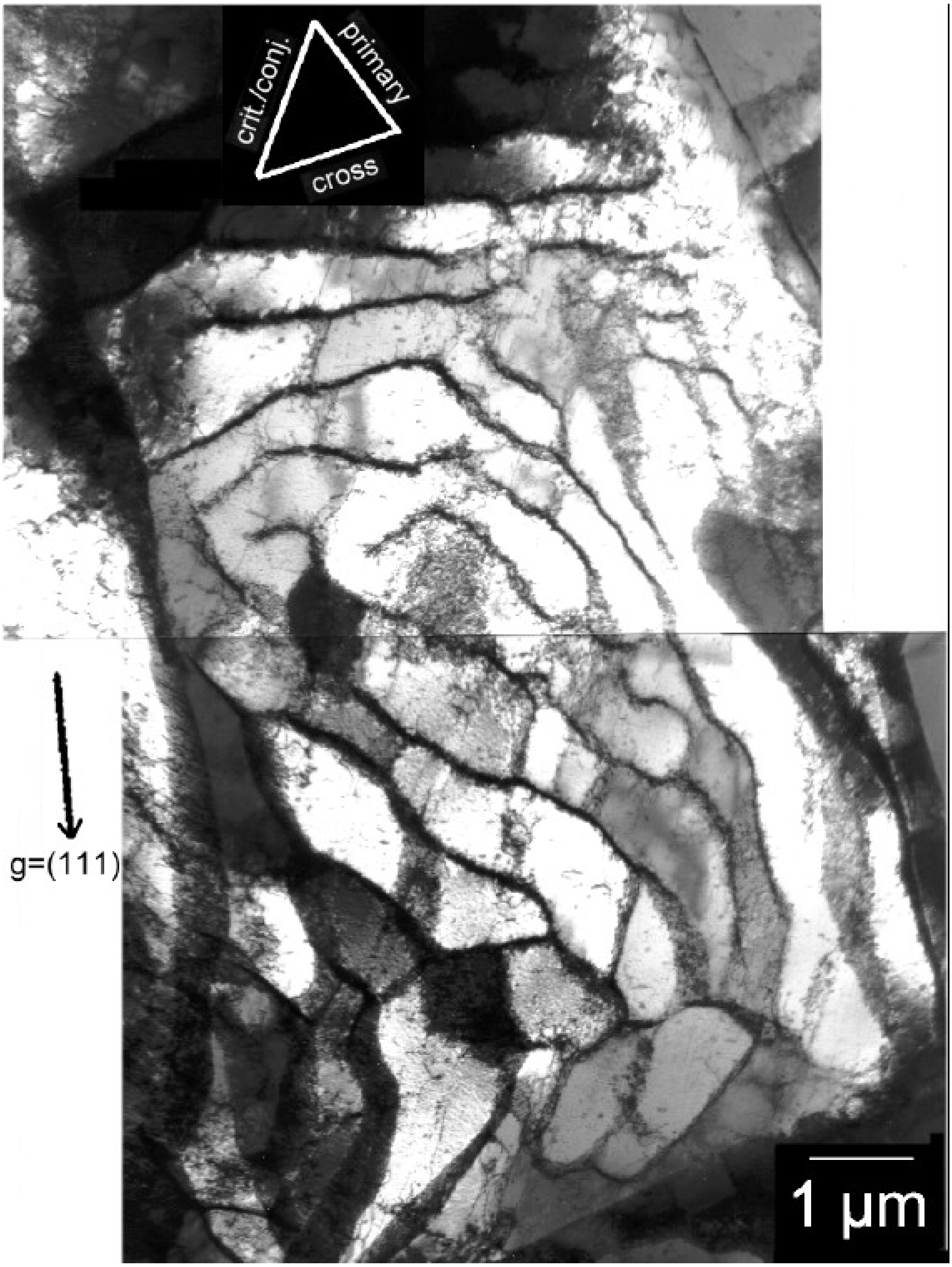

Figure 5.12 Cell structure observed in Cu-15%Zn cycled at $e_{pa}=3.3x10^{-3}$ *for N=8333 cycles. The Hollow Cone technique was used when recording this micrograph.*

To investigate the influence of the crystallographic orientation on the dislocation microstructures (wavy or planar), a number of grains with different structures were investigated in a Cu-15%Zn specimen cycled at ε_{pa}=3.3x10^{-3}. For each grain a distinction was made between three types of structures: wavy structures (walls), planar structures (arrays) and cell structures. In some grains it was impossible to say that either one of these structures were dominating. These grains were denoted 'mixed' grains. The crystallographic orientation, given in Euler angles, was determined for each grain by means of Kikuchi patterns (see chapter 0 on page 40 for the experimental details). The orientations are plotted in an inverse pole figure on Figure 5.13. The conversion between the Euler angles φ_1, ϕ and φ_2 and the coordinates x and y in the pole figure is described in HANSEN *ET AL.* (1978).

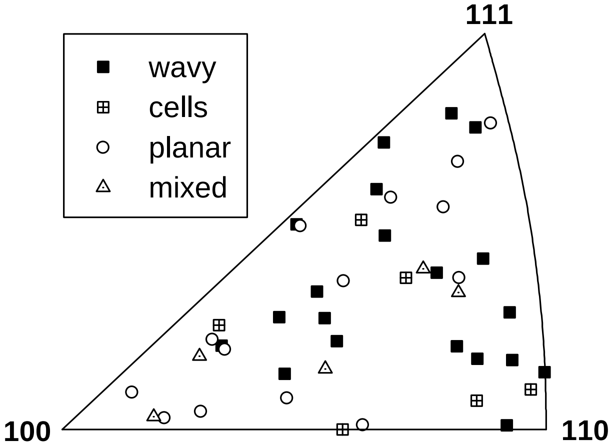

Figure 5.13 The coupling between the dislocation microstructure and crystallographic orientation of different grains in a Cu-15%Zn polycrystal cycled at e_{pa}=3.3x10^{-3}. The orientations is plotted in an inverse pole figure and it includes 45 grains.

Figure 5.13 indicates that no correlation exists between the observed dislocation microstructure and the orientation of a polycrystal grain in Cu-15%Zn. The grain- and twin boundaries, however, seem to play an important role in the formation of the wavy slip structures. In Figure 5.14 a grain with an annealing twin is shown. The twin and the neighbouring grain seem to have an influence on the formation of wall structures. The walls are formed between the twin boundary and the grain boundary but seem to be in the process of spreading to the rest of the grain, which contains more planar-like structures. Another example of the formation of wavy slip structures near grain boundaries is shown in Figure 5.15. In this case it is an early stage of cell formation.

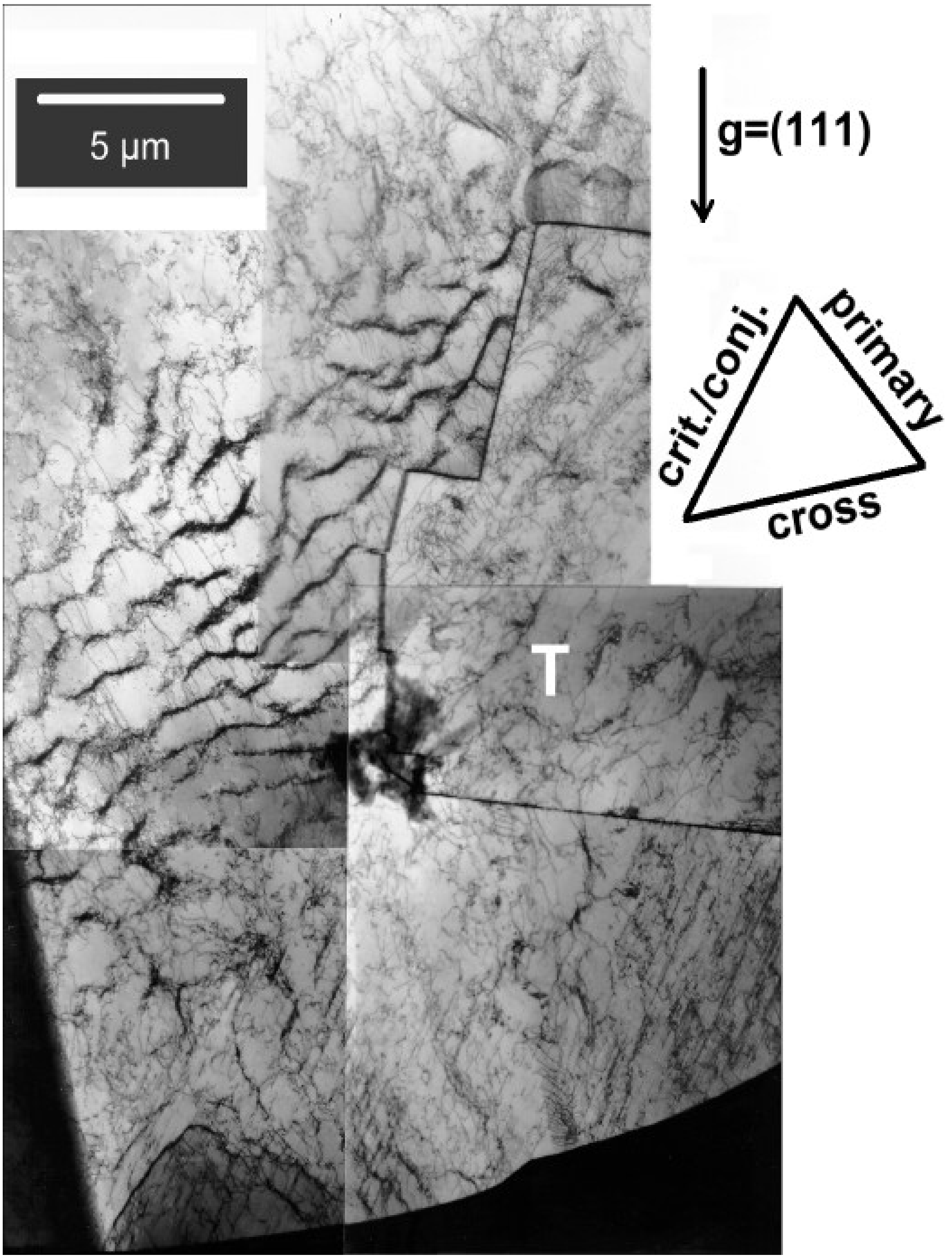

Figure 5.14 Formation of wall structures in a Cu-15%Zn grain containing an annealing twin (marked with T). The walls form between the twin boundary and the grain boundary, but seem to be in the process of spreading to the other parts of the grain. The structures in the lower right part of the micrograph are planar-like structures. $e_{pa}=3.3x10^{-3}$, *N=8333. The Hollow Cone technique was used to obtain this micrograph.*

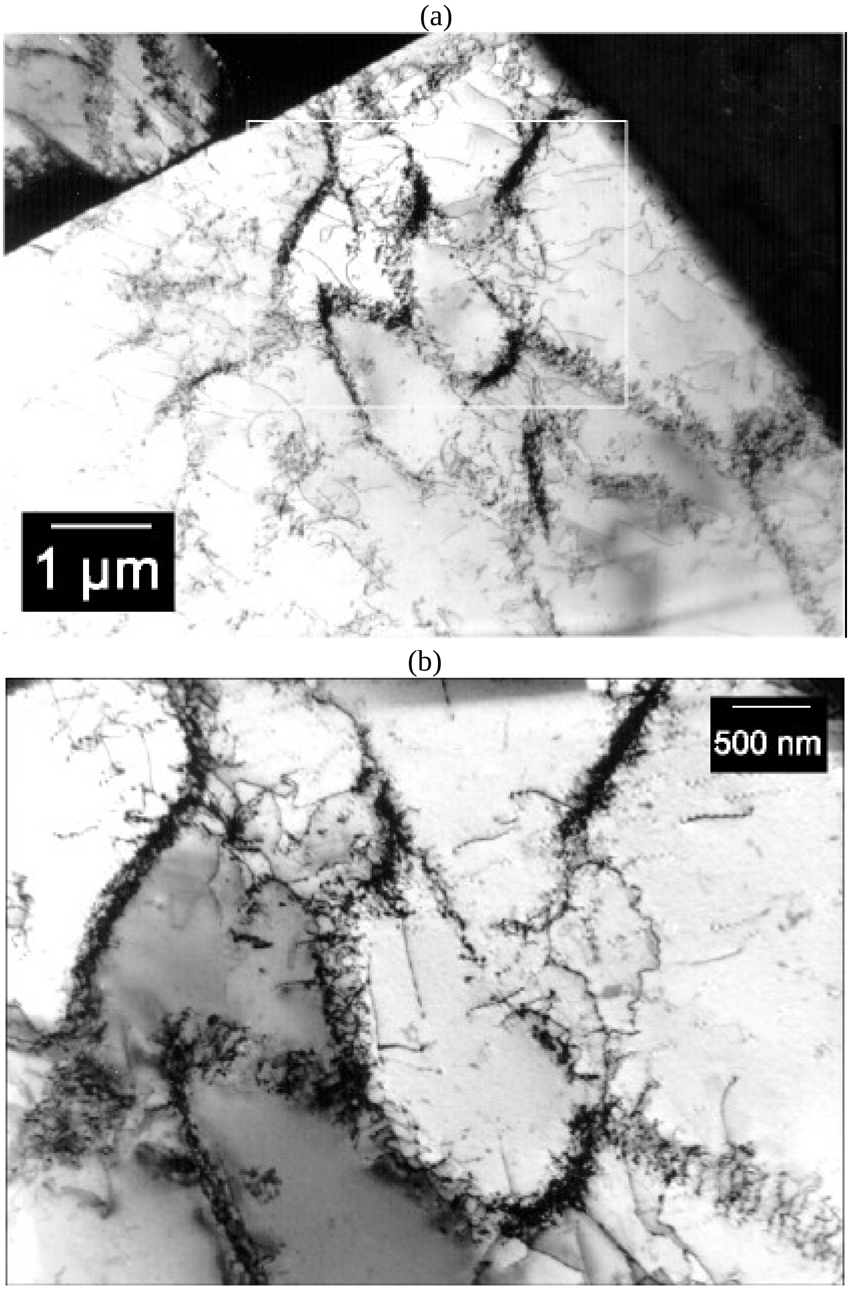

Figure 5.15 (a) Early stage of cell formation near a grain boundary in Cu-15%Zn. (b) Detail from (a) at different diffraction condition. e_{pa}*=1.6x10*$^{-3}$*, N=16666.*

5.2 Damage

The study of fatigue damage has been focused on Cu-30%Zn to reveal the damage process in a planar slip metal. Investigations of surface slip bands and microcracks in this alloy will be presented.

5.2.1 Surface slip bands

In Cu-30%Zn Sachs type single slip is dominating even at plastic strain amplitudes, ε_{pa}, as high as $5x10^{-3}$. Examples are shown in Figure 5.16.

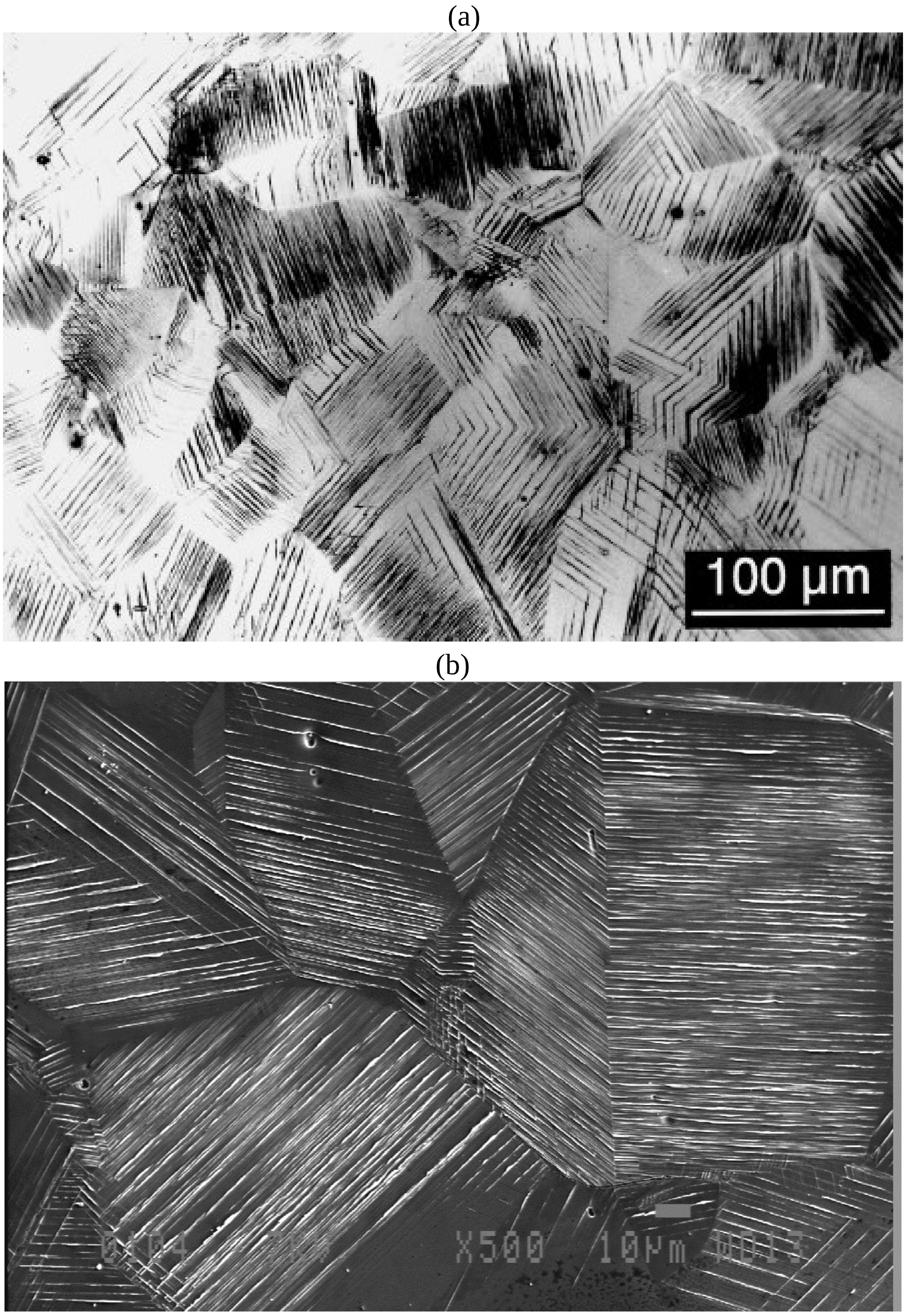

Figure 5.16 (a) Optical micrographs showing only one set of parallel slip lines in each crystal grain of Cu-30%Zn. This Sachs type single slip is dominating even at plastic strain amplitudes as high as $5x10^{-3}$. The micrograph show the surface of a specimen cycled at a plastic strain amplitude of $e_{pa}=3.4x10^{-3}$. (b) SEM micrograph from the same specimen.

Intense shear bands (ISBs) was found to form preferentially at grain boundaries and grow into the crystal (see Figure 5.8 on page 68). This process is illustrated in Figure 5.17 by series of SEM micrographs from a specific surface grain.

The formation of ISBs seems to spread across the grain and eventually the entire grain is filled with slip lines. Figure 5.18 shows examples of grains entirely filled with slip lines, i.e. after the ISB process has been completed. Another example of the ISB process is shown in Figure 5.19 for grains with annealing twins. Figure 5.19 shows clearly the easy transfer of slip across the twins, and it also shows the different rates of slip band formation in the different crystal grains.

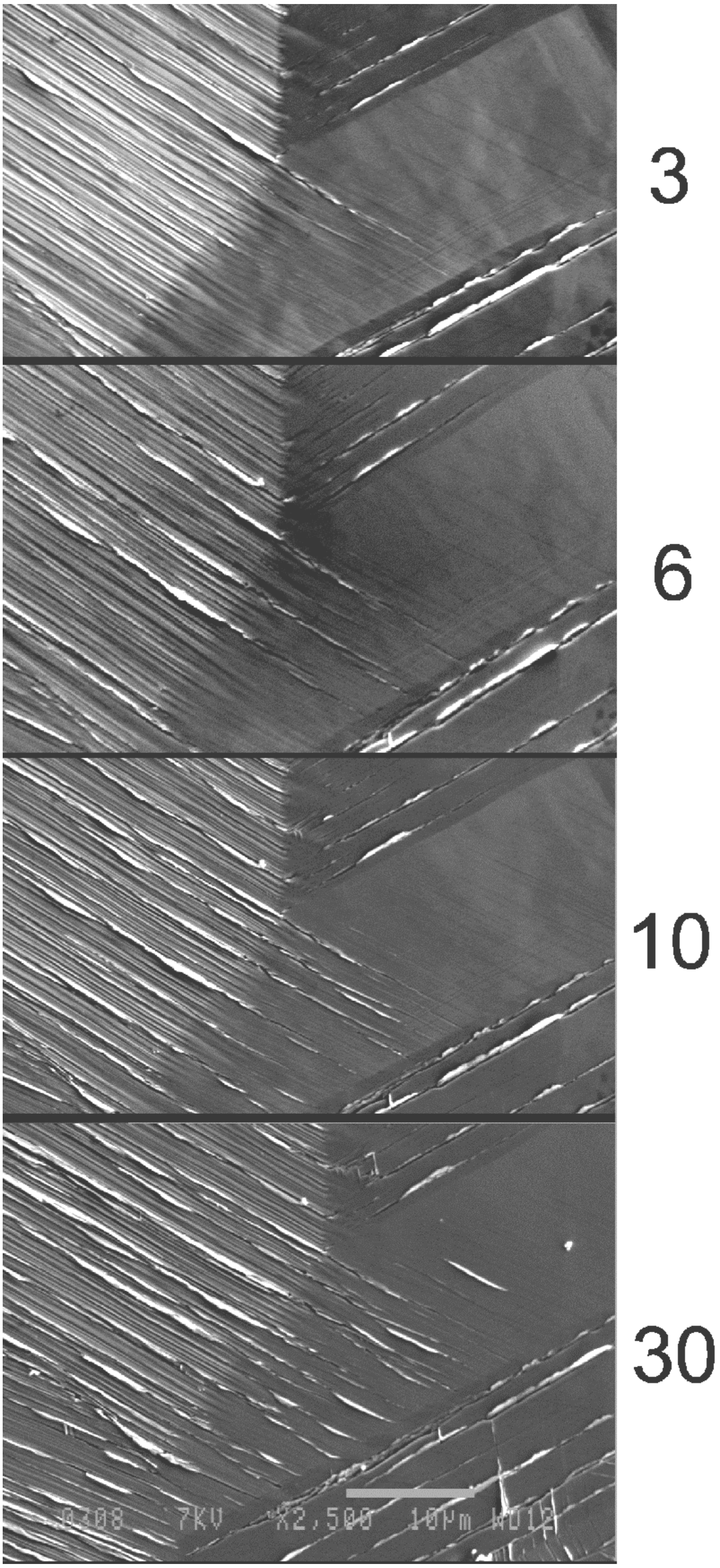

Figure 5.17 Process of ISB formation and growth on a specimen cycled at $e_{pa}=1.1x10^{-3}$. The ISB form at the grain boundary triggered by shear in the neighbouring grain. The ISB grow until it traverse the grain. More and more ISBs form and eventually the grain is covered with slip lines. The SEM micrographs show the same surface grain after 3, 6, 10 and 30 kilocycles.

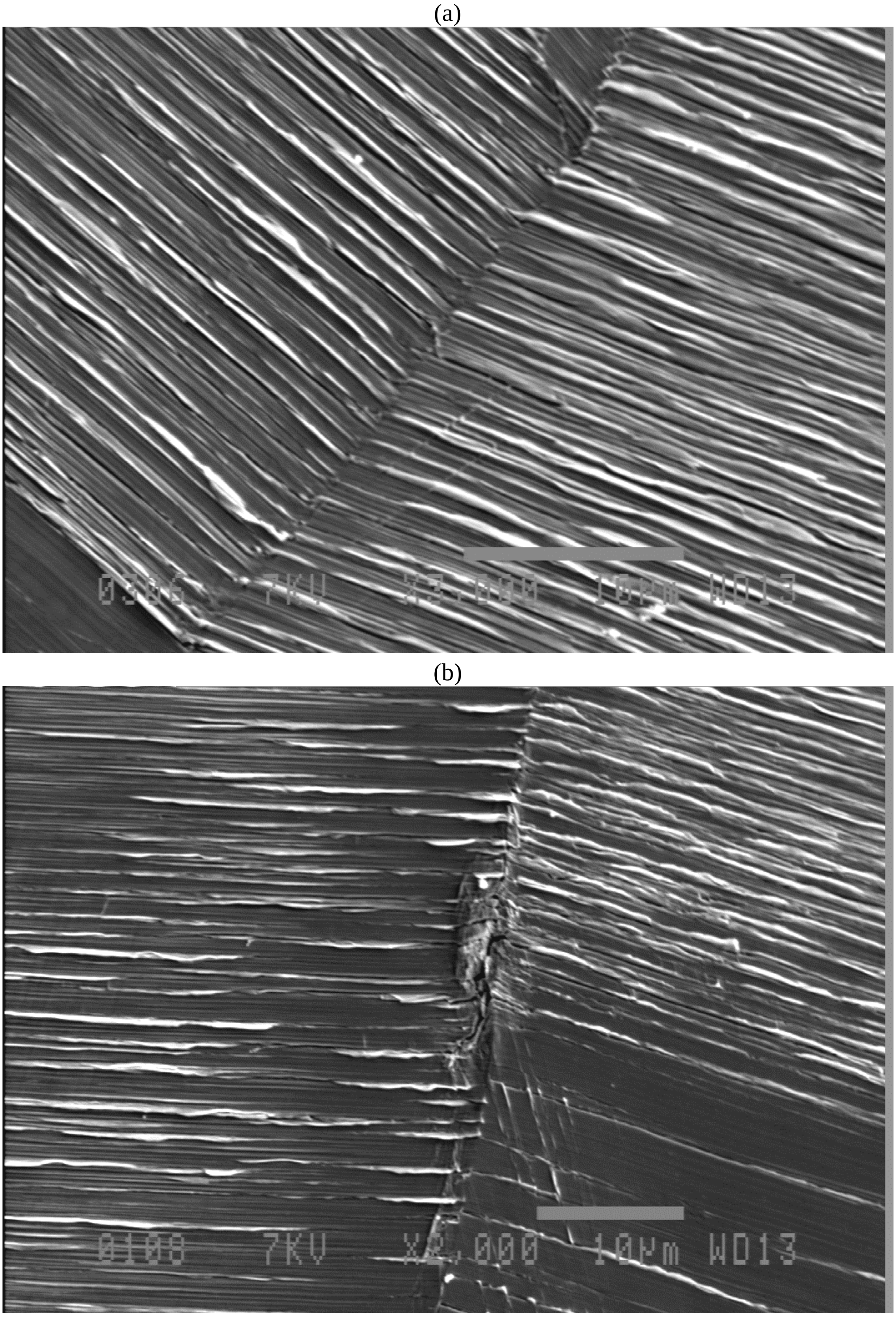

Figure 5.18 The polycrystal grains are covered with slip lines after the ISB process has been completed. The two examples are from the surface of a specimen after 8000 cycles at $e_{pa}=3.4x10^{-3}$. *Figure (b) shows initiation of an intergranular crack.*

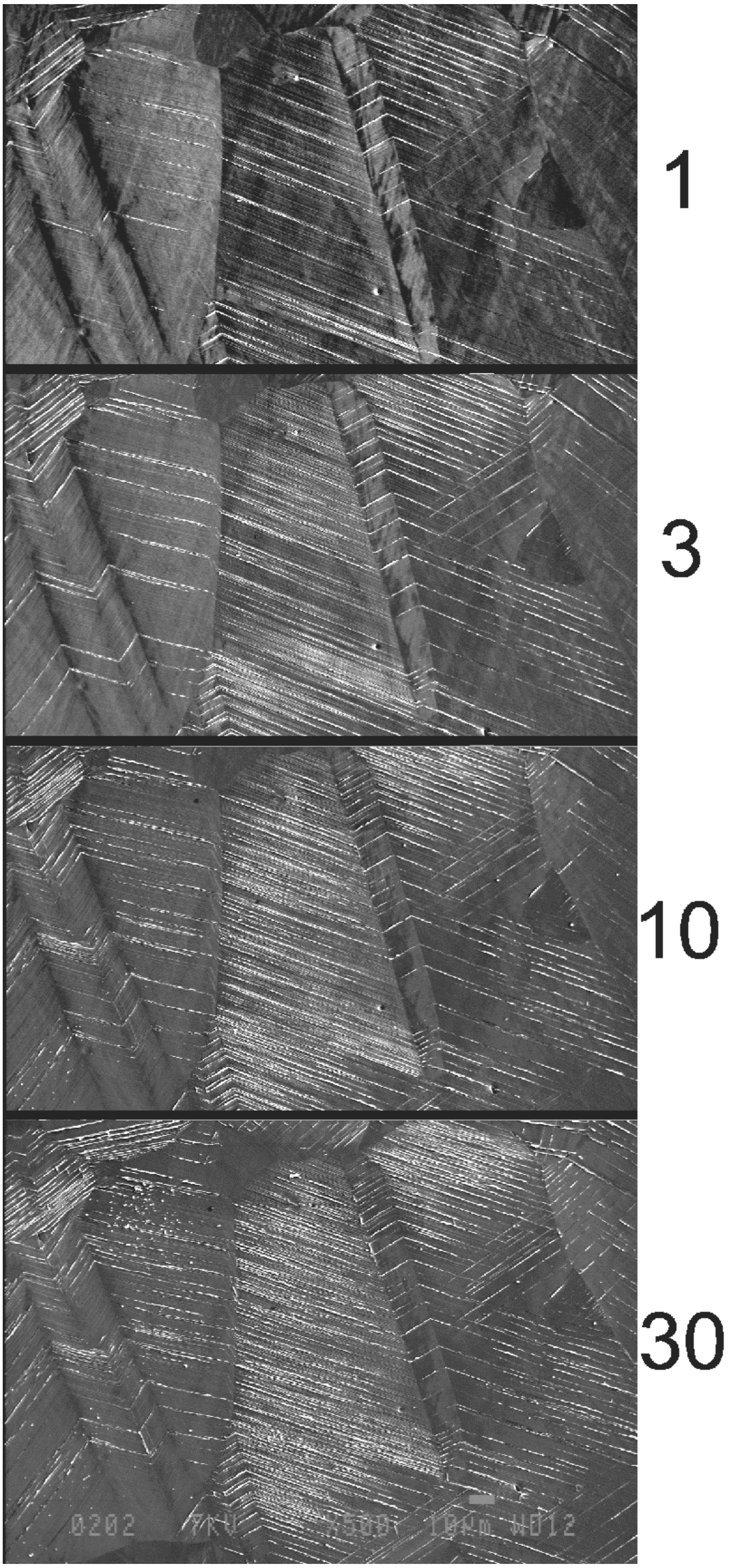

Figure 5.19 The ISB formation shown in grains with annealing twins on a specimen cycled at e_{pa}=2.2x10^{-3}. The easy transfer of slip across the twins is evident. The SEM micrographs show the grains after 1, 3, 10 and 30 kilocycles.

At imposed plastic strain amplitudes below a certain limit the resolved shear stresses are in some crystal grains not sufficient to activate slip. This means that even at final failure some grains are without slip lines on the surface. KITAGAWA *ET AL.* (1979) suggested that the slip activity, i.e. the ratio between the number of surface grains with slip lines and the total number of surface grains, is proportional to the imposed plastic strain amplitude. This has been investigated for Cu-30%Zn fatigued at different plastic strain amplitudes and the results are shown in Figure 5.20.

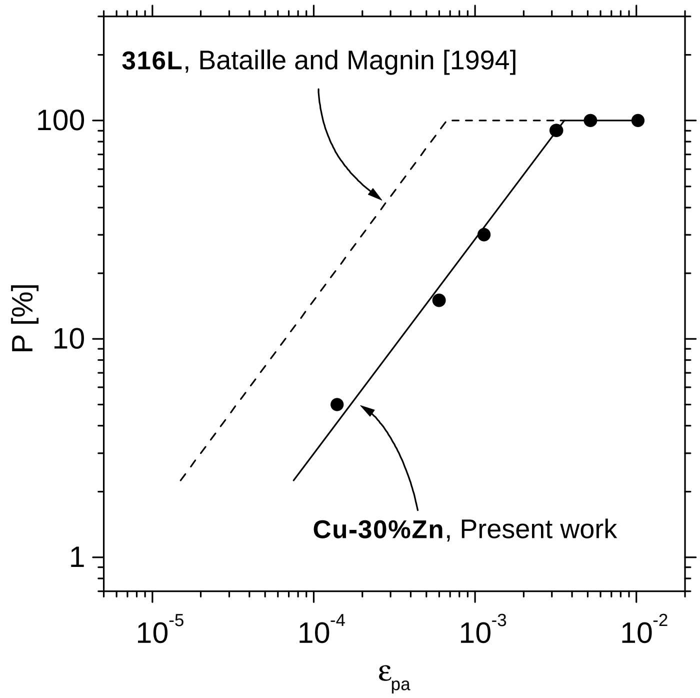

Figure 5.20 The slip activity, P, is proportional to the imposed plastic strain amplitude. Comparison with 316L steel show, that P is lower for Cu-30%Zn at a given plastic strain amplitude.

Kitagawa's suggestion seems to apply to Cu-30%Zn and it also applies to the 316L steel investigated by BATAILLE & MAGNIN (1994), as shown on Figure 5.20. The following relations are found for Cu-30%Zn and 316L steel (for $P \leq 100\%$):

$$P = C \cdot \varepsilon_{pa} \qquad \text{where } C = \begin{cases} 284 & \text{for Cu}-30\%\text{Zn} \\ 1500 & \text{for 316L steel} \end{cases} \tag{5.1}$$

which show that at a given plastic strain amplitude the number of plastically activated grains are less for Cu-30%Zn than for 316L steel.

5.2.2 Surface cracks

Both transgranular and intergranular cracks are seen on fatigued Cu-30%Zn. Two examples are shown in Figure 5.21.

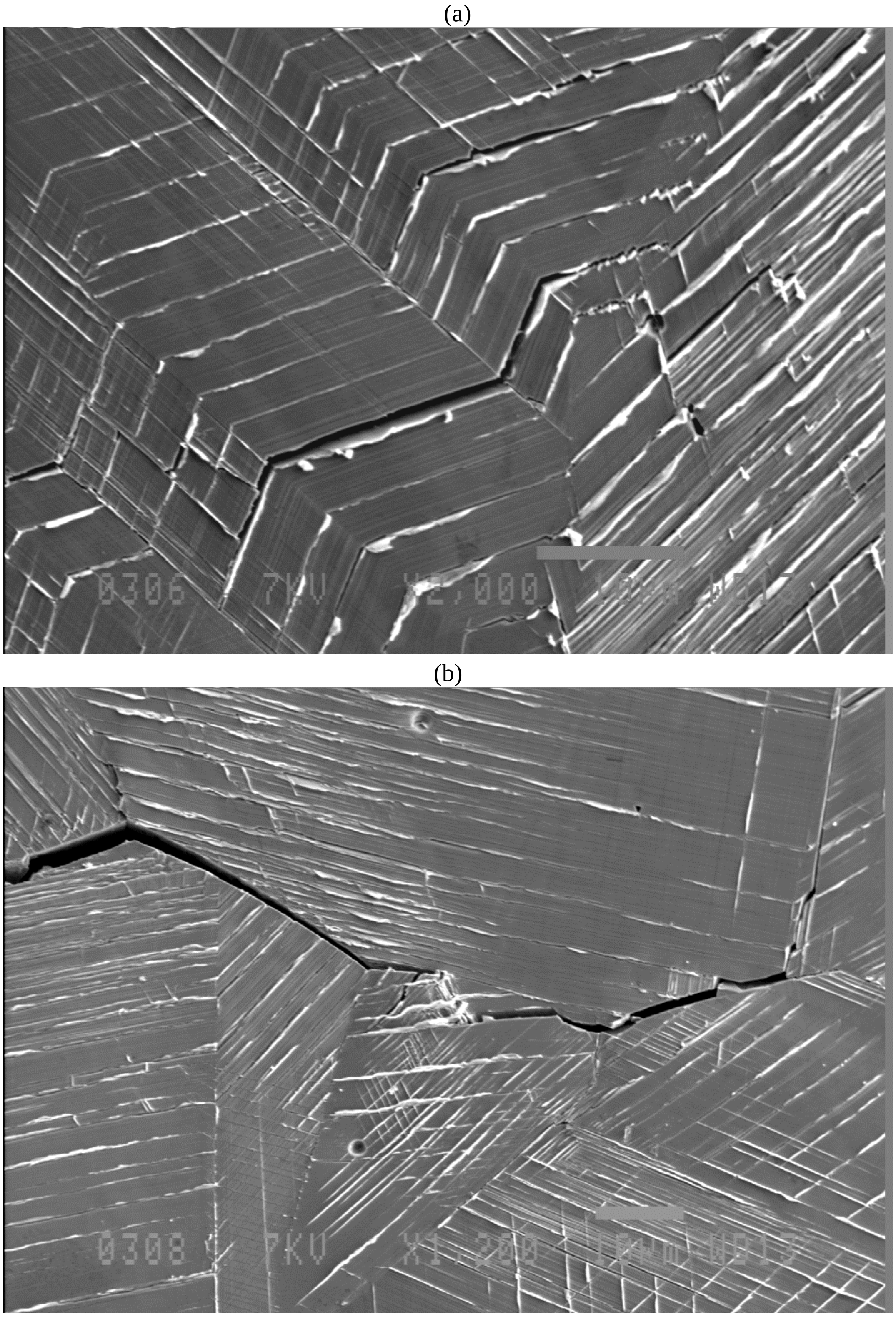

Figure 5.21 Transgranular cracks (a) are seen on fatigued Cu-30%Zn but intergranular crack growth (b) is dominating. The SEM micrographs are taken from a specimen cycled at $e_{pa}=2.2\text{x}10^{-3}$ *for 16000 cycles.*

The intergranular crack growth is dominating in Cu-30%Zn. It seems easier for the intergranular cracks to pass grain joints than for the transgranular cracks to pass grain boundaries. This dominance becomes increasingly more pronounced with increasing plastic strain amplitude. In Figure 5.22 more examples are shown of intergranular cracks.

(a)

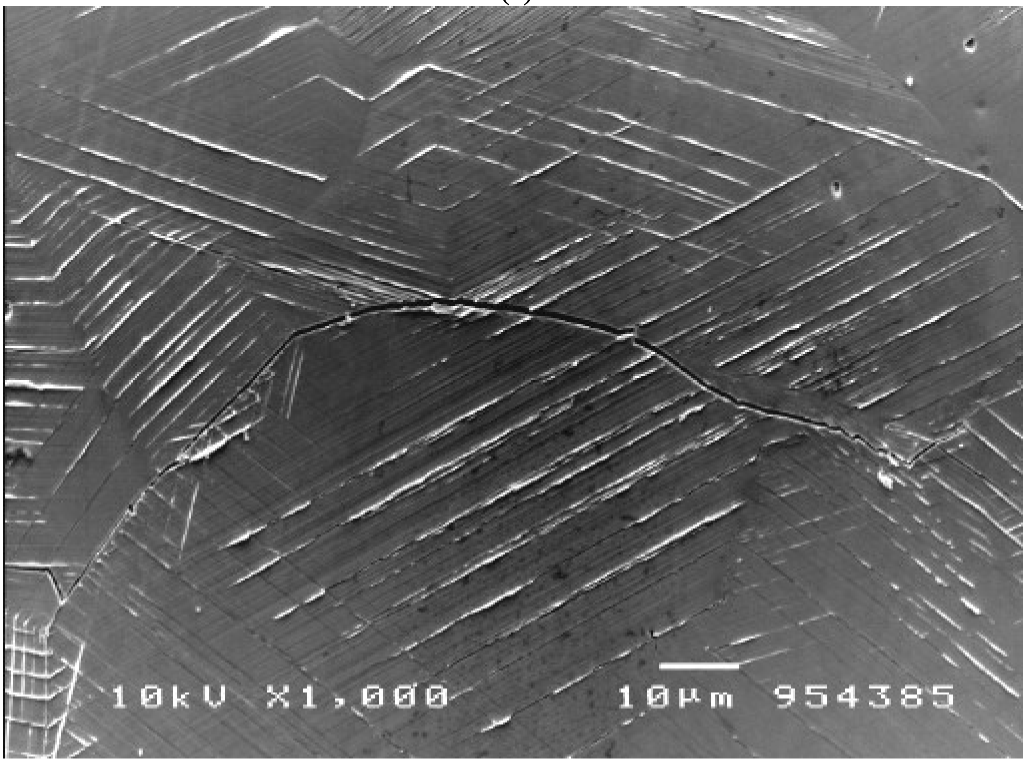

(b)

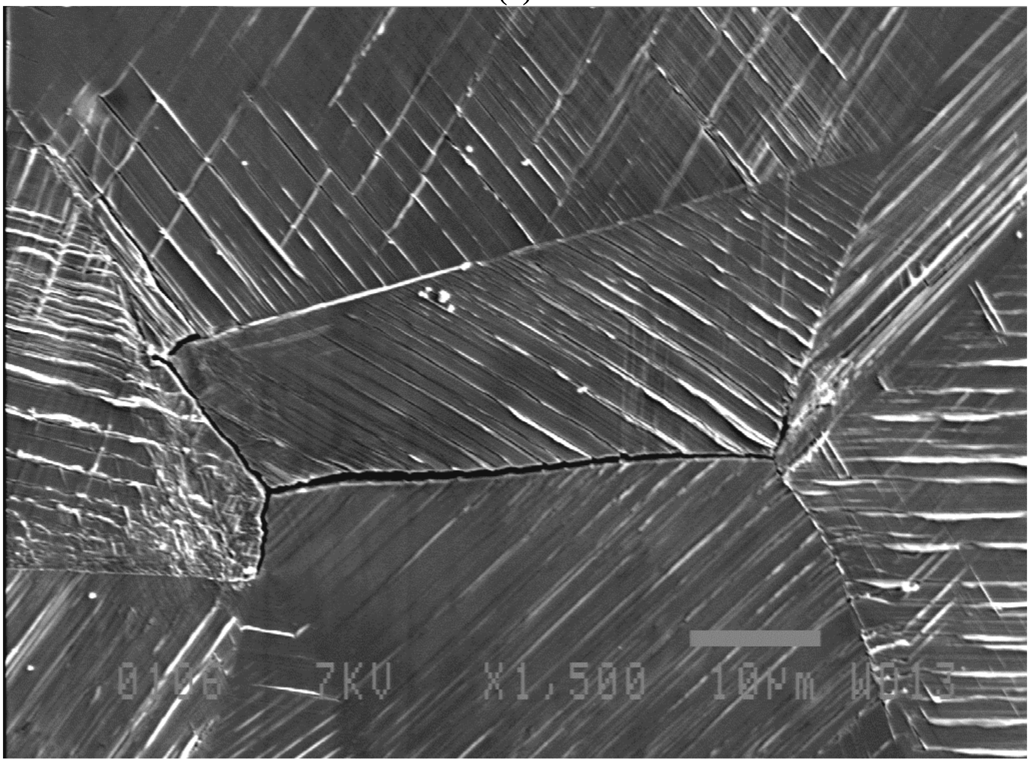

Figure 5.22 Intergranular cracks on Cu-30%Zn cycled at (a) $e_{pa}=1.1x10^{-3}$ *for 30000 cycles, and (b)* $e_{pa}=3.4x10^{-3}$ *for 8000 cycles.*

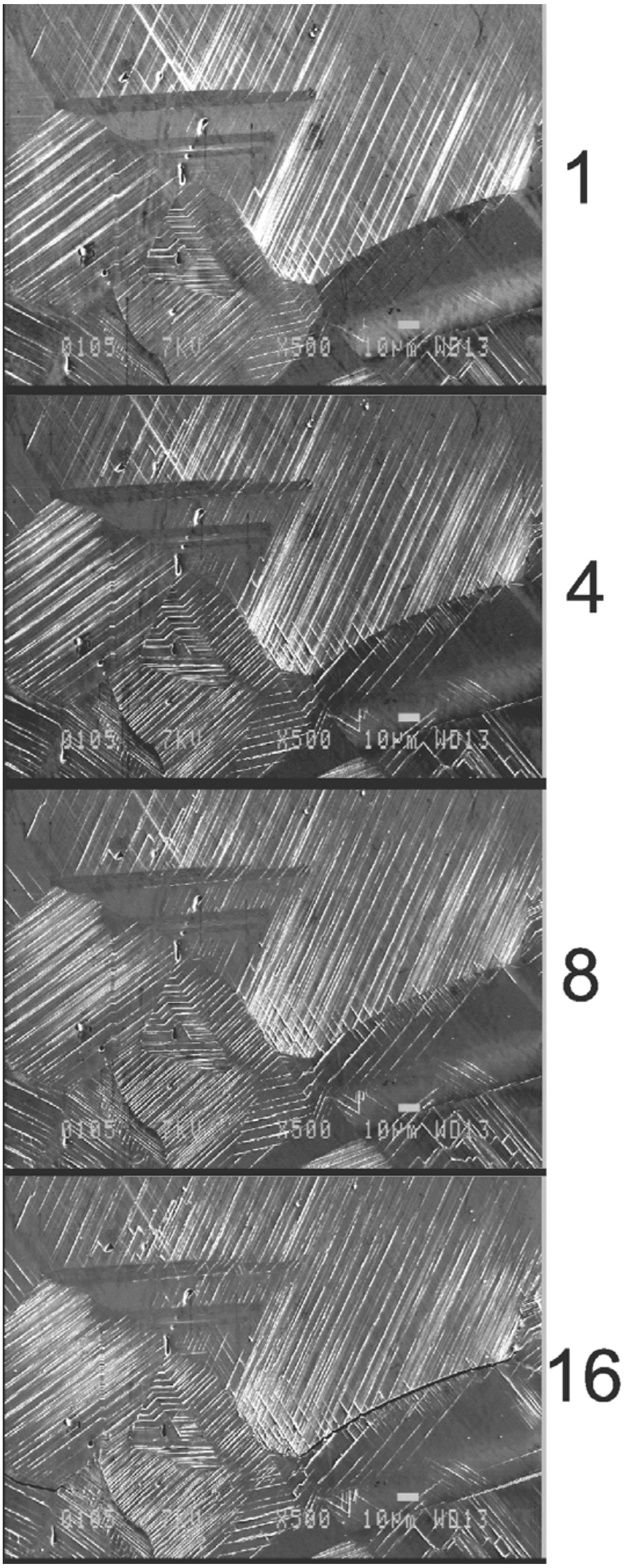

Figure 5.23 Initiation of intergranular crack on a specimen cycled at $e_{pa}=2.2\times10^{-3}$*. The SEM micrographs show the same surface area after 1, 4, 8 and 16 kilocycles.*

In Figure 5.23 the crack initiation and growth process on Cu-30%Zn is is illustrated with series of micrographs. The high intergranular stresses is seen to activate secondary slip near the grain boundary. The secondary slip lines become more an more pronounced and eventually the boundary opens to form a crack. The intergranular crack can easily pass the grain joints. In 316L transgranular crack growth dominates (Bataille & Magnin, 1994) so grain boundary crack blocking controls the short crack growth.

5.2.3 Evolution of surface cracks

The evolution of surface cracks can be characterized in different ways. One way is to classify the cracks according to their surface length and growth behaviour using the grain size as a scale. This was first suggested by Magnin *et al.* (1985): type I cracks have surface lengths less than one grain size, type II cracks have surface lengths between one and three grain sizes and type III cracks have surface lengths exceeding three grain sizes. This classification is shown in Figure 5.24.

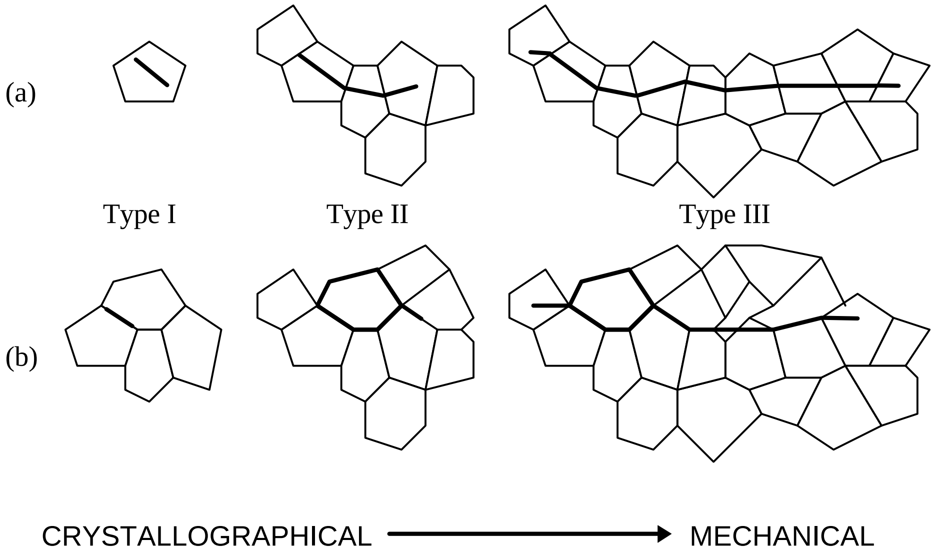

Figure 5.24 Classification of surface microcracks according to surface length and growth behaviour for (a) transgranular growth, and (b) intergranular growth. Type I cracks grow crystallographically while type III cracks grow mechanically. The growth of type II cracks is influenced by growth barriers such as grain boundaries and grain joints.

The physical distinction is that type I cracks grow crystallographically, i.e. within slip bands or grain boundaries, while type III cracks are driven by stress intensity and grow mechanically, i.e. perpendicular to the loading direction. In Figure 5.25 the transition from crystallographical to mechanical growth is illustrated for an intergranular crack which has become a type III crack.

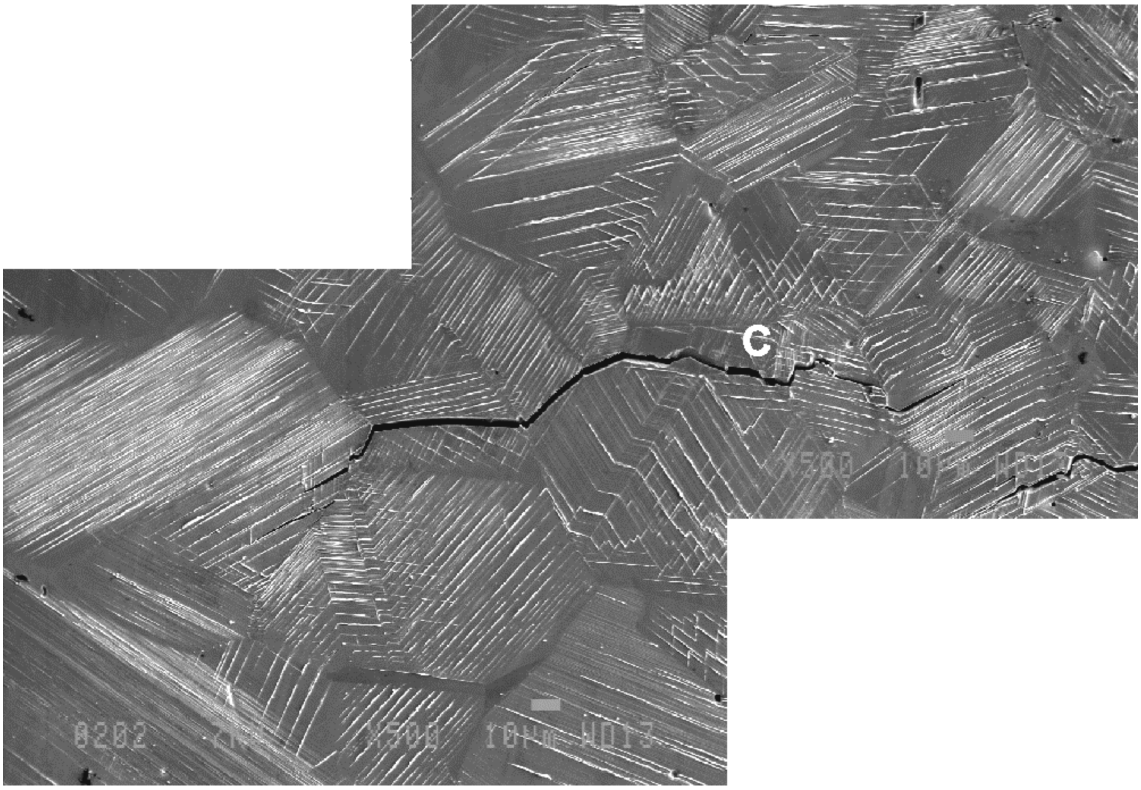

Figure 5.25 A transition from crystallographical to mechanical crack growth is seen when the crack reaches a certain length. The SEM micrograph shows an intergranular crack initially following the grain boundaries but with an apparent change in growth behaviour (marked with C) after the surface crack length has exceeded ~170μm. The micrograph is taken on a Cu-30%Zn specimen cycled at $e_{pa}=2.2x10^{-3}$ *for 16000 cycles.*

This transition is influenced by growth barriers such as grain boundaries (for transgranular growth) or grain joints (for intergranular growth). Thus it is not possible to define a specific growth behaviour for the type II cracks. When the length of a surface crack exceeds 10 grain sizes it is referred to as a type IV crack, and this fatal crack will form and grow very rapidly during the last 5-10% of the fatigue life (MAGNIN *ET AL.*, 1985). It is convenient to define fatigue life as the number of cycles, N_i, needed to form such a type IV crack (see page 54).

The above classification of cracks forms the basis of a numerical Monte Carlo type model for simulation of fatigue damage suggested by BATAILLE & MAGNIN (1994). With the aim of applying this model (see chapter 7.2) the surface crack evolution on Cu-30%Zn was characterized using this classification. Shouldered specimens were fatigued to different percentages of N_i and the densities of the different types of cracks were measured on each specimen to give the evolution of surface cracks. In Figure 5.26 the results for Cu-30%Zn are compared with those for 316L. The crack densities, ρ_{crack}, are plotted as a function of reduced life N/N_i.

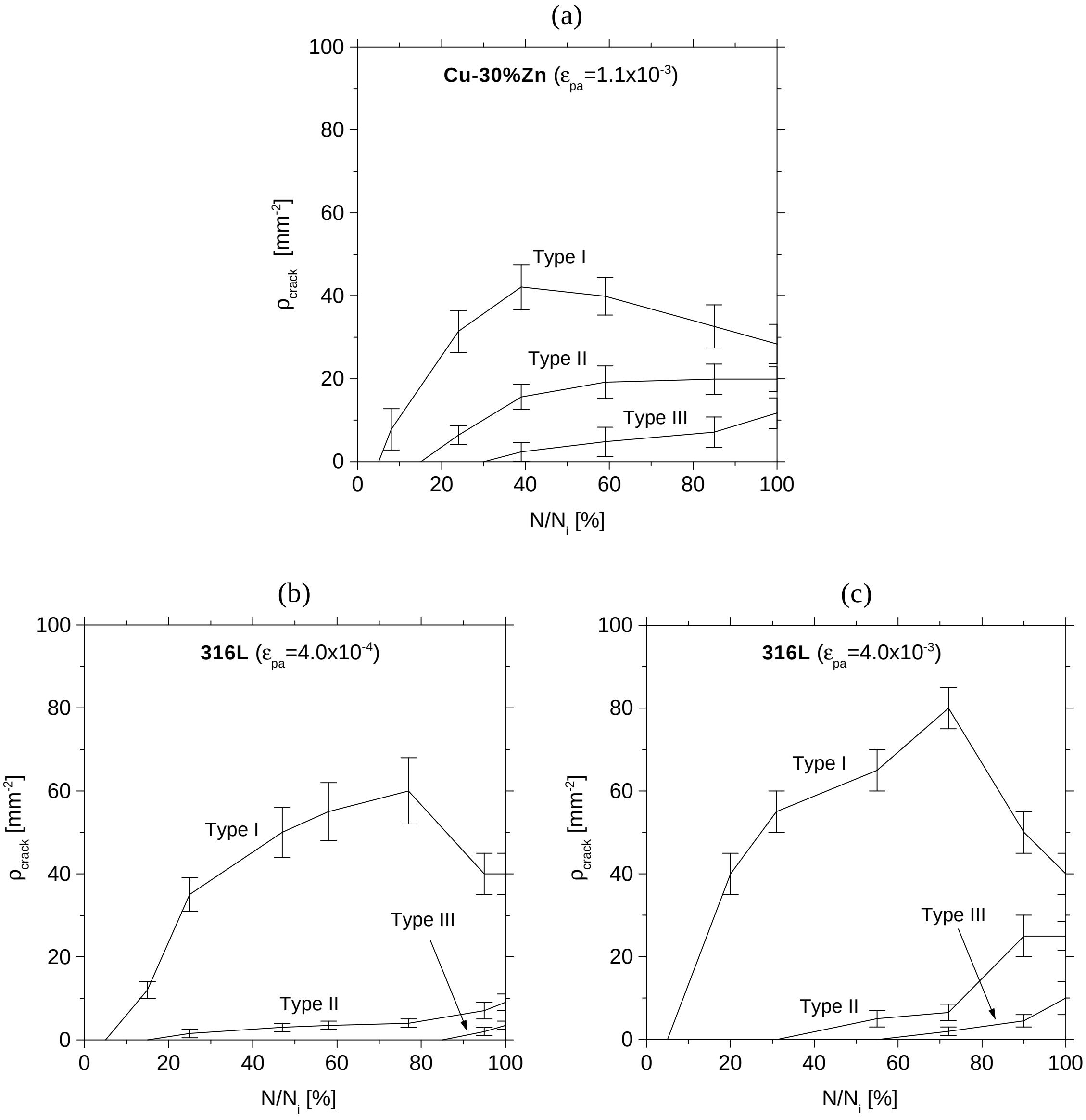

Figure 5.26 Surface crack evolution for (a) Cu-30%Zn cycled at $e_{pa}=1.1x10^{-3}$, (b) 316L steel cycled at $e_{pa}=4x10^{-4}$, and (c) 316L steel cycled at $e_{pa}=4x10^{-3}$. The data for 316L steel are taken from B*ATAILLE* & M*AGNIN* *(1994).*

It is noted, that the type I crack densities in Cu-30%Zn are lower than in 316L. This has to be correlated with the lower number of slip active grains in Cu-30%Zn (cf. Figure 5.20 on page 80). It is further noted, that the initial type II and III cracks appear much earlier on Cu-30%Zn at $\varepsilon_{pa}=1.3x10^{-3}$ than on 316L at $\varepsilon_{pa}=4x10^{-3}$, although the lower value of ε_{pa} for Cu-30%Zn should delay the appearance of type III cracks.

The growth rates of fatigue cracks were measured on specimens of Cu-30%Zn cycled at different plastic strain amplitudes. The experimental procedure is described in chapter 3.4.2 . On Figure 5.27, Figure 5.28 and Figure 5.29 the experimental results are shown at three different plastic strain amplitudes. dL/dN is plotted vs. L on the figures to the left and 1/L·dL/dN is plotted vs. L on the figures to the right. The ranges of type I, II and III cracks are indicated on the top of each figure. The average grain size of Cu-30%Zn was 65 μm and thus type III cracks have surface lengths larger than 195 μm.

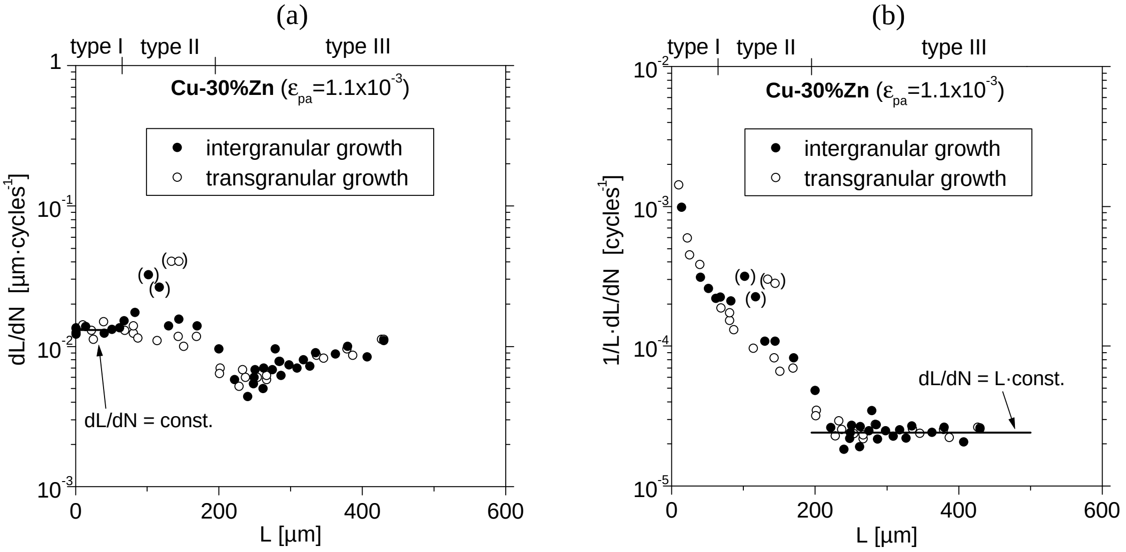

Figure 5.27 Crack growth rates for specimens cycled at $e_{pa}=1.1x10^{-3}$. In (a) dL/dN is plotted vs. N revealing that dL/dN=const. for the type I cracks, and in (b) 1/L·dL/dN is plotted vs. N revealing that dL/dN=const.·L for type III cracks.

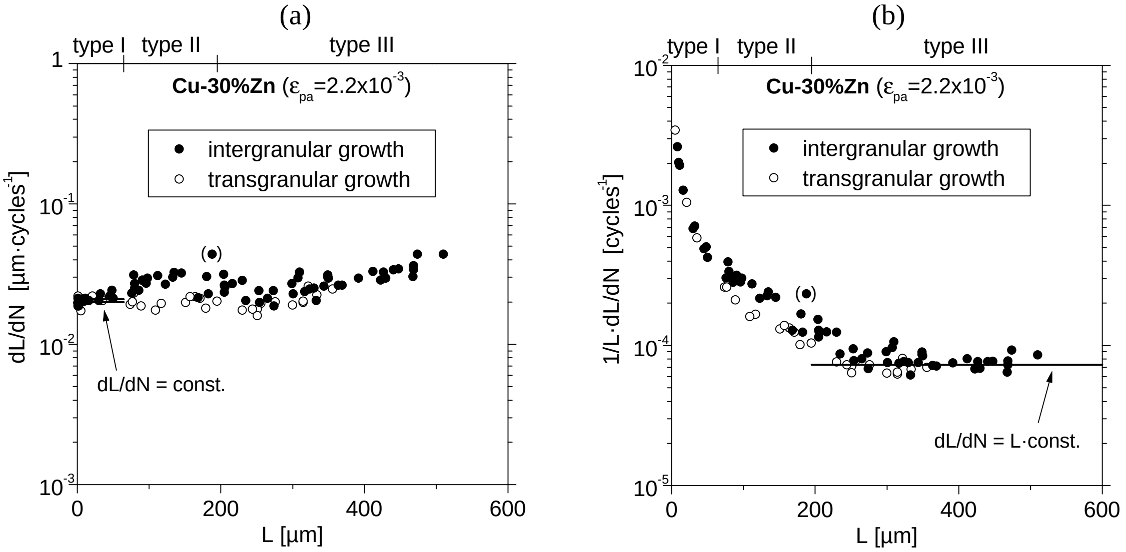

Figure 5.28 Crack growth rates for specimens cycled at $e_{pa}=2.2x10^{-3}$. In (a) dL/dN is plotted vs. N revealing that dL/dN=const. for the type I cracks, and in (b) 1/L·dL/dN is plotted vs. N revealing that dL/dN=const.·L for type III cracks.

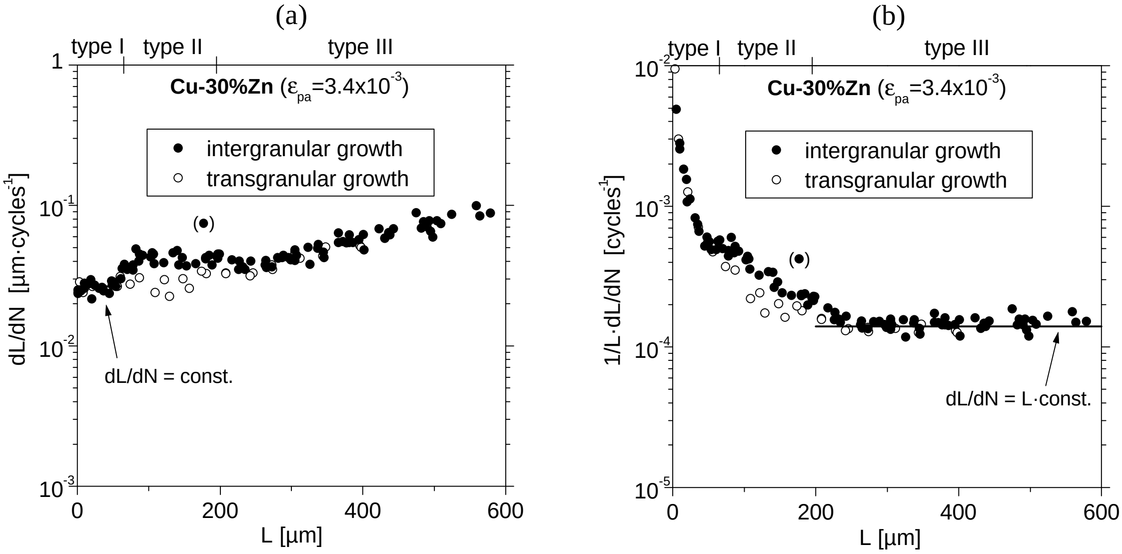

Figure 5.29 Crack growth rates for specimens cycled at e_{pa}=3.4x10^{-3}. In (a) dL/dN is plotted vs. N revealing that dL/dN=const. for the type I cracks, and in (b) 1/L·dL/dN is plotted vs. N revealing that dL/dN=const.·L for type III cracks.

The figures reveal that at a given plastic strain amplitude dL/dN=const. for type I cracks and dL/dN=L·const. for type III cracks. The proportionality constants increase with ε_{pa}, so we can express dL/dN as a function of ε_{pa}. In Figure 5.30 dL/dN and 1/L·dL/dN are plotted vs. ε_{pa} for type I and type III cracks respectively. The results are compared with similar measurements on 316L steel (RAMADE, 1990).

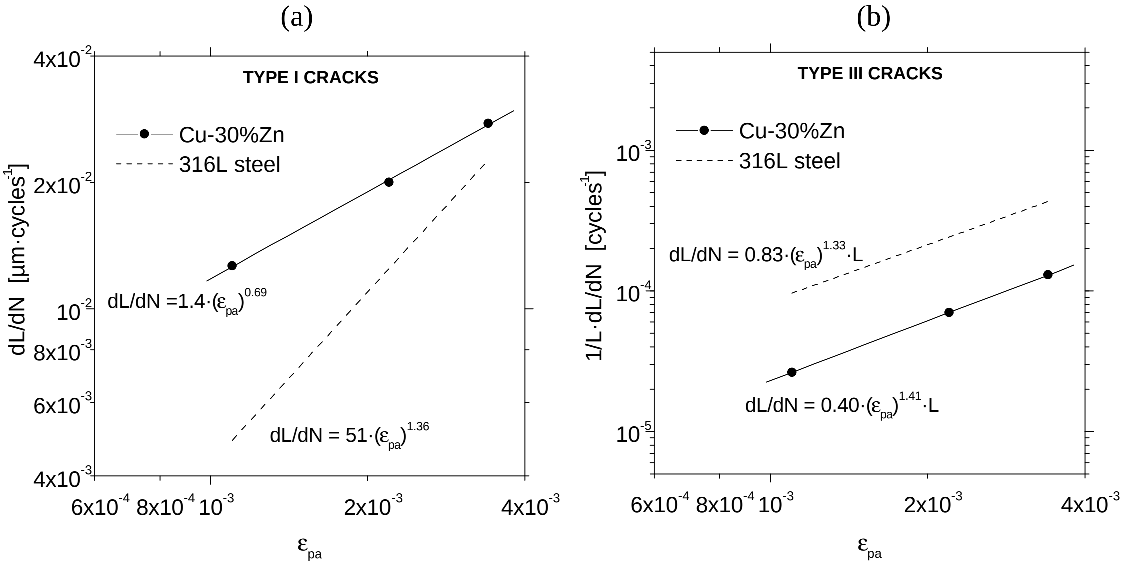

Figure 5.30 The cracks growth rates vs. the plastic strain amplitude for (a) type I cracks, and (b) type III cracks. The straight line on a double logarithmic plot indicates a power law function.

The power law relations reflected by Figure 5.30 describe the crack growth rates, and for Cu-30%Zn they can be expressed as:

type I: $$\frac{dL}{dN} = 1.4 \cdot \left(\varepsilon_{pa}\right)^{0.69} \tag{5.2}$$

type III: $$\frac{dL}{dN} = 0.40 \cdot \left(\varepsilon_{pa}\right)^{1.4} \cdot L \tag{5.3}$$

A similar relation cannot be established for type II cracks, as they are influenced by growth barriers and thus do not have a well-defined growth behaviour.

5.3 Discussion

Cyclic softening has been investigated in polycrystalline Cu-30%Zn using transmission electron microscopy (TEM). Plastic strain controlled cyclic deformation of this alloy reveals successive stages of primary hardening, softening and secondary hardening (see Figure 5.1 on page 61). During the primary hardening stage dipole arrays form and grow and at the end of this stage extended arrays of dipoles are seen in comparatively undislocated crystal (Figure 5.3 on page 63). These structures resemble those found in the first stage of monotonic deformation of Cu-Zn (NEUHÄUSER *ET AL.*, 1986; OLFE & NEUHÄUSER, 1988) and Cu-Al (e.g. PANDE & HAZZLEDINE, 1971), but similar structures have also been reported in cyclic deformation of Cu-Al (e.g. LAIRD & BUCHINGER, 1985; INUI *ET AL.*, 1990) and 316LN steel (VOGT *ET AL.*, 1991). A variety of configurations of the dipole arrays can be detected and in particular the dipole height and spacing is seen to vary considerably. It has been shown by OLFE & NEUHÄUSER (1988) that their configuration is influenced by the friction forces on the dislocation exerted by the solute atoms and that the variety of configurations can be explained if the friction stress and its diminution by the dislocations cutting through the obstacles is taken into account. The observed variations in dipole spacing therefore seem to be explained in terms of variations in friction stress. In Figure 5.4 on page 64 dipole arrays with different heights and spacings are shown. The dipole array in Figure 5.4b is of particular interest because it, at first sight, appears to be an extended stacking fault due to the fringe pattern. The detailed analysis in Figure 5.5 and Figure 5.6 on page 66, however, reveals that the fringe pattern is simply a Moiré effect caused by very closely spaced dislocations. A similar effect has previously been observed by others (e.g. SWANN & LOUAT, 1963; HAZZLEDINE, 1967) but Figure 5.6c is the first attempt to resolve the individual dislocations of the closely spaced dipoles.

The formation of the dipole arrays is suggested to be promoted by the presence of short-range ordered (SRO) domains. The ordered domains are in a lower energy level than the surrounding matrix so that if a dislocation passes through such a domain the order will be destroyed and the crystal structure shifts to a higher energy level. This is an endothermic process and thus the ordered domains act as obstacles to dislocation movement. The dislocations will tend to move as groups in planes with the lowest density of ordered domains. The group formation is favoured by the tendency of the moving dislocations to destroy the SRO obstacles and in TEM the groups appear as pile-ups (see e.g. OLFE & NEUHÄUSER, 1988). The dislocation groups are the sources of the formation of the dipole arrays. A model of this formation, based on a cross slip mechanism, has been suggested by JACKSON (1985). In Figure 5.31 the principles of this model is shown.

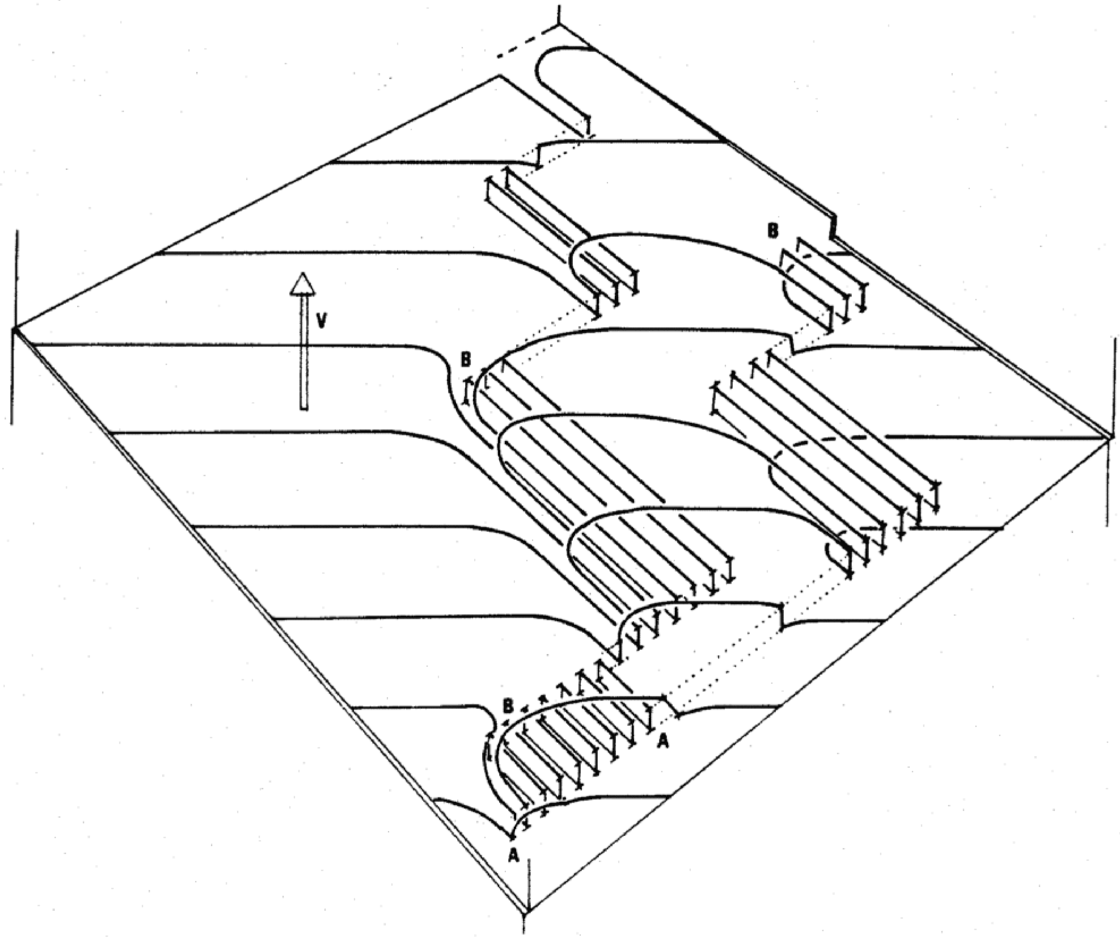

Figure 5.31 Perspective sketch showing how multipolar debris can be created by the cross-slip of a procession of dislocations that glides along V. Dipoles are first deposited as a result of cross-slip along AA. Dipoles are terminated by cross-slip when they bend into screw orientation behind arrays of previously formed loops, in regions like B. For clarity regular arrays are drawn. In practice arrays will be less uniform and may also be plastically relaxed (JACKSON, 1985).

In Figure 5.2 on page 62 a TEM micrograph from the early stage of primary hardening (ε_{cum}=0.1) show the initial formation of a dipole array. This observation clearly seems to support the formation mechanism depicted in Figure 5.31. Other experimental observations indicative of the cross-slip mechanism can be found in the work of SWANN & NUTTING (1961), STEEDS & HAZZLEDINE (1964), OLFE & NEUHÄUSER (1988), and INUI *ET AL.* (1990).

The dipole arrays are considered to first form on the "softest" slip planes, i.e. the slip planes with the lowest friction stress, and extend until these slip planes become "hard". Then the deformation shifts to other primary slip planes to form more dipole arrays and they continue to form and grow until a certain resolved shear stress triggers the formation of ISBs. These shear bands initiate at grain boundaries (Figure 5.8 on page 68) and spread out into the grains destroying the dipole arrays. This explains the cyclic softening. More ISBs form and cyclic softening continues until all the dipole arrays have been destroyed. At this point the polycrystal is found to contain a fairly uniform structure of planar dislocation arrays (cf. Figure 5.9 on page 69). During continued cycling the morphology remains virtually unchanged, but the structure is not static as there is a continuous increase of the dislocation density (cf. Figure 5.10 on page 70). This leads to an increase of the friction stresses (cf. Figure 4.5 on page 49), which accounts for the secondary hardening.

The process of ISB formation is illustrated in Figure 5.17-Figure 5.19 on pages 77-79 by series of SEM micrographs taken at the surface of cyclically deformed Cu-30%Zn specimens. Initially the deformation is localized in few ISBs but more ISBs form and eventually the polycrystal grains are completely filled with slip lines (Figure 5.18). This reflects a more homogeneously distributed deformation in the individual grains. In Cu-Al a similar deformation behaviour has been observed. LAIRD & BUCHINGER (1985) investigated single crystals of Cu-16at.%Al and found a plateau on the CSS curve. In the plateau range ($1.5x10^{-3} < \gamma_{pa} < 5x10^{-3}$) they observed regions of localized strain. YAN *ET AL.*, 1986 used interferometric techniques to study this localization and they found that the localized slip shifts around the surface, which eventually becomes filled with slip lines. Because of this behaviour, the slip bands were called Persistent Lüders Bands (PLBs), so as to indicate a distinction from PSBs. However, each slip band was found to have a very short active life and therefore the persistence of these bands is controversial. For this reason the term ISB has been chosen in this thesis and it is suggested, that the plateau found for single crystals of Cu-30%Zn (WANG, 1994) is correlated with the formation of ISBs. The plateau seems to range from $\gamma_{pa}\approx10^{-3}$ (see Figure 4.10 on page 52) corresponding to $\varepsilon_{pa}\approx\gamma_{pa}/m_S=4.5x10^{-4}$. This implies, that ISBs are formed above this amplitude, which can explain the bends on the cyclic hardening curves at amplitudes where no softening is observed (Figure 4.3b on page 47).

The dislocation structures observed in Cu-15%Zn clearly reflect a dependency on the plastic strain amplitude. Planar slip structures seem to dominate at low amplitudes and wavy slip structures dominate at high amplitudes. This correlates well with the observed shift of the CSS curve, which was discussed in chapter 4.5, and it resembles the observations made in 316L steel (KRUML *ET AL.*, 1997). The cyclic softening observed in Cu-15%Zn is therefore likely to be related to formation of PSB-like structures rather than ISBs. This would explain the observation that Cu-15%Zn tends to saturate after cyclic softening. No PSB-like structures were found in the present study, but such structures have previously been reported in single crystals of Cu-15%Zn (LUKÁS & KLESNIL, 1970; 1971). The cell structures observed at high amplitudes in Cu-15%Zn were also found in 316L steel (e.g. GERLAND *ET AL.*, 1989) and they are frequently observed in copper. Cell structures were not observed in Cu-30%Zn. The crystallographic orientations of polycrystal grains in Cu-15%Zn were measured and related to the microstructures discovered in each grain. No correlation was found between the dislocation structures and the crystallographic orientation (Figure 5.13 on page 73), which is similar to observations made in polycrystalline copper (e.g. WINTER *ET AL.*, 1981). Instead, the presence of neighbouring grains or twins seem to play an important role in the formation of the wavy slip structures (see Figure 5.14 and Figure 5.15 on page 75). The wavy slip walls and cells appear to initially form at or near grain- or twin boundaries, presumably induced by deformation in the neighbouring grains or twins. This resembles the formation of ISBs, as discussed above, and it suggests that the simple orientation analysis presented in Figure 5.13 do not provide realistic information about orientation dependency. Somehow, the orientations of neighbouring grains have to be included in such an analysis. This, however, is beyond the scope of this thesis.

When comparing the dislocation structures found in Cu-15%Zn and Cu-30%Zn with those found in 316L and 316LN steel, it is seen that the increase of zinc content in brass corresponds to an increase of nitrogen content in 316L steel. The 316LN steel is the high nitrogen version of 316L, and in this steel the slip mode is planar (VOGT *ET AL.*, 1991). The structures in 316LN resembles those found in Cu-30%Zn, while the structures in 316L are similar to those found in Cu-15%Zn. The structural similarities also reflect on the mechanical behaviour, as discussed in chapter 4.5, and therefore brass appears to be a unique model material for the austenitic stainless steels. The addition of nitrogen to 316L does not, like in brass, have an effect on the stacking fault energy (VOGT *ET AL.*, 1991). This supports the idea that local order, rather than the stacking fault energy, is responsible for the slip planarity, as suggested by VOGT *ET AL.* (1990).

In Cu-30%Zn intergranular cracking is dominating (Figure 5.21-Figure 5.23 on pages 81-83). This can be correlated with the high intergranular stresses, which would be expected as a result of the pronounced single slip (Figure 5.16 on page 76). Presumably the single slip behaviour is caused by high latent hardening (PEDERSEN *ET AL.*, 1982), which is extended by the slip planarity of this alloy. The dominance of intergranular cracks becomes increasingly more pronounced with increasing plastic strain amplitude, which suggests an increase of the intergranular stresses with the plastic strain amplitude. The crack initiation process illustrated in Figure 5.23 seems to show the effect of high intergranular stresses, activating secondary slip near the grain boundary and eventually leading to intergranular crack formation. The intergranular cracks are observed to grow very rapidly, virtually unaffected by the grain joints. This reflects on the surface crack evolution, as shown in Figure 5.26 on page 86. Compared to 316L steel, which is dominated by transgranular cracking, the type II and III cracks form much earlier on Cu-30%Zn. This is likely to be related to the higher intergranular crack growth rate. In Figure 5.32 the surface crack evolution observed on a ferritic steel is shown (RAMADE, 1990). This steel is also dominated by intergranular cracking.

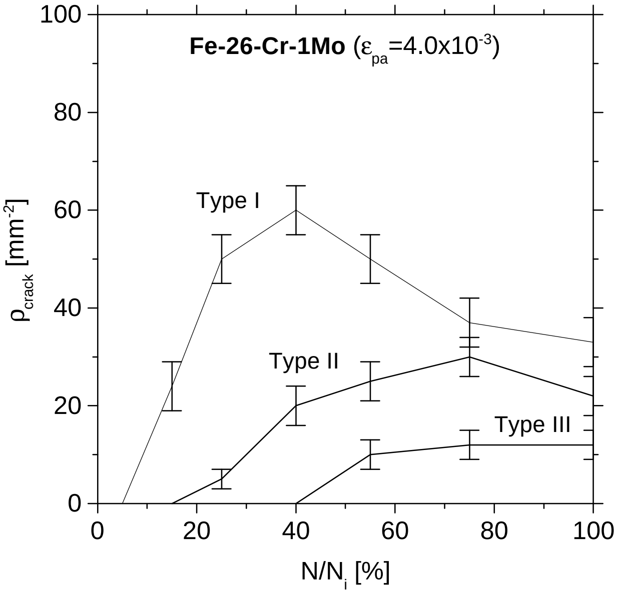

Figure 5.32 Surface crack evolution for a ferritic steel (RAMADE, 1990), which is dominated by intergranular cracking. The formation of type II and III cracks appear early in fatigue life, as observed in Cu-30%Zn.

When comparing the crack evolution of this ferritic steel with that of Cu-30%Zn (Figure 5.26a on page 86) the similarities are striking. The crack mode thus seems to be reflected by the crack evolution, when the cracks are classified according to their surface length, and early type II and III crack formation appears to be related to intergranular cracking. By itself the higher intergranular crack growth rate would imply a shorter fatigue life for Cu-30%Zn than for 316L, but as shown in Figure 4.14 on page 55 the two materials have approximately the same fatigue life curve. Thus an explanation of the fatigue life of brass and 316L evidently requires additional damage characteristics. It is possible that the lower crack density in Cu-30%Zn compensates for the rapid growth of intergranular cracks. Coalescence of cracks becomes less frequent when fewer cracks are present, which reduces the overall crack growth rate and helps to prolong the fatigue life. Another possible explanation lies in the fraction, P, of plastically activated grains. As shown in Figure 5.20 on page 80, Cu-30%Zn have fewer active grains than 316L at a given plastic strain amplitude. The plastically inactive grains act as obstacles to type III cracks, which is reflected by the growth rates on Figure 5.30b (page 88). Type III cracks grow slower in Cu-30%Zn than in 316L, and this effect also helps to prolong fatigue life and compensates for the rapid growth of intergranular cracks. Altogether it seems clear, that damage characteristics such as the crack initiation rate, the crack growth rate, crack coalescence and slip activity must all be considered in order to account for the fatigue life in terms of physical mechanisms. This will be dealt with in chapter 6.2.

6 Mechanisms and Modelling

To model the fatigue behaviour of a given material one has to include both cyclic plasticity, damage evolution and fatigue life. This is not an easy task and it is common to confine a model to cover only one of these topics. In this chapter two different models will be presented and used to describe the fatigue behaviour of Cu-15%Zn and Cu-30%Zn.

6.1 Cyclic stress-strain curve

Plastic deformation in crystalline materials occurs by slip, i.e. shear of the crystal lattice in certain directions on certain crystal planes. The relation between the stress/strain applied to a single crystal and the stress/strain resolved on its primary slip plane is given by:

$$\sigma = m \cdot \tau \tag{6.1}$$

$$\varepsilon = \frac{\gamma}{m} \tag{6.2}$$

where m is the orientation factor or the inverse Schmid factor, τ is the resolved shear stress and γ is the resolved shear strain. For polycrystals an effective orientation factor has to be used due to the orientation distribution of the crystal grains, and different plasticity models has been proposed to deal with this problem. The two extreme models are the ones by SACHS (1928) and TAYLOR (1938) and they lead to different effective orientation factors. The former assumes that the individual grains of the polycrystal deform independently by single slip on their most highly stressed slip systems resulting in an effective orientation factor m_S=2.238. The use of the Sachs model was suggested in polycrystalline copper by the observation that the individual surface grains tend to contain only one set of parallel slip bands (THOMPSON *ET AL.*, 1956; RASMUSSEN & PEDERSEN, 1980; MUGHRABI & WANG, 1982) and it was further envisaged when similar observations were made for bulk grains (WINTER *ET AL.*, 1981). Presumably this single slip behaviour is assumed to be caused by high latent hardening (PEDERSEN *ET AL.*, 1982), i.e. a hardening of the secondary slip systems, and in copper it is dominating up to $\varepsilon_{pa} \approx 10^{-3}$ (RASMUSSEN & PEDERSEN, 1979). The Taylor model, requiring multiple slip in the individual grains, does not provide a realistic description of the polycrystal CSS curve and it cannot account for the cyclic saturation stress of copper polycrystals (PEDERSEN *ET AL.*, 1982).

6.1.1 Self-consistent Sachs-Eshelby model

PEDERSEN *ET AL.* (1982) developed a Sachs model for fatigue employing the “self-consistent approximation” suggested by KRÖNER (1961) and the theory of ESHELBY (1957) in attempt to describe the CSS behaviour of polycrystals. This model will be referred to as the self-consistent Sachs-Eshelby model or the SCSE model. It is based on a yield criterion, which identifies the applied stress, σ, with the cyclic saturation stress, σ_{sat}, by assuming that for $\sigma=\sigma_{sat}$ the grains will be at the point of plastic flow when:

$$\tau = \tau_{plat} \tag{6.3}$$

where τ_{plat} is the plateau stress measured for a single crystal. In copper the single crystal CSS plateau is correlated with the formation of PSBs and in brass it is likely to be related to the formation of ISBs (cf. chapter 5.3). Equation 6.3 thus constitutes an analogy between plastic flow and the formation of a PSB/ISB.

The limiting factor of the Sachs model is the assumption of single slip in the individual grains, which gives rise to compatibility problems. The grains deform in only one direction, which is different for each grain, and thus they cannot fit together at the grain boundaries (see Figure 6.1b).

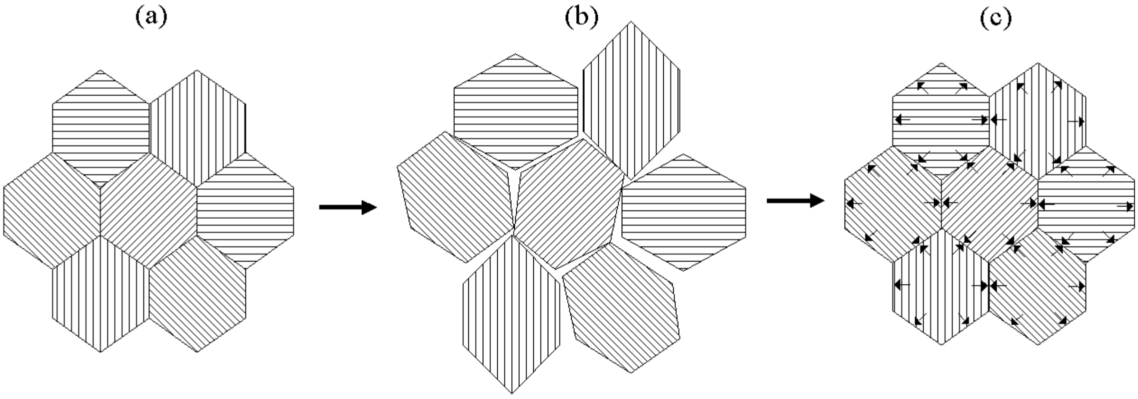

Figure 6.1 In a polycrystal (a) the single slip assumption of the Sachs model gives rise to compatibility problems at the grain boundaries (b). For small plastic strain amplitudes compatibility can be obtained by elastic accommodation. This, however, leads to intergranular stresses (c).

In the SCSE model the grains are assumed to be matched by elastic deformation. This is known as elastic accommodation which leads to intergranular stresses. Therefore the saturation stress of a polycrystal can be expressed as:

$$\sigma_{sat} = \sigma_{plat} + \sigma_i \qquad (6.4)$$

where σ_{plat} is the stress obtained by simply combining Equations 6.1 and 6.3, i.e. the stress that would be expected in the plateau range if no intergranular stresses were present. By using the principle of ‘inclusion stress’ (ESHELBY, 1957) the intergranular stress, σ_i, was estimated by PEDERSEN *ET AL.* (1982). Representing the whole aggregate of grains by a single grain with the effective orientation factor $m=m_S$, they obtained the following relations:

$$\sigma_{plat} = m_S \cdot \tau_{plat} \qquad (6.5)$$

$$\sigma_i = \left(m_S^2 - 3\right) \cdot \mu \cdot \Gamma \cdot \varepsilon_{pa} \qquad (6.6)$$

where μ is the elastic shear modulus and Γ is the so-called accommodation factor. Γ indicates the ability of the surrounding grains to accommodate the deformation of the representative grain. For a representative spherical grain ESHELBY (1957) provides:

$$\Gamma = \frac{7 - 5 \cdot \nu}{15 \cdot (1 - \nu)} \qquad (6.7)$$

where ν is Poisson's ratio. Inserting the Sachs factor, m_S=2.238, Equation 6.4 can be expressed in the following way:

$$\sigma_{sat} = 2.24 \cdot \tau_{plat} + 2.02 \cdot \mu \cdot \Gamma \cdot \varepsilon_{pa} \tag{6.8}$$

Following the scheme of Budiansky & Wu (1962) the relation between σ_{sat} and ε_{pa} was also derived using many representative grains instead of a single representative grain (Pedersen *et al.*, 1982). The resulting expression differs slightly from Equation 6.8:

$$\sigma_{sat} = 2.19 \cdot \tau_{plat} + 1.85 \cdot \mu \cdot \Gamma \cdot \varepsilon_{pa} \tag{6.9}$$

The important result of Equations 6.8 and 6.9 is the prediction of a linear grain-size independent CSS curve with a texture-dependent upward slope. In the following Equation 6.9 will be used, as it provides the most realistic predictions based on many representative grains. The model requires information of the CSS plateau stress measured for single crystals, τ_{plat}. In Figure 6.2 the available CSS data are plotted for single crystals of copper, Cu-22%Zn and Cu-30%Zn.

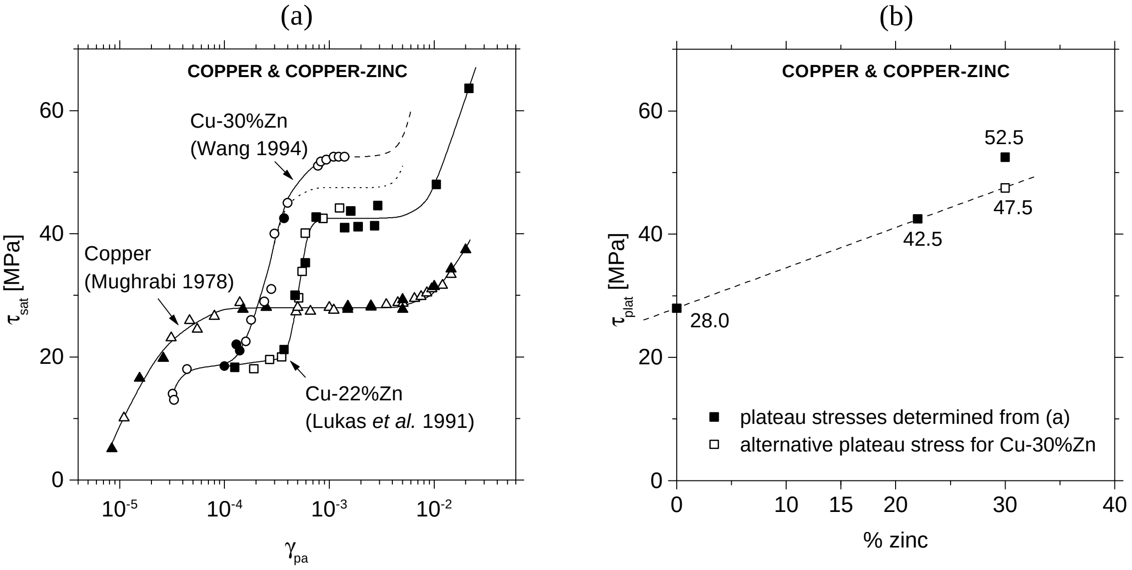

Figure 6.2 (a) CSS curves for single crystals of copper, Cu-22%Zn and Cu-30%Zn. The solid symbols indicate single amplitude tests while the open symbols indicate ascending step tests. (b) The plateau stress for Cu-15%Zn can be estimated by assuming a linear relation between the plateau stress and the zinc content. This also suggests an alternative plateau stress for Cu-30%Zn.

The single crystal CSS curves for copper and Cu-22%Zn are determined by both single amplitude tests and ascending step tests, while for Cu-30%Zn it is determined mainly by ascending step test of one single crystal. Lukás & Klesnil (1973) found that in copper (wavy slip) the saturation stress amplitude is independent of the strain history, i.e. the saturation stress is a unique function of the applied strain amplitude independent of the preceding levels of strain amplitude. However, for Cu-31%Zn they found, that the stress amplitude is always higher when preceding levels of strain amplitudes have been applied. This suggests that the saturation stress amplitudes found in ascending step tests on Cu-30%Zn would be expected to be higher than those found in single amplitude tests. Assuming a linear relation between the plateau stress, τ_{plat}, and the zinc content it is therefore suggested, that τ_b for Cu-30%Zn should be 47.5 MPa instead of 52.5. This is indicated on Figure 6.2b and the possible CSS curve is sketched on Figure 6.2a (the dotted curve). The linear relation between the plateau stress, τ_b, and zinc content can be expressed as follows:

$$\tau_{plat} = 28 + 0.65 \cdot \%\text{zinc} \tag{6.10}$$

From this relation the plateau stress for Cu-15%Zn can be estimated to 37.8 MPa. The following data is therefore available for modelling of the CSS behaviour of polycrystalline Cu-15%Zn and Cu-30%Zn:

*Table 6.1 Available data for modelling of the CSS behaviour of polycrystalline brass. The values marked with * are taken from* SIMMONS *&* WANG *(1971).*

Material	ν^*	μ [MPa]	τ_{plat} [MPa]
Cu-15%Zn	0,343	44676	37,8
Cu-30%Zn	0,343	40953	47,5

The shear moduli, μ, are calculated using the measured moduli of elasticity, E (see Table 3.2 on page 33). Insertion of these data into Equations 6.7 and 6.9 leads to the following expressions:

$$\sigma_{sat} = \begin{cases} 83 + 44323 \cdot \varepsilon_{pa} & \text{for Cu} - 15\%\text{Zn} \\ 104 + 40630 \cdot \varepsilon_{pa} & \text{for Cu} - 30\%\text{Zn} \end{cases} \tag{6.11}$$

which constitute the essence of the SCSE model.

6.1.2 Model predictions

For texture-free copper polycrystals the SCSE model can account for the CSS behaviour up to $\varepsilon_{pa} \approx 10^{-3}$ (PEDERSEN *ET AL.*, 1982). Addition of zinc to copper increases the tendency toward slip planarity and would be expected to increase the range of validity of the model. In Figure 6.3 the predictions of the SCSE model are compared with the experimental observations in Cu-15%Zn and Cu-30%Zn. This comparison reveal, that the range of validity of the SCSE model is increased with increasing zinc content. The agreement between model and experiments is within 10-15% and it extends to $\varepsilon_{pa} \approx 5 \cdot 10^{-3}$ for Cu-30%Zn.

Apart from predicting the CSS behaviour in the near-plateau range the SCSE model also provides estimates of the intergranular stresses, σ_i, which contributes to the effective back stresses, σ_b^{eff}, as discussed in chapter 4.2. In Figure 6.4 the estimated σ_i are compared to σ_b^{eff} which are measured using the Cottrell scheme (cf. Figure 4.4 and Figure 4.5 on page 49). The three regimes indicated on the figure correspond to the ones mentioned in chapter 4.3 (see Figure 4.11 on page 52). The intergranular stresses are negligible in regime I, but they become increasingly more important in regime II. The transition from regime II to III (at $\varepsilon_{pa} \approx 10^{-3}$) corresponds to the point where the intergranular stress contribution becomes the larger part of the effective back stress. The saturation stresses in regime III thus seems to be exceedingly controlled by the intergranular stresses.

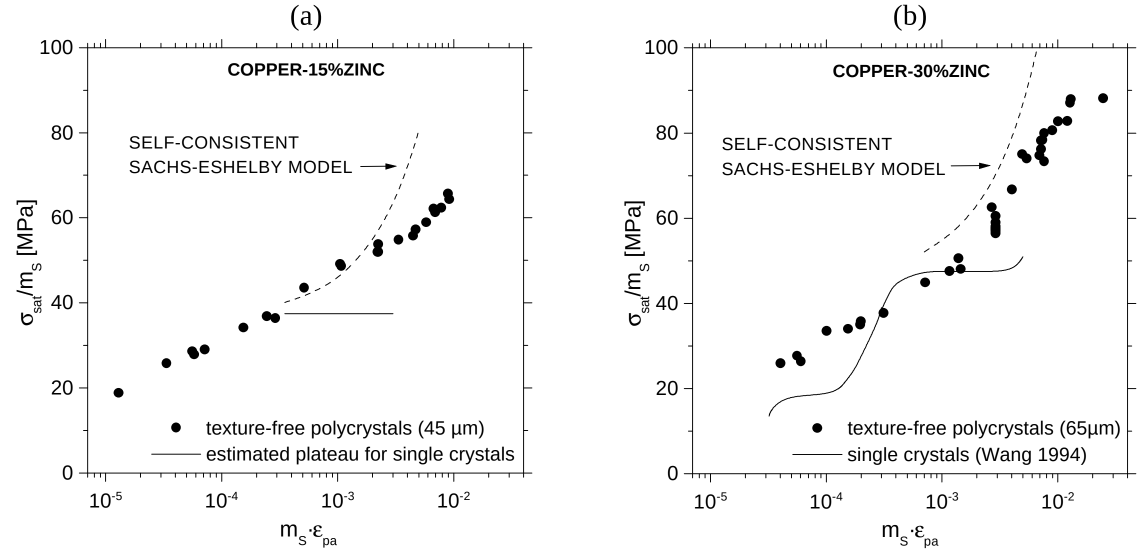

Figure 6.3 (a) In Cu-15%Zn the SCSE model can account for the CSS behaviour up to e_{pa}»2x10^{-3}. (b) In Cu-30%Zn a good agreement is established up to e_{pa}»5x10^{-3}. The model predictions are shown with dashed lines, and they are not straight lines in these semi-logarithmic plots.

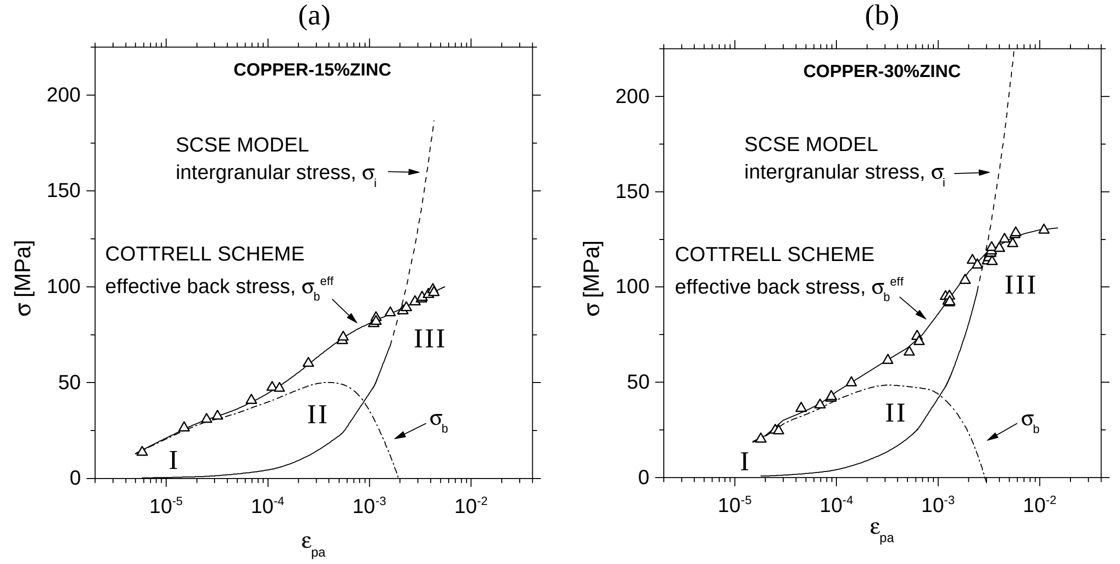

Figure 6.4 The effective back stresses, s_b^{eff}, can be divided into contributions from intergranular stresses, s_i, and intragranular stresses, s_b, by using the predictions of the SCSE model. s_b is simply the difference between the measured s_b^{eff} and the predicted s_i. (a) Cu-15%Zn, and (b) Cu-30%Zn.

6.2 Damage evolution and fatigue life

To analyze or, if possible, to predict the failure of machine parts or other structures is one of the main goals of engineering science. Consequently fracture mechanics became one of its leading branches. It was based on the analysis of existing macrocracks larger than a certain critical length. However, this might be too late to prevent failure, especially under conditions of cyclic loading where the growth of macrocracks (Type IV cracks, cf. chapter 5.2.3) involve only the last 5-10% of N_F (BATAILLE & MAGNIN, 1994). Therefore, the question regarding the precursory state, i.e. the evolution of damage before macrocracks form, was then posed, and a new branch of engineering science developed: damage mechanics.

Damage mechanics is based on the so-called damage parameter, D, defined in the one-dimensional case as (LEMAITRE, 1992):

$$D = \frac{S_D}{S} \tag{6.12}$$

where S_D is the area of damaged material on a plane with the area S as illustrated in Figure 6.5.

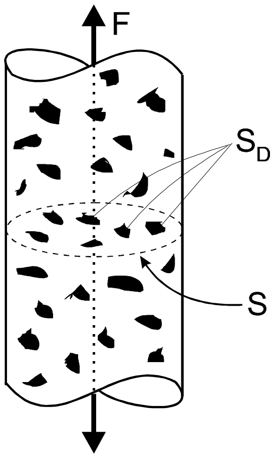

Figure 6.5 One-dimensional damaged element in a specimen loaded by the force F. The area of damaged material, S_D, is indicated on a plane with the area S. Redrawn from LEMAITRE (1992).

Based on the so-called *Strain Equivalence Principle* and the *State Kinetic Coupling theory* a set of constitutive equations is derived to characterize damage. The damage evolution, or the rate of damage is given by the following expression (LEMAITRE, 1992):

$$\dot{D} = \begin{cases} \frac{Y}{S}\dot{\varepsilon}_{cum} & \text{if } \varepsilon_{cum} \geq \varepsilon^D_{cum} \\ 0 & \text{if } \varepsilon_{cum} < \varepsilon^D_{cum} \end{cases} \tag{6.13}$$

where Y is the strain energy density release rate, i.e. the energy released by loss of stiffness of the volume in which the damage occurs; S is a material constant, $\dot{\varepsilon}_{cum}$ is the accumulated plastic strain rate, and ε^D_{cum} is a damage threshold below which no damage occurs.

Equation 6.13 describes the damage evolution from the undamaged state (D=0) until a macro crack has formed, corresponding to a critical damage $D=D_c$. It is based on the assumption (or simplification) that damage is homogeneously distributed in the bulk of the material. This is realistic in many cases and damage mechanics is now well developed and widely used in fields where bulk damage is observed, e.g. tensile deformation or creep of ductile metals where the damage process is nucleation and growth of voids. In fatigue of metals and alloys (excluding composite or particle containing materials), however, damage is a near-surface phenomena and far from a homogeneous bulk distribution. In its existing formulation damage mechanics thus seems unsuitable for modelling of fatigue damage (Notwithstanding, damage mechanics is often used when modelling fatigue damage in metals and alloys, see e.g. AKTAA & SCHINKE, 1996 or CHEN *ET AL.*, 1996).

Alternatively, another type of modelling has been suggested by BATAILLE & MAGNIN (1994) in which fatigue damage is considered merely a surface phenomena. It is based on statistical physics and it involves damage mechanisms established from experimental observations of surface cracks which are classified according to surface length and growth behaviour (cf. Figure 5.24 on page 84). A modification of the model, including the problem of grain boundary crack blocking, has recently been suggested by MADELAINE-DUPUICH *ET AL.* (1998). In the following fatigue damage mechanisms will be characterized forming the basis of the modified numerical modelling, which will be described in broad outline. Subsequently simulated results will be compared with the observed microcrack evolution and fatigue life found in chapters 5.2.3 and 4.4, respectively. Parts of the results have been presented elsewhere (CARSTENSEN & PEDERSEN, 1997A).

6.2.1 Damage mechanisms

The physical description of fatigue damage can be divided into a number of parameters which all have to be considered in the simulation in order account for the fatigue life. These are listed in Table 6.2.

Table 6.2 The parameters comprising the physical description of fatigue damage.

Damage parameters
crack initiation rate
crack growth rate(s)
crack growth mode
crack growth barriers
slip activity
crack coalescence
"fracture criterion"

The parameters are all based on the experimental damage observations depicted in chapter 5.2 as well as observations taken from the literature. They will be described in the following:

crack initiation rate

The first fatigue cracks initiate after 5-10% of N_i (MAGNIN *ET AL.*, 1985; BATAILLE & MAGNIN, 1994) thus defining the damage threshold. The fatigue microcracks initiate at a rate which can be determined from the experimentally measured surface crack evolution (see Figure 5.26 on page 86). The initiation rate is simply the initial slope of the type I crack curve.

crack growth rate(s)

Short fatigue cracks grow at rates proportional to the plastic zone size, r_p, ahead of their crack tips (EDWARDS & ZHANG, 1994). However, it is difficult and time consuming to measure r_p and thus a different correlator for fatigue crack growth is preferable. BATAILLE & MAGNIN (1994) showed that a power law dependency existed between the plastic strain amplitude, ε_{pa}, and the short fatigue crack growth rate. This has now been supported by the present measurements on Cu-30%Zn (see formula (6.1) and (6.2) on page 89).

crack growth mode

Fatigue cracks grow crystallographically (type I and II) or mechanically (type III) dependent on their surface length. Crystallographical growth can be either transgranular or intergranular. In Cu-30%Zn intergranular crack growth is dominating but transgranular growth are also observed (cf. Figure 5.21 on page 81). The original model introduced by Bataille & Magnin (1994) has therefore been modified to account for the intergranular crack growth.

crack growth barriers

When transgranular cracks grow they are obstructed by grain boundaries. Zhang & Edwards (1992) found that the growth rate of fatigue short cracks begin to retard when their relatively large plastic zones, not their crack tips, are blocked by grain boundaries. Some cracks are able to pass the grain boundaries while others remain permanently blocked throughout the fatigue life. Typically a crack is temporarily arrested and further propagation occurs only when the stress concentration, due to the pile-up of dislocations in the blocked plastic zone, is of sufficient magnitude to overcome the barrier caused by the misorientation of grains and thus activate a slip source in the next grain (Stroh, 1955). The stress operating on the nearest dislocation source in the neighbouring grain has been given by Navarro & de los Rios (1988):

$$\sigma_{\text{operating}} = \frac{\sigma}{\sqrt{2}\cdot\sqrt{\frac{r_p+r_0}{\ell}}}\left(1-\frac{2\cdot\sigma_f\cdot\cos^{-1} n}{\pi\cdot\sigma}\right)+\sigma_f \tag{6.14}$$

$$n = \frac{\ell}{c} = \Phi\cdot\cos\left(\frac{\pi\cdot\sigma}{2\cdot\sigma_0}\right) \tag{6.15}$$

where σ is the applied stress, σ_f is the friction stress, σ_0 is the cohesive stress in the yield zone, ℓ is half the crack length, c is half the crack length including the plastic zone ($c = \ell + r_p$) and r_0 is the distance to the nearest dislocation source in the next grain (see Figure 6.6).

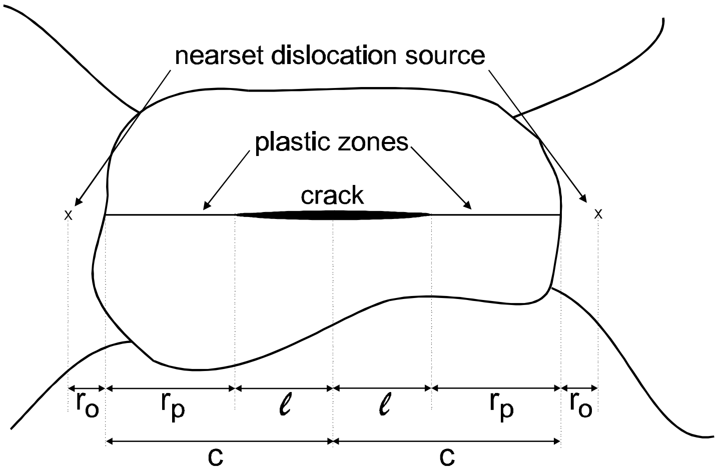

Figure 6.6 Crack and slip band blocked at the grain boundary. The transfer of plastic slip into the neighbouring grain will take place whenever the stress concentration, due to pile-up of dislocations in the plastic zone, is sufficiently high to activate an appropriate dislocation source, situated a distance r_0 ahead of the plastic zone.

Equation 6.15 was first obtained by DUGDALE (1960) for the tensile problem and later by BILBY *ET AL* (1963) for a crack under shear. The parameter Φ was introduced by EDWARDS & ZHANG (1994) in order to correlate the predicted plastic zone size with that experimentally measured by means of selected area electron channeling patterns. They found that $r_p/\ell \cong 0.5$ for type I cracks and thus $n \cong 0.67$ ($r_p/\ell = (1-n)/n$). The magnitude of Φ is thereby determined through correlation.

In metals exhibiting cyclic saturation a unique relation can be established between stress amplitude and plastic strain amplitude, when cycling beyond the damage threshold (N>5-10%N_i). Thus the applied stress, σ, in Equation 6.14 is a function of ε_{pa}. However, in Cu-30%Zn cyclic saturation is absent (cf. chapter 4.2), so the applied stress is a function of both ε_{pa} and the number of cycles, N. This function can be approximated by making simple linear fits on the cyclic hardening/softening curves. In Figure 6.7a this is done for N>5%N_i at different plastic strain amplitudes.

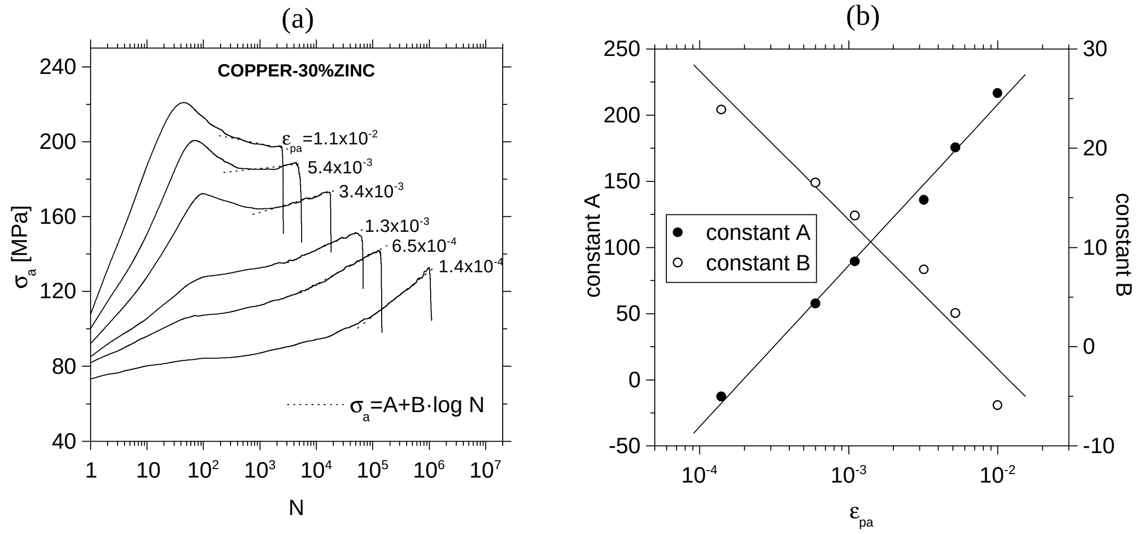

Figure 6.7 (a) Beyond the damage threshold linear fits (s_a=A+B·logN) can be applied to the cyclic hardening/softening curves of Cu-30%Zn, (b) The values of the fitting constants A and B are linear functions of loge$_{pa}$.

The following relation can be established from Figure 6.7a:

σ B N (6 16)

ε_{pa} Figure 6.7b. This can be expressed as:

$$A = A_1 + A_2 \cdot \log \varepsilon_{pa} \tag{6.17}$$

$$B = B_1 + B_2 \cdot \log \varepsilon_{pa} \tag{6.18}$$

The values of A_1, A_2, B_1 and B_2 are determined to be 452, 122, -32 and -15 respectively. Thus Equation 6.16 can be written as:

$$\sigma_a = 452 + 122 \cdot \log \varepsilon_{pa} - 32 \cdot \log N - 15 \cdot \log \varepsilon_{pa} \cdot \log N \tag{6.19}$$

This equation provides an approximate value of the applied stress (amplitude) to be inserted in Equations 6.14 and 6.15 for the calculation of the stress operating on the nearest dislocation source. The activation of such a dislocation source requires the attainment of a critical stress $\sigma_{critical}$, either to bow out a dislocation segment (Frank-Read source) or to unlock pinned dislocations. The slip plane of the source will not, in general, lie in the plane of maximum shear stress, therefore the critical condition of activation of a source in terms of stress is written as (ARMSTRONG *ET AL.*, *1962)*:

$$\sigma_{activation} = \frac{1}{2} \cdot m \cdot \sigma_{critical} \qquad (6.20)$$

where m is the orientation factor which resolves the applied stress onto the slip plane of the source. The critical stress, $\sigma_{critical}$, corresponds to the onset of first yield (see Table 3.2 on page 33). A crack approaching a grain boundary will thus be able to pass into the neighbouring grain if the operating stress (Equation 6.14) exceeds the activation stress (Equation 6.20). However, temporary arrest is often observed before the crack can pass the grain boundary (ZHANG & EDWARDS, 1992). This means that the operating stress is less than the activation stress when the plastic zone meets the grain boundary. With continued cycling more dislocations pile up in the blocked plastic zone leading to a stress accumulation. Eventually the operating stress exceeds the activation stress and the crack is able to pass the barrier. This stress accumulation is not included in Equation 6.14, but it corresponds to an increase in the cohesive stress, σ_0, in the yield zone. σ_0 is generally taken as twice the yield stress for cyclic loading, but BROWN (1988) argued that twice the tensile strength, σ_u, should be used instead, as cohesive stress represents flow stress at the crack tip. For strain-hardening materials flow stress will relate to tensile strength (TOMKINS, 1968), and provide the correct upper-bound solution for collapse load. Therefore it is suggested that the stress accumulation corresponds to an increase in σ_0 from $2 \cdot \sigma_y$ to $2 \cdot \sigma_u$ over a certain number of cycles, $N_{blocked}$. This number of cycles depends on the imposed plastic strain amplitude, but no experimental data is available to determine the relation. Instead simulated fatigue lives were compared to those measured experimentally, and by trial and error the following relation was established:

$$N_{blocked} = 100 \cdot \left(\varepsilon_{pa}\right)^{-0.25} \qquad (6.21)$$

The present investigations (see chapter 6.2.3) show that Equation 6.21 apply to both Cu-30%Zn and 316L.

The grain boundaries were found to act as crack growth barriers for transgranular cracks with surface length less than 5 grain sizes in an aluminium alloy (ZHANG & EDWARDS, 1992). This approximately corresponds to type I and type II cracks, and thus it is suggested that the mechanically growing type III cracks are not affected by the grain boundaries. Also, in the present study of Cu-30%Zn no observations were made on intergranular cracks blocked at grain joints, whereas many observations were made on blocked transgranular cracks. This indicates that, compared to grain boundaries, grain joints are less efficient crack growth barriers, and for simplicity it is assumed, that intergranular cracks are not affected by grain joints. Thus Equations. 6.14-6.21 are used only to characterize the growth of transgranular cracks of type I and II.

slip activity

When Cu-30%Zn is cyclically deformed at plastic strain amplitudes below a certain limit not all grains contain slip bands, i.e. some grains are slip inactive, even when cycled to failure (see Figure 5.20 on page 80). KITAGAWA *ET AL.* (1979) suggested that the slip activity P, i.e. the ratio between the number of slip active grains and the total number of grains, is proportional to the imposed plastic strain amplitude. This apply to both Cu-30%Zn and 316L steel, cf. Equation 6.1 on page 80. Cracks can only initiate in/at grains that are plastically active and therefore the slip activity affects the crack initiation rate and the crack density (cf. chapter 5.3).

crack coalescence

Crack coalescence is important for the fatigue damage accumulation process (see e.g. FEDELICH *ET AL.*, 1996). Experimental and statistical investigations of fatigue surface cracks (OCHI *ET AL.*, 1985) reveal that the coalescence of two cracks depend on the distance between their facing tips, h_t, and on their total surface length:

$$h_t = H \cdot (L_1 + L_2) \tag{6.22}$$

where L_1 and L_2 are the surface lengths of the two cracks. If two cracks are closer than the fraction H of their total surface length, they are bound to coalesce. OCHI *ET AL.* (1985) found That H varies for materials with different slip character. For two wavy slip materials (Cu and a ferritic steel) the value of H was found to be 0.16, whereas for a planar slip material (304L austenitic stainless steel) it was 0.11. To a first approximation it is assumed, that Equation 6.22 apply to fatigue of all metals and alloys, and that the value H=0.11 apply to materials with planar slip.

"fracture criterion"

Fatigue life, N_i, is defined as the number of cycles to form a type IV crack, corresponding to a fast decrease in stress amplitude (cf. Figure 4.13 on page 54). This constitutes the "fracture criterion" in terms of a critical crack length (the length of a type IV crack).

6.2.2 Monte Carlo type modelling

Together the above described damage mechanisms form the basis of a numerical damage model (for details see BATAILLE & MAGNIN, 1994 and MADELAINE-DUPUICH *ET AL.*, 1998). The surface crack evolution is simulated on polycrystalline texture-free metals fatigued at constant plastic strain amplitudes using a simplified grain structure (see Figure 6.8). The original model has been further developed to account for the pronounced intergranular crack growth observed in polycrystalline Cu-30%Zn.

Quasi-hexagons correspond to surface grains which are 36-fold segmented, as shown on Figure 6.8. Each grain is singled by its orientation in terms of a random value of the angle between the surface emergence of slip bands and the loading axis. By this a texture-free grain structure is generated. The mesh used in the simulation consists of 150 grains corresponding to a surface area of approximately 0.5 mm^2 when the average grain size is 65 µm.

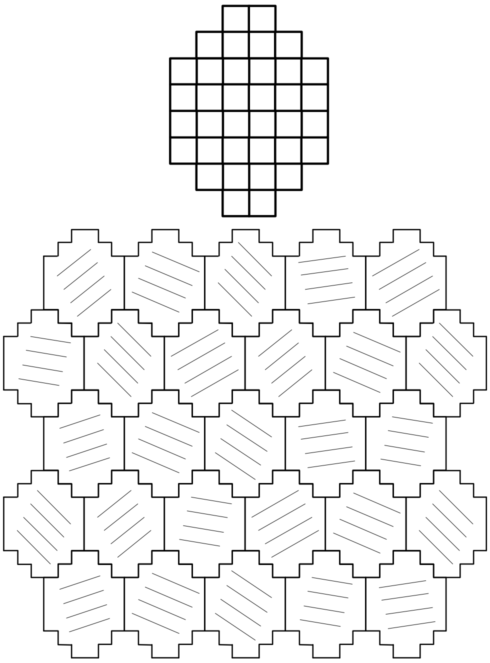

Figure 6.8 A simplified grain structure is chosen for the simulation. The grains consists of 36 “unit cells” forming a quasi-hexagon. In each grain the orientation with respect to the loading axis (which is vertical on this figure) is random to make the material texture-free.

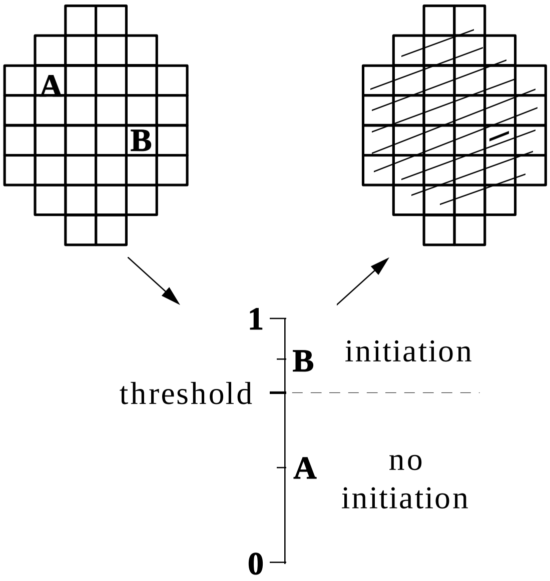

Figure 6.9 The principles of transgranular crack initiation in a Monte Carlo type simulation. For each unit cell a random number is generated and compared to an initiation threshold. If the number is higher than the threshold value (as in unit cell B), a short crack will cross the unit cell.

The high crack densities in low cycle fatigue favor statistical aspects of the fatigue damage accumulation. Both nucleation and propagation can be considered as random processes which calls for a Monte Carlo type simulation. The principles are sketched in Figure 6.9 with transgranular crack initiation as an example. In a binary-type sampling each unit cell is continuously sampled for crack initiation. A random number is generated and compared to an initiation threshold. If the random number is higher than the threshold value, a short crack will cross the unit cell. The threshold value is determined from the slope of the experimentally observed type I crack evolution (cf. chapter 0 on page 101). The same sampling procedure is used for the crack propagation and the propagation threshold is simply the operating stress, $\sigma_{operating}$, divided by the activation stress, $\sigma_{activation}$ (see Equations 6.14 and 6.20) when the cracks meet a grain boundary. The cracks grow according to the above described mechanisms and for simplicity the intergranular cracks are assumed to initiate at the grain joints and grow, like type III cracks, uninfluenced by the grain boundaries. For crack coalescence the criterion suggested by OCHI *ET AL*. (1985) is used (Equation 6.22).

The simulation procedure is as follows: each unit cell is sampled for initiation, propagation and coalescence. One simulation increment corresponds to running over all unit cells in the mesh. After each increment the cracks are grouped according to their surface length to reveal the evolution of type I, II and III cracks. An average incremental crack growth, ΔL_{inc}, can be calculated, and from the experimentally observed crack growth rates (Equations 5.2 and 5.3 on page 89) it is possible to correlate ΔL_{inc} with an equivalent increment in number of cycles, ΔN_{inc}:

Type I: $$\Delta N_{inc}^{I} = 0.71 \cdot \Delta L_{inc}^{I} \cdot \left(\varepsilon_{pa}\right)^{-0.69} \tag{6.23}$$

Type III: $$\Delta N_{inc}^{III} = 2.5 \cdot \frac{\Delta L_{inc}^{III}}{L} \cdot \left(\varepsilon_{pa}\right)^{-1.4} \tag{6.24}$$

where L is the average crack length. Equation 6.23 is used until a few type III cracks has developed and after this Equation 6.24 is used. This is due to the localization of the deformation in the type III cracks. However, this calculation does not include the problem of crack blocking at grain boundaries. Consider at situation with only one crack growing. If this crack is blocked by a grain boundary, the number of cycles will still increase. Therefore we need an additional increment in cycle number, ΔN_{inc}^{add}, which is determined by trial and error (cf. Equation 6.21 on page 104):

$$\Delta N_{inc}^{add} = 100 \cdot \frac{n_{blocked}}{n_{total}} \cdot \left(\varepsilon_{pa}\right)^{-0.25} \tag{6.25}$$

where $n_{blocked}$ is the number of blocked cracks and n_{total} the total number of cracks in the mesh. This increment in cycle number adds to the increment found by Equation 6.23 and it can be thought of as being a semi-adjustable parameter. It is adjusted at one plastic strain amplitude and after that kept constant for simulations at other plastic strain amplitudes.

The described procedure is repeated until the longest crack exceeds the fatal crack length and become a type IV crack. The number of cycles reached at this point (i.e. $\Sigma\Delta N_{inc}$) determines the fatigue life, N_i. A number of simulations, corresponding to a larger surface area, is runned at each plastic strain amplitude to account for the random nature of fatigue crack growth.

6.2.3 Simulated results

The model accounts for the evolution of the three different crack types. In Figure 6.10 the simulated crack evolution is shown for Cu-30%Zn fatigued at ε_{pa}=1.1x10^{-3}. It is the result of 30 simulations and the average surface crack densities are shown and compared to those measured experimentally (see Figure 5.26 on page 86). For clarity the standard deviations have been excluded.

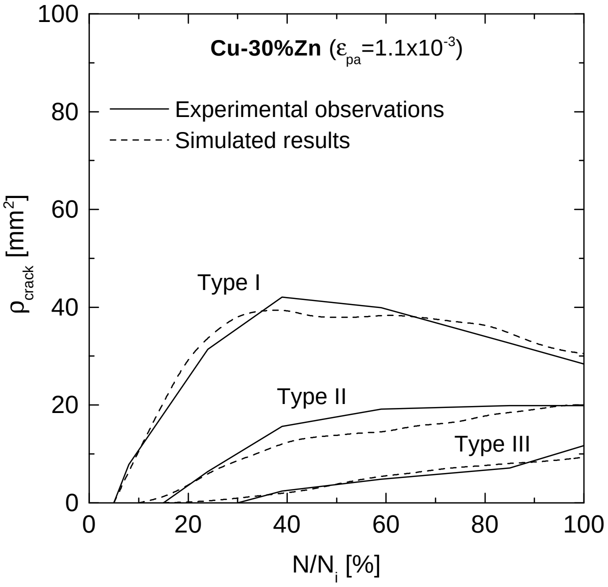

Figure 6.10 Result of 30 fatigue damage simulations on Cu-30%Zn. The average surface crack density is shown vs. reduced life N/N$_i$ for cyclic deformation at e_{pa}=1.1x10^{-3}. The full and dashed lines indicate experimental and simulated results, respectively.

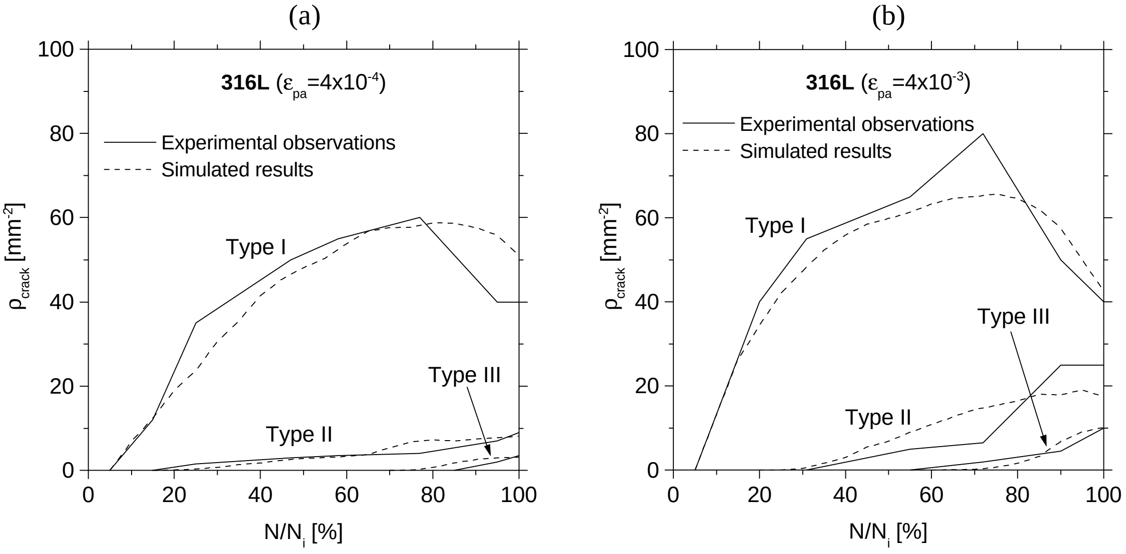
(a)

(b)

Figure 6.11 Results of 30 fatigue damage simulations on 316L steel. The average surface crack density is shown vs. reduced life N/N$_i$ for cyclic deformation at (a) e_{pa}=4x10^{-4}, and (b) e_{pa}=4x10^{-3}. The full and dashed lines indicate experimental and simulated results, respectively. The experimental results are taken from BATAILLE & MAGNIN (1994).

The dashed lines on Figure 6.10 are the simulated results and they agree quite well with the experimental observations. To further judge the efficacy of the model, fatigue damage simulations were made for 316L steel cycled at two different plastic strain amplitudes. In Figure 6.11 the results are compared to experimental observations made by BATAILLE & MAGNIN (1994). From these figures it seems reasonable to state, that the model is capable of simulating the fatigue damage evolution on different materials and at different plastic strain amplitudes. Furthermore, the model provides estimates of fatigue lives which are in close agreement with experimental observations. This is demonstrated on Figure 6.12.

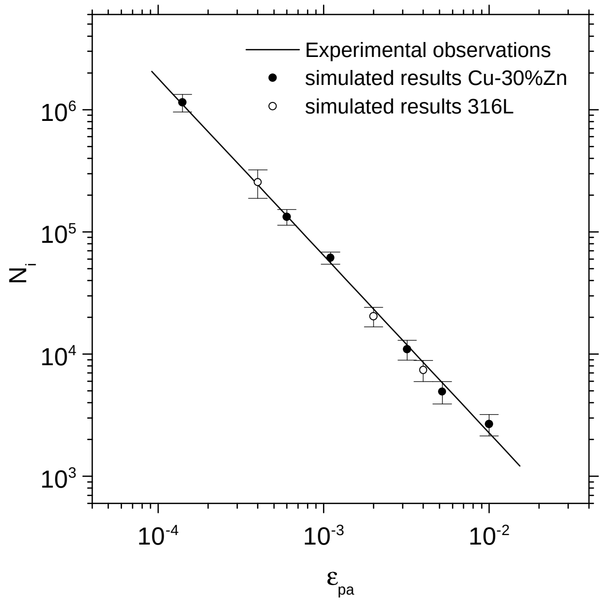

Figure 6.12 Simulated fatigue lives for Cu-30%Zn and 316L steel cycled at different plastic strain amplitudes. The standard deviations correspond to 30 simulations at each amplitude, and the full line is the experimentally measured fatigue life curve.

6.3 Discussion

The fatigue behaviour of polycrystalline brass has been modeled using two simple models, which are both based on observed fatigue mechanisms. The models are capable of predicting the cyclic stress-strain behaviour and fatigue life of the investigated alloys. More important, the models help to understand the importance of different mechanisms, and they provide tools to correct or improve suggested mechanisms.

As discussed in chapter 4.5 the construction of a CSS curve for brass is controversial due to the absence of cyclic saturation. The CSS curve is not as well-defined as in copper, which obviously complicates the modelling of this curve. Nonetheless, the SCSE model has been applied to brass in order to account for the CSS curve. The Sachs type single slip behaviour observed in copper and brass is the main mechanism on which the SCSE model is based. This mechanism is more pronounced in brass and thus the range of validity of the model is expected to be increased with the addition of zinc to copper. Figure 6.3 on page 99 shows that these expectations are fulfilled and that the range of validity extends to $\varepsilon_{pa} \approx 5\text{x}10^{-3}$ for Cu-30%Zn, as compared to $\sim 10^{-3}$ for copper. The agreement between model and experiments are good, especially when considering the controversial construction of the CSS curve.

Another important benefit from the SCSE model is, that it provides an estimate of the intergranular stresses, σ_i. The intergranular stresses, σ_i, contribute to the effective back stresses, σ_b^{eff}, and in Figure 6.4 on page 99 the predicted σ_i are compared with σ_b^{eff} measured using the Cottrell scheme. This comparison shows, that the intergranular stresses becomes the dominating part of σ_b^{eff} in regime III. However, in this regime secondary slip tends to relax the intergranular stresses, and this relaxation mechanism is not included in the model. The consequence of this is an overestimation of σ_i, as shown on Figure 6.4. In the plateau range σ_b is expected to display a plateau coincident with the plateau observed on the CSS curve for single crystals (see Figure 6.2 on page 97), but due to the overestimated σ_i this is not the case in Figure 6.4, where σ_b is calculated as (σ_b^{eff}- σ_i). If this is corrected, i.e. by holding σ_b constant in the plateau range and calculating σ_i as (σ_b^{eff}- σ_b), the evolution of σ_i and σ_b will be as shown on Figure 6.13.

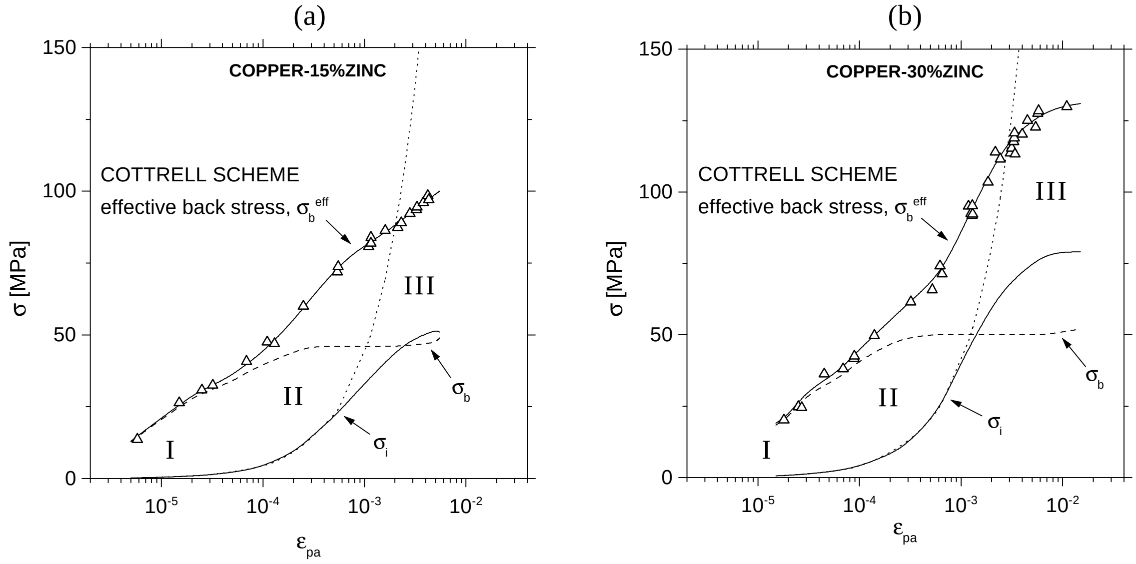

Figure 6.13 By using the effective back stresses, s_b^{eff}, measured by the Cottrell scheme, it is possible to account for the secondary slip in regime III and thus to correct the overestimation of the intergranular stresses, s_i. This is done by assuming that the intragranular stresses, s_b, are constant in the plateau range so that s_i can be calculated as (s_b^{eff}-s_b). The dotted lines show the predictions of the SCSE model.

This is probably a more realistic picture of σ_i and σ_b, and it shows the relaxation of σ_i in regime III. It also indicates, that the intergranular stresses are relatively more important in Cu-30%Zn than in Cu-15%Zn, as would be expected due to the more pronounced Sachs type behaviour. Figure 6.13 suggests, that the SCSE model should fail to predict the CSS behaviour near the transition to from regime II to regime III ($\varepsilon_{pa} \approx 10^{-3}$), where the intergranular stresses are relaxed by secondary slip. Nevertheless, Figure 6.3 shows that the range of validity of the model extends into regime III, which can be explained by the increase of friction stresses accompanying the relaxation of σ_i (cf. Figure 4.12 on page 53). This is a result of the pronounced Sachs type behaviour associated with high latent hardening, which makes it difficult to operate the secondary slip systems and thus induce an increase of friction stresses. So even though the SCSE model cannot quantitatively predict the intergranular stresses, it provides estimates which are qualitatively correct. The model predicts a linear increase of σ_i with ε_{pa} in agreement with the observations of intergranular cracks which become increasingly more pronounced with increasing ε_{pa} (cf. chapter 5.2.2). The predicted increase of σ_i can also explain the absence of a plateau on the polycrystal CSS curve, which is observed in both copper and brass (cf. chapter 2 and 4.2).

The most important result of the SCSE model is perhaps, that it predicts a linear grain-size independent CSS curve with a texture-dependent upward slope. This is consistent with experimental observations made on copper (e.g. PEDERSEN, 1981; MULVAD, 1983; LUKÁS & KUNZ, 1987; POLÁK *ET AL.*, 1991; LLANES *ET AL.*, 1993; PERALTA *ET AL.*, 1995). This also supports the discussion in chapter 4.4, where unexpected low cyclic stress amplitudes, observed in Cu-30%Zn by POLÁK *ET AL.* (1974), were suggested to be due to the presence of a soft texture. The SCSE model therefore seems to qualitatively predict the influence of grain size and texture on the CSS behaviour of polycrystalline Sachs-type deforming metals.

The SCSE model is a simple model, but it proves to be a useful tool for making qualitative (and to some extent quantitative) predictions of the CSS behaviour. The second model used in this work is also a simple model, in which fatigue damage is reduced to a 1D problem. This model considers the statistical aspects of low cycle fatigue damage in using Monte Carlo type principles for the simulation of crack initiation and growth. Fatigue damage mechanisms, established from experimental observations, form the basis of the model, which is able to account for the experimentally observed damage evolution on specimens fatigued at constant plastic strain amplitude (Figure 6.10 and Figure 6.11 on page 108). It also provides estimates of fatigue lives which are in close agreement with experimental observations (Figure 6.12 on page 109). The model includes only one adjustable parameter (Equation 6.21 on page 104), which can be thought of as a ‘waiting time’ for transgranular cracks blocked at grain boundaries. As mentioned, this parameter is semi-adjustable, because it is adjusted at one plastic strain amplitude and after that kept constant for simulations at other plastic strain amplitudes. The need for this parameter is due to the fact that the mechanism of grain boundary crack blocking is not well understood. However it turns out, that the same parameter can be used for simulations of both Cu-30%Zn and 316L. This implies, that the parameter is a phenomenological parameter, which is identical for all materials. More investigations of different materials is needed to confirm this suggestion.

The experimental work needed to establish the different fatigue mechanisms is time consuming, even though all observations is confined to the surface of fatigued specimens. Especially the measurements of crack growth rates are encumbered with a considerable amount of effort. However, the power law proportionality between growth rates and plastic strain amplitudes found in the present study (see Equations 5.2 and 5.3 on page 89), is easier to establish than e.g. the proportionality between growth rates and plastic zone sizes found by EDWARDS & ZHANG (1994). By investigating different materials it will be possible to establish fatigue mechanisms which are more general. Eventually, this will reduce the amount of experimental work needed to use the model on a specific material.

One objection against the model is its neglection of the 2D nature of fatigue cracks. The model does not consider bulk propagation of cracks even though it is obvious that fatigue failure is coupled with cracks propagating into the bulk. BASINSKI & BASINSKI (1984; 1985B) used a so-called ‘sharp-corner’ technique to study bulk propagation of cracks in PSBs of copper single crystals. Their results are shown in Figure 6.14.

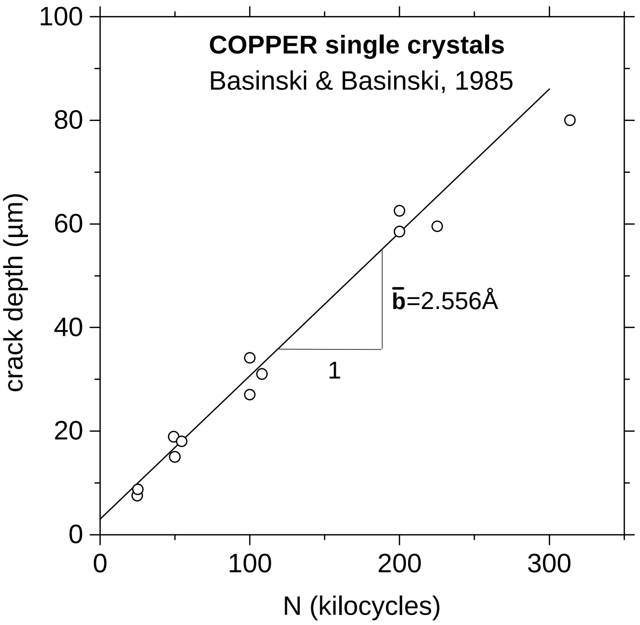

Figure 6.14 Depth of the deepest crack measured using the sharp-corner technique on sections from copper crystals fatigued at $e_{pa}=10^{-3}$, as a function of numbers of cycles (BASINSKI & BASINSKI, 1985B).

They observed that the depth of the deepest crack increased linearly at a rate of the order of one Burgers vector per cycle. This monotonous crack growth suggests that it proceeds by operation of a fundamental mechanism, for example the classical type proposed by MOTT (1958). Recent studies of fatigue short cracks using confocal scanning laser microscopy (VARVANI-FARAHANI ET AL., 1996) indicate, that fatigue short cracks have semi-elliptical shapes and that their shape factor (depth to length ratio) remains constant, and equal to 0.42, in a wide range of surface lengths (up to 1000 µm). These observations clearly demonstrate, that there is a direct relation between the surface length and crack depth of fatigue short cracks.

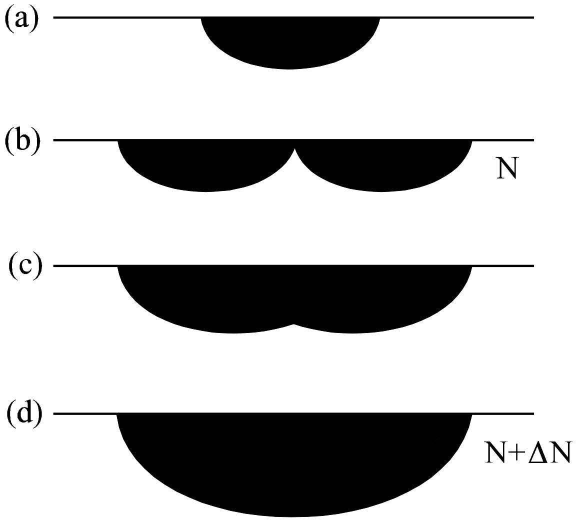

Figure 6.15 When short fatigue cracks grow their semi-elliptical shape seems to remain constant (a). If two cracks coalesce, the resulting crack will not be a semi-ellipse (b), and therefore a certain number of cycles, DN, are needed to regain the semi-elliptical shape (c and d). This means that after coalescence the growth of the crack is retarded for DN cycles.

The transition from surface-controlled to bulk-controlled propagation appears to be confined to the growth of the fatal crack (type IV), and thus the 1D simplification can be justified for all cracks considered in the model. However recently STOLARZ (1997) argued, that the 1D surface crack model tends to overestimate the influence of crack coalescence. The reason for this is due to the coalescence mechanism depicted in Figure 6.15. This mechanism predicts a retardation of the crack growth after coalescence, resembling the ‘waiting time’ introduced in the model to account for the blocking of transgranular cracks at grain boundaries. A similar waiting time could therefore be introduced to account for the proposed mechanism of coalescence. Without this waiting time, the model predictions, however, agrees quite well with the experimental fatigue lives, as shown of Figure 6.12 on page 109. This could be interpreted as if the coalescence waiting time had no significant influence on fatigue life. However, it is more likely, that the coalescence waiting time is somewhat included in the waiting time for grain boundary crack blocking, as these mechanisms are qualitatively the same. It is thus suggested to introduce the coalescence waiting time in the model, which will result in two semi-adjustable parameters similar to Equation 6.21. This wasn’t done in the present study, because STOLARZ’s arguments appeared while this thesis was in the process of being written.

7 Conclusions

The mechanisms of slip mode modification and damage in plastic strain controlled fatigue were studied with polycrystalline brass as a model system. The addition of zinc to copper changes the slip mode from wavy slip to planar slip and the present results show that this leads to an improvement of the fatigue resistance. The mechanisms responsible for this increase were investigated, and a fatigue behaviour remarkably different from that of copper was revealed. The following specific conclusions can be made:

Absence of saturation. While copper displays a prominent stage of cyclic saturation, characterized by constant stress amplitudes for several hundred thousand cycles, the present experiments demonstrates for the first time that cyclic saturation is absent in plastic strain controlled fatigue of brass. This obviously complicates the construction of a cyclic stress-strain (CSS) curve and it complicates the comparison with copper. This complication was overcome in the present study by using the $(d\sigma_a/dN)_{min}$ locus in the construction of the CSS curve for polycrystalline brass.

Sachs deformation. The combined effects of polycrystallinity and slip planarity were studied by electron- and optical surface microscopy of fatigued brass. These studies show that individual grains tend to deform on a single slip system, and they demonstrate clearly that such 'Sachs type' deformation behaviour is more pronounced in brass than in copper. The self-consistent Sachs-Eshelby (SCSE) model was applied to describe the single slip behaviour and associated intergranular stresses, and it was found to account for the CSS curve of brass within 10-15% in the single slip domain, which extends to a plastic strain amplitude of ~$5\text{x}10^{-3}$ in Cu-30%Zn, as opposed to $1\text{x}10^{-3}$ in copper.

Inter/intragranular stresses. The plastic strain controlled cyclic deformation of polycrystalline brass reveals successive stages of primary hardening, softening and secondary hardening. An analysis of this behaviour, based on the Cottrell scheme, implies that the primary hardening and softening is due mainly to changes of the effective back stresses (intergranular stresses plus intragranular back stresses), while a continued increase of friction stresses apparently accounts for the secondary hardening. Based on the predictions of the SCSE model the hardening is suggested to be mainly due to an increase of the intergranular stresses.

Mechanisms of softening. The structural evolution in plastic strain controlled fatigue of polycrystalline Cu-30%Zn was investigated by transmission electron microscopy to account for the observed hardening/softening behaviour. These investigations show, that extended dipole arrays form during primary hardening, apparently by a cross-slip mechanism. The dipole arrays first form on the "softest" slip planes, i.e. the slip planes with the lowest friction stresses, and grow until these slip planes become "hard". The friction stresses are associated with short-range order (SRO), and the deformation shifts to harder volumes where more dipole arrays are formed. These arrays continue to form and grow until the applied stress is sufficient to trigger the formation of intense shear bands (ISBs). The ISBs initiate at grain boundaries and spread out into the grains thereby destroying the dipole arrays. This explains the cyclic softening which apparently is explained by the presence of SRO. SRO can also account for the slip planarity observed in brass, which raises the question of the importance of the stacking fault energy (SFE) in the promotion of planar slip.

Slip modes and chemical composition. The present results reveal, that Cu-30%Zn is a pure planar slip alloy, while Cu-15%Zn displays both planar and wavy slip. At low plastic strain amplitudes the deformation mode in Cu-15%Zn is dominated by planar slip, but at ~10^{-3} there is a transition towards a more wavy slip mode. At high amplitudes the dislocation structures consist of walls, cells and planar arrays, apparently uncorrelated with the crystallographic orientation of the polycrystal grains. This transition is also reflected in the shape of the CSS curve; at low amplitudes the CSS curve for Cu-15%Zn and Cu-30%Zn coincide, while at high amplitudes the CSS curve for Cu-15%Zn shifts towards the curve for copper. The transition in slip mode found in Cu-15%Zn is similar to recent findings in 316L austenitic stainless steels, which also display a comparable cyclic hardening/softening behaviour. Moreover, the present investigations show that Cu-30%Zn and 316L have approximately the same fatigue life curve. These structural and mechanical similarities emphasize brass as being a convenient model system for the industrially important austenitic steels.

Damage characterization and analysis. A quantitative fatigue damage characterization was carried out using a classification of surface cracks based on their length and growth behaviour. This was done with the aim of using the Monte Carlo type model introduced by Bataille & Magnin. The model had to be further developed in order to account for the pronounced intergranular cracking observed in Cu-30%Zn, which was found to dominate increasingly with increasing plastic strain amplitude. This is suggested to be an effect of the Sachs type intergranular stresses. The damage characterization led to the identification of damage parameters, which provide a basis of the numerical model. The model was capable of accounting for the observed damage evolution and the fatigue life curve for Cu-30%Zn and 316L austenitic stainless steel.

.

References

(The references to which the present author has contributed are highlighted with **bold** writing)

ABEL, A (1978)
Fatigue of Copper Single Crystals at Low Constant Plastic Strain Amplitudes
Mater. Sci. Engng. **36**, pp. 117-124.

ABEL, A., WILHELM, M. & GEROLD, V. (1979)
Low-Cycle Fatigue of Single Crystals of a Cu-Al Alloys
Mater. Sci. Engng. **37**, pp. 187-200.

AKTAA, J. & SCHINKE, B. (1996)
The Influence of the Hardening State on Time Dependent Damage and Its Consideration in a Unified Damage Model
Fatigue Fract. Engng. Mater. Struct. **19**, pp. 1143-1151.

ARMSTRONG, R., CODD, I., DOUTHWAITE, R. M. & PETCH, N. J. (1962)
The Plastic Deformation of Polycrystalline Aggregates
Phil. Mag. **7**, pp. 45-58.

ASHBY, M. F. (1970)
The Deformation of Plastically Non-homogeneous Materials
Phil. Mag. **21**, pp. 399-424.

BASINSKI, S. J., BASINSKI, Z. S. & HOWIE, A. (1969)
Early Stages of Fatigue in Copper Single Crystals
Phil. Mag. **19**, pp. 899-924.

BASINSKI, Z. S. (1964)
Dislocation Distribution in Deformed Copper Single Crystals
Disc. Faraday Soc. **38**, 93-102.

BASINSKI, Z. S. & BASINSKI, S. J. (1984)
Formation and Growth of Subcritical Fatigue Cracks
Scripta metall. **18**, pp. 851-856.

BASINSKI, Z. S. & BASINSKI, S. J. (1985A)
Low Amplitude Fatigue of Copper Single Crystals - II. Surface Observations
Acta metall. **33**, pp. 1307-1317.

BASINSKI, Z. S. & BASINSKI, S. J. (1985B)
Low Amplitude Fatigue of Copper Single Crystals - III. PSB Sections
Acta metall. **33**, pp. 1319-1327.

BASINSKI, Z. S., KORBEL, A. S. & BASINSKI, S. J. (1980)
The Temperature Dependence of the Saturation Stress and Dislocation Substructure in Fatigued Copper Single Crystals
Acta metall. **28**, pp. 191-207.

BASINSKI, Z. S., PASCUAL, R. & BASINSKI, S. J. (1983)
Low Amplitude Fatigue of Copper Single Crystals - I. The Role of the Surface in Fatigue Failure
Acta metall. **31**, pp. 591-602.

BASQUIN, O. H. (1910)
The Exponential Law of Endurance Tests
Proc. Am. Soc. Testing and Materials **10**, pp. 625-630.

BATAILLE, A. & MAGNIN, T. (1994)
Surface Damage Accumulation in Low-Cycle Fatigue: Physical Analysis and Numerical Modelling
Acta metall. Mater. **42**, pp. 3817-3825.

BILBY, B. A., COTTRELL, A. H. & SWINDEN, K. H. (1963)
The Spread of Plastic Yield from a Notch
Proc. Roy. Soc. London **272**, pp. 304-314.

BOUTIN, J., DICKSON, J. I. & BAÏLON, J.-P. (1984A)
The Cyclic Deformation of 70-30 α-Brass: Internal and Effective Stresses and Dislocation Substructures
In: Time Dependent Fracture. Proceedings of the 11th Canadian Fracture Conference (ed. A. S. Kranz), Martinus Nijhoff, The Hague, pp. 14-26.

BOUTIN, J., MARCHAND, N., BAÏLON, J.-P. & DICKSON, J. I. (1984B)
An Intermediate Plateau in the Cyclic Stress-Strain Curve of a Brass
Mater. Sci. Engng. **67**, pp. L23-L27.

BRECHET, Y., MAGNIN, T. & SORNETTE, D. (1992)
The Coffin-Manson Law as a Consequence of the Statistical Nature of the LCF Surface Damage
Acta metall. mater. **40**, pp. 2281-2287.

BROWN, L. M. (1981)
Dislocations and the Fatigue Strength of Metals
In: Dislocation Modelling of Physical Systems. Proceedings of the International Conference (eds. M. F. Ashby; R. Bullough; C. S. Hartley; J. P. Hirth), Pergamon Press, New York, pp. 51-68.

BROWN, L. M. & OGIN, S. L. (1985)
Role of Internal Stresses in the Nucleation of Fatigue Cracks
In: Fundamentals of Deformation and Fracture. Proceedings of the Eshelby Memorial Symposium (eds. B. A. Bilby; K. J. Miller; J. R. Willis), Cambridge University Press, Cambridge, pp. 501- 528.

BROWN, M. W. (1988)
Aspects of Fatigue Crack Growth
Proc. Instn. Mech. Engrs. **202**, pp. 19-29.

BRØNDSTED, P., BILDE-SØRENSEN, J. B. & PEDERSEN, O. B. (1983)
Cyclic Deformation of Copper and Copper-Alumina Polycrystals
In: Deformation of Multi-Phase and Particle Containing Materials. Proceedings of the 4th Risø International Symposium on Metallurgy and Materials Science (eds. J. B. Bilde-Sørensen; N. Hansen; A. Horsewell; T. Leffers; H. Lilholt), Risø National Laboratory, Roskilde, pp. 179-188.

BUCHINGER, L., CHENG, A. S., STENZL, S. & LAIRD, C. (1986)
The Cyclic Stress-Strain Response and Dislocation Structures of Cu-16 at.%Al Alloy. III: Single Crystals Fatigued at Low Strain Amplitudes
Mater. Sci. Engng. **80**, pp. 155-167.

BUDIANSKY, B & WU, T. T. (1962)
Theoretical Prediction of Plastic Strains of Polycrystals
In: Proceedings of the 4th US National Congress of Applied Mechanics, Am. Soc. Mech. Engnrs, p.1175.

CARSTENSEN, J. V. & PEDERSEN, O. B. (1997A)
Damage in Low Cycle Fatigue of Brass
In: Physics and Mechanics of Finite Plastic & Viscoplastic Deformation. Proceedings of the 6th International Symposium on Plasticity and Its Current Applications (ed. A. S. Khan), Neat Press, Maryland, pp. 187-188.

CARSTENSEN, J. V. & PEDERSEN, O. B. (1997B)
Texture and Grain-Size Effects on Cyclic Plasticity in Copper and Copper-Zinc
Mater. Sci. Engng. **A234-236**, pp. 497-500.

CARSTENSEN, J. V. & PEDERSEN, O. B. (1998)
Slip Modes and Micromechanics of Cyclic Plasticity in Polycrystalline Copper-Zinc
To be submitted to Mater. Sci. Engng.

CARTER, C.B. (1984)
What's New in Dislocation Dissociation
In: Core Structure and Physical Properties. Proceedings of C.N.R.S. International Colloquium on Dislocations (eds. P. Veyssière; L. Kubin; J. Castaing), C.N.R.S., Aussois, pp. 227-251.

CHEN, X., GAO, Q. & SUN, X. F. (1996)
Low-Cycle Fatigue under No-Porportional Loading
Fatigue Fract. Engng. Mater. Struct. **19**, pp. 839-854.

CHRISTOFFERSEN, H. (1996)
Mikrostrukturen i valset kobber (in danish)
Ph.D.thesis, University of Copenhagen (Risø Report No. 958), 147 p.

COCKAYNE, D. J. H. (1973)
The Principles and Practice of the Weak-Beam Method of Electron Microscopy
J. Microscopy **98**, pp. 116-134.

COFFIN, L. F. (1971)
A Note on Low Cycle Fatigue Laws
J. Mater. **6**, pp. 388-402.

COTTRELL, A. H. (1953)
In: *Dislocations and Plastic Flow in Crystals*
Oxford University Press, London, p. 111, 132.

DICKSON, J. I., BOUTIN, J. & HANDFIELD, L. (1984)
A Comparison of Two Simple Methods for Measuring Cyclic Internal and Effective Stresses
Mater. Sci. Engng. **64**, pp. L7-L11.

DUGDALE, D. S. (1960)
Yielding of Steel Sheets Containing Slits
J. Mech. Phys. Solids **8**, pp. 100-104.

ECKERT, R., LAIRD, C. & BASSANI, J. (1987)
Mechanisms of Fracture Produced by Fatigue Cycling with a Positive Mean Stress in Copper
Mater. Sci. Engng. **91**, pp. 81-88.

EDWARDS & ZHANG (1994)
Investigation of Small Fatigue Cracks
Acta metall. mater. **42**, pp.1413-1421, 1423-31.

ESCAIG, B. (1968)
Sur le Glissement Dévié des Dislocations dans la Structure Cubique a Faces Centrées
J. Phys. (France) **29**, pp. 225-239.

ESHELBY, J. D. (1957)
The Determination of the Elastic Field of an Ellipsoidal Inclusion, and Related Problems
Proc. Roy. Soc. **A241**, pp. 376-396.

ESSMANN, U., GÖSELE, U. & MUGHRABI, H. (1981)
A Model of Extrusions and Intrusions in Fatigued Metals. I. Point-Defect Production and the Growth of Extrusions
Phil. Mag. **44**, pp. 405-426.

ESSMANN, U. & MUGHRABI, H. (1979)
Annihilation of Dislocations during Tensile and Cyclic Deformation and Limits of Dislocation Densities
Phil. Mag. **A40**, pp. 731-756.

EXNER, H. E. (1966)
Die Mikroskopische Bestimmung von räumlichen Korngröbenverteilungen in undurchsichtigen Stoffen
Prakt. Metallographie **3**, pp. 334-341.

EXNER, H. E. (1972)
Analysis of Grain- and Particle-Size Distributions in Metallic Materials
Int. metall. Rev. **17**, pp. 25-42.

FEDELICH, B., FRENZ, H., ÖSTERLE, W. & STARK, K. (1996)
Experimental and Numerical Evaluation of Fatigue Crack Initiation and Propagation for IN738LC at 850°C.
In: Proceedings of the 11th European Conference on Fracture, EMAS, Poitiers-Futuroscope, pp. 128-133.

FIGUEROA, J. C., BHAT, S. P., DE LA VEAUX, R., MURZENSKI, S. & LAIRD, C. (1981)
The Cyclic Stress-Strain Response of Copper at Low Strains - I. Constant Amplitude Testing
Acta metall. **29**, pp. 1667-1678.

FLEISCHER, R. L. (1959)
Cross Slip of Extended Dislocations
Acta metall. **7**, pp. 134-135.

FORREST, P. G. & TATE, A. E. L. (1965)
The Influence of Grain Size on the Fatigue Behaviour of 70/30 Brass
J. Inst. Metals **93**, pp. 438-444.
FRIEDEL, J. (1957)

Dislocations and Mechanical Properties of Crystals
Wiley, New York, 243 p.

GALLAGHER, P. C. J. (1970)
The Influence of Alloying, Temperature, and Related Effects on the Stacking Fault Energy
Metall. Trans. **1**, pp. 2429-2461.

GERLAND, M., AIT SAADI, B. & VIOLAN, P. (1987)
Corduroy Contrast in Type 316L Stainless Steel after Cyclic Plastic Deformation
Mater. Sci. Engng. **96**, pp. L1-L4.

GERLAND, M., MENDEZ, J., VIOLAN, P. & AIT SAADI, B. (1989)
Evolution of Dislocation Structures and Cyclic Behaviour of a 316L-type Austenitic Stainless Steel Cycled in vacuo at Room Temperature
Mater. Sci. Engng. **A118**, pp. 83-95.

GEROLD, V. & KARNTHALER, H. P. (1989)
On the Origin of Planar Slip in F.C.C. Alloys
Acta metall. **37**, pp. 2177-2183

GONG, B., WANG, Z., WANG, Z. G. & ZHANG, Y. (1996)
Cyclic Deformation Response and Dislocation Structure of Cu Single Crystals Oriented for Double Slip
Mater. Sci. Engng. **A210**, pp. 94-101.

GONG, B., WANG, Z. & WANG, Z. G. (1997)
Cyclic Deformation Behaviour and Dislocation Structures of [001] Copper Single Crystals - I. Cyclic Stress-Strain Response and Surface Feature.
Acta mater. **45**, pp. 1365-1377.

HANCOCK, J. R. & GROSSKREUTZ, J. C. (1969)
Mechanisms of Fatigue Hardening in Copper Single Crystals
Acta metall. **17**, pp. 77-97.

HANSEN, M. & ANDERKO, K. (1958)
Constitution of Binary Alloys
McGraw-Hill, New York, p. 650.

HANSEN, J., POSPIECH, J. & LÜCKE, K. (1978)
Tables for Texture Analysis of Cubic Crystals
Springer-Verlag, Berlin, p. 9.

HANSEN, N. & RALPH, B. (1982)
The Strain and Grain Size Dependence of the Flow Stress of Copper
Acta metall. **30**, pp. 411-417.

HAWKINS, D. T. (1973)
Metals Handbook, Vol. 8
American Society for Metals, Ohio, p. 301, 359.

HAZZLEDINE, P. M. (1967)
The Contrast on Electron Micrographs caused by Closely Spaced Edge Dislocation Multipoles
Phil. Mag. **15**, pp. 27-42.

HEDWORTH, J. & POLLARD, G. (1971)
The influence of stacking-fault energy on the creep behaviour of a-brasses
Metal Sci. J. **5**, pp. 41-46.

HIRSCH, P. B. (1962)
Extended Jogs in Dislocations in Face-centered Cubic Metals
Phil. Mag. **7**, pp. 67-92.

HIRSCH, P. B., HOWIE, A., NICHOLSON, R. B., PASHLEY, D. W. & WHELAN, M. J. (1965)
Electron Microscopy of Thin Crystals
Butterworths, London, pp. 311-316.

HIRTH, J. P. & LOTHE, J. (1992)
Theory of Dislocations (2nd Edition)
Krieger Publishing Company, Florida, p. 839.

HOLZWARTH, U. & ESSMANN, U. (1994)
Temperature-Induced Rearrangement of the Dislocation Pattern of Persistent Slip Bands in Copper Single Crystals
Appl. Phys. **A58**, pp. 197-210.

HONG, S. I. & LAIRD, C. (1990A)
Mechanisms of Slip Mode Modifications in F.C.C. Solid Solutions
Acta metall. Mater. **38**, pp. 1581-1594.

HONG, S. I. & LAIRD, C. (1990B)
Cyclic Deformation Behaviour of Cu-16at.%Al Single Crystals, Part II: Cyclic Hardening and Slip Behaviour
Mater. Sci. Engng. **A128**, pp. 55-75.

HULL, D. & BACON, D. J. (1984)
Introduction to Dislocations (3rd Edition)
Pergamon Press, Oxford, 257 p.

HUNSCHE, A. & NEUMANN, P. (1988)
Crack Nucleation in Persistent Slipbands
In: Basic Questions in Fatigue: Volume I. ASTM-STP 924 (eds. J. T. Fong; R. J. Fields), American Society for Testing and Materials, Philadelphia, pp. 26-38.

INUI, H., HONG, S. I. & LAIRD, C. (1990)
A TEM Study of Dislocation Structures in Fatigued Cu-16at.%Al Single Crystals.
Acta metall. Mater. **38**, pp. 2261-2274.

JACKSON, P. J. (1985)
Dislocation Modelling of Shear in F.C.C. Crystals
Progress Mater. Sci. **29**, pp. 139-175.

JIN, N. Y. (1989)
Formation of Dislocation Structures During Cyclic Deformation of F.C.C. Crystals - I. Formation of PSBs in Crystals Oriented For Single-Slip
Acta metall. **37**, pp. 2055-2066.

JIN, N. Y. & WINTER, A. T. (1984)
Dislocation Structures in Cyclically Deformed [001] Copper Crystals
Acta metall. **32**, pp. 1173-1176.

JUUL JENSEN, D., HANSEN, N., KJEMS, J. K. & LEFFERS, T. (1984)

In-Situ Texture Measurements by Neutron Diffraction Used in a Study of Recrystallization Kinetics
In: Microstructural Characterization of Materials by Non-Microscopical Techniques. Proceedings of the 5th Risø International Symposium on Metallurgy and Materials Science (eds. N. H. Andersen; M. Eldrup; N. Hansen; D. Juul Jensen; T. Leffers; H. Lilholt; O. B. Pedersen; B. N. Singh), Risø National Laboratory, Roskilde, pp. 325-332.

KANESHIRO, H., KATAGIRI, K., MORI, H., MAKABE, C. & YAFUSO, T. (1988)
Dislocation Structures in the Strain Localized Region in Fatigued 85/15 Brass
Metall. Trans. **19A**, pp. 1257-1262.

KATAGIRI, K., OMURA, A., KOYANAGI, K., AWATANI, J., SHIRAISHI, T. & KANESHIRO, H. (1977)
Early Stage Crack Tip Dislocation Morphology in Fatigued Copper
Metall. Trans. **8A**, pp. 1769-1773.

KELLY, A. & GROVES, G. W. (1970)
Crystallography and Crystal Defects
Longman Group Ltd., Bristol, UK, p. 189.

KEMSLEY, D. S. & PATERSON, M. S. (1960)
The Influence of Strain Amplitude on the Work Hardening of Copper Crystals in Alternating Tension and Compression
Acta metall. **8**, pp. 453-467.

KETTUNEN, P.O. & KOCKS, U. F. (1972)
Fatigue Hardening and Fatigue Life
Acta metall. **20**, pp. 95-103.

KETTUNEN, P. O. & TIAINEN, T. (1981)
Strain Hardening in Monotonic and Cyclic Deformation of Polycrystalline FCC Metals
In: Deformation of Polycrystals: Mechanisms and Microstructures. Proceedings of the 2nd Risø International Symposium on Metallurgy and Materials Science (eds. N. Hansen; A. Horsewell; T. Leffers; H. Lilholt), Risø National Laboratory, Roskilde, pp. 437-444.

KITAGAWA, H., TAKAHASHI, S., SUH, C. M. & MIYASHITA, S. (1979)
Quantitative Analysis of Fatigue Process - Microcracks and Slip Lines Under Cyclic Strains
In: Fatigue Mechanisms. Proceedings of an ASTM-NBS-NSF symposium, ASTM-STP 675 (ed. J. T. Fong), American Society for Testing and Materials, Kansas City, pp. 420-439.

KRIEGER LASSEN, N. C. (1995)
Computerized Analysis of Kikuchi Patterns
In: Microstructural and Crystallographic Aspects of Recrystallization. Proceedings of the 16th Risø International Symposium on Materials Science (eds. N. Hansen; D. Juul Jensen; Y. L. Liu; B. Ralph), Risø National Laboratory, Roskilde, pp. 405-411.

KRÖNER, E. (1961)
Zur Plastischen Verformung des Vielkristalls
Acta metall. **9**, pp. 155- 161.

KRUML, T., POLÁK, J., OBRTLIK, K. & DEGALLAIX, S. (1997)
Dislocation Structures in the Bands of Localised Cyclic Plastic Strain in Austenitic 316L and Austenitic-Ferritic Duplex Stainless Steels.
Acta mater. **45**, pp. 5145-5151.

KUHLMANN-WILSDORF, D. & LAIRD, C. (1979)

Dislocation Behaviour in Fatigue. II. Friction Stress and Back Stress as Inferred from an Analysis of Hysteresis Loops
Mater. Sci. Engng. **37**, pp. 111-120.

KUOKKALA, V.-J., LEPISTO, T. & KETTUNEN, P. (1982)
Random Strain Cycling of Large-Grained Polycrystalline Copper
Scripta metall. **16**, pp. 1149-1152.

LAIRD, C. & BUCHINGER, L. (1985)
Hardening behaviour in Fatigue
Metall. Trans. **16A**, pp. 2201-2214.

LAIRD, C. & FELTNER, C. E. (1967)
The Coffin-Manson Law in Realtion to Slip Character
Trans. metall. Soc. AIME **239**, pp. 1074-1083.

LAIRD, C., STANZL, S., DE LA VEAUX, R. & BUCHINGER, L. (1986)
The Cyclic Stress-Strain Response and Dislocation Structures of Cu-16 at.%Al Alloy - II: Polycrystalline Behaviour
Mater. Sci. Engng. **80**, pp. 143-154.

LAUFER, E. E. & ROBERTS, W. N. (1964)
Dislocation Structures in Fatigued Copper Single Crystals
Phil. Mag. **10**, pp. 883-885.

LEMAITRE, J. (1992)
A Course on Damage Mechanics
Springer-Verlag, Berlin, 210 p.

LEPISTÖ & KETTUNEN (1986)
Comparison of the Cyclic Stress-Strain Behaviour of Single- and <111> Multiple-slip-oriented Copper Single Crystals
Mater. Sci. Engng. **83**, pp. 1-15.

LI, Y. & LAIRD, C. (1994)
Cyclic Response and Dislocation Structures of AISI 316L Stainless Steel
Mater. Sci. Engng. **A186**, pp. 65-86, 87-103.

LISIECKI, L. L. & PEDERSEN, O. B. (1991)
Temperature Dependence of Cyclic Saturation in Low Amplitude Fatigue of Copper Single Crystals
Acta metall. **39**, pp. 1449-1456.

LIU, C. D., YOU, D. X. & BASSIM, M. N. (1994)
Cyclic Strain Hardening in Polycrystalline Copper
Acta metall. Mater. **42**, pp. 1631-1638.

LLANES, L., ROLLETT, A. D., LAIRD, C. & BASSANI, J. L. (1993)
Effect of Grain Size and Annealing Texture on the Cyclic Response and the Substructure Evolution of Polycrystalline Copper
Acta metall. mater. **41**, pp. 2667-2679.

LORETTO, M. H. & SMALLMAN, R. E. (1975)
Defect Analysis in Electron Microscopy
Chapman and Hall Ltd., London, pp. 91-98.
LUKÁS, P. & KLESNIL (1970)
Dislocation Structures in Fatigued Cu-Zn Single Crystals

Phys. Stat. Sol. **37**, pp. 833-842.

LUKÁS, P. & KLESNIL, M. (1971)
Dislocation Structures in Fatigued Single Crystals of Cu-Zn System
Phys. Stat. Sol. (a) **5**, pp. 247-258.

LUKÁS, P. & KLESNIL, M. (1973)
Cyclic Stress-Strain Response and Fatigue Life of Metals in Low Amplitude Region
Mater. Sci. Engng. **11**, pp. 345-356.

LUKÁS, P., KLESNIL, M. & KREJCÍ (1968)
Dislocations and Persistent Slip Bands in Copper Single Crystals Fatigued at Low Stress Amplitudes
Phys. Stat. Sol. **27**, pp. 545-557.

LUKÁS, P., KLESNIL, M. & POLÁK, J. (1974)
High Cycle Fatigue Life of Metals
Mater. Sci. Engng. **15**, pp. 239-245.

LUKÁS, P. & KUNZ, L. (1985)
Is There a Plateau in the Cyclic Stress-Strain Curves of Polycrystalline Copper?
Mater. Sci. Engng. **74**, pp. L1-L5.

LUKÁS, P. & KUNZ, L. (1987)
Eccect of Grain Size on High Cycle Fatigue Behaviour of Polycrystalline Copper
Mater. Sci. Engng. **85**, p. 67-75.

LUKÁS, P. & KUNZ. L. (1996)
Fatigue Behaviour of Single Crystals and Polycrystals
In: The Johannes Weertman Symposium. TMS Annual Meeting (eds. R. J. Arsenault; D. Cole; T. Gross; H. Sizek; P. Liaw; S. Parameswaran; G. Kostorz), The Minerals, Metals & Materials Society, Anaheim, pp. 279-290.

LUKÁS, P., KUNZ, L., COCHNAR, Z. & BARTOS, J. (1991)
Cyclic Stress-Strain Curve of Single Crystals of Cu-22%Zn Alloy
Mater. Sci. Engng. **A145**, pp. L19-L21.

LUKÁS, P., KUNZ, L. & KREJCÍ, J. (1992)
Fatigue Behaviour of Single Crystals of a Cu-22%Zn Alloy
Mater. Sci. Engng. **A158**, p. 177-183.

MA, B.-T. & LAIRD, C. (1989)
Overview of Fatigue Behaviour in Copper Single Crystals - I. Surface Morphology and Stage I Crack Initiation Sites for Tests and Constant Strain Amplitude.
Acta metall. **37**, pp. 325-336.

MA, B.-T., WANG, Z. G., RADIN, A. L. & LAIRD, C. (1990)
Asymmetry Behaviour Between Tension and Compression in the Cyclic Deformation of Copper Single Crystals and Other Ductile Metals
Mater. Sci. Engng. **A129**, pp. 197-206.

MADELAINE-DUPUICH, O., CARSTENSEN, J. V., STOLARZ, J. & MAGNIN, T. (1998)
Numerical Simulation of Low Cycle Fatigue Damage in Multiphase Materials
To be submitted to Fatigue Fract. Engng. Mater. Struct.
MAGNIN, T., COUDREUSE, L. & LARDON, J. M. (1985)
A Quantitative Approach to Fatigue Damage Evolution in FCC and BCC Stainless Steels
Scripta metall. **19**, pp. 1487-1490.

MAGNIN, T., RAMADE, C., LEPINOUX, J. & KUBIN, L. P. (1989)
Low-Cycle Fatigue Damage of F.C.C. and B.C.C. Polycrystals: Homologous Behaviour?
Mater. Sci. Engng. **A118**, pp. 41-51.

MARCHAND, N., BAÏLON, J.-P. & DICKSON, J. I. (1983)
The Cyclic Response and Strain Life Behaviour of Polycrystalline Copper and a-Brass
In: Defects, Fracture and Fatigue. Proceeding of the 10th Canadian Fracture Conference (eds. G. C. Sih & J. W. Provan), Martinus Nijhoff Publishers, The Hague, pp. 195-208.

MCGRATH, J. T. & THURSTON, R. C. A. (1963)
The Effect of Cross Slip on the Fatigue Behaviour of Copper and Copper-Zinc Alloys
Trans. Metall. Soc. AIME **227**, pp. 645-650.

MOTT, N. F. (1958)
A Theory of the Origin of Fatigue Cracks
Acta metall. **6**, pp. 195-197.

MUGHRABI, H. (1978)
The Cyclic Hardening and Saturation Behaviour of Copper Single Crystals
Mater. Sci. Engng. **33**, pp. 207-223.

MUGHRABI, H. (1979)
Plateaus in the Cyclic Stress-Strain Curves of Single- and Polycrystalline Metals
Scripta metall. **13**, pp. 479-484.

MUGHRABI, H., ACKERMANN, F. & HERZ, K. (1979)
Persistent Slip Bands in Fatigued Face-Centered and Body-Centered Cubic Metals
In: Fatigue Mechanisms. Proceedings of an ASTM-NBS-NSF symposium, ASTM-STP 675 (ed. J. T. Fong), American Society for Testing and Materials, Kansas City, pp. 69-97.

MUGHRABI, H. & WANG, R. (1981)
Cyclic Deformation of Face-Centered Cubic Polycrystals: A Comparison With Observations on Single Crystals
In: Deformation of Polycrystals: Mechanisms and Microstructures. Proceedings of the 2nd Risø International Symposium on Metallurgy and Materials Science (eds. N. Hansen; A. Horsewell; T. Leffers; H. Lilholt), Risø National Laboratory, Roskilde, pp.87-98.

MUGHRABI, H. & WANG, R. (1982)
Cyclic Strain Localization and Fatigue Crack Initiation in Persistent Slip Bands in Face-Centered Cubic Metals and Single-Phase Alloys
In: Proceedings of the International Symposium on Defects and Fracture (eds. G. C. Sih; H. Zorski), Martinus Nijhoff Publishers, The Hague, pp. 15-28.

MUGHRABI, H., WANG, R., DIFFERT, K. & ESSMANN, U. (1983)
Fatigue Crack Initiation by Cyclic Slip Irreversibilities in High Cycle Fatigue
In: Fatigue Mechanisms: Advances in Quantitative Measurements of Physical Damage. ASTM-STP 811 (eds. J. Lankford; D. L. Davidson; W. L. Morris; R. P. Wei), American Society for Testing and Materials, Kansas City, pp. 5-45.

MULVAD, C. (1983)
Monoton og cyklisk deformation i kobber polykrystal. Kornstørrelse og tekstureffekt (in danish)
M. Sc. thesis, Technical University of Denmark, 82. p.
NAVARRO, A. & DE LOS RIOS, E. R. (1988)
Short and Long Fatigue Crack Growth: A Unified Model.
Phil. Mag. **57A**, pp. 15-36.

NEUHÄUSER, H., ARKAN, O. B. & POTTHOFF, H.-H. (1986)
Dislocation Multipoles and Estimation of Frictional Stress in f.c.c. Copper Alloys
Mater. Sci. Engng. **81**, pp. 201-209.

OLFE, J. & NEUHÄUSER, H. (1988)
Dislocation Groups, Multipoles, and Friction Stresses in α-CuZn Alloys
Phys. Stat. Sol. **A109**, pp. 149-160.

OCHI, Y., ISHII, A. & SASAKI, S. K. (1985)
An Experimental and Statistical Investigation of Surface Fatigue Crack Initiation and Growth
Fatigue Fract. Engng. Mater. Struct. **8**, pp. 327-339.

PANDE, C. S. & HAZZLEDINE, P.M. (1971)
Dislocation Arrays in Cu-Al Alloys
Phil. Mag. **24** (2), pp. 1039-1057, 1393-1410

PEDERSEN, O. B. (1981)
Persistent Slip in Copper Polycrystals
In: Deformation of Polycrystals: Mechanisms and Microstructures. Proceedings of the 2nd Risø International Symposium on Metallurgy and Materials Science (eds. N. Hansen; A. Horsewell; T. Leffers; H. Lilholt), Risø National Laboratory, Roskilde, pp. 451-457.

PEDERSEN, O. B. (1990)
Mechanism Maps for Cyclic Plasticity and Fatigue of Single Phase Materials (Overview No. 89)
Acta metall. mater. **38**, pp. 1221-1239.

PEDERSEN, O. B. (1996)
A Static-Dynamic Model for the Process of Cyclic Saturation in Fatigue of Metals
Phil. Mag. **A73**, pp. 829-858.

PEDERSEN, O. B., JUUL JENSEN, D. & POLÁK, J. (1997)
Texture measurements carried out at Risø's reactor DR3 on polycrystalline copper used in the investigations by POLÁK *ET AL.* (1991). A [111]⟨100⟩ texture was unveiled.

PEDERSEN, O. B., RASMUSSEN, K. V. & WINTER, A. T. (1982)
The Cyclic Stress-Strain Curve of Polycrystals
Acta metall. **30**, pp. 57-62.

PEDERSEN, O. B. & WINTER, A. T. (1982)
Fatigue Hardening and Nucleation of Persistent Slip Bands in Copper
Acta metall. **30**, pp. 711-718.

PEDERSEN, O. B. & WINTER, A. T. (1995)
Cyclic Hardening and Slip Localization in Single Slip Oriented Copper Crystals
Phys. Stat. Sol. **A149**, pp. 281-296.

PERALTA, P., LLANES, L., CZAPKA, A. & LAIRD, C. (1995)
Effect of Texture and Grain Size as Independent Factors in the Cyclic Behaviour of Polycrystalline Copper
Scripta metall. Mater. **32**, pp. 1877-1881.

PLESSING, J., ACHMUS, CH., NEUHÄUSER, H., SCHÖNFELD & KOSTORZ, G. (1997)
Short-Range Order and the Mode of Slip in Concentrated Cu-based Alloys
Z. Metallkd. **88**, pp. 630-635.

PLUMBRIDGE, W. J. & RYDER, D. A. (1969)

The Metallography of Fatigue
Metall. Rev. **14**, pp. 119-142.

POHL, K., MAYR, P. & MACHERAUCH. E. (1980)
Persistent Slip Bands in the Interior of a Fatigued Low Carbon Steel
Scripta metall. **14**, pp. 1167-1169.

POLÁK, J., KLESNIL, M. & LUKÁS, P. (1974)
High Cycle Plastic Stress-Strain Response of Metals
Mater. Sci. Engng. **15**, pp. 231-237.

RAMADE, C. (1990)
Mecanisme de microfissuration et endommagement en fatigue oligocyclique de polycristaux monophasés
Ph.D.thesis, Ecole des Mines de St. Etienne.

RASMUSSEN, K. V. & PEDERSEN, O. B. (1979)
Cyclic Deformation of Copper Polycrystals
In: Proceedings of the 5th International Conference of the Strength of Metals and Alloys (Eds. P. Haasen; V. Gerold; G. Kostorz), Pergamon Press, Elmsford, N.Y., pp. 1219-1222.

RASMUSSEN, K. V. & PEDERSEN, O. B. (1980)
Fatigue of Copper Polycrystals at Low Plastic Strain Amplitudes
Acta metall. **28**, pp. 1467-1478.

RASMUSSEN, T. (1997)
Atomic Scale Simulation of Dislocation Reactions
Ph.D. thesis, Tech. Univ. Denmark, 61 p.

RASMUSSEN, T., JACOBSEN, K. W., LEFFERS, T. & PEDERSEN, O. B. (1997A)
Simulations of the Atomic Structure, Energetics, and Cross Slip of Screw Dislocations in Copper
Phys. Rev. **B56**, pp. 2977-2990.

RASMUSSEN, T., JACOBSEN, K. W., LEFFERS, T., PEDERSEN, O. B., SRINIVASAN, S. G., & JÓHNSON, H (1997B)
Atomistic Determination of Cross-Slip Pathway and Energies
Phys. Rev. Letters **79**, pp. 3676-3679.

REINHARD, L., SCHÖNFELD, B., KOSTORZ, G. & BÜHRER, W. (1990)
Short-range Order in a-Brass
Phys. Rev. **B41**, pp. 1727-1734.

ROLIM LOPES, L. C. & CHARLIER, J. (1993)
Effect of Grain Size and Intergranular Stresses on the Cyclic Behaviour of a Ferritic Steel
Mater. Sci. Engng. **A169**, pp. 67-77.

SACHS, G. (1928)
Zur Ableitung einer Fliebbedingung
Z. Ver. Dtsch. Ing. **72**, pp. 734-736.

SEEGER, A. (1957)
Dislocations and Mechanical Properties of Crystals
Wiley, New York, 243 p.

SEGALL, R. L. & FINNEY, J. M. (1963)

The Relation Between Physical Properties and the Observed Dislocation Distribution in Fatigued Metals
Acta metall. **11**, pp. 685-690.

SIMMONS, G. & WANG, H. (1971)
Single Crystal Elastic Constants and Calculated Aggregate Properties: A Handbook
M.I.T. Press, Cambridge MA, p. 185.

STEEDS, J. W. & HAZZLEDINE, P. M. (1964)
Dislocation Configurations in Deformed Copper and Copper 10%(Atomic) Aluminium Alloy
Disc. Faraday Soc. **38**, pp. 103-110.

STOLARZ, J. (1997)
Multicracking in Low Cycle Fatigue - a Surface Phenomenon?
Mater. Sci. Engng. **A234-236**, pp. 861-864.

STROH, A. N. (1954)
Constrictions and Jogs in Extended Dislocations
Proc. Phys. Soc. London **B67**, pp. 427-436.

STROH, A. N. (1955)
Brittle Fracture and Yielding
Phil. Mag. **46**, pp. 968-972.

STRUTT, P. R. (1963)
Dislocation Mechanisms in Cycled a-Brass Single Crystals
J. Australian Inst. Metals **8**, pp. 115-126.

SWANN & LOUAT, N. (1963)
Moiré Fringes at Stacking Faults in Stainless Steels and Copper Alloys
J. Inst. Metals **91**, pp. 243-244.

SWANN & NUTTING (1961)
The Influence of Stacking-Fault Energy on the Modes of Deformation of Polycrystalline Copper Alloys
J. Inst. Metals **90**, pp. 133-138.

TAYLOR, G. I. (1938)
Plastic Strain in Metals
J. Inst. Met. **62**, pp. 307-324.

THOMPSON, N., WADSWORTH, N. & LOUAT, N. (1956)
The Origin of Fatigue Fracture in Copper
Phil. Mag. **1**, pp. 113-126.

TOMKINS, B. (1968)
Fatigue Crack Propagation - An Analysis
Phil. Mag. **18**, pp. 1041-1066.

VAN VLACK, L. H. (1970)
Materials Science for Engineers
Addison-Wesley Publishing Company, Massachusetts, 545 p.

VARIVANI-FARAHANI, A., TOPPER, T. H. & PLUMTREE, A. (1996)
Confocal Scanning Laser Microscopy Measurements of the Growth and Morphology of Microstructurally Short Fatigue Cracks in Al 2024-T351 Alloy
Fatigue Fract. Engng. Mater. Struct. **19**, pp. 1153-1159.

VOGT, J.-B., FOCT, J., REGNARD, C., ROBERT, G. & DHERS, J. (1991)
Low Temperature Fatigue of 316L and 316LN Austenitic Stainless Steels
Metall. Trans. **22A**, pp. 2385-2392.

VOGT, J.-B., MAGNIN, T. & FOCT, J. (1990)
Factors Influencing Planar Slip During Fatigue in FCC Stainless Steels
In: Fatigue 90. Proceedings of the 4th International Conference on Fatigue and Fatigue Thresholds (eds. H. Kitagawa; T. Tanaka), Materials and Component Engineering Publications, Honolulu, pp. 87-92.

VOGT, J.-B., MAGNIN, T. & FOCT, J. (1993)
Effective Stresses and Microstructure in Cyclically Deformed 316L Austenitic Stainless Steel: Effect of Temperature and Nitrogen Content
Fatigue Fract. Engng. Mater. Struct. **16**, pp. 555-564.

WADSWORTH, N. J. (1963)
Work Hardening of Copper Crystals under Cyclic Straining
Acta metall. **11**, pp. 663-673.

WANG, R. & MUGHRABI, H. (1984)
Secondary Cyclic Hardening in Fatigued Copper Monocrystals and Polycrystals
Mater. Sci. Engng. **63**, pp. 147-163.

WANG, R., MUGHRABI, H., MCGOVERN, S. & RAPP, M. (1984)
Fatigue of Copper Single Crystals in Vacuum and in Air. I: Persistent Slip Bands and Dislocation Microstructures
Mater. Sci. Engng. **65**, pp. 219-233.

WANG, Z. (1994)
Cyclis Stress-Strain Response of Alpha Brass Single Crystals Oriented for Easy Glide
Mater. Sci. Engng. **A183**, pp. L13-L17.

WINTER, A. T. (1974)
A Model for the Fatigue of Copper at Low Plastic Strain Amplitudes
Phil. Mag. **30**, pp. 719-738.

WINTER, A. T., PEDERSEN, O. B. & RASMUSSEN, K. V. (1981)
Dislocation Microstructures in Fatigued Copper Polycrystals
Acta metall. **29**, pp. 735-748.

WOODS, P. J. (1973)
Low-Amplitude Fatigue of Copper and Copper-5 at.%Aluminium Single Crystals
Phil. Mag. **28**, pp. 155-191.

WOLF. K., GUDLADT, H.-J., CALDERON. H. A. & KOSTORZ, G. (1994)
Transition between Planar and Wavy Slip in Cyclically Deformed Short-Range Ordered Alloys
Acta metall. mater. **42**, pp. 3759-3765.
YAN, B. D., CHENG, A. S., BUCHINGER, L., STANZL, S. & LAIRD, C. (1986)

The Cyclic Stress-Strain Response of Single Crystals of Cu-16at.%Al Alloy, I: Cyclic Hardening and Strain Localization
Mater. Sci. Engng. **80**, pp. 129-142.

YOUSSEF, T. H. (1970)
Dislocations in α-Brass Single Crystals Fatigued at Low Stress Amplitude
Phys. Stat. Sol. **A3**, pp. 801-810.

ZHANG, Y. H. & EDWARDS, L. (1992)
The Effect of Grain Boundaries on the Development of Plastic Deformation ahead of Small Fatigue Cracks
Scripta metall. Mater. **26**, p. 1901-1906.

Appendix A - Relevant Information about Brass

In this appendix relevant information about brass will be given to support the observations and discussions offered throughout the thesis. A basic description of the dislocation behaviour in fatigue is included to introduce the concept of cross slip. For further information about dislocation theory the reader is referred to the text by HIRTH & LOTHE (1992).

A.1 Crystal structure

Brass is copper with up to 50% zinc. Copper and zinc have atomic numbers 29 and 30 respectively and there are only small differences in size and weight of the copper atom and the zinc atom. The terms weight percent and atomic percent thus have approximately the same meaning and it is sufficient to state the fraction of zinc in percent (%). This is done throughout this thesis.

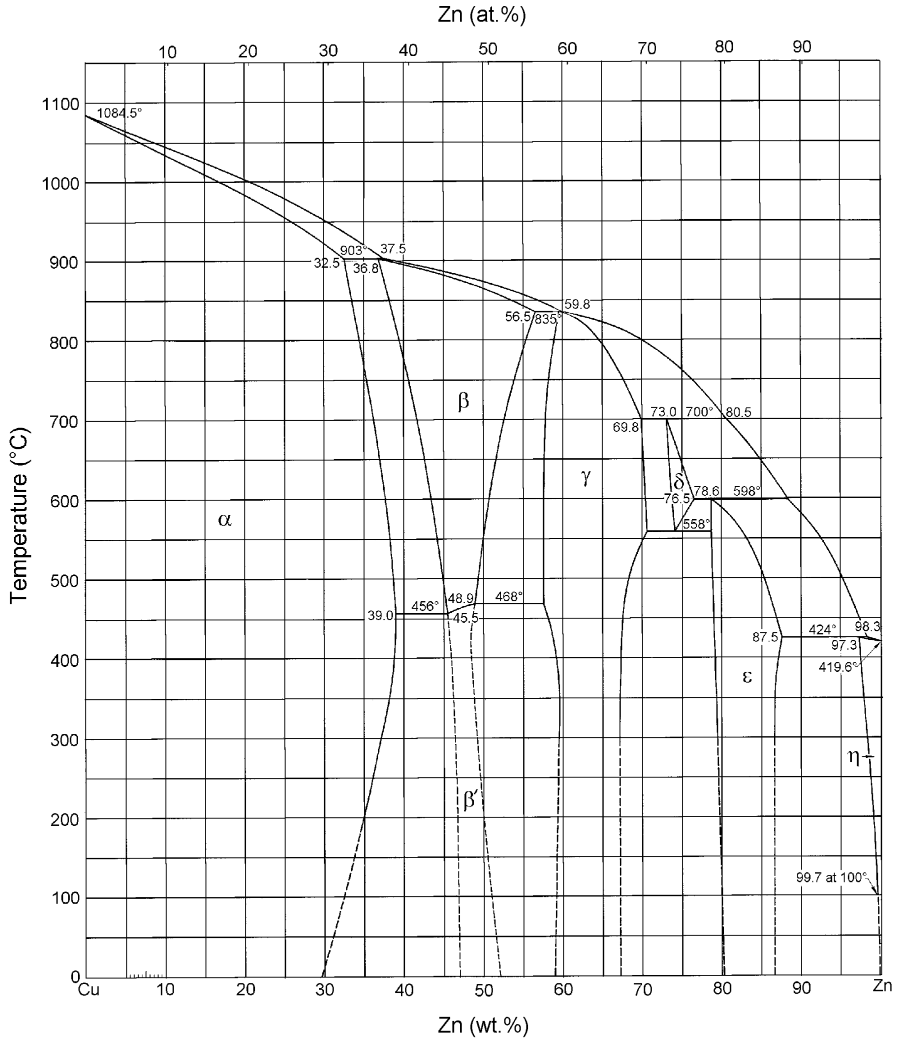

Figure A.1 The Cu-Zn phase diagram revealing single phase α-brass up to 35wt% zinc at room temperature (HANSEN & ANDERKO, 1958; HAWKINS, 1973).

The atomic diameter of copper is 2.556 Å while it is 2.665 Å for zinc, a size difference of 4% (VAN VLACK, 1970). This makes brass a substitutional alloy. Pure copper has a face centered cubic (FCC) crystal structure while pure zinc is hexagonal close-packed (HCP). The Cu-Zn phase diagram shown in Figure A.1 reveal that brass is single phased at room temperature for zinc contents up to approximately 31%. This phase, called α-brass, is FCC, but at zinc contents higher than 31% (at room temperature) a second phase, β´, will be present. β-brass has got a body centered cubic (BCC) crystal structure but the brasses studied in the present project are both single phase α-brasses and thus have a FCC structure.

A.2 Ordering

A strong tendency exists for the copper atoms to surround themselves with zinc atoms and vice versa. This preference for the formation of unlike pairs of atoms, rather than like pairs, is expressed by the inequality

$$E_{CuZn} < \tfrac{1}{2}\cdot(E_{Cu} + E_{Zn}) \tag{A.1}$$

where E_{CuZn} is the energy of an unlike bond, and E_{Cu} and E_{Zn} are the energies of like bonds. It means that, in some cases, the atoms tends to arrange themselves in a preferred manner within the solid solution. The random structure is changed to an ordered structure and the resulting arrangement can be described as a lattice of Cu-atoms interpenetrating a lattice of Zn atoms. This is called a superlattice (HULL & BACON, 1984) and to illustrate it, let us first use β-brass as an example. Imagine that the BCC lattice of β-brass is composed of two sets of sites: *A*-sites at the corners of the unit cell, and *B*-sites at the body centers. When the atomic fraction of Cu and Zn are the same, respectively, as the fractions of *A*-sites and *B*-sites, we have a stoichiometric composition, and perfect ordering can result. This is called long-range order and it is present in CuZn, which is the chemical formula for β-brass. The ordered CuZn structure is shown in Figure A.2a.

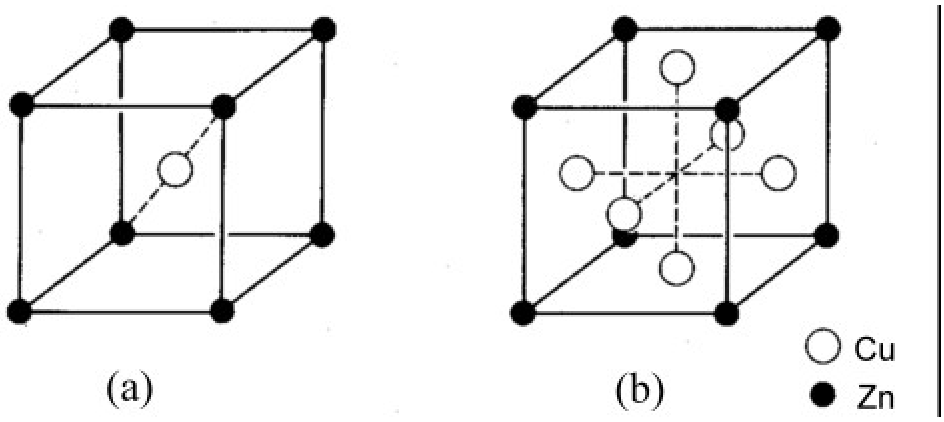

Figure A.2 The ordered structure in (a) CuZn (b-brass, BCC) with zinc at the corners (A-sites) and copper at the body centers (B-sites), and (b) Cu_3Zn (a-brass, FCC) with zinc at the corners (A-sites) and copper at the face centers (B-sites). Note that in the ordered form both the BCC and FCC lattice are based on a simple cubic Bravais lattice.

Imagining the FCC lattice of α-brass with the corners designated as *A*-sites and the face centers as *B*-sites, we also have a stoichiometric composition in the case of Cu-25%Zn or Cu_3Zn. This is illustrated on Figure A.2b, but looking at the phase diagram in Figure A.1 it is noted, that Cu_3Zn does not exist as an individual phase. This means that long-range order is absent in α-brass. Instead a different type of order, called local order, may be present. Local order constitutes a departure from randomness in the sense that each Cu-atom may have other than a random number of Cu- and Zn-atoms surrounding it, and similarly for the Zn-atoms. The degree of local order, α_{local} , can be expressed as (VAN VLACK, 1970),

$$\alpha_{local} = 1 - \frac{P_{Zn(Cu)}}{X_{Zn}} \tag{A.2}$$

where $P_{Zn(Cu)}$ is the probability that Zn-atom is located next to a Cu-atom. If an average Cu-atom has a random number of Zn-neighbours, $P_{Zn(Cu)}=X_{Zn}$ and local order is absent. In fact Cu-atoms prefer to surround themselves with Zn-atoms (as stated in equation (A.1)) and thus $P_{Zn(Cu)}>X_{Zn}$ and α_{local} is negative. This is described as short-range order (SRO). In some systems, like the austenitic steels, there is a tendency for the formation of like bonds rather than unlike bonds. Under such circumstances, $P_{Zn(Cu)}<X_{Zn}$ and α_{local} is positive. This situation is called clustering.

It should be emphasized that local order is not merely a reduced amount of long range order. If long range order exists the Zn-atoms are found principally in the same crystallographic positions (e.g. the corner of each cube) and this order is preserved for a large number of neighboring unit cells. Local order implies that there is no preferred position in the lattice for a Zn-atom; on the other hand, the probability of finding a Cu-atom next to a Zn-atom is greater than the random probability.

The presence of SRO is not easily detected and in brass the similarities of the Cu- and Zn-atom makes it even more difficult. For a quantitative investigation of short-range order, diffuse neutron and x-ray scattering are well suited. In comparison with x-rays, the coherent scattering contrast between Cu and Zn is considerably higher for neutrons (8% instead of 0.1%) and can be increased even further (by a factor 3.6) using the ^{65}Cu isotope. In a ^{65}Cu-31.1at.%Zn single crystal, investigated by neutron scattering, REINHARD *ET AL.* (1990) revealed the presence of short-range order and they suggested the ordered phase to be a Cu_3Zn type with a so-called DO_{23} structure. The critical temperature, T_{crit}, was estimated to be ≈330 K.

A.3 Stacking fault energy

When zinc is added to copper the SFE is reduced. This affects the movement of the dislocations during cyclic plastic deformation. In Table A.1 the SFEs of selected materials are compared to the SFE of Cu-15%Zn and Cu-30%Zn. The table reveals the problem of research on industrial materials. The SFE of austenitic steels vary from low to intermediate values dependent on the various alloying elements. It is thus difficult to investigate basic fatigue mechanisms of austenitic steels in general. Because of this the research on fatigue of austenitic steels has been concentrated on a few specific steel types. One of these, the AISI 316L austenitic stainless steel, is mentioned in this thesis. It has a SFE of approximately 28 mJ/m^2 (MAGNIN *ET AL.*, 1989).

Table A.1 Stacking fault energies of selected materials including Cu-15%Zn and Cu-30%Zn studied in this project. The data are taken from (1) Hirth and Lothe (1992), (2) Carter (1984), (3) Rasmussen (1997), (4) Hedworth and Pollard (1971), and (5) Gallagher (1970).

Material	Stacking fault energy [mJ/m^2]
Aluminum	166 (1)
Zinc	140 (1)
Nickel	125 (1,2)
Copper	55 (3)
Austenitic steels	18-55 (2)
Cu-15%Zn	27 (4,5)
Cu-30%Zn	15 (4,5)

A.4 Cross slip

In general, screw dislocations tend to move in certain crystallographic planes. Thus, in FCC materials the screw dislocations move in {111} type planes, but can switch from one {111} type plane to another. This process, known as *cross slip*, is illustrated in Figure A.3 for a small loop of dislocation line, Burgers vector **b** = $\frac{1}{2}[110]$, expanding under the influence of a local stress field.

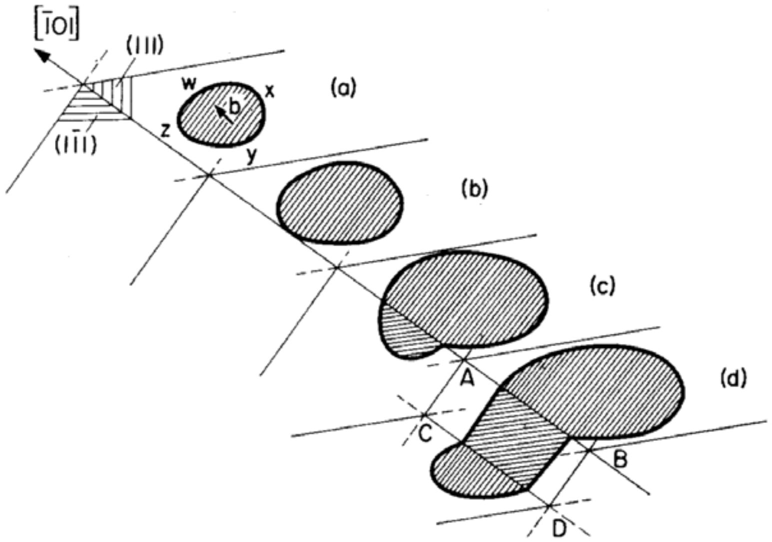

Figure A.3 Cross slip in a FCC crystal. The $[\bar{1}01]$ direction is common to (111) and $(1\bar{1}1)$ close-packed planes. A screw dislocation at z is free to glide in either of these planes. Cross slip produces a non-planar slip surface. Double cross slip is shown in (d) (Hull & Bacon, 1984).

If the local stress field changes, so that motion is preferred on $(1\bar{1}1)$ instead of (111), the screw dislocation will cross slip as shown in Figure A.3(b) and (c). This is possible because the screw dislocations (x and z) have the same Burgers vectors and line vectors in both the primary slip plane and in the cross slip plane. For edge dislocations (w and y) the line vectors are different in the primary slip plane and the cross slip plane and thus edge dislocations cannot cross slip.

Cross slip is more difficult to achieve when dissociation occurs, for a $\frac{1}{6}\langle 112\rangle$ vector lies in only one {111} plane so an individual Shockley partial cannot cross slip. An extended dislocation is therefore constrained to glide in the {111} of its fault. However, it is possible to form a constriction in the screw dislocation and then the unit dislocation at the constriction will be free to move in other planes. Several possible cross-slip mechanisms have been proposed (SEEGER, 1957; FLEISCHER, 1959; HIRSCH, 1962) but recently the model by FRIEDEL (1957) and ESCAIG (1968) has attracted most attention. In this model (denoted the FE model) the dissociated screw dislocation must be constricted over a short length, comparable to a few times the dissociation width, in the primary glide plane before the subsequent redissociation in the cross-slip plane, see Figure A.4.

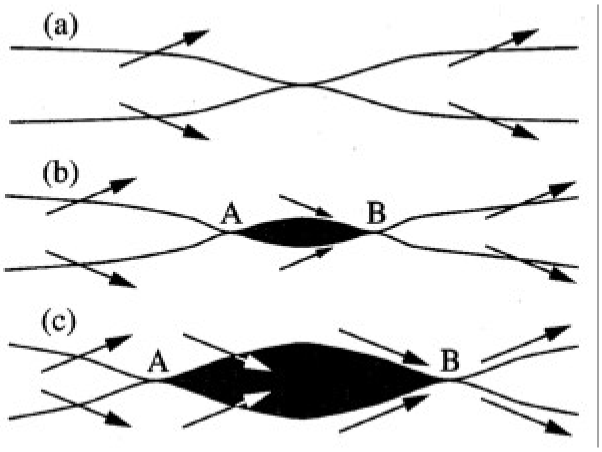

Figure A.4 The Friedel-Escaig mechanism for cross-slip.(a) Creation of a Stroh-type constriction in the primary plane. (b) Dissociation in the cross-slip plane (shaded) creating two twisted constrictions A and B. (c) Two non-interacting constrictions. The Burgers vectors are indicated by arrows. Due to the different characters of the Shockley partials, the two constrictions are not equivalent. The constrictions A and B are denoted "edgelike" and "screwlike", respectively (RASMUSSEN ET AL., 1997A).

The FE model is derived on the basis of the line tension approximation following the method for calculating the constriction energy and shape by STROH (1954). Recent work on nanoscale atomistic simulations of cross slip in copper (RASMUSSEN *ET AL.*, 1997B) support the Friedel-Escaig mechanism.

The formation of a constriction is a thermally activated process and hence the ease of cross slip decreases with decreasing temperature. The amount of energy associated with the formation of the constriction depends on the width of the stacking fault. Constrictions will form more readily in metals with high or intermediate stacking fault energies (and thus narrow stacking faults) such as aluminium or copper. In metals with low stacking fault energy, such as brass, cross slip will be more difficult, and this have influence on the deformation behaviour.

Cross slip is a key parameter in cyclic deformation because it controls both the multiplication and the annihilation of dislocations. In the following two possible mechanisms will be presented.

A.4.1 Multiplication of dislocations

During cyclic deformation the loading direction is continuously reversed and thus the dislocations are moving back and forth. A plausible multiplication process is shown in Figure A.5.

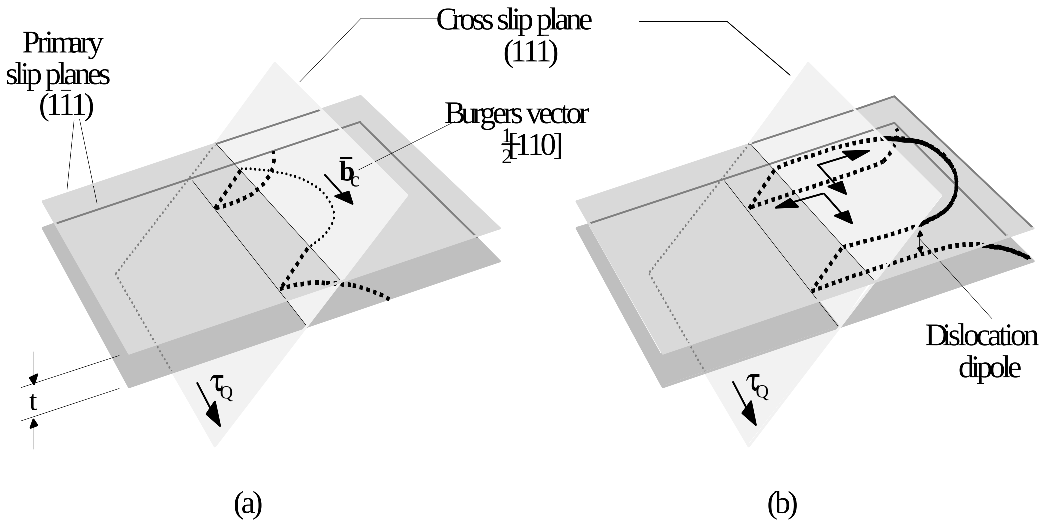

Figure A.5 Multiplication mechanism for dislocations during cyclic deformation. (a) An extended screw dislocation performs double cross slip from one primary slip plane to another, (b) Extended dislocations now spread out in two primary slip planes under the action of an applied shear stress resulting in two edge dislocation dipoles.

A constriction enables an extended screw dislocation, moving in a $(\bar{1}11)$ primary slip plane, to cross slip on to a $(1\bar{1}1)$ cross slip plane (cf. Figure A.4). The dislocation spreads out in the cross slip plane until a second constriction enables cross slip back to a another $(\bar{1}11)$ primary slip plane. This double cross slip process is shown in Figure A.5(a). Extended screw dislocations are now spreading out in two $(\bar{1}11)$ planes under the action of a shear stress τ_Q applied in the [110] direction. The edge segments of the extended dislocations have line vectors of opposite signs in the two $(\bar{1}11)$. This results in two edge dislocation dipoles with a dipole height, *t*, corresponding to the spacing between the two $(\bar{1}11)$. The dipole formation is shown in Figure A.5(b).

A.4.2 Annihilation of dislocations

Dislocations with opposite directions attract each other with elastic forces and if they are close enough to each other they can form a stabile couple, a dipole. In Figure A.6 a schematic representation of a screw dislocation dipole is shown. The spacing between the two dislocations is called the dipole height, and dipoles below a certain height collapses due to the mutual attraction of the dislocations. This height is called the annihilation distance, y. Screw dislocations collapse very easy as screw dislocations are able to cross slip. The screw annihilation distance, y_s, is thus larger than the edge annihilation distance, y_e.

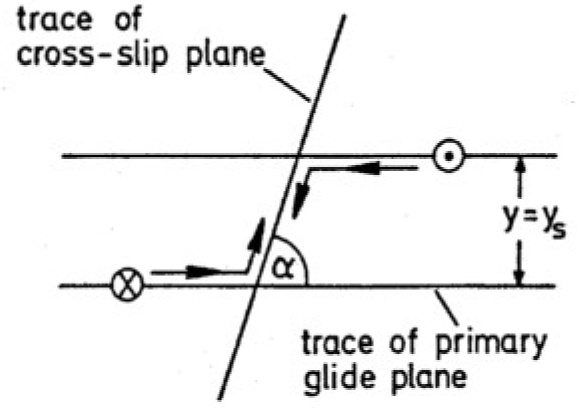

Figure A.6 Annihilation of screw dislocations of opposite sign by cross slip. If the screw dislocations are less distant than y_s they will annihilate. y_s is called the screw annihilation distance (MUGHRABI & WANG, 1982).

Cross slip is frequently induced by internal stresses and related in particular to the mutual attraction and annihilation of unlike screw dislocations on glide planes spaced less than a critical distance apart (BASINSKI, 1964; STEEDS & HAZZLEDINE, 1964). This distance, the screw annihilation distance, decreases not only with decreasing stacking fault energy, increasing strain rate, and decreasing temperature, but also with increasing yield stress and the presence of short-range order. The parameter y_s is thus considered to be more suitable for characterizing the slip mode (wavy or planar) than just the stacking-fault energy (MUGHRABI *ET AL.*, 1983). In copper y_s has been estimated to ~50nm (ESSMANN & MUGHRABI, 1979), whereas in Cu-30%Zn it is considered to be ~5nm (MUGHRABI & WANG, 1982).

Appendix B - Etchants and Electrolytes

D2 - electrolyte used for electropolishing of Cu and Cu-alloys: 250 ml phosphoric acid (H_3PO_4), 500 ml alcohol (e.g. CH_3CH_2OH), 5 ml propane (C_3H_8), 5 g uric acid, 2 ml Vogels inhibitor (prevents corrosion).

Nickel chloride solution - etchant used for surface smoothening of Cu and Cu-alloys: 800 ml nitric acid (HNO_3), 200 ml water (H_2O), 2 g nickel chloride ($NiCl_3$).

OP-S solution - colloidal silica suspension used for final polishing: 96 ml Struers OP-S, 2 ml ammonia (NH_3), 2 ml hydrogen peroxide (H_2O_2).

Potassium dichromate solution - etchant used for enhancement of grain structure: 2g potassium dichromate ($K_2Cr_2O_7$), 8 ml sulfuric acid (H_2SO_4), 100 ml water (H_2O). At use: 1 drop of hydrochloric acid (HCl) per 25 ml solution.

Appendix C - List of Symbols and Abbreviations

Symbol	Meaning	Units
b	Burgers vector	(-)
BCC	Body Centered Cubic (crystal structure)	
CSS(C)	Cyclic Stress Strain (Curve)	
$\overline{D}$	average grain size	(µm)
D	damage parameter	(-)
D_c	critical damage (“fracture criterion”)	(-)
E	modulus of elasticity	(GPa)
f_{PSB}	volume fraction of PSBs	(-)
FCC	Face Centered Cubic (crystal structure)	
FE	Friedel-Escaig (model)	
g	diffraction vector	(-)
h	dipole height	(Å)
h_t	distance between two surface cracks tips	(µm)
HCP	Hexagonal Closed Packed (crystal structure)	
LRO	Long Range Order	
L	crack length	(µm)
L_α	length of gridline α	(µm)
l_β	length of individual gridline intercepts	(µm)
ΔL	crack growth	(µm)
m_S	Sachs factor = 2.238	(-)
m_T	Taylor factor = 3.06	(-)
N	number of cycles	(-)
N_i	number of cycles to initiate a type IV crack = fatigue life	(-)
N_F	number of cycles to fracture	(-)
N^{min}	number of cycles at the minimum locus $(d\sigma/dN)_{min}$	(-)
N^{100}	number of cycles at $\varepsilon_{cum}=100$	(-)
n	constant (power law CSS relation)	(-)
n_α	number of boundaries intersected by gridline α	(-)
ODF	Orientation Distribution Function	
OM	Optical Microsco(e/y)	
PLB	Persistent Lüders Band	
PSB	Persistent Slip Band	
PSL	Persistent Slip Line	
R	radius of curvature	(mm)
r_p	plastic zone size	(µm)
SCSE	Self-Consistent Sachs-Eshelby (model)	
SD	Static-Dynamic (model)	
SEM	Scanning Electron Microscop(e/y)	
SFE	Stacking Fault Energy	
SRO	Short Range Order	
TEM	Transmission Electron Microscop(e/y)	
T_{crit}	critical temperature (above which no order is present)	(K)
T_m	melting point	(K)
w	width of a dislocation image	(nm)
ø	diameter	(mm)
Y	strain energy density release rate	(J/m^3)
y_e	edge (dislocation) annihilation distance	(nm)
y_s	screw (dislocation) annihilation distance	(nm)
α	Basquin parameter	(-)

α_{local}	degree of local order	(-)
β	Manson-Coffin parameter	(-)
δ	cyclic softening parameter = $(\sigma_{max}-\sigma_{min})/\sigma_{max}$	(%)
ε	strain	(-)
$\dot{\varepsilon}$	strain rate	(s^{-1})
ε_{comp}	compressive plastic strain amplitude	(-)
ε_{cum}	cumulative plastic strain = $4 \cdot N \varepsilon_{pa}$	(-)
ε_{cum}^{D}	damage threshold	(-)
ε_e	elastic strain	(-)
$\varepsilon_{anelastic}$	anelastic strain	(-)
ε_p	plastic strain	(-)
ε_{pa}	plastic strain amplitude = $\Delta\varepsilon_p/2$	(-)
ε_{tens}	tensile plastic strain amplitude	(-)
ε_{tot}	total strain	(-)
$\Delta\varepsilon_p$	plastic strain range = $\varepsilon_{tens}-\varepsilon_{comp}$	(-)
Γ	Eshelby factor	(-)
γ	resolved shear strain	(-)
γ_{matrix}	resolved plastic shear strain amplitude in the matrix structure	(-)
γ_p	resolved plastic shear strain	(-)
γ_{pa}	resolved plastic shear strain amplitude	(-)
γ_{PSB}	resolved plastic shear strain amplitude in Persistent Slip Band	(-)
γ_{SFE}	stacking fault energy	(mJ/m^2)
θ	dipole angle	(°)
ρ_{crack}	crack density	(mm^{-2})
ρ_G	density of geometrically necessary dislocations	(mm^{-2})
σ	stress	(Mpa)
σ_0	constant (power law CSS relation)	(MPa)
$\sigma_{0.2}$	yield stress	(Mpa)
σ_a	average stress amplitude = $\Delta\sigma/2$	(Mpa)
σ_b^{eff}	effective back stress	(MPa)
σ_{comp}	compressive stress amplitude	(Mpa)
$\sigma_{critical}$	onset of first yield	(MPa)
σ_f	friction stress	(MPa)
σ_i	intergranular stress	(MPa)
σ_{max}	maximum stress reached after initial cyclic hardening	(Mpa)
σ_{min}	minimum stress after cyclic softening, before secondary hardening	(MPa)
σ_{plat}	Sachs estimated plateau stress = $m_S \cdot \tau_{plat}$	(MPa)
σ_{sat}	saturation stress	(MPa)
σ_{tens}	tensile stress amplitude	(Mpa)
σ_y	hysteresis yield stress	(MPa)
$\Delta\sigma$	stress range = $\sigma_{tens}-\sigma_{comp}$	(Mpa)
τ	resolved shear stress	(Mpa)
τ_a	resolved shear stress amplitude	(Mpa)
τ_{plat}	single crystal plateau stress	(MPa)
τ_{sat}	resolved saturation shear stress	(MPa)
ξ_g	extinction distance	(nm)

Bibliographic Data Sheet **Risø-R-1005(EN)**

Title and authors

Structural Evolution and Mechanisms of Fatigue in Polycrystalline Brass

Jesper Vejlø Carstensen

(This thesis is part of the requirements to obtain the Ph.D. degree from the Technical University of Denmark)

ISBN			ISSN
87-550-2347-9			0106-2840
Department or group			Date
Materials Research Department			March 1998
Pages	Tables	Illustrations	References
144	9	94	177

Abstract (max. 2000 characters)

The plastic strain controlled fatigue behaviour of polycrystalline Cu-15%Zn and Cu-30%Zn has been investigated with the aim of studying the effect of slip mode modification by the addition of zinc to copper. It has been clearly demonstrated, that true cyclic saturation does not occur in the plastic strain controlled fatigue of brass. This complicates the construction of a cyclic stress-strain (CSS) curve and thus the comparison with copper. A method to overcome this complication has been suggested. Surface observations on fatigued brass specimens show that individual grains tend to deform by Sachs type single slip. This behaviour has been described by the self-consistent Sachs-Eshelby model, which provides estimates of the CSS curve for brass polycrystals. Successive stages of primary hardening, softening and secondary hardening has been observed in the plastic strain controlled fatigue of brass. It has been found that the primary hardening is attributed to an increase of intergranular stresses whereas the secondary hardening apparently is attributed to an increase of friction stresses. Investigations of the structural evolution show that the softening behaviour can be explained by the presence of short-range order (SRO). SRO promote the formation of extended dipole arrays which hardens the material. The formation of intense shear bands destroy the dipole arrays, which explains the cyclic softening. The present results reveal that Cu-30%Zn is a pure planar slip alloy, while Cu-15%Zn displays both planar and wavy slip. The mechanical and structural behaviour observed in brass resembles recent observations in 316L austenitic stainless steels, and the present results reveal that Cu-30%Zn and 316L have approximately the same fatigue life curve. This emphasizes brass as being a convenient model system for the industrially important austenitic steels. A quantitative fatigue damage characterization has been carried out using a classification of surface cracks based on their length and growth behaviour. This has provided the basis for using a numerical Monte Carlo type model, which has been further developed to account for the observed intergranular damage evolution on Cu-30%Zn. With these modifications the model predicts the fatigue life curve of Cu-30%Zn and 316L.

Descriptors INIS/EDB

brass, crack propagation, deformation, dislocations, fatigue, grain boundaries, mathematical model, mechanisms, Monte Carlo method, polycrystals, scanning electron microscopy, slip, strains, stresses, transmission electron microscopy.

Available on request from Information Service Department, Risø National Laboratory,
(Afdelingen for Informationsservice, Forskningscenter Risø), P.O.Box 49, DK-4000 Roskilde, Denmark.
Telephone +45 46 77 40 04, Telefax +45 46 77 40 13